

Copyright

by

Hyun Wook Kang

2006

**The Dissertation Committee for Hyun Wook Kang Certifies that this is the
approved version of the following dissertation:**

**ENHANCEMENT OF HIGH POWER PULSED LASER ABLATION
AND BIOLOGICAL HARD TISSUE APPLICATIONS**

Committee:

Ashley J. Welch, Supervisor

Thomas E. Milner

Shaochen Chen

Stanislav Emelianov

Joel M.H. Teichman

**ENHANCEMENT OF HIGH POWER PULSED LASER ABLATION
AND BIOLOGICAL HARD TISSUE APPLICATIONS**

by

HYUN WOOK KANG, B.S.M.E.; M.S.M.E.

Dissertation

Presented to the Faculty of the Graduate School of

The University of Texas at Austin

in Partial Fulfillment

of the Requirements

for the Degree of

Doctor of Philosophy

The University of Texas at Austin

December, 2006

To My Dear Parents

Acknowledgements

I would like to express my most heartfelt appreciation and gratitude to my supervisor, Prof. A.J. Welch, for giving me an opportunity and leading me to accomplish my PhD degree in the United States. It has been such an honor to be a graduate student under the supervision of Dr. Welch. His continuous support and encouragement through this research have enabled me to work independently and repeat many trials and errors and learn. None of this work would have been achieved without his thoughtful insight and endless patience. My gratitude goes to Prof. Thomas E. Milner for providing me with theoretical and experimental skills to solve complicated problems. His intuition and critical questions regarding biomedical optics have been instrumental in my research. I would also like to thank Dr. Teichman at St. Paul's Hospital in Canada for his invaluable advices and collaboration. My appreciations go to Prof. Stanislav Emelianov and Prof. Shaochen Chen for serving on my dissertation committee, allowing me to use their laser systems and providing me with advice to improve the quality of my research.

I wish to thank Dr. Ho Lee for being my source of encouragement. Ho introduced me to biomedical research and helped me persevere throughout my studies for which I am ever grateful. I also owe a special debt of thanks to Dr. Jeehyun Kim and Dr. Jihoon Kim for their support and understanding. Jeehyun's meticulous preparations and many creative ideas have been exemplary throughout my academic life in BELL, and I have always enjoyed Jihoon's laid-back and witty personality.

Another person who has had a tremendous influence on my research and Austin life is Dr. Junghwan Oh. While staying up late together in ENS 20E, he patiently taught me innumerable technical skills pertaining to academic research, which none would ever have been willing to provide me. He always encouraged me to overcome wisely and resolutely any ordeal that I had endured. Also, his efforts and enthusiasm toward academic research have been a paragon to me and have shown me the real significance of academic collaboration. I hope that we will keep in touch and continue our collaborations in the future.

I would also like to extend my appreciations to my fellow graduate researchers in biomedical optics lab, who have created an enjoyable work atmosphere. In particular, I am thankful to Chris Condit for tolerating my disturbances with proofreading. With his exceptional corrections, I could persistently develop my academic writing skills. I will never forget Chris

Humphrey who helped me cope with all the UT red tape. A special gratitude also goes to Dr. Kin F. Chen, an ex-longhorn, for his valuable advice and ideas.

I would like to express my love and appreciation to my dear family for their years of sacrifices and prayers. The support of my parents and their trust in me from the beginning to the end has been immeasurable. Everything I have achieved is for both of you. My dear sister, Hyun Jung Kang, supported me by caring for my health and encouraging me all the time. To my lovely wife, Min Ji Kim, I thank you for arguing, caring, loving, and putting up with me.

Last but not least, I would appreciate the Albert W. and Clemie A. Caster Foundation, Biolase Technology, Convergent Laser Technologies, Omniguide, and Stanford University for funding my research and providing their laser systems.

ENHANCEMENT OF HIGH POWER PULSED LASER ABLATION AND BIOLOGICAL HARD TISSUE APPLICATIONS

Publication No. _____

Hyun Wook Kang, Ph.D.

The University of Texas at Austin, 2006

Supervisor: Ashley J. Welch

Pulsed lasers are used therapeutically to selectively remove tissue with minimal thermal and mechanical damage to peripheral tissue. The aims of this research are to understand the governing mechanisms of pulsed infrared laser tissue ablation, to obtain optimal laser parameters for precise laser treatment without collateral damage, and to develop methods for efficient tissue removal with the aid of liquid confinement.

The effect of a liquid layer on laser metal ablation was examined. Acoustic pressure and optical reflectance provided information for determining the dominant mechanisms during metal ablation. The liquid-assisted ablation improved ablation efficiency and reduced the ablation threshold by as much as

40 % with respect to ablation in air. The degree of ablation was contingent on thermal and mechanical properties of the type of metal.

The dynamics of laser osteotomy in a liquid environment was explored. The underlying mechanisms during liquid-assisted ablation included rapid vaporization, plasma confinement, and cavitation with jet formation. Compared to direct ablation, the liquid-confined ablation with higher ablation volume and augmented acoustic excitation demonstrated the feasibility of liquid-enhanced laser osteotomy.

Acoustic transient measurement with a piezoelectric microphone, Schlieren flash photography, and temperature measurement with an IR camera were employed to study ablation mechanisms and the effect of water spray during long-pulsed laser ablation of dental tissues. Spray-assisted ablation created larger pressure transients and enhanced ablation efficiency. Water cooling by the spray provided a safe and efficient modality for dental treatment.

Finally, optimal laser parameters for laser lithotripsy such as wavelength and pulse duration were studied. Higher light absorption of the Er:YAG ($\lambda = 2.94 \mu\text{m}$) laser produced more material removal than the Ho:YAG laser. In addition, during Ho:YAG laser lithotripsy, a smaller fiber diameter with a shorter pulse duration reduced the operative time and cumbersome process due to retropulsive kidney stone movement, providing efficient laser lithotripsy.

Table of Contents

List of Tables.....	xvi
List of Figures.....	xvii
Chapter 1: Introduction	1
1.1 Motivation	1
1.2 Goal of Research	2
1.3 Overview	4
1.4 Nomenclature and Notation	8
1.5 References	9
Chapter 2: Pulsed Laser-induced Ablation.....	11
2.1 Introduction	11
2.2 Near-Far Infrared Radiation	12
2.3 Laser-tissue Interaction Mechanisms	12
2.3.1 Laser-induced Ablation in non-scattering media	12
2.3.2 Photothermal Ablation	13
2.3.3 Photomechanical Ablation	15
2.3.4 Plasma-mediated Ablation (Photodisruption)	16
2.4 Ablation Plume Dynamics	18
2.4.1 Plume formation and Expansion	18
2.4.2 Recoil Stress	19
2.5 Ablation Models	19
2.6 Optimal and Selective Ablation	20
2.7 References	21
Chapter 3: Laser Ablation in a Liquid-confined Environment Using a Nanosecond Laser Pulse	23

3.1	Abstract	23
3.2	Introduction	23
3.3	Materials and Methods	25
3.4	Results	28
3.5	Discussion	33
3.6	Conclusion.....	37
3.7	References	38
Chapter 4: Evaluation of Liquid-assisted Laser Ablation with Various Metal		
	Samples	40
4.1	Abstract	40
4.2	Introduction	40
4.3	Materials and Methods	42
4.4	Results	46
4.5	Discussion	55
4.6	Conclusion.....	59
4.7	References	60
Chapter 5: Enhancement of Bovine Bone Ablation Assisted by a Transparent		
	Liquid Layer on a Target Surface	62
5.1	Abstract	62
5.2	Introduction	63
5.3	Materials and Methods	65
5.3.1	Specimen	65
5.3.2	Laser Source and Delivery	67
5.3.3	Plasma and Acoustic Wave Detection	69
5.3.4	Ablation Efficiency	69
5.4	Results	70
5.5	Discussion	82
5.6	Conclusion.....	92

5.7	References	93
Chapter 6: Investigations on Laser Hard Tissue Ablation under Various Liquid		
	Environments	97
6.1	Abstract	97
6.2	Introduction	98
6.3	Materials and Methods	100
6.3.1	Specimen	100
6.3.2	Experimental Setup	102
6.4	Results	105
6.4.1	Energy Loss Measurement	105
6.4.2	Ablation Efficiency	105
6.4.3	Thermal Side Effects	106
6.5	Discussion	109
6.6	Conclusion.....	113
6.7	References	114
Chapter 7: Effect of Liquid Thickness on Laser Ablation Efficiency		
	(Experimental Study)	117
7.1	Abstract	117
7.2	Introduction	118
7.3	Materials and Methods	119
7.4	Results	122
7.5	Discussion	125
7.6	Conclusion.....	128
7.7	References	129
Chapter 8: Mechanisms of Spray-assisted Laser Ablation of Dental Hard Tissue		
	131
8.1	Abstract	131
8.2	Introduction	132

8.3	Materials and Methods	135
8.3.1	Specimen	135
8.3.2	Laser Source and Water Spray System	136
8.3.3	High-speed Imaging and Acoustic Wave Monitoring.....	137
8.3.4	Beam Profile.....	138
8.3.5	Light Transmission and Temperature Measurement.....	140
8.3.6	Ablation Threshold and Efficiency	142
8.4	Results	143
8.4.1	Beam Profile.....	143
8.4.2	Effect of Water Spray Flow Rate	144
8.4.3	Ablation Threshold.....	146
8.4.4	Transmission Measurement.....	146
8.4.5	Temperature Measurement.....	147
8.4.6	Ablation Efficiency	149
8.4.7	Pressure Measurements	153
8.4.8	High-speed Imaging	159
8.5	Discussion	162
8.6	Conclusion.....	177
8.7	References	178
Chapter 9: Urinary Calculus Fragmentation During Ho:YAG and Er:YAG		
	Lithotripsy	182
9.1	Abstract	182
9.2	Introduction	183
9.3	Materials and Methods	184
9.4	Results	189
9.4.1	Beam Profiles	189
9.4.2	Cross-sectional Profiles.....	192
9.4.3	Crater Depth and Width	197

9.4.4	Ablation Volume	197
9.5	Discussion	203
9.6	Conclusion.....	212
9.7	References	213
Chapter 10: Dependence of Calculus Retropulsion on Pulse Duration During		
	Ho:YAG Laser Lithotripsy.....	217
10.1	Abstract	217
10.2	Introduction	218
10.3	Materials and Methods	220
10.4	Results	227
10.4.1	Retropulsion Distance Measurements	227
10.4.2	Ablation Volume Measurements.....	227
10.4.3	Comparison of Normalized Stone Retropulsion	230
10.4.4	Fast-flash Photography of Laser-induced Bubble Formation	230
10.4.5	Acoustic Transients: Ablation in Water	231
10.4.6	Comparison of Bubble collapse	235
10.4.7	Acoustic transients: Ablation in contact mode.....	235
10.5	Discussion	238
10.6	Conclusion.....	247
10.7	References	247
Chapter 11: Conclusions and Future Studies		
11.1	Objectives.....	251
11.2	Effect of Liquid Confinement on Ablation Efficiency.....	251
11.3	Clinical Implications of Laser Lithotripsy	253
11.4	Future Directions.....	254
11.4.1	Role of Individual Pulse in Macropulse Ablation	254
11.4.2	Mid-Infrared Pulsed Laser Ablation	254

11.4.3	Evaluation of Hollow Waveguide for Er:YAG Laser Lithotripsy	255
11.5	References	256
Appendix A: Calculus Fragmentation in Laser Lithotripsy		257
A.1	Abstract	257
A.2	Introduction	258
A.3	Laser-induced Ablation (Fragmentation)	259
A.3.1	Photothermal Ablation	263
A.3.2	Photoacoustical/Photomechanical Ablation	267
A.4	Review of Laser lithotripsy	276
A.5	Future Devices	282
A.6	Conclusion	287
A.7	References	288
Bibliography		296
Vita		320

List of Tables

Table 1.1	Symbols used in this dissertation.....	8
Table 3.1	The properties of aluminum and water used for calculations.....	35
Table 4.1	Optical, thermal, and mechanical properties of target materials...	43
Table 4.2	Damage, acoustic, and plasma thresholds of dry and wet ablation for all the materials.....	53
Table 5.1	Optical, thermal, and mechanical properties for water and bone..	66
Table 6.1	Optical and thermal properties of bone, water, and perfluorocarbon.....	101
Table 8.1	Optical, thermal, and mechanical properties of water and enamel.....	135
Table A.1	Nomenclature of laser parameters and tissue properties.....	261
Table A.2	Characteristics of infrared optical fibers to deliver Er:YAG laser (λ = 2.94 μm) light.....	286

List of Figures

Figure 2.1	Penetration depth (δ) of laser light in tissue as a function of laser pulse duration (τ_p) for various lasers: each dotted line determines a governing mechanism of laser-induced tissue ablation18
Figure 3.1	Schematic illustration of laser ablation with optical reflectance and acoustic pressure measurements. BS: beam splitter, M: mirror, PD: photodetector, IF: interference filter27
Figure 3.2	(a) Cross-sectional profiles of craters produced on Aluminum during dry (top) and wet (bottom) ablation ($H = 1.43 \text{ J/cm}^2$ per pulse and 500 pulses) and (b) comparison of ablation rates for dry and wet conditions as a function of radiant exposure per pulse ($n = 3$ and 100 pulses).....30
Figure 3.3	Comparison of peak acoustic amplitudes for dry and wet ablation as a function of radiant exposure ($n = 10$ and single pulse).....30
Figure 3.4	Comparison of transient acoustic pressure (left-hand side column) and optical reflectance (right-hand side column) at various radiant exposures with a single pulse: (a) $H = 0.31 \text{ J/cm}^2$ (top), (b) $H = 0.41 \text{ J/cm}^2$ (wet damage threshold, middle), and (c) $H = 0.61 \text{ J/cm}^2$ (bottom).....32
Figure 3.5	SEM images of Aluminum for wet ablation with (a) $H = 1.43 \text{ J/cm}^2$ and a single pulse and (b) $H = 2.24 \text{ J/cm}^2$ per pulse and 100 pulses (Arrows indicate the trace of bubbles).....32
Figure 3.6	Temperature distribution after the short laser pulse (1 ns) inside water and aluminum media at $H = 0.41 \text{ J/cm}^2$35
Figure 4.1	Schematic (a) and photograph (b) of the experimental setup used in laser ablation.....45
Figure 4.2	Cross-sectional profiles created during dry (left-handed side column) and wet (right-handed side column) ablation with 100 pulses at various fluences per pulse: (a) indium at 1.7 J/cm^2 per pulse, (b) tin at 1.94 J/cm^2 per pulse, (c) aluminum at 3.57 J/cm^2 per pulse, (d) copper at 1.3 J/cm^2 per pulse, and (e) nickel at 2.67 J/cm^2 per pulse. Note a different scale in ablation depth.....50
Figure 4.3	Comparison of ablation depth between dry and wet ablation with 100 pulses as a function of fluence per pulse using various metals: (a) indium, (b) tin, (c) aluminum, (d) copper, and (e) nickel. Note a different scale in ablation depth.....51

Figure 4.4	Comparison of plasma peak intensity (left-handed side column) and lifetime (right-handed side column) as a function of fluence using a single pulse on various metals: (a) indium, (b) tin, (c) aluminum, (d) copper, and (e) nickel.....	53
Figure 4.5	Comparison of peak acoustic amplitudes for dry and wet ablation as a function of fluence using various metals: (a) indium, (b) tin, (c) aluminum, (d) copper, and (e) nickel. Note that no acoustic signal was measured during dry ablation of nickel.....	54
Figure 4.6	Optical reflectance signals measured during wet ablation on (a) aluminum and (b) nickel at various fluences. Note that the signal thresholds for aluminum and nickel were 0.41 J/cm^2 and 0.77 J/cm^2 , respectively.....	55
Figure 5.1	Schematic of an experimental setup to measure plasma formation and acoustic transients using a Q-switched Nd:YAG laser system. BS: beam splitter; PD: photodetector.....	68
Figure 5.2	Vertical cross-sectional images of laser-induced craters with a Q-switched laser with twenty pulses for a dry case at the radiant exposure of (a) 14.9 J/mm^2 and (b) 22.2 J/mm^2 and a wet case at (c) 14.9 J/mm^2 and (d) 22.2 J/mm^2	71
Figure 5.3	Comparison of ablation efficiency for dry and wet ablation as a function of radiant exposure with ten and twenty pulses: (a) crater depth and (b) ablation volume.....	72
Figure 5.4	Top-view images of bovine bone for (a) dry damage threshold ($H = 3.5 \text{ J/mm}^2$) and (b) wet damage threshold ($H = 2.1 \text{ J/mm}^2$).....	73
Figure 5.5	Acoustic signal measured by a piezoelectric transducer during single-pulse ablation in water produced with 22.2 J/mm^2	75
Figure 5.6	Temporal behaviors of transient pressure for (a) dry and (b) wet ablation. Note the difference in scale for dry and wet ablation...	76
Figure 5.7	Comparison of acoustic amplitudes for dry and wet cases as a function of radiant exposure ($n = 10$). (a) Entire radiant exposure and (b) lower radiant exposures between 0 and 10 J/mm^2 expanded from (a) (dotted lines guide a signal trends of each case).....	77
Figure 5.8	Temporal laser pulse and plasma transient detected by a fast photodetector for dry and wet cases at the radiant exposure $H = 17.7 \text{ J/mm}^2$ on the time scale ranging (a) from 0 to 80 ns and (b) from 0 to $2.25 \mu\text{s}$ (entire signal trace).....	80
Figure 5.9	Comparison of laser-induced plasma between dry and wet cases. (a) plasma decay constant and (b) plasma lifetime ($n = 10$).....	81
Figure 5.10	Ratio of $P_{\text{water}}/P_{\text{air}}$ based on 1-D analysis of pressure generation induced by plasma process.....	88

Figure 6.1	Experimental setup for bone ablation study under different environments: (a) wet ablation using water and perfluorocarbon and (b) spray ablation using water. Note the 500 μm distance between fiber tip and the sample surface.....	104
Figure 6.2	Energy transmission as a function of incident pulse energy for three conditions: 500 μm water layer, 500 μm perfluorocarbon layer, and water spray of 8 ml/min.....	107
Figure 6.3	Comparison of ablation volume measured with OCT as a function of radiant exposure with five pulses for various experimental conditions: dry, wet (500 μm water and perfluorocarbon layers), and spray (water, flow rate = 8 ml/min) ablation.....	107
Figure 6.4	Cross-sectional OCT (the leftmost column, $H = 47 \text{ J/cm}^2$) and top view (the middle column, $H = 42 \text{ J/cm}^2$ for the left and $H = 37 \text{ J/cm}^2$ for the right spot) images of bone tissues ablated with a sequence of five pulses. Another top view image (the rightmost column) shows osteotomy cuts with multiple sequences of five pulses at $H = 47 \text{ J/cm}^2$ (lateral resolution = 200 μm every five pulses). Four different conditions were tested: (a) dry, (b) wet (500 μm water layer), (c) wet (500 μm perfluorocarbon layer), and (d) spray ablation (flow rate of 8 ml/min).....	108
Figure 7.1	Experimental setup for liquid-assisted laser ablation. Four different liquid layer thicknesses were tested (500 μm , 1 mm, 2 mm, and 3 mm).....	121
Figure 7.2	OCT cross-sectional images of laser-induced craters using a Q-switched laser at 5.7 J/mm^2 per pulse for a dry case (a) and a wet case with a 500 μm liquid layer (b) and using a free-running Er:YAG laser at 4.2 J/mm^2 per pulse for a dry case (c) and a wet case with a 3 mm liquid layer (d).....	123
Figure 7.3	Ablation efficiency as a function of applied liquid thickness using a sequence of five pulses from each of the two laser systems: (a) Q-switched Nd:YAG at 5.7 J/mm^2 per pulse and (b) free-running Er:YAG at 4.2 J/mm^2 per pulse ($n = 5$). Note that 0 mm thickness represents dry ablation.....	124
Figure 8.1	Schematic illustration of experimental set-up for laser-induced acoustic measurement and Schlieren flash photography during enamel tissue ablation (PD: photodetector, t_0 : laser onset time, and Δt : delay time).....	139
Figure 8.2	Experimental set-up to measure the beam profile at the distal end of the delivery fiber and sapphire tip.....	139

Figure 8.3	Experimental arrangements to (a) quantify the efficiency of light transmission and (b) measure temperature distribution during a single laser pulse with and without water spray.....141
Figure 8.4	Beam profile of the Er,Cr:YSGG laser (pulse energy $Q_0 = 10$ mJ).....144
Figure 8.5	Comparison of ablation volume as a function of radiant exposure and water spray flow rate ($n = 3$).....145
Figure 8.6	<i>Probit</i> curves of ablation thresholds for dental enamel under different sample conditions: (a) dry ($H_{th} = 1.2$ J/cm ²) and (b) spray ($H_{th} = 2.1$ J/cm ²) ($n = 33$ and flow rate = 8 ml/min).....146
Figure 8.7	Energy transmission as a function of incident radiant exposure (flow rate = 8 ml/min).....147
Figure 8.8	Thermal images of heat diffusion measured by IR thermal camera during (b) dry ($H = 1.3$ J/cm ² and $\Delta T = 51$ °C) and (c) spray process ($H = 3.6$ J/cm ² and $\Delta T = 40$ °C) (Note that the flow rate was 8 ml/min. Temperature increase index is displayed in the far left column, and time elapsed after the onset of the 150 μ s laser pulse is shown above each image).....150
Figure 8.9	Top view ((a) and (b)) and cross-sectional OCT ((c) and (d)) images of enamel tissues ablated with ten pulses for dry ((a) and (c), $H = 38.7$ J/cm ² per pulse) and spray ablation ((b) and (d), $H = 35.8$ J/cm ² per pulse). Note that flow rate = 8 ml/min and each dotted line in (a) and (b) indicates a cross-section of the crater for OCT image.....151
Figure 8.10	Comparison of ablation volume measured with OCT for dry and spray conditions as a function of radiant exposure with ten pulses (flow rate = 8 ml/min).....152
Figure 8.11	Temporal behaviors of the Er,Cr:YSGG laser pulse (top) and the measured transient pressures (bottom) for (a) dry and (b) spray ablation from the enamel surface and for (c) spray (no ablation) from the glass surface. Note difference in scale. ($H = 18.1$ J/cm ² , average of ten signals, and flow rate = 8 ml/min).....156
Figure 8.12	FFT analysis of acoustic signal for (a) dry and (b) spray ablation. In case of spray condition, the acoustic signal induced by the spray on a non ablative material is included for comparison. Note difference in scale. ($H = 18.1$ J/cm ² , average of ten signals, and flow rate = 8 ml/min).....157

Figure 8.13	Comparison of acoustic amplitudes at 15 mm from the enamel sample surface for dry and spray cases as a function of radiant exposure with a single pulse ($n = 10$, initial radiant exposure = 3.5 J/cm^2 , and flow rate = 8 ml/min). The line through dry ablation was based upon a curve fit using equation 8.2.....	158
Figure 8.14	Compilation of enamel ablation process for (a) dry and (b) spray conditions. Note that the radiant exposure was 32.5 J/cm^2 . Time elapsed after the onset of the $150 \text{ } \mu\text{s}$ laser pulse is shown above each image.....	161
Figure 8.15	A time resolved photograph of a laser-induced vapor bubble in water at $90 \text{ } \mu\text{s}$ after the onset of laser pulse ($H = 1.8 \text{ J/cm}^2$).....	165
Figure 9.1	Experimental setup for calculus ablation measurement.....	188
Figure 9.2	Experimental setup used to measure the beam profile at the focal plane (on target surface) during laser lithotripsy.....	188
Figure 9.3	Normalized energy transmitted past knife-edge at the focal plane (on target surface). The average of five measurements is presented. Total pulse energy was 100 mJ	190
Figure 9.4	Beam diameters as a function of the distance from the focal point. Error bars represent the standard deviation of five measurements. X-axis represents the distance from the focal point while the laser beam diverges.....	190
Figure 9.5	Beam profiles measured with a pyroelectric solid-state camera. (a) Er:YAG laser with 20 mJ ($H = 33 \text{ J/cm}^2$) and (b) Ho:YAG laser with 20 mJ ($H = 30 \text{ J/cm}^2$).....	191
Figure 9.6	Vertical cross-sectional topography of Er:YAG and Ho:YAG laser-induced craters on COM. (a) Er:YAG, Single pulse, $Q_0 = 400 \text{ mJ}$ ($H = 668 \text{ J/cm}^2$), (b) Er:YAG, five pulses, $Q_0 = 400 \text{ mJ}$ ($H = 668 \text{ J/cm}^2$) per pulse, (c) Ho:YAG, Single pulses, $Q_0 = 387 \text{ mJ}$ ($H = 578 \text{ J/cm}^2$), and (d) Ho:YAG, five pulses, $Q_0 = 387 \text{ mJ}$ ($H = 578 \text{ J/cm}^2$) per pulse.....	193
Figure 9.7	Vertical cross-sectional topography of Er:YAG and Ho:YAG laser-induced craters on Uric Acid. (a) Er:YAG, Single pulse, $Q_0 = 479 \text{ mJ}$ ($H = 801 \text{ J/cm}^2$), (b) Er:YAG, five pulses, $Q_0 = 479 \text{ mJ}$ ($H = 801 \text{ J/cm}^2$) per pulse, (c) Ho:YAG, Single pulses, $Q_0 = 439 \text{ mJ}$ ($H = 656 \text{ J/cm}^2$), and (d) Ho:YAG, five pulses, $Q_0 = 439 \text{ mJ}$ ($H = 656 \text{ J/cm}^2$) per pulse.....	194
Figure 9.8	Vertical cross-sectional topography of Er:YAG and Ho:YAG laser-induced craters on Cystine. (a) Er:YAG, Single pulse, $Q_0 = 479 \text{ mJ}$ ($H = 801 \text{ J/cm}^2$), (b) Er:YAG, five pulses, $Q_0 = 479 \text{ mJ}$ ($H = 801 \text{ J/cm}^2$) per pulse, (c) Ho:YAG, Single pulses, $Q_0 = 524 \text{ mJ}$	

	($H = 782 \text{ J/cm}^2$), and (d) Ho:YAG, five pulses, $Q_0 = 524 \text{ mJ}$ ($H = 782 \text{ J/cm}^2$) per pulse.....	195
Figure 9.9	Microscopic top views of Er:YAG and Ho:YAG laser-induced craters on Uric Acid. (a) Er:YAG, Single pulse, $Q_0 = 74 \text{ mJ}$ ($H = 124 \text{ J/cm}^2$), (b) Er:YAG, five pulses, $Q_0 = 74 \text{ mJ}$ ($H = 124 \text{ J/cm}^2$) per pulse, (c) Ho:YAG, Single pulses, $Q_0 = 105 \text{ mJ}$ ($H = 157 \text{ J/cm}^2$), and (d) Ho:YAG, five pulses, $Q_0 = 105 \text{ mJ}$ ($H = 157 \text{ J/cm}^2$) per pulse.....	196
Figure 9.10	Crater depth as a function of radiant exposure per pulse. (a) Er:YAG, COM; (b) Ho:YAG, COM; (c) Er:YAG, Uric Acid; (d) Ho:YAG, Uric Acid; (e) Er:YAG, Cystine; (f) Ho:YAG, Cystine.....	199
Figure 9.11	Crater width as a function of radiant exposure per pulse. (a) Er:YAG, COM; (b) Ho:YAG, COM; (c) Er:YAG, Uric Acid; (d) Ho:YAG, Uric Acid; (e) Er:YAG, Cystine; (f) Ho:YAG, Cystine.....	200
Figure 9.12	Crater volume as a function of radiant exposure per pulse. (a) Er:YAG, COM; (b) Ho:YAG, COM; (c) Er:YAG, Uric Acid; (d) Ho:YAG, Uric Acid; (e) Er:YAG, Cystine; (f) Ho:YAG, Cystine.....	201
Figure 9.13	Comparison of normalized crater volume of five pulses and the crater volume of single pulse. (a) COM, (b) Uric Acid, and (c) Cystine.....	202
Figure 9.14	Temporal evolution of ablation process and temperature as a function of depth. The scattering of the light has been neglected. Numbers indicate the time sequence. The highlight indicates the ablation zone. Both lasers have a flat top beam with the same diameter. The scattering of the light was neglected. Bold arrows in the Ho:YAG process indicate the lateral and axial expansion of ablated material in deep ablation zone.....	208
Figure 10.1	Two different pulse duration regimes of the clinical Ho:YAG laser: (a) optical pulse profiles measured by a photodetector ($Q_0 = 800 \text{ mJ}$ and $n = 32$) and (b) various pulse durations as a function of laser pulse energy.....	225
Figure 10.2	Experimental setup for retropulsion study (a) to monitor the stone movement during laser lithotripsy and (b) to image the cavitation process using fast flash photography and to measure the laser-induced acoustic transients.....	226
Figure 10.3	Comparison of stone retropulsion induced with a single Ho:YAG pulse as a function of pulse energy for three different diameters of fibers: (a) $273 \text{ }\mu\text{m}$, (b) $365 \text{ }\mu\text{m}$, and (c) $550 \text{ }\mu\text{m}$ ($n = 5$).....	228

Figure 10.4	Ablation volume as a function of pulse energy and fiber diameter using (a) short pulse and (b) long pulse durations ($n = 5$).....	229
Figure 10.5	Retropulsion distance normalized with ablation volume as a function of pulse energy for various fibers with a diameter of (a) 273 μm , (b) 365 μm , and (c) 550 μm ($n = 5$).....	232
Figure 10.6	Compilation of bubble expansion and collapse in water at room temperature for two laser pulse durations: (a) short pulse ($\tau_p \sim 150 \mu\text{sec}$ at FWHM) and (b) long pulse ($\tau_p \sim 280 \mu\text{sec}$ at FWHM). Note that the fiber diameter was 365 μm and the pulse energy was 800 mJ. Time elapsed after the onset of the laser pulse is shown above each image.....	233
Figure 10.7	Temporal profile of the Ho:YAG laser pulses (top) and the measured pressure for each figure: (a) short pulse ($\tau_p \sim 150 \mu\text{sec}$ at FWHM) and (b) long pulse ($\tau_p \sim 280 \mu\text{sec}$ at FWHM). Note that the fiber diameter was 365 μm and the pulse energy was 800 mJ. A small pressure bump characteristic of both pulses was detected after laser onset. Bubble collapse occurred at 450 μsec and 510 μsec respectively producing a pressure peak > 20 bars. Rebound and recollapse were also detected approximately 100 μs after the first bubble collapse.....	234
Figure 10.8	Images of calculus retropulsion with noncontact laser lithotripsy at 800 mJ with a single pulse using different pulses: (a) short pulse ($\tau_p \sim 150 \mu\text{sec}$ at FWHM) and (b) long pulse ($\tau_p \sim 280 \mu\text{sec}$ at FWHM). The fiber diameter was 365 μm . Stone movement of approximately 1.5 mm was observed in case of the short pulse while no movement was seen for the long pulse.....	237
Figure 10.9	Comparison of the amplitudes of collapse pressure produced during lithotripsy with two different pulse durations: short pulse ($\tau_p \sim 150 \mu\text{sec}$ at FWHM) and (b) long pulse ($\tau_p \sim 280 \mu\text{sec}$ at FWHM) ($n = 5$).....	237
Figure 10.10	Cross-sectional topography of laser-induced craters produced with short pulse ($\tau_p \sim 120 \mu\text{sec}$ at FWHM) using (a) 273 μm and (b) and 550 μm fibers and long pulse ($\tau_p \sim 210 \mu\text{sec}$ at FWHM) using (c) 273 μm and (d) and 550 μm fibers. Note that the applied pulse energy was 400 mJ.....	244

Figure A.1	The primary mechanism for photofragmentation is contingent on pulse duration. (a) Pure photoacoustical/photomechanical ablation is associated with internal fractures and large calculus dissociation. (b) Photothermal ablation with internal fractures involves minor photoacoustical/photomechanical effects. (c) Localized photothermal ablation without collateral damage to adjacent tissue is the most desirable phenomenon for laser lithotripsy. (d) Photothermal ablation with thermal damage to surrounding tissue (carbonization).....262
Figure A.2	Cross-sectional topography of laser-induced craters was acquired with optical coherence tomography (OCT). Single pulse of Ho:YAG laser at different levels of laser energy was applied to struvite calculus through 273 μm optical fiber. Localized photothermal ablation created the hemisphere shape crater in the calculus.....265
Figure A.3	Schematic illustration of photothermal interaction. (a) Incidence of laser light on the target surface. (b) Optical energy absorption in the laser-affected zone and subsequent temperature rise. (c) Photothermal ablation with plume formation and phase transfer with little heat diffusion for shorter pulse durations (i.e. $\tau_p \ll \tau_{th}$). (d) Laser-induced ablation accompanied with collateral tissue damage (e.g. carbonization or coagulation) due to longer pulse duration (i.e. $\tau_p > \tau_{th}$).....266
Figure A.4	The illustration describes the spallation process. (a) The incident light produces a temperature and pressure profile that follows the fluence distribution along the laser beam axis. (b) Laser-induced stress waves (initially compressive waves) travel in two directions (upward and downward). The upward wave becomes a tensile wave upon the reflection at the target surface. (c) The wave with two poles keeps propagating into the target. (d) If the material tensile strength at a certain location is weaker than the strength of the tensile wave, spallation (photoacoustical/photomechanical ablation) takes place.....272
Figure A.5	Laser-induced microexplosion. (a) Incidence of laser light on the tissue containing water. (b) Vaporization of water in the tissue due to optical energy absorption. (c) Pressure increase in water following water vaporization. (d) Photomechanical ablation after rupturing the tissue, associated with large fragments, plume, and internal fractures.....273

Figure A.6	Schematic illustrations of shock wave induced ablation. (a) The initiation of optical breakdown (ionization process). (b) Plasma formation and its shielding of the incident light in an early stage. (c) Plasma expansion accompanied with generation of shock waves. (d) Photoacoustical ablation with mechanical fractures inside the crater.....	274
Figure A.7	Top view of laser-induced craters is shown. A Q-switched Nd:YAG laser ($\tau_p = 20$ ns, $r_o = 0.75$ mm, $F = 14$ J/cm ²) was irradiated on cystine. Photoacoustical/photomechanical effects caused calculus fragmentation with fracture and large calculus dissociation. (a) 50 pulses of laser light were irradiated on dry calculus. (b) 30 pulses were applied to wet calculus, which was immersed in deionized water for a minimum of 24 hours prior to ablation experiment.....	275

Chapter 1: Introduction

1.1 MOTIVATION

The motivation of this dissertation research originated from my M.S. research of laser-material interactions with solid-liquid interfaces. Although the initial question with regard to mechanisms of pulsed laser ablation came from the application of a liquid layer for laser machining, my research has become involved in the underlying physics of the pulsed laser (near- and mid-IR) ablation of biological hard tissues assisted by a liquid layer or spray.

The role of a liquid layer during laser ablation is to enhance optic-acoustic energy coupling via explosive liquid vaporization [1-3], confine plasma formation/expansion at high laser irradiance [4-7], and provide cooling as a heat sink [8,9]. Previous studies reported that the application of a thin liquid film on a target surface induces lower damage threshold as well as improved ablation efficiency and surface quality [3,7-11], which suggest the potential application of liquid for laser hard tissue ablation.

Laser ablation of tissue is employed in many clinical applications. Although tissue ablation with high power pulsed lasers can be quite effective, scientists and physicians still question the basic mechanism(s) associated with the ablation process. Most important is the improvement of ablation performance and minimization of undesirable mechanical/thermal damage to peripheral tissue. Hence, my dissertation research is motivated by the desire to obtain a better comprehension of underlying mechanisms of liquid-assisted hard tissue ablation for clinical applications.

1.2 GOAL OF RESEARCH

The overall aim of this research is to comprehend physical phenomena that take place during pulsed laser ablation of biological hard tissue and to develop methods for efficient removal of tissue with minimal collateral damage to surrounding regions with the aid of liquid confinement. The appropriate selection of laser parameters such as wavelength, pulse duration, and radiant exposure and the application of a transparent liquid layer on a target surface are essential to improve ablation performance and reduce undesirable tissue damage.

The central hypothesis of the research is that variations in optical parameters and the application of a liquid layer enhance the ablation process due to efficient light absorption and explosive liquid vaporization. The specification of enhanced laser tissue ablation has significant implications in laser therapeutics.

Therefore, my dissertation focuses on experimental evaluation of high power pulsed laser radiation with biological hard tissue to identify optimal laser parameters and specify the role of a transparent liquid layer in terms of augmented ablation efficiency.

The specific objectives of this research are (1) to quantify photoacoustical/photomechanical and photothermal effects during high power laser radiation, (2) to demonstrate the enhancement of hard tissue ablation efficiency by the application of a transparent liquid layer or liquid spray on the target surface, and (3) study the effect of pulsed IR laser wavelength, pulse duration, and liquid thickness on ablation efficiency.

The interaction of high power pulsed laser light with material is a very complex phenomenon with many mechanisms. When biological tissue is the target, these mechanisms become even more complicated. In order to achieve these objectives, I have designed and performed experiments to (1) study dominant laser ablation mechanisms in hard tissue, (2) optimize laser parameters for ablation, and (3) provide an efficient means to remove targeted tissue and minimize undesirable damage.

Due to the usage of various laser sources, the preceding goals have been accomplished in the Biomedical Engineering Laser Laboratory (BELL) at the University of Texas at Austin, W.W. Hansen Experimental Physics Laboratory at Stanford University, and Biolase Technologies at Irvine, CA. Experimental

results have been verified by theoretical concepts of laser-tissue interaction and have been applied to clinical studies of hard tissue ablation.

1.3 OVERVIEW

The research described in this dissertation is divided into four major sections: laser metal ablation, laser osteotomy, laser dental ablation, and laser lithotripsy. The dynamics and mechanisms of liquid-assisted ablation for machining are explored in the laser metal ablation section. The other sections focus on clinical implications, including studies of (i) ablation mechanism(s) with hard tissues (bovine bone, human dental tissue, and human calculus) and (ii) the role of a liquid layer and water spray during tissue ablation.

This dissertation contains eleven chapters, which have been presented at conferences, published, or submitted for publication.

Chapter 2: Fundamental physics of laser-tissue interaction is discussed regarding three mechanisms: photothermal, photoacoustical/photomechanical, and plasma-mediated. Post-ablation phenomena (for example, plume dynamics and recoil stress) and analytical ablation models are presented.

Chapter 3: Liquid-assisted metal ablation using a nanosecond laser pulse is presented. Ablation process on a metal surface covered by a liquid layer is experimentally characterized by means of ablation rate and acoustic pressure measurements. Optical reflectance and SEM (scanning electron microscope)

images provide data for the role of bubble formation/expansion during metal ablation. The laser source used in this study is the Ti:Sapphire (Ti:S) laser at Stanford University. (To be submitted to *Optics Express*, and currently in review by colleagues at Stanford University)

Chapter 4: A variety of metals with different material properties for liquid-assisted ablation is examined. Various measurements such as ablation threshold and depth, plasma formation, acoustic pressure, and optical reflectance are conducted as a function of applied fluence. Results from these experiments implicate the role of material properties in the ablation process during liquid-assisted ablation. The Ti:Sapphire (Ti:S) laser at Stanford University is used for these experiments. (To be submitted to *Optics Express*, and currently in review by colleagues at Stanford University)

Chapter 5: The enhancement of bone ablation assisted by a liquid layer is explored. Both acoustic and plasma signals describe the dynamics of bone ablation in a liquid environment. Ablation volume measured with OCT (optical coherence tomography) shows the feasibility of improved laser osteotomy with application of a transparent liquid layer. The laser source for this study is the Q-switched Nd:YAG laser. (Published in *IEEE Journal of Quantum Electronics* [12])

Chapter 6: The effect of various liquid environments on laser bone ablation is investigated. Ablation performance is experimentally compared by the application of a liquid layer using different liquid types (water and

perfluorocarbon) and water spray. Microscope images depict the post-ablation phenomena of each ablation condition. A clinical Er,Cr:YSGG laser is used for this study. (To be submitted to *Medical Physics*, and currently in review by colleagues at Biolase Technology, CA)

Chapter 7: The effect of liquid thickness on laser ablation performance is discussed. Experiments during liquid-assisted laser ablation are conducted to determine the optimal liquid layer thickness for Q-switched Nd:YAG and free-running Er:YAG lasers. Ablation efficiency is compared as a function of liquid thickness. (Currently in review at *Journal of Applied Physics*)

Chapter 8: Ablation mechanisms of spray-assisted laser dental ablation using a clinical Er,Cr:YSGG laser are evaluated. Simultaneous fast flash photography and acoustic transient measurements using a piezoelectric transducer are performed to study the ablation processes. Various parameters such as energy loss and spray flow rate are experimentally measured for the optimal ablation efficiency. Temperature distribution and ablation volume measurement demonstrate the medical advantages of the spray-assisted ablation during enamel laser treatment. (To be submitted to *Biophysical Journal*, and currently in review by colleagues at Biolase Technology, CA)

Chapter 9: Urinary calculus fragmentation between the free-running Ho:YAG and Er:YAG lasers is compared. A previous study suggests that the Er:YAG laser can be the efficient laser lithotripter due to its high absorption of

calculus at 2.94 μm [13]. By comparing the laser-induced crater width, depth, and volume with the Ho:YAG laser, the feasibility of Er:YAG laser lithotripsy is examined. (Published in *Lasers in Surgery and Medicine* [14])

Chapter 10: The effect of pulse duration on calculus retropulsion during laser lithotripsy is described. A clinical Ho:YAG laser with two discrete pulse durations is employed to fragment calculus phantoms as well as to evaluate phantom retropulsion and ablation volume. High speed imaging monitors the dynamics of the recoil action of a phantom. Fast flash photography and acoustic transient measurements using a hydrophone characterize the dependence of retropulsion process on bubble formation and collapse during laser lithotripsy. (Published in *Lasers in Surgery and Medicine* [15])

Chapter 11: The major conclusions of my dissertation research are summarized, and future directions for further research in laser-tissue ablation are briefly outlined.

Appendix A: Lasers previously studied and clinically used in laser lithotripsy are reviewed. This appendix provides the background of laser lithotripsy and the direction toward efficient laser fragmentation of calculi. (Published in *Minerva Urologica e Nefrologica* [16])

1.4 NOMENCLATURE AND NOTATION

The following table outlines the descriptions and dimensions of all the nomenclature used throughout the dissertation.

Table 1.1. Symbols used in this dissertation

Symbol	Description	Units
FUNDAMENTAL PARAMETERS		
ρ	density	kg/m ³
m	mass	kg
A	area	cm ²
V	volume	cm ³
v	specific volume	m ³ /kg
z	distance	cm
t	time	s
v	velocity	m/s
E	energy	J
OPTICAL PARAMETERS		
λ	wavelength	μm
τ_p	pulse duration	ns, μs
μ_a	absorption coefficient	cm ⁻¹
δ	penetration depth	cm
R	reflectivity	
n	index of refraction	
r_0	spot size	μm
Q_0	radiant energy	J
H	radiant exposure at the surface	J/cm ²
H_{th}	threshold radiant exposure	J/cm ²
h_{abl}	heat of ablation	J/cm ³
F	fluence	J/cm ²
P	radiant power	W
ϕ	fluence rate	W/cm ²
E_0	irradiance	W/cm ²

THERMAL PARAMETERS

T	temperature	K
T_c	critical temperature	K
k	thermal conductivity	W/m·K
c_v	specific heat at constant volume	J/kg·K
c_p	Specific heat at constant pressure	J/kg·K
γ	ratio of specific heat	
α	thermal diffusivity	mm ² /s
τ_{th}	thermal diffusion time	μs

MECHANICAL PARAMETERS

σ	surface tension	N/m
P or p	pressure	N/m
p_{rec}	recoil stress	N/m
τ_a	acoustic diffusion time	μs
Z	acoustic impedance	kg/m ²
c	speed of sound	m/s

UNIVERSAL CONSTANTS AND MISCELLANEOUS

R or R_a	universal gas constant = 8.234	J/mol·K
k_b	Boltzmann constant = 1.381×10^{-23}	W·s/K
G_c	Gaussian correlation	
p	probability	
r_c	critical radius for bubble formation	μm
d	thickness	m

1.5 REFERENCES

1. Kim D, Lee H. Enhanced ablation and photoacoustic excitation in near-threshold laser ablation of liquid-coated surfaces. J Appl Phys 2001;89:5703-5706.
2. Hong MH, Koh ML, Zhu S, Lu YF, Chong TC. Steam-assisted laser ablation and its signal diagnostics. Appl Surf Sci 2002;197-198:911-914.
3. Kim D, Oh B, Lee H. Effect of liquid film on near-threshold laser ablation of a solid surface. Appl Surf Sci 2004;222:138-147.

4. Fabbro R, Fournier J, Ballard P, Devaux D, Virmont J. Physical study of laser-produced plasma in confined geometry. *J Appl Phys* 1990;68:775-784.
5. Devaux D, Fabbro R, Tollier L, Bartnicki E. Generation of shock waves by laser-induced plasma in confined geometry. *J Appl Phys* 1993;74:2268-2273.
6. Dupont A, Caminat P, Bournot P. Enhancement of material ablation using 248, 308, 532, 1064 nm laser pulse with a water film on the treated surface. *J Appl Phys* 1995;78:2022-2028.
7. Zhu S, Lu YF, Hong MH, Chen XY. Laser ablation of solid substrates in water and ambient air. *J Appl Phys* 2001;89:2400-2403.
8. Kruusing A. Underwater and water-assisted laser processing: Part I - general features, steam cleaning and shock processing. *Opt Laser Eng* 2004;41:307-327.
9. Daminelli G, Krüger J, Kautek W. Femtosecond laser interaction with silicon under water confinement. *Thin Solid Films* 2004;467:334-341.
10. Choo KL, Ogawa Y, Kanbargi G, Otrá V, Raff LM, Komanduri R. Micromachining of silicon by short-pulse laser ablation in air and under water. *Mater Sci Eng, A* 2004;372:145-162.
11. Ren J, Kelly M, Heeselink L. Laser ablation of silicon in water with nanosecond and femtosecond pulses. *Opt Lett* 2005;30:1740-1742.
12. Kang HW, Lee H, Chen S, Welch AJ. Enhancement of Bovine Bone Ablation Assisted by a Transparent Liquid Layer on a Target Surface. *IEEE J Quantum Electron* 2006;42:633-642.
13. Chan KF, Choi B, Vargas G, Hammer DX, Sorg B, Pfefer TJ, Teichman JMH, Welch AJ, Jansen ED. Free Electron Laser Ablation of Urinary Calculi: An Experimental Study. *IEEE J Sel Top Quantum Electron* 2001;7:1022-1033.
14. Lee H, Kang HW, Teichman JMH, Oh J, Welch AJ. Urinary Calculus Fragmentation During Ho:YAG and Er:YAG Lithotripsy. *Lasers Surg Med* 2006;38:39-51.
15. Kang HW, Lee H, Teichman JMH, Oh J, Kim J, Welch AJ. Dependence of Calculus Retropulsion on Pulse Duration During Ho:YAG Laser Lithotripsy. *Lasers Surg Med* 2006;38:762-772.
16. Welch AJ, Kang HW, Lee H, Teichman JMH. Calculus fragmentation in laser lithotripsy. *Minerva Urol Nefrol* 2004;56:49-63.

Chapter 2: Pulsed Laser-induced Ablation

2.1 INTRODUCTION

Clinical applications of laser ablation began in the 1980's for ophthalmic dissection [1]. Since then, medical procedures employing pulse lasers have been presented in a variety of medical subspecialties such as dermatology, dentistry, gynecology, neurosurgery, orthopedics, and urology [2-7]. In the infrared (IR) region, pulsed lasers evaluated for the usage in clinical field are the Q-switched Nd:YAG ($\lambda = 1.064 \mu\text{m}$), Thulium:YAG ($\lambda = 2.01 \mu\text{m}$), Holmium:YAG ($\lambda = 2.12 \mu\text{m}$), Erbium,Cr:YSGG ($\lambda = 2.79 \mu\text{m}$), Erbium:YAG ($\lambda = 2.94 \mu\text{m}$), CO₂ ($\lambda = 10.6 \mu\text{m}$), and FEL (Free Electron Laser, $\lambda = 2 \sim 8 \mu\text{m}$). The pulsed IR lasers provide the means to achieve precise and efficient cutting and to minimize either excessive thermal and/or mechanical damage to the peripheral tissue. The appropriate selection of laser parameters, thereby, is essential to obtain a successful outcome from pulsed laser surgery.

2.2 NEAR-FAR INFRARED RADIATION

In the infrared spectral region, the principal light absorbers are water and protein. The absorption spectrum of water is governed by the resonance of its symmetric and asymmetric stretch modes, which correspond to strong absorption peaks of water at $\lambda = 0.96, 1.44, 1.95, 2.94, 4.68,$ and $6.1 \mu\text{m}$ [8]. In case of protein, a variety of vibrational modes of the peptide bond ($\text{O}=\text{C}-\text{N}-\text{H}$) dominate infrared spectra. Of particular interests are the amide I and amide II bands at $\lambda = 6.1 \mu\text{m}$ and $\lambda = 6.45 \mu\text{m}$, respectively due their strong light absorption [9]. It is noted that water and protein share an absorption peak at $\lambda = 6.1 \mu\text{m}$, which provide an alternative wavelength suitable for efficient laser-tissue ablation.

2.3 LASER-TISSUE INTERACTION MECHANISMS

2.3.1 LASER-INDUCED ABLATION IN NON-SCATTERING MEDIA

The goal of laser-induced ablation is the efficient removal of target tissue with minimum damage to surrounding tissue. Physical interactions of later-tissue ablation are contingent upon laser parameters (wavelength, pulse duration, and radiant exposure) and tissue properties (optical, thermal, mechanical, and chemical) [10-18]. Regardless of ablation mechanisms, absorption of laser energy initiates ablation. Assuming that a target tissue is a non-scattering medium, the absorption of laser energy can be characterized by the absorption coefficient, μ_a [cm^{-1}] of the target. The higher the absorption coefficient, the more absorbed

laser energy is concentrated at the surface of the target. The fluence, $F(z)$ [J/cm²] of a laser beam inside a target, which represents the energy distribution as a function of depth, z [cm], is determined by both the incident laser radiant exposure at the surface, H [J/cm²] and the absorption coefficient (μ_a), assuming light scattering is no larger than absorption [15,16,19]. According to Beer's law, the fluence, $F(z)$ [J/cm²] exponentially decreases with the depth, z [cm]:

$$F(z) = (1 - R) \cdot H \cdot \exp(-\mu_a \cdot z) \quad (2.1)$$

where R represents the reflectivity of a target surface. The optical penetration depth, δ [cm] is the depth at which the energy of a collimated laser is reduced by 37% (a factor of $1/e$) of the incident energy. This depth is defined as the reciprocal of the wavelength dependent absorption coefficient, $\mu_a(\lambda)$

$$\delta(\lambda) = \frac{1}{\mu_a(\lambda)} \quad (2.2)$$

Typically, the outcome of laser-induced tissue ablation is the combination of two or more mechanisms. Nevertheless, in pursuit of simplicity, laser ablation mechanisms are typically categorized into two groups dependent upon pulse duration: photothermal and photomechanical.

2.3.2 PHOTOTHERMAL ABLATION

Temperature rise in tissue induced by laser pulse durations over 100 μs is the most common laser-tissue interaction feature. In a photothermal interaction, the absorption of laser light converts optical energy into thermal energy (heat). For high peak temperatures, vaporization, carbonization, and melting occur [16,19].

Thermal energy in the irradiated zone that dissipates into surrounding regions through the process of heat diffusion can generate undesirable collateral damage. Damage to adjacent tissue can be minimized or eliminated by the selection of wavelengths and pulse durations that reduce the degree of thermal diffusion. The time which is required for the initial deposited laser energy to move beyond the irradiated volume is called thermal diffusion time, τ_{th} [μs] and is defined as

$$\tau_{th} = \frac{\delta^2}{4\alpha} \quad \text{when } r_0 \geq \delta \quad (2.3)$$

$$\tau_{th} = \frac{r_0^2}{4\alpha} \quad \text{when } r_0 < \delta \quad (2.4)$$

where α is the thermal diffusivity [mm^2/s] and r_0 is the laser spot radius [μm]. When the laser pulse duration, τ_p [μs] is shorter than the thermal diffusion time, τ_{th} (i.e. $\tau_p < \tau_{th}$), the absorbed energy accumulates within the region of absorbed photons which is characterized by the laser spot diameter and penetration depth of

the laser beam. Since little heat diffusion from this region occurs during the laser pulse, the accumulated thermal energy results in local destruction and removal of the irradiated tissue without significant heat diffusion to adjacent regions. From the onset of laser pulse to the end of the pulse or the occurrence of ablation, the temperature rise (ΔT) inside the region of light absorption is estimated as a function of the absorption coefficient as follows:

$$\Delta T = \frac{\mu_a \cdot (1 - R) \cdot H}{\rho c_p} e^{-\mu_a z} \quad (2.5)$$

where ρ is the tissue density (kg/m^3), c_p is the specific heat at constant pressure ($\text{J/kg}\cdot\text{K}$), and z is depth (cm). Typically, a temperature increase to $\geq 100^\circ\text{C}$ induces vaporization of water and/or thermal decomposition (ablation).

When $\tau_p > \tau_{th}$, the absorbed laser energy is not confined to the ablation process, and thermal damage occurs in the form of coagulation and carbonization of tissue.

2.3.3 PHOTOMECHANICAL ABLATION

With sub-microsecond laser pulses, photomechanical/photoacoustical interactions result from the conversion of laser energy into mechanical energy by the rapid temperature increase. Thus, a target tissue experiences impulsive stress waves (for example, acoustic and shock waves) during the laser pulse. To induce

the accumulation of stress waves responsible for the ablation process and/or physical damage to adjacent tissue, the laser pulse duration (τ_p) should be shorter than the acoustic diffusion time, τ_a [μ s] which is the time required for the stress wave to propagate out of the irradiated volume in the tissue. Since the stress wave travels through a medium at the speed of sound in the tissue, c [m/s], the acoustic diffusion time is defined as

$$\tau_a = \frac{\delta}{c} \quad (2.6)$$

Photomechanical/photoacoustical interactions when $\tau_p < \tau_a$ build up mechanical stresses, inducing tissue ablation initiated by thermoelastic expansion, intense acoustic pressure/shock waves, ablative recoil, and cavitation disruption [16,19].

2.3.4 PLASMA-MEDIATED ABLATION (PHOTODISRUPTION)

For pulse durations in the nanosecond and ultrashort range, the physical mechanism responsible for optical breakdown has been identified as avalanche ionization via inverse bremsstrahlung [16,20]. Upon the initial vaporization of a superficial layer, one or more seed electrons generated via thermal ionization at a target surface can absorb the incident photons and collide with atoms or molecules (inverse bremsstrahlung absorption), resulting in more free electrons.

Thus, the electron density grows exponentially and exceeds a critical electron density of $10^{18} - 10^{20} \text{ cm}^{-3}$ during the laser pulse, which consequently generates high temperature (up to 10000 K) and pressure ($> 1 \text{ GPa}$) plasma [16,21-23]. Once formed, the plasma leads to rapid heating of material in the focal volume, accompanied with shock wave generation and cavitation along with jet formation in liquid. For nanosecond pulses, the laser-induced mechanical impact is responsible for tissue ablation, which is termed as *photodisruption* [16]. When the laser pulse duration exceeds the onset of plasma formation, the plasma further absorbs and scatters the incident laser energy, which consequently gives rise to plasma shielding.

For each dominant confinement region, it may be possible to optimize laser parameters and to enhance ablation performance for particular clinical applications. Figure 2.1 illustrates the pulse duration versus optical penetration depth for various lasers, and the dotted lines describe the dominant confinement during ablative process.

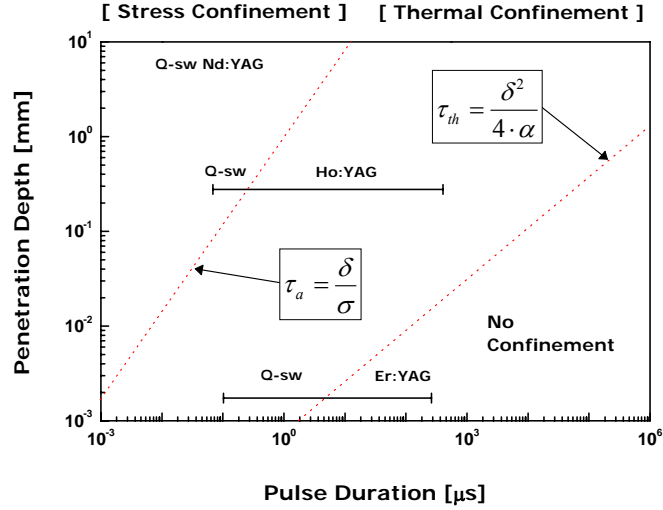


Figure 2.1. Penetration depth (δ) of laser light in tissue as a function of laser pulse duration (τ_p) for various lasers: each dotted line determines a governing mechanism of laser-induced tissue ablation [12]

2.4 ABLATION PLUME DYNAMICS

2.4.1 PLUME FORMATION AND EXPANSION

Typically, material rejection in the form of a plume and vaporization characterize the ablation process. The ablation plume consists of water vapor, gaseous organic products, and particulate tissue fragments. For nanosecond pulses, the initial ablation occurs along with a plume that propagates a shock wave to the surrounding air; this is followed by the ejection of a majority of the ablated material. On the other hand, for microsecond pulses longer than 100 μ s, plume formation and expansion concomitantly take place during laser irradiation:

an ablation plume develops on a much longer time scale, influencing the optical energy coupling to the target as well as plume dynamics. Dominant mechanisms of tissue ablation for both pulse regimes are a phase explosion for mechanically weak materials and water components in the tissue.

2.4.2 RECOIL STRESS

Recoil stresses occur during plume expansion and particle ejection, which impart recoil momentum to the tissue. Under stress confinement of tissue ablation, the compressive transient of recoil stress superimposing on a bipolar thermoelastic wave is used to determine the ablation threshold [24]. The recoil stresses generated via phase explosion can also cause a secondary material expulsion process in liquids or a molten layer of tissue during ablation, leading to the increase of ablation efficiency. Material ablation is promoted when the radial component of recoil stress exceeds the mechanical strength of the tissue.

2.5 ABLATION MODELS

Based on knowledge of laser parameters, many ablation models have been proposed including heuristic (blow-off and steady-state) models, mechanistic (steady-state vaporization and thermomechanical) models, and molecular dynamics simulations [25-28]. These models predict ablation quantities; for example, the amount of material removed, the threshold radiant exposure, or zone

of residual thermal damage. Since ablation phenomena are complex processes involved in various laser and tissue parameters, it is quite difficult to develop a single model to represent all ablation mechanisms. However, future experimental studies and empirical findings will provide greater insight into the physics of laser-induced ablation. More sophisticated models can thereby be established to yield more accurate predictions for ablation outcome.

2.6 OPTIMAL AND SELECTIVE ABLATION

The accomplishment of high precision in laser tissue ablation requires the selection of the optimal laser wavelength and short pulse duration: the appropriate wavelength can achieve a small optical penetration depth confining the energy deposition to a small volume in tissue, and the short pulse duration can sufficiently provide thermal confinement for precise ablation or even stress confinement for more efficient material removal. In order to remove a target tissue with minimal collateral damage, the laser ablation process needs to be limited to the targeted structure. Therefore, the achievement of selective ablation involves understanding/utilizing of the optical properties of the tissues and online monitoring with active feedback of laser ablation procedure.

2.7 REFERENCES

1. Vogel A, Hentschel W, Holzfuss J, Lauterborn W. Cavitation bubble dynamics and acoustic transient generation in ocular surgery with pulsed neodymium:YAG lasers. *Ophthalmology* 1986;93:1259-1269.
2. Zenzie HH, Altshuler GB, Smirnov MZ, Anderson RR. Evaluation of cooling methods for laser dermatology. *Lasers Surg Med* 2000;26:130-144.
3. Fried D, Ashouri N, Breunig T, Shori R. Mechanism of Water Augmentation During IR Laser Ablation of Dental Enamel. *Lasers Surg Med* 2002;31:186-193.
4. Garry R, Shelley-Jones D, Mooney P, Phillips G. Six hundred endometrial laser ablations. *Obstetrics & Gynecology* 1995;85:24-29.
5. Loesel FH, Fischer JP, Götz MH, Horvath C, Juhasz T, Noack F, Suhm N, Bille JF. Non-thermal ablation of neural tissue with femtosecond laser pulses. *Appl Phys B* 1998;66:121-128.
6. Nelson JS, Orenstein A, Liaw LL, Berns MW. Mid-infrared Erbium:YAG laser ablation of bone: the effect of laser osteotomy on bone healing. *Lasers Surg Med* 1989;9:363-374.
7. Chan KF, Vassar GJ, Pfefer TJ, Teichman JMH, Glickman RD, Weintraub ST, Welch AJ. Holmium:YAG Laser Lithotripsy: A Dominant Photothermal Ablative Mechanism With Chemical Decomposition of Urinary Calculi. *Lasers Surg Med* 1999;25:22-37.
8. Downing HD, Williams D. Optical constants of water in the infrared. *J Geophys Res* 1975;80:1656-1661.
9. Harris DC, Bertolucci MD. Symmetry and Spectroscopy: An Introduction to Vibrational and Electronic Spectroscopy. New York: Dover Publications, 1990.
10. Boulnois J. Photophysical processes in recent medical laser development: a review. *Lasers Med Sci* 1986;1:47-66.
11. Rastegar D. Laser ablation of biological tissue (Doctoral Dissertation). Austin: The University of Texas at Austin, 1987.
12. Jacques SL. Laser-tissue interactions: photochemical, photothermal, photomechanical. *Lasers Gen Surg* 1992;72:531-558.
13. Miller JC. Laser ablation: principles and applications. Berlin: Springer-Verlag, 1994.
14. Jansen ED. Pulsed laser ablation of biological tissue: influence of laser parameters and tissue properties on thermal and mechanical damage (Doctoral Dissertation). Austin: The University of Texas at Austin, 1994.
15. Welch AJ, van Gemert MJC. Optical-thermal response of laser-irradiated tissue. New York: Plenum Press, 1995.
16. Niemz MH. Laser-tissue interactions. Berlin: Springer-Verlag, 1996.

17. Bäurele D. Laser processing and chemistry. Berlin: Springer, 2000.
18. Chan KF. Pulsed infrared laser ablation and clinical applications (Doctoral Dissertation). Austin: The University of Texas at Austin, 2000.
19. Jacques SL. Role of tissue optics and pulse duration on tissue effects during high-power laser irradiation. *Appl Opt* 1993;32:2447-2454.
20. Bloembergen N. Laser-induced Electric Breakdown in Solids. *IEEE J Quantum Electron* 1974;10:375-386.
21. Devaux D, Fabbro R, Tollier L, Bartnicki E. Generation of shock waves by laser-induced plasma in confined geometry. *J Appl Phys* 1993;74:2268-2273.
22. Berthe L, Fabbro R, Peyre P, Bartnicki E. Wavelength dependent of laser shock-wave generation in the water-confinement regime. *J Appl Phys* 1999;85:7552-7555.
23. Barnes PA, Rieckhoff KE. Laser induced underwater sparks. *Appl Phys Lett* 1968;13:282-284.
24. Esenaliev RO, Oraevsky AA, Letokhov VS, Karabutov AA, Malinsky TV. Studies of acoustic and shock in the pulsed laser ablation of biological tissue. *Lasers Surg Med* 1993;13:470-484.
25. Andrew JE, Dyer PE, PH K. Direct etching of polymeric materials using a XeCl laser. *Appl Phys Lett* 1983;43:717-719.
26. Gagliano FP, Paek UC. Observation of laser-induced explosion of solid materials and correlation with theory *Appl Opt* 1974;13:274-279.
27. Zweig AD, Weber HP. Mechanical and thermal parameters in pulsed laser cutting of tissue. *IEEE J Quantum Electron* 1987;23:1787-1793.
28. Zhigilei LV, Garrison BJ. Microscopic mechanisms of laser ablation of organic solids in the thermal and stress confinement irradiation regimes. *J Appl Phys* 2000;88:1281-1298.

Chapter 3: Laser Ablation in a Liquid-confined Environment Using a Nanosecond Laser Pulse

3.1 ABSTRACT

Laser ablation of Aluminum metal with 1 ns, 800 nm pulse was investigated in air (dry) and water (wet) environments. Compared to dry ablation, an approximately 8 times increase in ablation rate was associated with wet ablation. Based on optical reflectance and SEM images, bubble formation/collapse was responsible for augmented acoustic pressure and ablation rate. Temperature distributions during wet ablation were consistent with the occurrence of explosive water vaporization near the spinodal limit. Radial expansion of bubbles minimized the redeposition of debris, leading to improvements in energy coupling to the target and ablation performance.

3.2 INTRODUCTION

Enhancement of laser ablation in the presence of a liquid layer has been of interest in various technical and medical areas, such as surface contaminants cleaning [1-4], laser shock processing [5], nanoparticle formation [6], micro-

structure fabrication [7], laser osteotomy [8,9], and dental tissue ablation [10]. Depending on the applications of liquid-assisted ablation, various irradiation parameters such as wavelength, pulse duration, and radiant exposure have been investigated. In addition, the effect of water or other liquids on laser ablation has been evaluated in terms of inducing explosive vaporization and/or confining plasma expansion [11].

Recent studies reported enhanced ablation efficiency by the addition of water during laser irradiation [12,13]. Near the damage threshold regime, the steam-assisted process induced lower damage threshold as well as higher ablation performance than direct ablation, owing to the additional photomechanical effect associated with explosive vaporization [14]. At high radiant exposures, confinement of plasma expansion in the liquid layer intensified acoustic pressure and increased shockwave duration, consequently promoting material removal efficiency [12].

The role of liquids such as water during laser ablation involves heat transfer (conduction and/or convection) and bubble motion which contributes to the removal of ablated particles redeposited on the surface and reduces the oxidation of debris [13]; therefore, the increased energy coupling to the target leads to clean and precise laser machining. In addition, due to high heat capacity, water effectively cools the target preventing excessive heat accumulation. Rapid temperature increase during plasma formation/expansion produces cavitation

bubbles in the liquid [15], and the shockwave emission generated by bubble implosion and/or liquid-jet formation during bubble collapse provides a substantially strong pressure impact on the target as an additional photomechanical effect [16].

In this study, we describe the use of a nanosecond laser pulse in combination with a liquid layer. It is hypothesized that the liquid-assisted laser ablation will lower the damage threshold and augment ablation efficiency via explosive vaporization and cavitation. Liquid with a thickness of 1 mm is deposited on the surface of the aluminum, and the effect of bubble formation during laser ablation is monitored *in situ* by optical reflectance and acoustic wave measurements. Ablation efficiency of aluminum is evaluated for direct (termed “dry”) and liquid-assisted ablation (termed “wet”) over a broad range of laser radiant exposures in the nanosecond regime. All experiments are conducted below the plasma threshold.

3.3 MATERIALS AND METHODS

Mechanically polished Aluminum (1×1 inch) with a thickness of 0.032 inch was used for ablation experiments. Samples were irradiated at various radiant exposures with single and multiple pulses. To perform liquid-assisted ablation, a 1-mm thick plastic (Depron) ring was placed on the sample surface to

maintain a consistent liquid layer thickness. Distilled water was deposited inside the ring before the laser irradiation.

Laser ablation experiments were conducted using a Ti:Sapphire (Ti:S) laser at Stanford University ($\lambda = 800$ nm and $\tau_p = 1$ ns at FWHM). A schematic diagram for the experiments is shown in Figure 3.1. The laser beam produced a Gaussian spatial distribution of energy, and to achieve a long Rayleigh length, an Au lens with a focal length 2 m focused the laser beam on the sample surface in conjunction with two mirrors. Using a knife-edge measurement, the spot size was determined as 250 μm in diameter at the focal point. A polarizer was used to produce a triggering signal and to vary energy levels up to 1.1 mJ; pulse energy was monitored by an energy meter (Laserstar, Ophir Optronics, Inc., MA) with a beam splitter. Either single (3 Hz), 100 (10 Hz), or 500 (10 Hz) pulses was applied to evaluate ablation performance for dry and wet conditions. The absorption coefficient of the water at 800 nm was 0.01 cm^{-1} [17]; therefore, the liquid layer was rather transparent for the laser beam without substantial light absorption.

For single pulse experiments, the transient pressure generated during laser ablation was monitored experimentally using a commercial piezoelectric transducer with a bandwidth up to 100 MHz (WAT-04, Science Brothers, Inc., Houston, TX). The transducer was mounted below the target, and in order to match acoustic impedance between the sample and the transducer, a 1-mm thick

plastic ring was attached on the transducer surface and filled with distilled water. In case of multiple pulse experiments, ablation performance and surface tomography were examined with a stylus profilometer (CNMS, University of Texas at Austin) at various radiant exposures.

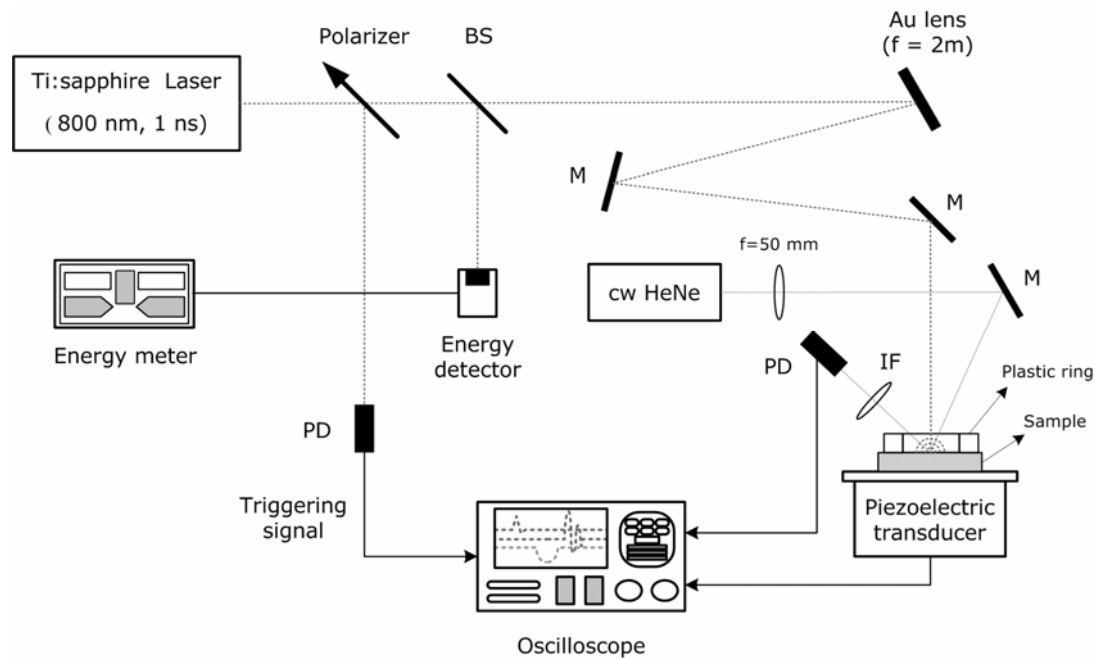


Figure 3.1. Schematic illustration of laser ablation with optical reflectance and acoustic pressure measurements. BS: beam splitter, M: mirror, PD: photodetector, IF: interference filter

Bubble formation during wet ablation was detected using the continuous wave HeNe probe laser beam ($\lambda = 632.8$ nm), which was directed with a 50 cm focal lens onto the center of the laser irradiated area. The reflectance signals were detected by a fast photodetector (DET 200, Thorlabs, NJ) along with an interference filter to reduce noise. The reflectance decreased due to scattering losses when bubbles formed on the surface [18]. Since the photothermal reflectance from the target surface was negligible, transient variation in the reflectance below the damage threshold of dry ablation provided an indicator of bubble dynamics on the surface. Both acoustic transients and optical reflectance signals were measured with an oscilloscope, which was triggered by the laser beam reflected at the polarizer. As a post-experimental analysis, the surface topography was evaluated by Scanning Electron Microscope (SEM). Damage thresholds for dry and wet cases were correlated with the measured acoustic transients and the SEM image of the ablated spot.

3.4 RESULTS

Figure 3.2(a) displays the cross-sectional images of aluminum sample under dry and wet ablation with 500 pulses at the radiant exposure $H = 1.43$ J/cm² per pulse. For dry ablation, an irregular profile of the ablation crater with a depth of 1.5 μ m and extruded ridges was evidently observed. By contrast, wet condition created a deeper (~ 12 μ m) ablation crater with relatively uniform V-

shape without a raised portion on the periphery. In these measurements, the topography of the ablated areas depended strongly on the applied radiant exposure. Ablation rates for both cases with 100 pulses were compared as a function of radiant exposure in Figure 3.2(b). The ablation rate was defined as the measured depth of each crater divided by the number of applied pulses. Wet ablation resulted in a significant increase in ablation rate compared to dry ablation over all exposures tested. The improvement factor of wet ablation was up to ~ 8 . Dry ablation demonstrated the saturation behavior of material removal rate after the onset of multiple-pulse ablation in our experiments; for the radiant exposures tested (all below plasma threshold), energy was insufficient to induce bulky material removal during dry ablation (see Figure 3.2(a)).

Peak acoustic amplitudes measured by a piezoelectric transducer during dry and wet conditions were compared at various radiant exposures with a single pulse (Figure 3.3). The acoustic signal threshold for dry ablation occurred at 0.71 J/cm^2 whereas wet ablation induced the lower acoustic inception at 0.41 J/cm^2 . Each acoustic threshold corresponded to the damage threshold (defined as surface disruption, for example, visible pits on the ablated spot near the threshold) confirmed by SEM images. The peak acoustic amplitudes for both conditions increased with radiant exposure. The peak pressure for wet ablation at the maximum radiant exposure (2.24 J/cm^2) was 2.7 bars, which was more than an order of amplitude higher than dry ablation at the same exposure.

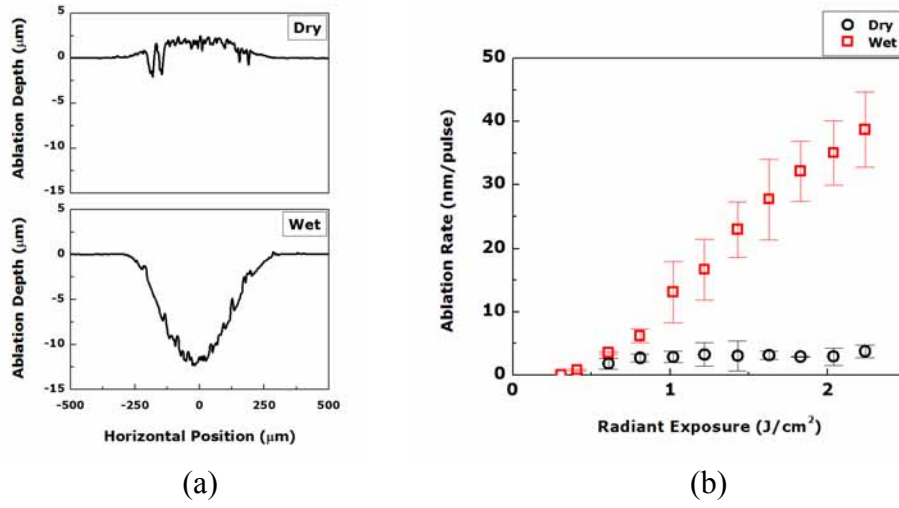


Figure 3.2. (a) Cross-sectional profiles of craters produced on Aluminum during dry (top) and wet (bottom) ablation ($H = 1.43 \text{ J}/\text{cm}^2$ per pulse and 500 pulses) and (b) comparison of ablation rates for dry and wet conditions as a function of radiant exposure per pulse ($n = 3$ and 100 pulses)

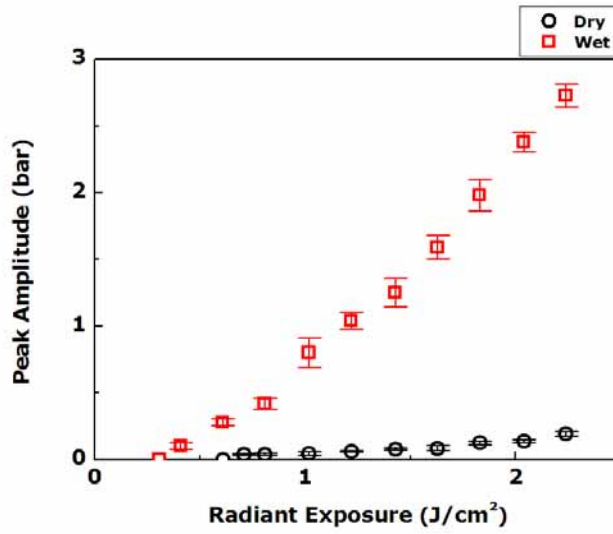


Figure 3.3. Comparison of peak acoustic amplitudes for dry and wet ablation as a function of radiant exposure ($n = 10$ and single pulse)

The kinetics of bubble growth was examined for wet ablation with a single pulse by monitoring surface reflectance of a HeNe beam in conjunction with the pressure measurements. At lower radiant exposures, the reflectance signal remained unchanged; however, when the radiant exposure exceeded the wet damage threshold (0.41 J/cm^2), transient changes of both the reflectance and pressure signals were observed as shown in Figure 3.4. Surface deformation of the Aluminum sample induced by cavitation during wet ablation was also observed in SEM images (Figure 3.5). A series of circular ripples was randomly distributed on the sample surface, which possibly resulted from multiple-bubble formation and expansion. In case of multiple pulses, the trace of cavitation bubble was less noticeable than single pulse due to material removal (Figure 3.5(b)).

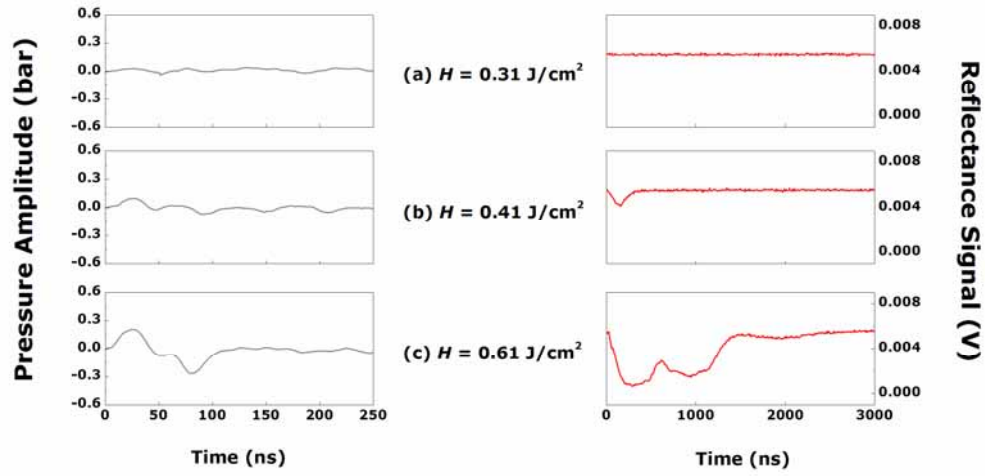


Figure 3.4. Comparison of transient acoustic pressure (left-hand side column) and optical reflectance (right-hand side column) at various radiant exposures with a single pulse: (a) $H = 0.31 \text{ J/cm}^2$ (top), (b) $H = 0.41 \text{ J/cm}^2$ (wet damage threshold, middle), and (c) $H = 0.61 \text{ J/cm}^2$ (bottom)

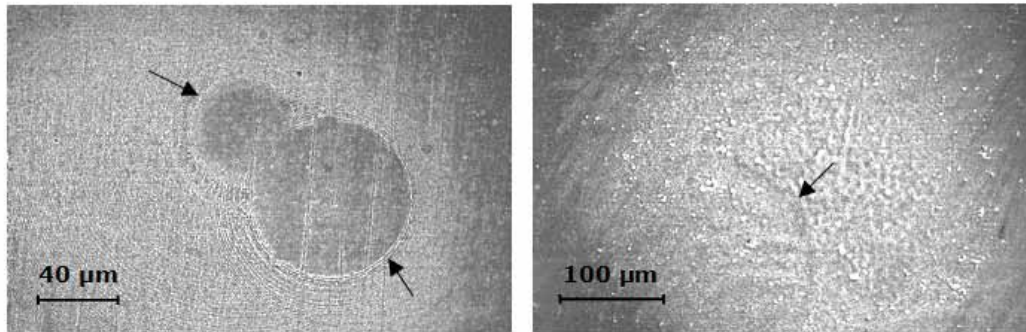


Figure 3.5. SEM images of Aluminum for wet ablation with (a) $H = 1.43 \text{ J/cm}^2$ and a single pulse and (b) $H = 2.24 \text{ J/cm}^2$ per pulse and 100 pulses (Arrows indicate the trace of bubbles)

3.5 DISCUSSION

The degree of wet damage threshold was documented by SEM images, which was correlated with the inception of acoustic and reflectance signals. Optical reflectance indicated the influence of bubble growth behavior on the ablation process at the wet threshold; the lower wet ablation threshold was associated with liquid vaporization. In contrast, due to rapid heating of the surface by the ns pulses, dry ablation was the result of surface vaporization at randomly distributed nucleation sites in a molten aluminum layer. An additional effect of bubble formation accounted for the wet process. To explain the effect of cavitation on wet damage threshold, a one dimensional temperature distribution at the end of the 1 ns pulse with $H = 0.41 \text{ J/cm}^2$ was calculated using conductive heat transfer between the water-aluminum interfaces (Figure 3.6) given by

$$(\rho c)_s \frac{\partial T_s}{\partial t} = \frac{\partial}{\partial z} \left(k_s \frac{\partial T_s}{\partial z} \right) + (1 - R) \mu_a \phi(t) \exp(-\mu_a z) \quad (3.1)$$

$$(\rho c)_l \frac{\partial T_l}{\partial t} = \frac{\partial}{\partial z} \left(k_l \frac{\partial T_l}{\partial z} \right) \quad (3.2)$$

where subscripts s and l indicate the aluminum and the water layer respectively, ρ density, c specific heat, T temperature, t time, z the coordinate normal to the sample surface, k thermal conductivity, R reflectivity of the laser beam at the aluminum surface, μ_a absorption coefficient of the aluminum, and $\phi(t)$ (W/m^2)

fluence rate. Although the peak temperature at the interface was lower than the vaporization point of aluminum, the temperature in the water medium (within 20 μm of the target) approached to the critical temperature of water ($T_c = 647 \text{ K}$) as $(\partial P/\partial V)_T = 0$ (P and V are pressure and volume of water, respectively), and the initiation of phase explosion developed as $T \sim 0.85T_c$ [19]. The critical radius (r_c) for homogeneous nucleation can be expressed as

$$r_c = \frac{2\sigma}{P_{sat}(T_l) \exp\{v_l [P_l - P_{sat}(T_l)] / R_a T_l\} - P_l} \quad (3.3)$$

where σ , T_l , P_{sat} , P_l , v_l , and R_a are the surface tension of the liquid, the temperature of the superheated liquid, the saturation pressure at the superheated liquid temperature, the pressure of the superheated liquid, specific volume, and gas constant, respectively [19]. Based on the equation 3.3, the estimated size of bubble for homogeneous nucleation when $T = 0.85T_c$ was $< 10 \text{ nm}$, which was much smaller than the superheated liquid region ($\sim 20 \mu\text{m}$). Thus, as the liquid layer became metastable (superheated), the metastable region initiated homogenous bubble formation accompanied by spherical shock wave generation. Therefore, this process validated the expectation of explosive vaporization (Figure 3.4). All the parameter values for calculations are listed in Table 3.1.

Table 3.1. The properties of aluminum and water used for calculations [20-22]

Property	Value	Property	Value
ρ_s (kg/m ³)	2684.95	R	0.87
ρ_l (kg/m ³)	1000	T_l (K)	550
c_s (J/kg·K)	900	P_{sat} (MPa)	5.942
c_l (J/kg·K)	4186.8	P_l (kPa)	101
k_s (W/m·K)	138.5	ν_l (m ³ /kg)	0.001317
k_l (W/m·K)	0.611	σ (N/m)	0.0197
μ_a (mm ⁻¹)	1327322.9	R_a (J/kg)	462

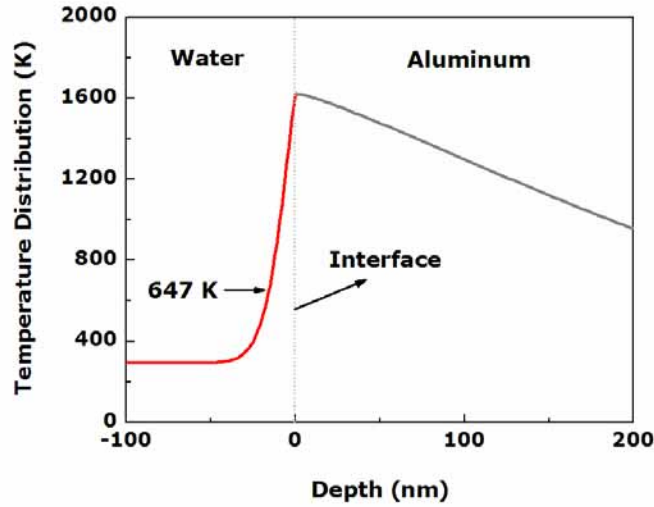


Figure 3.6. Temperature distribution after the short laser pulse (1 ns) inside water and aluminum media at $H = 0.41 \text{ J/cm}^2$

A strong pressure emitted during the rapid expansion of micro-bubbles caused surface damage [16], which was responsible for lower wet damage threshold and higher acoustic pressure (Figure 3.3), creating little pits on the aluminum surface. If the conical pits were generated on the surface, it was conceivable that vapor gas remained trapped in the pits. With the reduction of liquid pressure at higher radiant exposure, the conical pits could generate a stream of vapor bubbles as possible nucleation sites [23]. The effect of laser pulses at the liquid-aluminum interface increased temperature sufficiently to produce a phase change (melting of aluminum surface), which induced lower shear stress. Thus, bubble formation/collapse in the water impinged upon the aluminum creating surface deformation such as multiple circular ripples on the surface (Figure 3.5). In addition, previous studies reported that during both spherical and hemispherical bubble collapses near the rigid boundary, a high-speed, liquid-jet impinges on the surface. The jet is associated with high impulsive pressure (Figure 3.3) as additional mechanical impact improving ablation rate (Figure 3.2). Taking V as the collapse velocity, the pressure developed on impact is approximately $P \approx Z_{liquid} \cdot V$. Based on the solution of this equation for bubble collapse pressure (characteristic impedance of water $Z_{liquid} = 1.46 \times 10^6 \text{ kg/m}^2\text{s}$ and $V = 130 \text{ m/s}$) [23], one can obtain $P = 190 \text{ MPa}$, which exceeds the Vickers hardness of aluminum (167 MPa) responsible for plastic deformation and high pressure impact.

Another role of the water layer is a “cleaning” effect that prevents debris redeposition and increase energy coupling to the surface. As shown in Figure 3.5, radial water flow resulting from bubble expansion/collapse supplementarily precipitated the convective flow (v_r) of the aluminum molten layer due to variations in surface tension (σ_{al}) of the material (thermocapillary effect [24]). Since $v_r \propto \partial\sigma_{al}/\partial T$, for laser-light intensities with multiple pulses, the flow increased hydrodynamic instabilities (called Kelvin-Helmholtz [24]) at the water-aluminum interface. Therefore, more disturbances at the interface caused the pressure to increase with removal of ablated debris, resulting in enhancement of ablation performance.

3.6 CONCLUSION

We investigated laser ablation of Aluminum with 1 ns pulse under dry and wet conditions over a range of radiant exposures below the plasma threshold. The ablation rate of wet case was approximately 8 times faster than that of dry. Wet damage threshold was determined by pressure/optical reflectance detection and SEM images. Lower damage threshold and enhanced acoustic pressure with higher ablation performance during wet ablation were a result of explosive water vaporization and liquid-jet formation. Convective bubble motion contributed to the removal of debris redeposition, improving energy coupling and clean laser ablation process.

3.7 REFERENCES

1. Imen K, Lee SJ, Allen SD. Laser-assisted micron scale particle removal. *Appl Phys Lett* 1991;58:203-205.
2. Zapka W, Ziemlich W. Efficient pulsed laser removal of 0.2 mm sized particles from a solid surface. *Appl Phys Lett* 1991;58:2217-2219.
3. Tam AC, Leung WP, Zapka W, Ziemlich W. Laser-cleaning techniques for removal of surface particulates. *J Appl Phys* 1992;71:3515-3523.
4. She M, Kim D, Grigoropoulos CP. Liquid-assisted pulsed laser cleaning using near-infrared and ultraviolet radiation. *J Appl Phys* 1999;86:6519-6524.
5. Zhang W, Yao YL, Noyan IC. Microscale Laser Shock Peening of Thin Films, Part 1: Experiment, Modeling and Simulation. *J Manuf Scie-T ASME* 2004;126:10-17.
6. Kazakevich PV, Voronov VV, Simakin AV, Shafeev GA. Production of copper and brass nanoparticles upon laser ablation in liquids. *Quantum Electron* 2004;34:951-956.
7. Choo KL, Ogawa Y, Kanbargi G, Otrá V, Raff LM, Komanduri R. Micromachining of silicon by short-pulse laser ablation in air and under water. *Mater Sci Eng, A* 2004;372:145-162.
8. Ivanenko MM, Hering P. Wet bone ablation with mechanically Q-switched high-repetition-rate CO₂ laser. *Appl Phys B* 1998;67:395-397.
9. Kang HW, Lee H, Chen S, Welch AJ. Enhancement of Bovine Bone Ablation Assisted by a Transparent Liquid Layer on a Target Surface. *IEEE J Quantum Electron* 2006;42:633-642.
10. Fried D, Ashouri N, Breunig T, Shori R. Mechanism of Water Augmentation During IR Laser Ablation of Dental Enamel. *Lasers Surg Med* 2002;31:186-193.
11. Kruusing A. Underwater and water-assisted laser processing: Part I - general features, steam cleaning and shock processing. *Opt Laser Eng* 2004;41:307-327.
12. Zhu S, Lu YF, Hong MH, Chen XY. Laser ablation of solid substrates in water and ambient air. *J Appl Phys* 2001;89:2400-2403.
13. Ren J, Kelly M, Heeselink L. Laser ablation of silicon in water with nanosecond and femtosecond pulses. *Opt Lett* 2005;30:1740-1742.
14. Kim D, Oh B, Lee H. Effect of liquid film on near-threshold laser ablation of a solid surface. *Appl Surf Sci* 2004;222:138-147.
15. Vogel A, Busch S, Parlitz U. Shockwave emission and cavitation bubble generation by picosecond and nanosecond optical breakdown in water. *J Acoust Soc Am* 1996;100:148-165.

16. Isselin JC, Alloncle AP, Autric M. On laser induced single bubble near a solid boundary: Contribution to the understanding of erosion phenomena. *J Appl Phys* 1998;84:5766-5771.
17. Hale GM, Querry MR. Optical constants of water in the 200 nm to 200 mm wavelength region. *Appl Opt* 1973;12:555-563.
18. Yavas O, Leiderer P, Park HK, Grigoropoulos CP, Poon CC, Leung WP, Do N, Tam AC. Optical Reflectance and Scattering Studies of Nucleation and Growth of Bubbles at a Liquid-Solid Interface Induced by Pulsed Laser Heating. *Phys Rev Lett* 1993;70:1830-1833.
19. Yoo JH, Jeong SH, Mao XL, Greif R, Russo RE. Evidence for phase-explosion and generation of large particles during high power nanosecond laser ablation of silicon. *Appl Phys Lett* 2000;76:783-785.
20. Mills AF. Basic heat and mass transfer. Saddle River: Prentice-Hall, Inc., 1999.
21. Çengel YA, Boles MA. Thermodynamics: an engineering approach. New York: McGraw-Hill, 1998.
22. Palik ED. Handbook of optical constants of solids New York: Academic Press, Inc., 1985.
23. Young FR. Cavitation. London: McGraw-Hill, 1989.
24. Bäuerle D. Laser Processing and Chemistry. Berlin: Springer-Verlag, 2000.

Chapter 4: Evaluation of Liquid-assisted Laser Ablation with Various Metal Samples

4.1 ABSTRACT

We extended our previous investigation on the effect of a 1 mm water layer upon laser (800 nm, 1ns) ablation efficiency of aluminum to include indium, tin, copper, and nickel. Ablation threshold, crater depth, plasma characteristics, and acoustic transients as a function of fluence were compared to material properties. For all samples, wet ablation produced a larger ablation depth with increased acoustic transients than dry ablation. Wet ablation enhancement was the result of water vaporization, plasma confinement, and cavitation with jet impact. For dry and wet ablation, decrease of damage threshold and increase of ablation performance depended upon lower melting point and hardness in the order of indium, tin, aluminum, copper, and nickel.

4.2 INTRODUCTION

Pulsed laser ablation of materials with solid-liquid surface has long been a subject of interest due to increased ablation efficiency and improved surface

quality [1-4]. In our previous study with aluminum, a liquid layer lowers the damage threshold by 40 % and wet ablation yields eight times greater ablation rate than dry ablation. Higher acoustic pressures are generated during wet ablation [5]. The mechanisms of ablation under a layer of water appear to be a combination of explosive water vaporization with better optical-acoustic energy coupling, plasma confinement at high laser intensities, and cavitation with liquid jet formation [2,6-8].

To further understand the underlying mechanisms of liquid-assisted ablation and to improve the efficiency of laser processing, researchers have evaluated laser parameters (wavelength, pulse duration, radiant exposure, and number of pulse) [2] and various liquid configurations (spraying water vapor, flowing a water film, and submerging samples in a water cuvette) [1,6,9,10]. Although various studies in terms of liquid-assisted ablation have been carried out seeking an optimal combination of laser and liquid conditions, the influence of thermal and mechanical properties on laser ablation under liquid environment is poorly understood.

In this study, we evaluated the effect of liquid-confined laser ablation with a variety of metal samples of different material properties. A water layer of 1 mm thickness was deposited on each sample surface to minimize the effect of variations in liquid thickness. ‘Damage threshold’ was defined as surface modification such as tiny conical protrudes, determined by an optical microscope.

In situ examinations of plasma detection, acoustic transients, and optical reflectance were conducted to study the sequence of events associated with liquid-assisted ablation and the role that material properties have upon the ablation process. Ablation depth for each material was compared under direct (termed “dry”) and liquid-assisted conditions (termed “wet”) over a broad range of laser fluences in the nanosecond regime. The fluence used throughout this report represents the actual radiant exposure applied to the sample, excluding surface reflectance.

4.3 MATERIALS AND METHODS

For laser ablation tests, samples (25×25 mm and 0.5 mm thick) of indium, tin, aluminum, copper, and nickel were tested. Physical properties of these materials are listed in Table 4.1, and the reflectance of each sample was measured using a spectrophotometer (Cary 5E, Palo Alto, CA) at University of Texas at Austin. Each metal was irradiated at various fluences with either a single pulse gated while the laser was running at 3 Hz or 100 pulses (10 Hz) for ablation efficiency tests. A 1 mm thick plastic (Depron) ring was attached on top of a sample surface. Distilled water was deposited inside the ring prior to irradiation. The absorption coefficient of the water at the wavelength of interest (800 nm) was 0.01 cm^{-1} [11], so that the layer was effectively transparent for the laser beam with insignificant light absorption.

Experiments were carried out using a Ti:sapphire (Ti:S) laser at Stanford University (wavelength $\lambda = 800$ nm and pulse duration $\tau_p = 1$ ns at FWHM). A schematic diagram of the main experimental setup is illustrated in Figure 4.1. The laser beam had a Gaussian spatial distribution of energy, and a plano-convex lens with 1 m focal length focused the beam on the sample surface. The focal point spot diameter for all experiments was $105 \mu\text{m}$ ($1/e^2$). A polarizer with a half wave-plate for consistent beam attenuation was used to vary pulse energy levels up to 0.7 mJ; pulse energy was monitored by an energy meter (Ophir Optronics Inc., Danvers, MA) with a beam splitter. A high-speed Si photodetector (DET200, Thorlabs, NJ) detected reflected light from the lens surface for a triggering signal to measure plasma temporal profile, acoustic transients, and HeNe scattering signals on a digital oscilloscope (Tektronix TDS 620B).

Table 4.1. Optical, thermal, and mechanical properties of target materials [12-15].

Property	Indium	Tin	Aluminum	Copper	Nickel
Reflectance	0.79	0.76	0.56	0.84	0.67
Absorption coefficient (μm^{-1})	103.7	105.9	132.7	78.7	68.8
Melting point ($^{\circ}\text{C}$)	156.6	231.9	660.4	1083	1453
Boiling point ($^{\circ}\text{C}$)	2080	2270	2467	2567	2732
Thermal conductivity ($\text{W/m}\cdot\text{K}$)	81.8	66.8	237	401	90.9
Latent heat of evaporation (J/g)	2024	2497	10800	4796	6378
Thermal expansion ($\mu\text{m/m}\cdot\text{K}$ at 25°C)	32.1	22.0	23.1	16.5	13.4
Vickers hardness (MPa)	< 98	< 88.2	167	369	638

The transient pressure generated by a single pulse was monitored using a commercial piezoelectric transducer with a bandwidth up to 100 MHz (model WAT-04, Science Brothers, Inc., Houston, TX). The transducer was placed below that target, and a 1 mm thick plastic ring was attached on the transducer surface to match acoustic impedance between the sample and the transducer. Plasma formation was monitored with a photodetector with an interference filter. Plasma light reflected by a mirror was focused onto the photodetector by a 38.1 mm focal length lens mounted on the XY translation stage. In case of wet ablation, the HeNe laser beam ($\lambda = 632.8$ nm) was directed with a 333 mm focal length lens onto the center of the laser irradiated area, and reflected light was measured with the optical reflectance probe using a fast photodetector. An interference filter was inserted in front of the photodetector to reduce noise. The optical reflectance using the HeNe beam monitored decreased reflectance due to scattering losses when bubbles formed on the surface [16]. All the acoustic, plasma, and reflectance signals were recorded on the oscilloscope, which were triggered by the laser pulse.

For experiments with a sequence of 100 pulses at 10 Hz, the ablation efficiency and surface topography for all the targets tested were examined after the experiments with a stylus profilometer (CNMS, University of Texas at Austin).

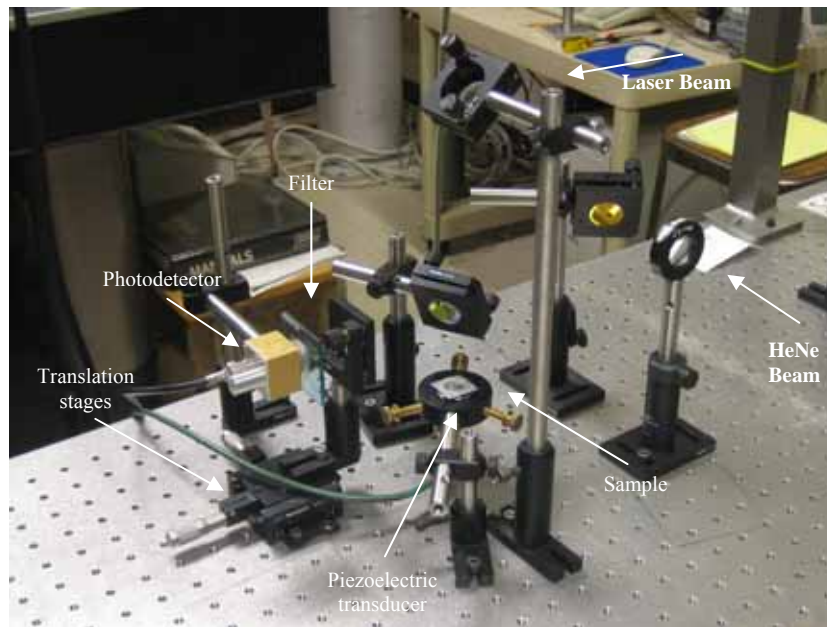
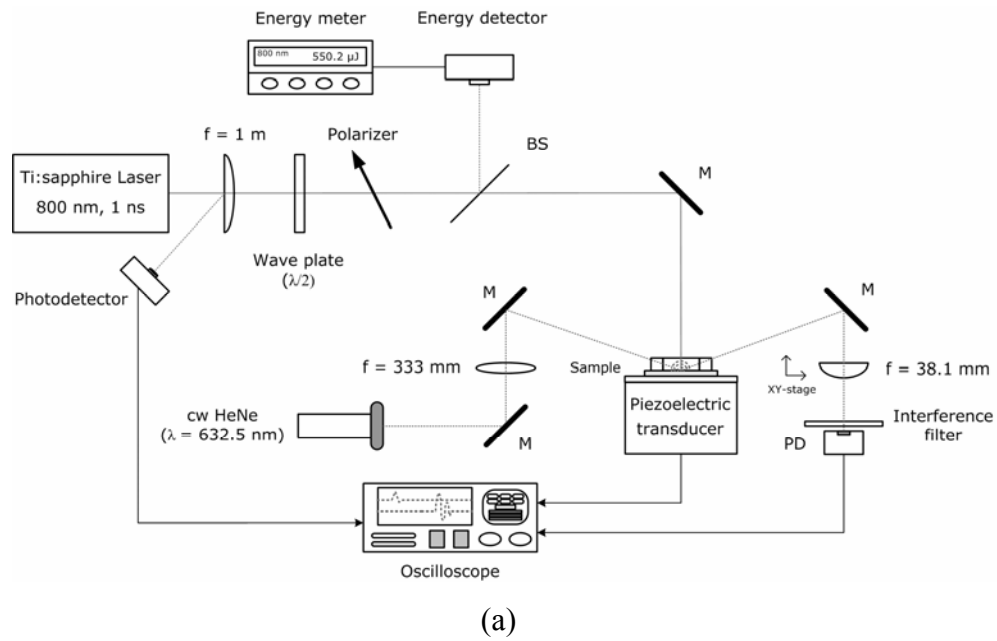


Figure 4.1. Schematic (a) and photograph (b) of the experimental setup used in laser ablation

4.4 RESULTS

Typical cross-sectional profiles of ablation craters for all the samples tested are presented in Figure 4.2. In general, wet ablation created deeper (~ 80 μm for indium) and wider ablation craters with relatively uniform and smooth shape and with either less or no extruded ridges around the spot, compared to dry ablation. However, there were wide differences in the degree of this trend. In the case of indium and tin which had lower melting points, dry ablation craters were slightly less deep with a raised portion on the periphery, compared to wet ablation craters. Aluminum samples had the greatest difference between dry and wet conditions in terms of material removal. Materials with higher melting point and hardness such as copper and nickel showed that wet ablation was more efficient than dry although the degree of material removal was much lower than other samples (note a different scale in ablation depth in Figure 4.2). To evaluate ablation performance for each material, ablation depth was displayed as a function of fluence per pulse (Figure 4.3). Fluence values were computed as actual pulse energy divided by spot size ($1/e^2$). The depth for dry and wet ablation increased with the fluence per pulse, and wet ablation resulted in significant increase of ablation depth compared to the dry condition. Wet ablation with 100 pulses induced material removal up to 85 μm where as dry ablation produced up to 62 μm (for indium shown in Figure 4.2). In case of indium and tin which had lower melting points and hardness, both dry and wet ablation presented a comparable

increased rate of ablation depth. On the other hand, the samples with relatively higher melting points and mechanical hardness had wet ablation depths approximately up to five times deeper than dry ablation. It was also noted that the degree of ablation efficiency decreased with increase of melting point and hardness.

A comparison of plasma peak intensity (the left-handed column) and plasma life time (the right-handed column) between dry and wet ablation as a function of fluence for various metal samples is shown in Figure 4.4. The plasma lifetime was defined as the duration time of plasma measured with a photodetector. For the samples tested, both peak intensity and plasma lifetime increased with fluence. It was noted that dry ablation yielded four times higher peak intensity and up to three times longer lifetime than the corresponding values for wet ablation. Overall, both dry and wet conditions had identical onset times of plasma formation although the thresholds of each metal sample were different. Material-dependent plasma thresholds are summarized in Table 4.2.

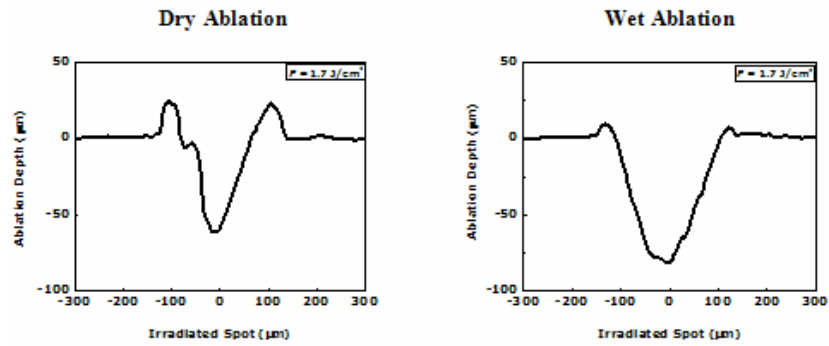
Peak acoustic amplitudes measured during dry and wet ablation were compared as a function of fluence for all the samples in Figure 4.5. In general, the peak amplitude for both dry and wet cases increased with the applied fluence, and wet ablation produced acoustic magnitudes up to four times greater than dry ablation. The acoustic thresholds for wet ablation were up to 50 % lower than

those of dry ablation (see Table 4.2); however, the acoustic signal for dry nickel ablation could not be measured since its amplitude was in the noise level.

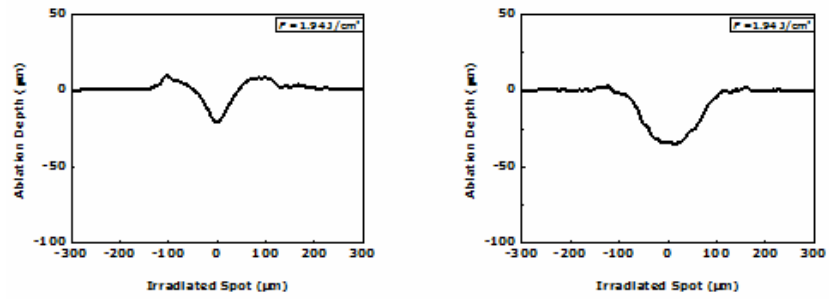
Fluences for acoustic thresholds (see Table 4.2) were equal to corresponding values for damage thresholds (defined as surface deformation), so pressure measurements signified the onset of material removal for both dry and wet conditions. For all the materials tested, wet ablation induced lower damage thresholds than dry ablation. The damage thresholds for both dry and wet ablation increased with melting point and material hardness. For example, indium with melting point of 156.6 °C and hardness of less than 98 MPa showed approximately 60 % lower damage threshold than nickel with 1453 °C and 638 MPa. According to Table 4.2, dry damage thresholds for all the samples occurred after plasma formation. On the other hand, in case of wet ablation, plasma formation was initiated after the occurrence of damage for indium, tin, and aluminum samples. Fluences for surface deformation of copper and nickel samples were higher than their plasma thresholds.

To examine the effect of cavitation on material removal, optical reflectance of the sample surface was measured for aluminum and nickel samples (Figure 4.6). For both samples, a transient change of the reflectance signals correlated with the inception of acoustic pressures at 0.41 J/cm² for aluminum and 0.77 J/cm² for nickel, respectively, which corresponded to the damage threshold for wet ablation. Since the plasma threshold for nickel was lower than the

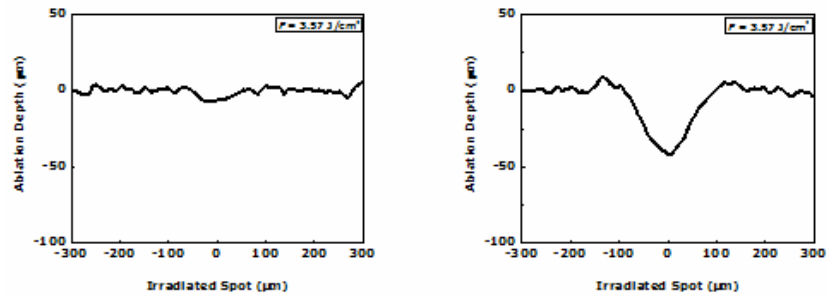
damage threshold fluence, change in reflectance signal may have been affected by both optical breakdown and cavitation above the sample surface.



(a) Indium



(b) Tin



(c) Aluminum

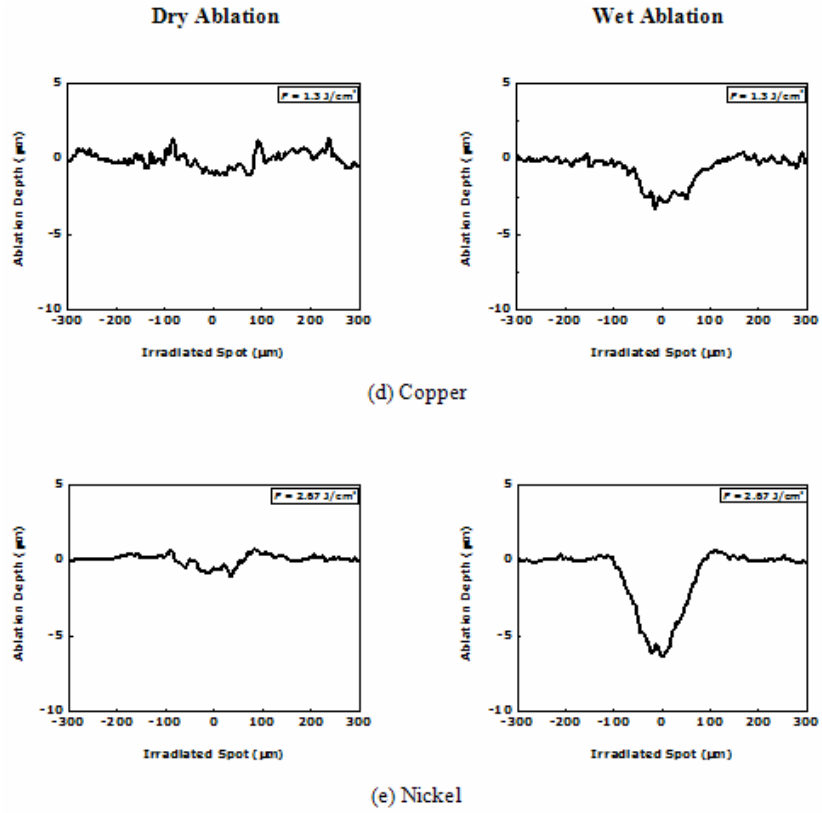
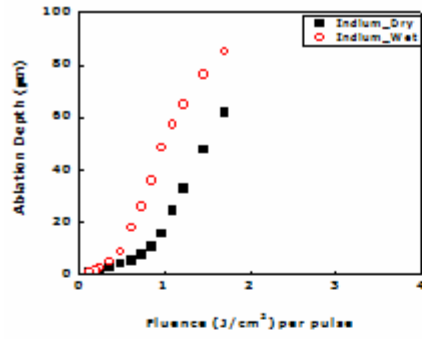
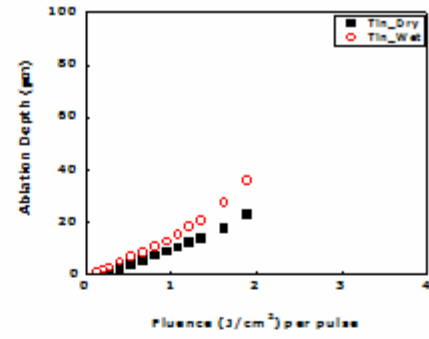


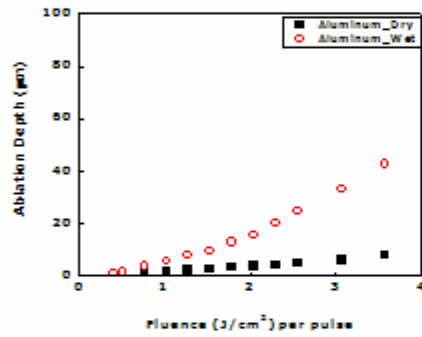
Figure 4.2. Cross-sectional profiles created during dry (left-handed side column) and wet (right-handed side column) ablation with 100 pulses at various fluences per pulse: (a) indium at 1.7 J/cm^2 per pulse, (b) tin at 1.94 J/cm^2 per pulse, (c) aluminum at 3.57 J/cm^2 per pulse, (d) copper at 1.3 J/cm^2 per pulse, and (e) nickel at 2.67 J/cm^2 per pulse. Note a different scale in ablation depth.



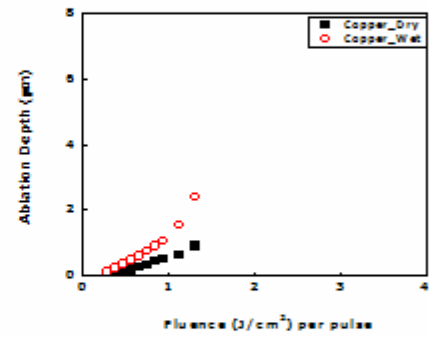
(a) Indium



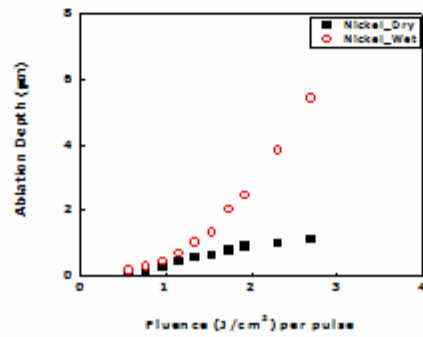
(b) Tin



(c) Aluminum

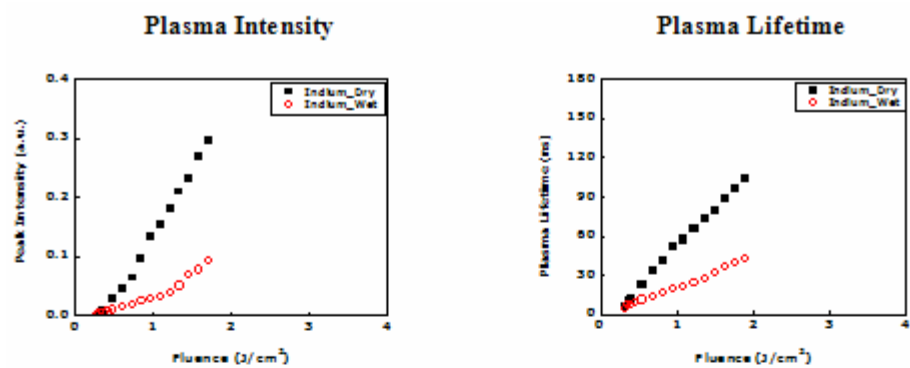


(d) Copper

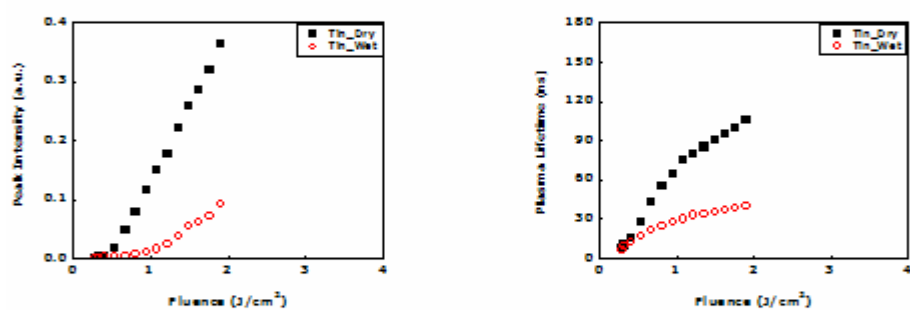


(e) Nickel

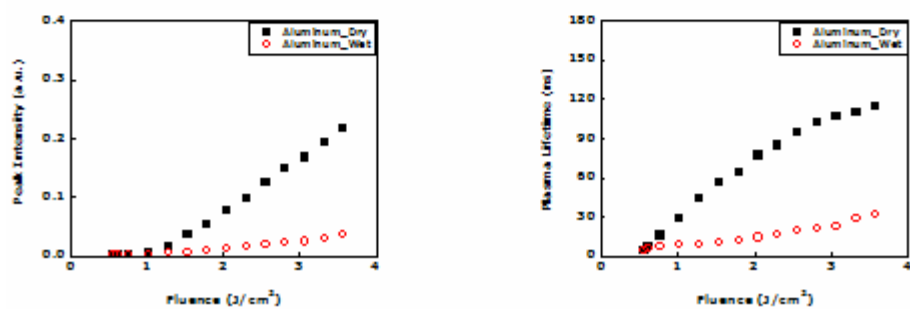
Figure 4.3. Comparison of ablation depth between dry and wet ablation with 100 pulses as a function of fluence per pulse using various metals: (a) indium, (b) tin, (c) aluminum, (d) copper, and (e) nickel. Note a different scale in ablation depth.



(a) Indium



(b) Tin



(c) Aluminum

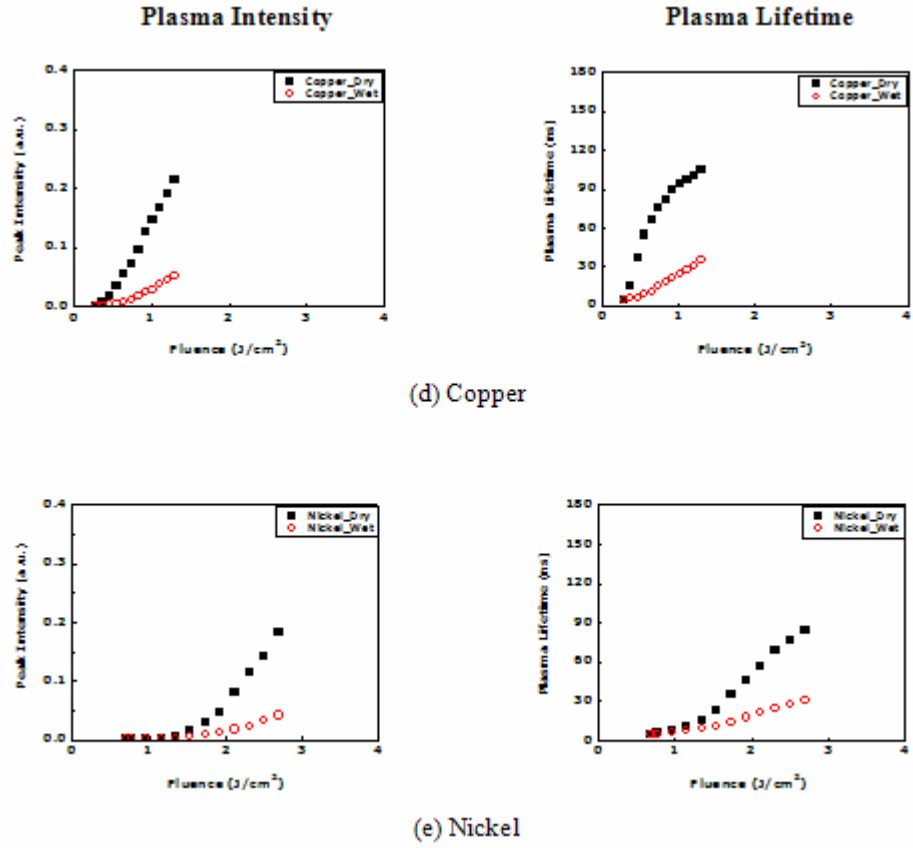
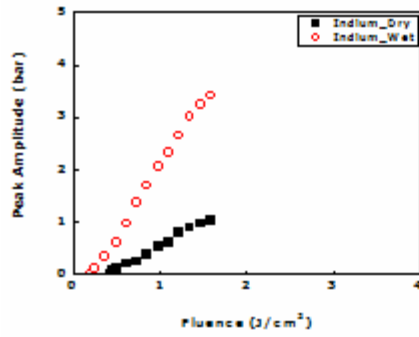


Figure 4.4. Comparison of plasma peak intensity (left-handed side column) and lifetime (right-handed side column) as a function of fluence using a single pulse on various metals: (a) indium, (b) tin, (c) aluminum, (d) copper, and (e) nickel

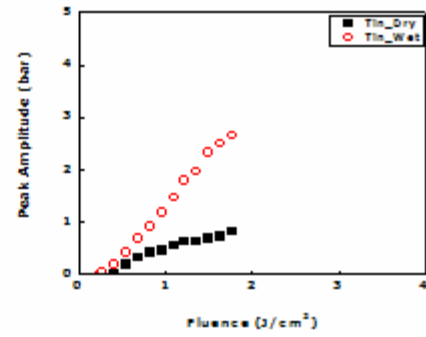
Table 4.2. Damage, acoustic, and plasma thresholds of dry and wet ablation for all the materials.

Sample	Dry Thresholds (J/cm ²)			Wet Thresholds (J/cm ²)			Threshold Difference (%) [*]	
	Damage	Acoustic	Plasma	Damage	Acoustic	Plasma	Damage	Acoustic
Indium	0.4	0.4	0.29	0.2	0.2	0.29	66.7	66.7
Tin	0.41	0.41	0.3	0.25	0.25	0.3	48.5	48.5
Aluminum	0.66	0.66	0.56	0.41	0.41	0.56	46.7	46.7
Copper	0.76	0.76	0.3	0.46	0.46	0.3	49.2	49.2
Nickel	0.96	N/A	0.69	0.77	0.77	0.69	22.0	N/A

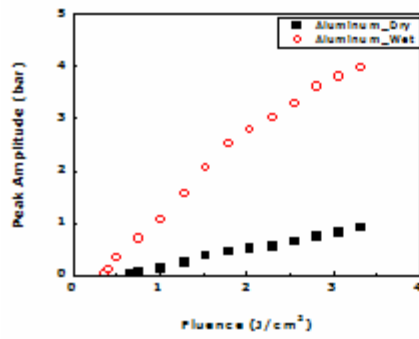
^{*}Threshold Difference (%) = $\left| \frac{Dry - Wet}{Dry + Wet} \right| \times 200$



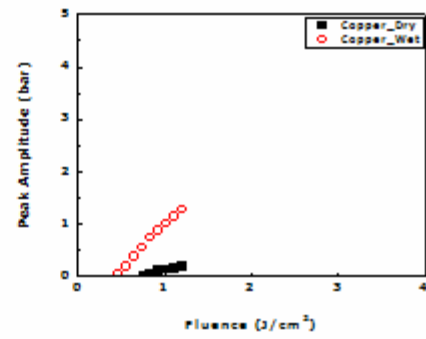
(a) Indium



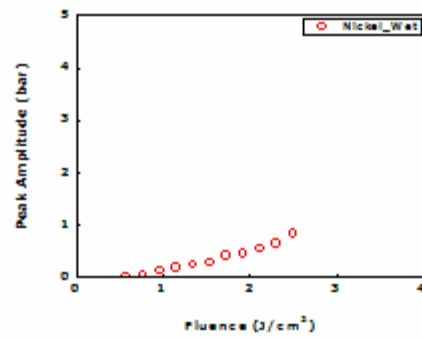
(b) Tin



(c) Aluminum



(d) Copper



(e) Nickel

Figure 4.5. Comparison of peak acoustic amplitudes for dry and wet ablation as a function of fluence using various metals: (a) indium, (b) tin, (c) aluminum, (d) copper, and (e) nickel. Note that no acoustic signal was measured during dry ablation of nickel.

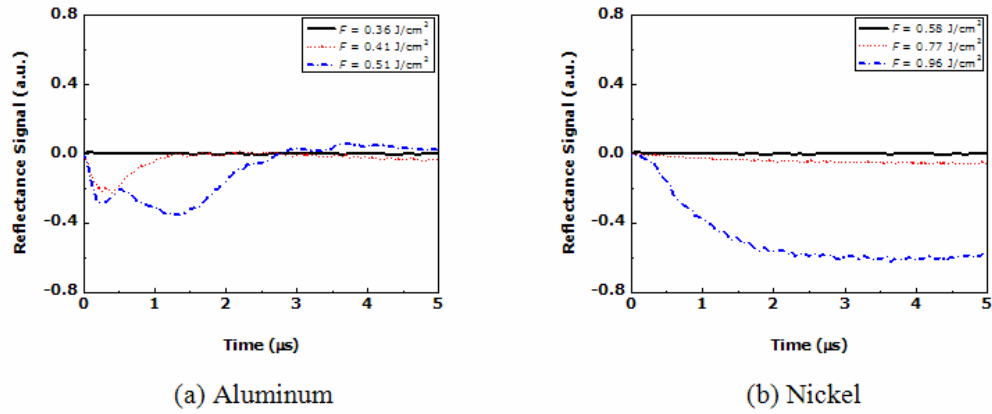


Figure 4.6. Optical reflectance signals measured during wet ablation on (a) aluminum and (b) nickel at various fluences. Note that the signal thresholds for aluminum and nickel were 0.41 J/cm^2 and 0.77 J/cm^2 , respectively.

4.5 DISCUSSION

According to our experimental results with various metals, a 1 mm water layer reduced damage thresholds and improved ablation efficiency. Since our dry damage thresholds were higher than plasma thresholds for all the materials, we agree with Bäuerle [17] that dry ablation was driven by plasma formation. It should be noted that ignition of a plasma resulting from emission of very few electrons to the air can occur prior to the bulk ablation of the metal. Additionally, due to plasma expansion during dry ablation, lower ablation efficiency (Figure 4.3) can be explained by enhanced plasma shielding that reduced pressure amplitude exerting on the sample surface (Figure 4.5) [17]. On the other hand, since the wet damage thresholds were lower than dry damage thresholds for all tested metals and these thresholds correlated with the onset of acoustic thresholds,

we believe that explosive liquid vaporization was involved in the wet ablation threshold [2,8]. In addition, shorter lifetime and lower intensities of wet plasmas (Figure 4.4) imply the dissipation of more thermal energy to the water layer during plasma expansion, leading to rapid water vaporization and cavitation [8]. However, since plasma luminescence in air is generally much brighter than plasma in water due to prevalent non-radiative dissipation [18], it should not be neglected that weak plasmas with lower intensity in water might exist below ablation threshold beyond our level of detection in this experiment. Accordingly, further investigations on detection of plasma threshold in water should be performed. Based on acoustic transients and optical reflectance for wet ablation, shock waves generated during explosive vaporization, plasma formation/expansion, and cavitation with jet formation were possibly applied to enhance the expulsion of molten or even non-molten material as additional mechanical impulses [19]. Thus, lowered damage thresholds and increased acoustic pressure resulted in enhanced ablation performance for all the samples in spite of possible plasma shielding [2,8]. Additional effects were surface cleaning associated with convective flow of water and cooling effect from higher heat of vaporization of water (2260 kJ/kg [20]) which prevented debris redeposition as well as excessive heat generation, enhancing optical energy coupling and surface morphology (Figure 4.2) [4].

In general, laser metal ablation in the nanosecond regime is based on thermal processes: temperature rise after light absorption can result in material removal with surface melting [17]. Since the surface peak temperature is contingent on the absorption coefficient of a sample, indium and tin with higher absorption coefficients (Table 4.1) had lower damage thresholds and larger ablation depths than the other samples. Furthermore, the irradiated spot initially experiences a liquid-phase transition through a melting process by laser heating with the ensuing ablation process; therefore, regardless of the ablation conditions, indium with the lowest melting point had the lowest damage threshold, followed by tin with the second lowest melting point and damage threshold (Table 4.2). Even though aluminum possessed the highest absorption coefficient (Table 4.1), its higher melting point caused aluminum to have a higher damage threshold fluence than either indium or tin. For copper and nickel, lower absorption and higher melting point delayed material removal process, requiring higher fluence for ablation (Table 4.2).

Since dry ablation generates a shock wave during plasma formation/expansion and the role of a water layer during wet ablation is to provide additional mechanical impact to the sample, indium and tin with lower hardness (see Table 4.1) were more susceptible to external mechanical forces, resulting in improvement of acoustic transients and ablation performance shown in Figures 4.3 and 4.5. For indium and tin, both dry and wet ablation showed a

relatively comparable increased rate of ablation performance; this phenomenon can be explained by the fact that the shock wave with higher plasma intensity (Figure 4.4) during dry ablation was sufficiently strong to remove mechanically weaker samples, compensating ablation performance (Figure 4.3). Therefore, regardless of plasma shielding, the advantage of additional impact during wet ablation was relatively minimized since lower melting point and hardness produced a slight difference between dry and wet ablation depth. In case of aluminum, the laser-induced acoustic amplitudes for dry and wet conditions were similar to those of indium and tin samples, respectively; however, for indium, tin, and aluminum, the depth of the resulting crater from either dry or wet ablation was determined by mechanical hardness of each material. It was conceivable that aluminum harder than indium and tin was more resistant to the shock wave with lower plasma intensity (Figure 4.4) generated during dry ablation; the role of a water layer became relatively significant to enhance ablation efficiency up to five times higher than dry ablation.

For dry and wet ablation, copper and nickel presented ablation depths up to ten times lower than less hard materials, which signified that the harder a metal, the more additional mechanical impact is required to obtain the same amount of material removal as a soft metal. Higher mechanical hardness possibly tolerated surface deformation induced by mechanical impact from shock wave generation during dry ablation, leading to higher damage threshold and lower ablation

efficiency (Table 4.2 and Figure 4.3). Although additional plasma threshold measurements would be useful, higher wet damage threshold fluence than plasma threshold for both copper and nickel samples (Table 4.2) implies that the emission of pressure wave during rapid vaporization of wet ablation was not strong enough to induce metal ablation; accordingly, this plasma-mediated explosive vaporization during wet ablation was essential to material removal, substantiating the necessity of greater mechanical impacts for mechanically hard metal ablation.

It should be noted that in terms of difference between dry and wet signal thresholds (Table 4.2), the mechanism reducing the damage threshold corresponds to the mechanism reducing the acoustic threshold; a water layer can provide more effective coupling of the laser pulse through impedance matching between material and water. Unlike indium and tin, other samples (aluminum, copper, and nickel) showed the advantage of wet ablation as a larger distinction in ablation depth between dry and wet conditions. According to Table 4.2 and Figure 4.3, the decrease of damage threshold and increase of ablation performance depended upon lower melting point and hardness in the order of indium, tin, aluminum, copper, and nickel. Hence, for both dry and wet ablation, thermal and mechanical properties were shown as important factors to promote a metal sample to be plastically deformed by mechanical impulse.

4.6 CONCLUSION

Laser ablation of metals with various material properties under dry and wet conditions was investigated experimentally. For the metals tested, wet ablation produced higher ablation efficiency with enhanced acoustic pressure than dry. Lower damage threshold with higher ablation performance during wet ablation resulted from a combination of explosive vaporization, plasma confinement, and cavitation. Melting point and material hardness were significant factors to determine the degree of ablation threshold and efficiency for metal samples under dry and wet conditions.

4.7 REFERENCES

1. Hong MH, Koh ML, Zhu S, Lu YF, Chong TC. Steam-assisted laser ablation and its signal diagnostics. *Appl Surf Sci* 2002;197-198:911-914.
2. Kruusing A. Underwater and water-assisted laser processing: Part I - general features, steam cleaning and shock processing. *Opt Laser Eng* 2004;41:307-327.
3. Choo KL, Ogawa Y, Kanbargi G, Otrava V, Raff LM, Komanduri R. Micromachining of silicon by short-pulse laser ablation in air and under water. *Mater Sci Eng, A* 2004;372:145-162.
4. Ren J, Kelly M, Heeselink L. Laser ablation of silicon in water with nanosecond and femtosecond pulses. *Opt Lett* 2005;30:1740-1742.
5. Kang HW, Welch AJ, Simanovskii D, Schwettman AH, Lee H. Laser ablation in a liquid-confined environment using a nanosecond laser pulse. *Opt Express* 2006;to be submitted.
6. Kim D, Oh B, Lee H. Effect of liquid film on near-threshold laser ablation of a solid surface. *Appl Surf Sci* 2004;222:138-147.
7. Zhu S, Lu YF, Hong MH, Chen XY. Laser ablation of solid substrates in water and ambient air. *J Appl Phys* 2001;89:2400-2403.
8. Kang HW, Lee H, Chen S, Welch AJ. Enhancement of Bovine Bone Ablation Assisted by a Transparent Liquid Layer on a Target Surface. *IEEE J Quantum Electron* 2006;42:633-642.

9. Lu J, Xu RQ, Chen X, Shen ZH, Ni XW, Zhang SY, Gao CM. Mechanisms of laser drilling of metal plates underwater. *J Appl Phys* 2004;95:3890-3894.
10. Dupont A, Caminat P, Bournot P. Enhancement of material ablation using 248, 308, 532, 1064 nm laser pulse with a water film on the treated surface. *J Appl Phys* 1995;78:2022-2028.
11. Hale GM, Querry MR. Optical constants of water in the 200 nm to 200 mm wavelength region. *Appl Opt* 1973;12:555-563.
12. Palik ED. Handbook of optical constants of solids III. San Diego: Academic Press, Inc., 1988.
13. Palik ED. Handbook of optical constants of solids New York: Academic Press, Inc., 1985.
14. Lide DR. CRC Handbook of Chemistry and Physics. Boca Raton: Taylor and Francis, 2006.
15. Samsonov GV. Handbook of the physicochemical properties of the elements. New York: IFI-Plenum, 1968.
16. Yavas O, Leiderer P, Park HK, Grigoropoulos CP, Poon CC, Leung WP, Do N, Tam AC. Optical Reflectance and Scattering Studies of Nucleation and Growth of Bubbles at a Liquid-Solid Interface Induced by Pulsed Laser Heating. *Phys Rev Lett* 1993;70:1830-1833.
17. Bäuerle D. Laser Processing and Chemistry. Berlin: Springer-Verlag, 2000.
18. Felix MP, Ellis AT. Laser-Induced Liquid Breakdown - A Step-By-Step Account. *Appl Phys Lett* 1971;19:484-486.
19. Vogel A, Venugopalan V. Mechanisms of Pulsed Laser Ablation of Biological Tissues. *Chem Rev* 2003;103:577-644.
20. Mackanos MA, Jansen ED, Shaw BL, Sanghera JA, Aggarwal I, Katzir A. Delivery of midinfrared (6 to 7-mm) laser radiation in a liquid environment using infrared-transmitting optical fibers. *J Biomed Opt* 2003;8:583-593.

Chapter 5: Enhancement of Bovine Bone Ablation Assisted by a Transparent Liquid Layer on a Target Surface

5.1 ABSTRACT

The purpose of this study was to investigate the laser-induced ablation of bovine bone assisted by a transparent liquid layer on top of the target surface. A Q-switched Nd:YAG laser was used to ablate bovine *tibia* at various energy levels. Distilled water was applied to the sample surface in order to examine the role of a transparent liquid layer during the ablation. Plasma generation and transient acoustic waves were monitored to identify dominant mechanisms involved in the ablation process. Ablation efficiency was measured from the cross-sectional tomography acquired by Optical Coherence Tomography (OCT). Ablation with a liquid layer lowered the damage threshold and enhanced both the laser-induced acoustic excitation and the ablation efficiency, which saturated at higher radiant exposures. The enhanced ablation of the liquid-assisted process is primarily due to photomechanical effects associated with explosive vaporization and plasma confinement. The saturation of the pressure amplitude and ablation efficiency was attributed to increased plasma shielding.

5.2 INTRODUCTION

Lasers have been of interest as a feasible alternative in orthopedic surgery since extensive studies for the potential use of lasers for osteotomy procedures began in the 1970s [1,2]. Standard tools in orthopedics such as saws, milling-machines, and mechanical drills induce severe mechanical vibrations and hemorrhage whereas lasers generally have significant advantages, allowing non-contact intervention, controlled bone excision, free cut geometry, hemostatic and aseptic effects, and minimal invasiveness [3]. Due to a strong absorption of infrared radiation by high water content and Amide I/II bands in bone tissue, several lasers such as Excimer, Ho:YAG, HF, Er:YAG, CO₂, and FEL have been investigated for surgical application in bone cutting, and their characteristics of bone ablation with various wavelengths and modes have been reported [4–9]. Since most lasers tested for osteotomy produced long pulse durations (i.e., > tens of microseconds), a temperature rise in the laser-affected zone is induced with minimal acoustic waves; therefore, material removal is thought to be initiated by photothermal mechanisms [10,11].

Recent studies demonstrated augmented ablation efficiency by application of a transparent liquid layer on the target surface (termed the “wet condition”) [12,13]. If damage threshold is defined as the initial surface deformation, then in the regime slightly above the damage threshold, the efficiency is promoted mainly by increased optical-acoustic coupling and the photomechanical effect in

association with explosive vaporization in the strongly superheated liquid layer [14]. Additionally, the liquid-assisted process lowered the damage threshold by 20-40 % along with the augmentation of ablation performance, compared to the direct ablation (termed the “dry condition”) [14]. At a high radiant exposure regime, it was reported that the laser-induced plasma is confined in the liquid layer, consequently inducing higher acoustic and shock waves than the dry condition [15,16]. The enhanced mechanical wave emission imposes significant effects on the mechanical response of the target surface resulting in more material removal.

Previous studies were conducted mostly with metal samples, and the near-threshold regime and plasma regime were investigated independently [12–16]. To our knowledge, this study provides the first experimental report to test laser ablation in liquid confinement on biological bone tissues. In this study, we tested the hypothesis that ablation of biological tissues, especially bovine bone, could be enhanced by increased photomechanical effects, which possibly result from plasma confinement along with the explosive vaporization of a liquid layer. A Q-switched Nd:YAG laser with a short pulse was used with various energy settings. Ablation efficiency was compared for bone samples in air and water environments as a function of radiant exposure with single and multiple pulses. By measuring plasma formation and acoustic wave propagation, the role of a liquid layer during the ablation process was examined.

5.3 MATERIALS AND METHODS

5.3.1 SPECIMEN

Bovine *tibia* obtained from a local slaughter house was used for the laser-tissue ablation experiment. The connective tissue and periosteum were peeled away from the bone specimen, and the sample was rinsed in tap water for approximately 10 minutes to remove hemocytes. To obtain uniform size samples (1.5×2.5 cm) of the samples, bone osteotomy was performed using a standard handsaw. The surface was polished using sandpaper with a grain size of 30 μm , maintaining the flat surface of the samples with a constant thickness of approximately 4 mm. Once all the samples were prepared, they were stored in a saline solution at 4 °C 24 hours prior to experimentation, possibly minimizing the change of hydration state of the tissue. In order to perform liquid-assisted ablation, a plastic (Depron) ring with 1 mm thickness was attached on top of a sample surface to maintain a consistent liquid layer thickness. Prior to laser-pulse irradiation, distilled water was deposited inside the ring. The absorption coefficient of water at the wavelength of interest (1064 nm) was 0.13 cm^{-1} , so that the water layer was relatively transparent with insignificant light absorption [17,18]. Optical, thermal, and mechanical properties of the target materials are provided in Table 5.1.

Table 5.1 Optical, thermal, and mechanical properties for water and bone [17] – [23]

Material Properties	Water	Bone
Optical Absorption Coefficient (cm^{-1})	0.13	N/A
Thermal Conductivity ($\text{W/m}\cdot\text{K}$)	0.611	0.373 – 0.496
Fracture Toughness ($\text{MPa/m}^{1/2}$)	N/A	2.0 – 5.6
Speed of Sound (m/s)	1481	2000 – 3441

5.3.2 LASER SOURCE AND DELIVERY

A number of craters were created on bone samples using a Q-switched Nd:YAG laser (Contium Surelite II10, Santa Clara, CA). The 1064 nm laser emitted FWHM pulses of approximately 30 ns. The applied pulse energy ranged from 11 mJ to 393 mJ, and either one, ten, or twenty pulses were applied with a repetition rate of 1 Hz. A schematic illustration for ablation experiments with the Q-switched Nd:YAG is presented in Figure 5.1. Two beam splitters were placed in the beam path; one was used to monitor the pulse energy, and the other to achieve a triggering signal. The laser pulse was reflected at an angle of 90 ° using a 1064 nm BK 7 mirror (CVI laser, Albuquerque, NM). By using a convex CaF₂ lens with a focal length of 50 mm, the laser beam was focused on the surface of the target sample with a spot diameter of 150 μm, which was determined from a knife-edge measurement. The spot size was defined as the distance between 10 % and 90 % clip points without multiplying the width adjust factor ($0.552\sqrt{2}$) which is used for the estimation of $1/e^2$ diameter of a Gaussian beam [24]. An energy detector (PE25BB-DIF, Ophir Optonics Inc., Danvers, MA) was used to monitor the applied pulse energy during the experiment. A fast Si photodetector (1 ns rise time, DET210, Thorlabs, NJ) was used to produce a triggering signal for a digital oscilloscope (Hewlett Packard *Infinium*, Colorado Springs, CO), which measured the temporal profile of plasma and acoustic transients.

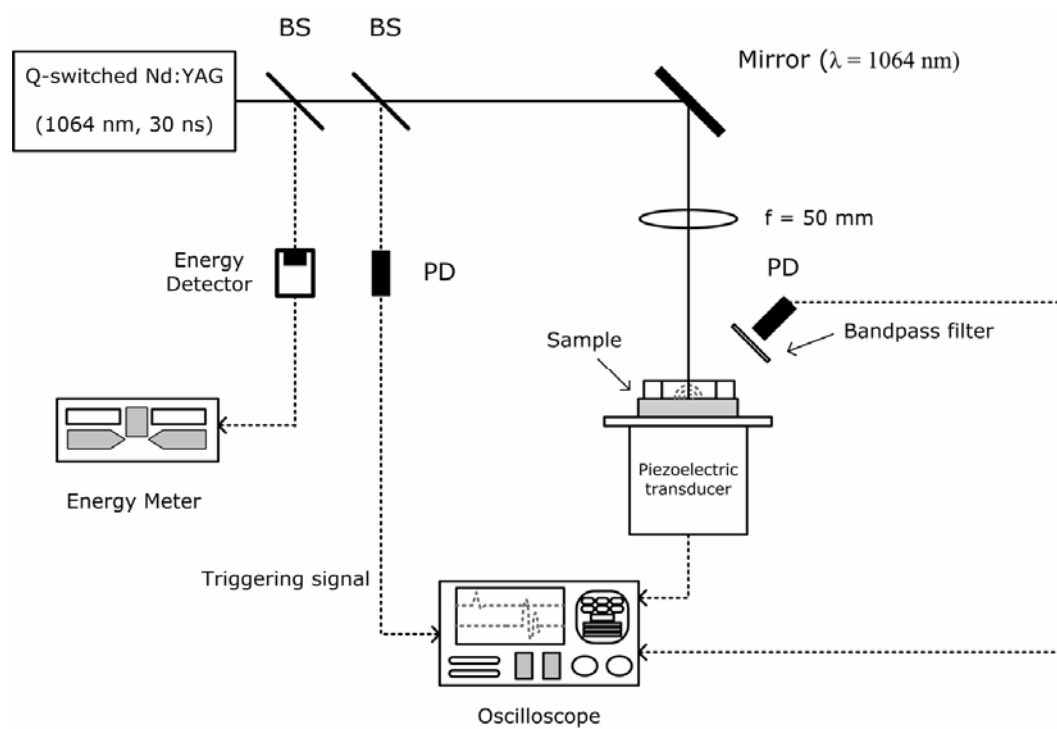


Figure 5.1. Schematic of an experimental setup to measure plasma formation and acoustic transients using a Q-switched Nd:YAG laser system. BS: beam splitter; PD: photodetector.

5.3.3 PLASMA AND ACOUSTIC WAVE DETECTION

To monitor plasma formation during the ablation process, a fast photodetector with a bandpass filter rejecting 1064 nm was placed approximately 3 cm above the irradiated spot. The breakdown process was detected by eye and confirmed by a photodetector. The laser-induced acoustic wave was monitored experimentally using a commercial piezoelectric transducer (model WAT-04, Science Brothers, Inc., Houston, TX). The transducer was mounted below the target, and a 1 mm thick plastic ring was attached on the transducer surface. During the experiment, the ring was filled with distilled water in order to maintain impedance match between the sample and the transducer. The transducer contained a lithium niobate element calibrated by the manufacturer over a bandwidth up to 100 MHz.

5.3.4 ABLATION EFFICIENCY

Ablation craters were produced with ten and twenty pulses of various radiant exposures for the purpose of comparing ablation efficiency between dry and wet cases. In order to maintain a consistent liquid layer thickness, distilled water was deposited after each laser pulse. Laser-induced craters were examined using an Optical Coherence Tomography (OCT) system ($\lambda_o = 1290$ nm, $\Delta\lambda = 42$ nm, and $P = 2.2$ mW) with lateral and axial resolution of ~ 20 μm to obtain quantitative ablation dimensions [25,26]. A series of vertical cross-sectional

images (direction parallel to laser beam propagation) were obtained over the entire crater. The step-size between images was 35 μm . Crater depth and ablation volume were estimated from the OCT cross sections. Craters produced with a single pulse were also observed with an optical microscope to evaluate the damage threshold for each case.

5.4 RESULTS

Figure 5.2 displays the OCT cross-sectional images of the bone samples at 14.9 J/mm² and 22.2 J/mm². Samples were ablated with twenty pulses for both conditions. The craters induced by wet ablation showed larger crater depth and higher ablation volume than those of dry ablation. The laser pulse produced relatively rough and irregular contours. Dimensions of ablation craters for dry and wet cases are compared in Figure 5.3. Ten and twenty pulses with various radiant exposures were applied to the samples. Regardless of the radiant exposure, both ablation depth and volume increased with the number of pulses. Crater depth and volume of wet ablation were up to three and six times greater than those of dry condition respectively. The result shows that the ablation depth and volume increased rapidly as the radiant exposure increased to 8.9 J/mm², but with higher radiant exposure, the rate of increase in ablation performance began to diminish.

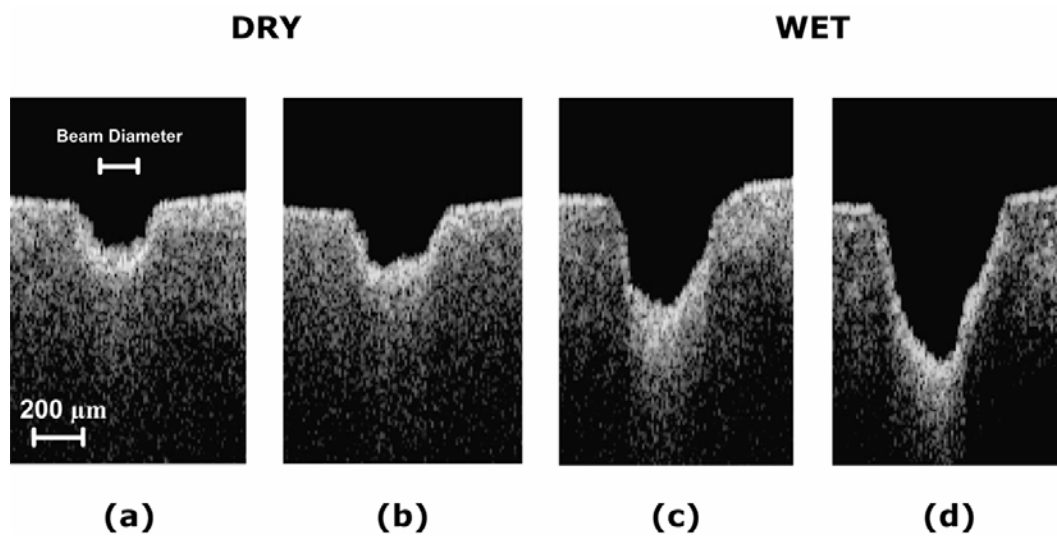
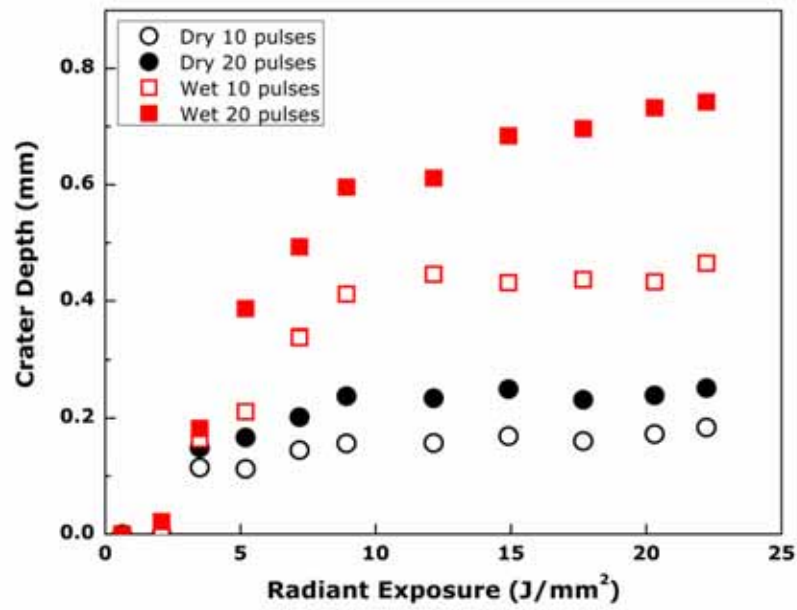
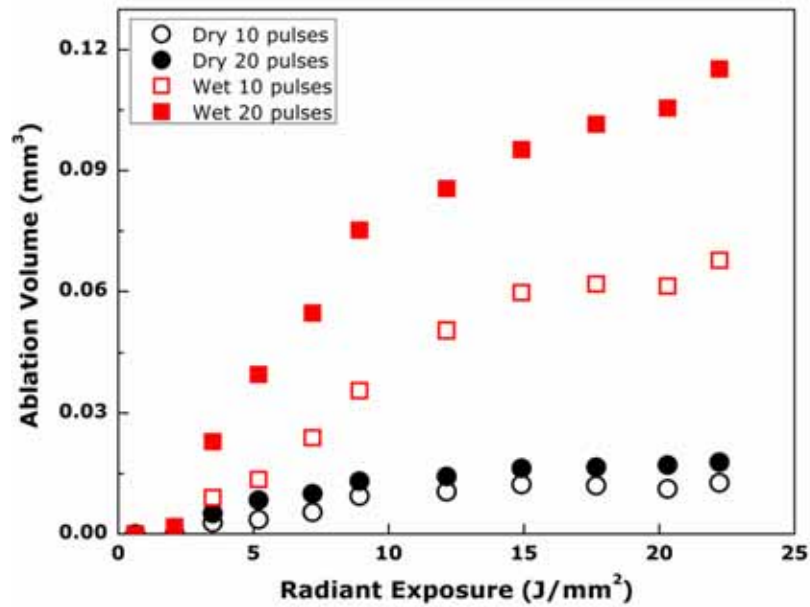


Figure 5.2. Vertical cross-sectional images of laser-induced craters with a Q-switched laser with twenty pulses for a dry case at the radiant exposure of (a) 14.9 J/mm² and (b) 22.2 J/mm² and a wet case at (c) 14.9 J/mm² and (d) 22.2 J/mm².



(a)



(b)

Figure 5.3. Comparison of ablation efficiency for dry and wet ablation as a function of radiant exposure with ten and twenty pulses: (a) crater depth and (b) ablation volume

The observation with an optical microscope for single pulse damage (ablation) thresholds for both cases is shown in Figure 5.4. From the microscope images, we could estimate the damage threshold radiant exposure at which the morphological deformation started on the surface. The damage thresholds for dry and wet ablation occurred at 3.5 J/mm^2 and 2.1 J/mm^2 respectively. Irradiated samples for both cases had randomly propagating cracks at the surface, indicating the mechanical effect during ablation. In particular, the wet image exhibited material removal along with the mechanically-induced crack, compared to the dry which showed little/no removal.

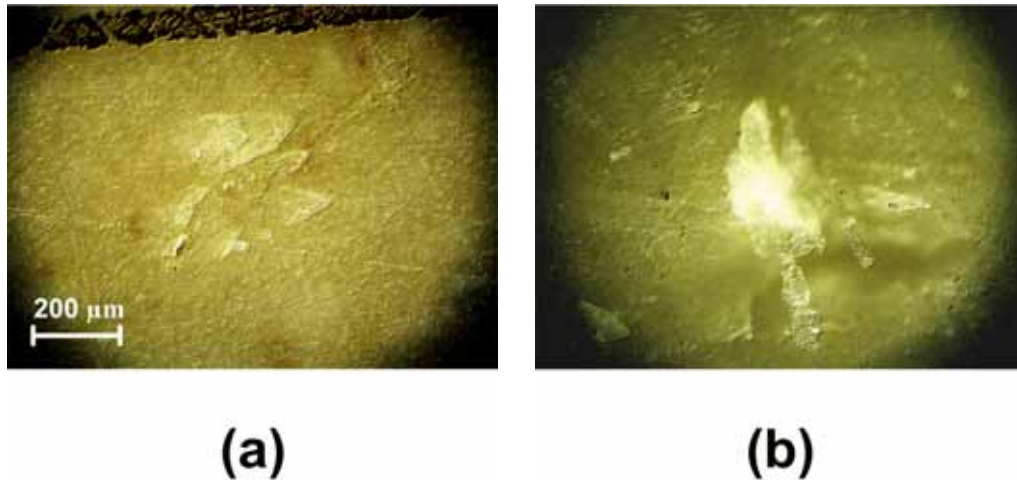


Figure 5.4. Top-view images of bovine bone for (a) dry damage threshold ($H = 3.5 \text{ J/mm}^2$) and (b) wet damage threshold ($H = 2.1 \text{ J/mm}^2$)

A typical trace of the acoustic transducer is shown in Figure 5.5 (single pulse, wet ablation at $H = 22.2 \text{ J/mm}^2$ where H is the radiant exposure). The laser pulse was triggered at $0 \text{ } \mu\text{s}$. The acoustic transient was generated approximately $2.1 \text{ } \mu\text{s}$ after the onset of the laser pulse. The speed of sound for bovine bone was found to range from 2000 m/s to 3441 m/s , which is dependent on bone density [3]. The time for shock wave propagation through the bone sample and 1 mm water layer for impedance match can be roughly evaluated by the following equation

$$t_{shock} = \frac{d_{bone}}{c_{bone}} + \frac{d_{water}}{c_{water}} \quad (5.1)$$

where t_{shock} is the total propagation time (s), d_{bone} and d_{water} are the sample and layer thickness (m) respectively, c_{bone} and c_{water} are the speed of sound (m/s) for each material. By using Table 5.1, the propagation time was calculated to range from $1.84 \text{ } \mu\text{s}$ to $2.68 \text{ } \mu\text{s}$, which corresponded to the measured onset of the acoustic wave at $2.1 \text{ } \mu\text{s}$.

The signatures of the pressure pulse for dry and wet ablation were investigated at various radiant exposures ranging from 0.6 J/mm^2 to 22.2 J/mm^2 and are compared in Figure 5.6. In the dry condition, the acoustic wave was composed of compressive pressure followed by a tensile wave. The acoustic shape of the wet condition mainly consisted of a compressive part within $1 \text{ } \mu\text{s}$

along with a peak amplitude up to six times greater and a compressive wave two to three times longer in duration. The peak acoustic amplitudes of the two conditions are compared in Figure 5.7 as a function of radiant exposure. The threshold radiant exposures for the acoustic excitation were identical for both dry and wet conditions at 2.1 J/mm^2 . However, the wet ablation produced a stronger pressure wave than dry ablation over the entire radiant exposures (Figure 5.7(a)). At low radiant exposures, the pressure amplitude of the wet condition was found to be approximately twice that of the dry (Figure 5.7(b)). It is noted that a transition in peak amplitude comparison between the two cases was found at the radiant exposure of 3.5 J/mm^2 .

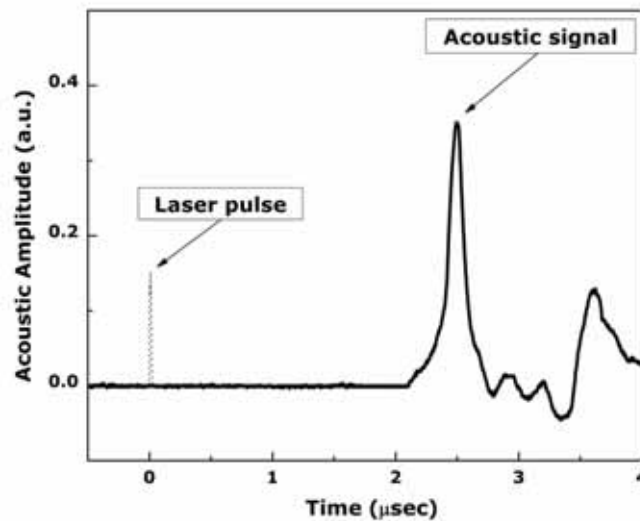
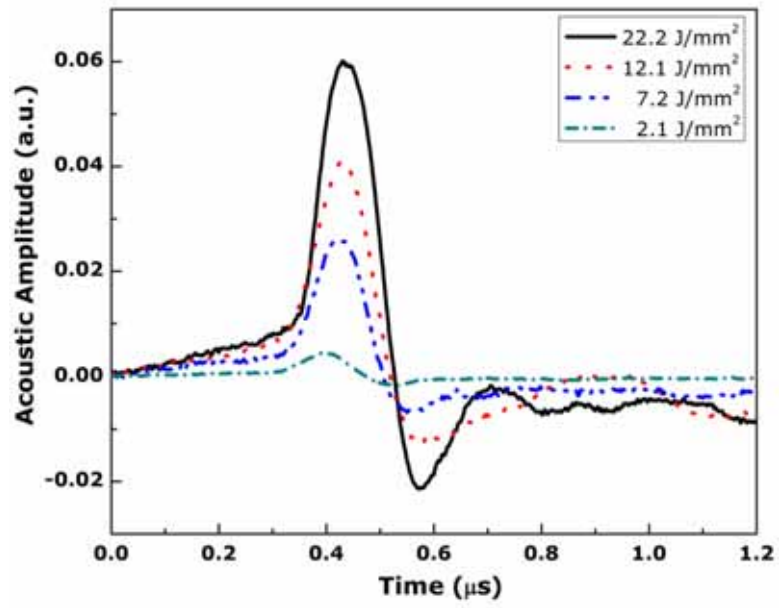
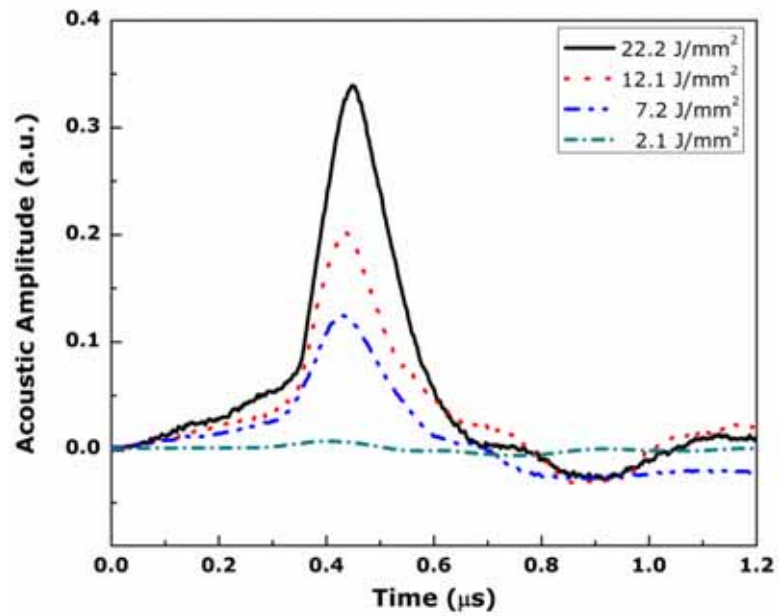


Figure 5.5. Acoustic signal measured by a piezoelectric transducer during single-pulse ablation in water produced with 22.2 J/mm^2 .

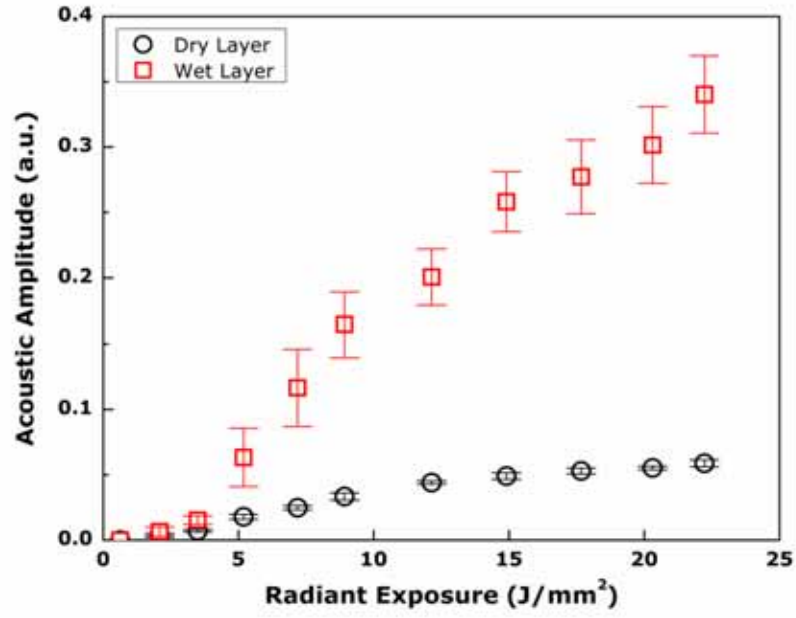


(a)

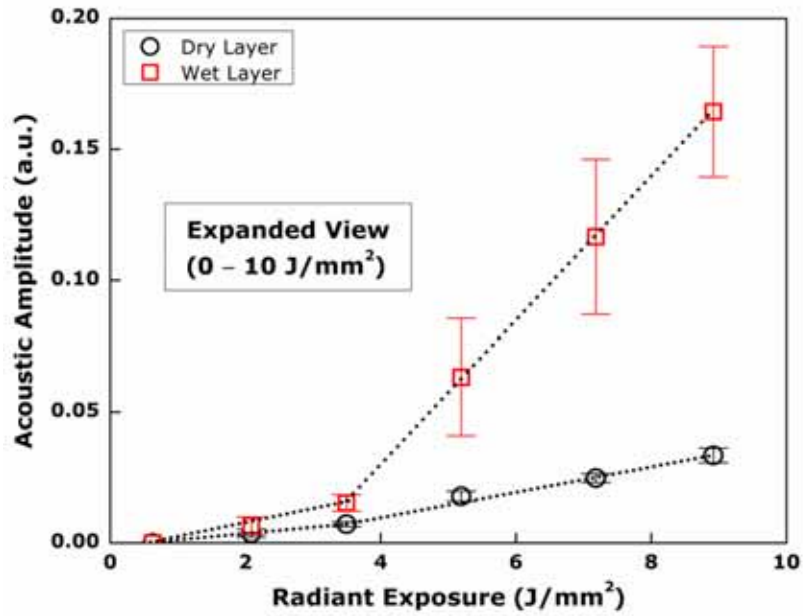


(b)

Figure 5.6. Temporal behaviors of transient pressure for (a) dry and (b) wet ablation. Note the difference in scale for dry and wet ablation.



(a)



(b)

Figure 5.7. Comparison of acoustic amplitudes for dry and wet cases as a function of radiant exposure ($n = 10$). (a) Entire radiant exposure and (b) lower radiant exposures between 0 and 10 J/mm² expanded from (a) (dotted lines guide a signal trends of each case)

The onset of optical breakdown was observed with a Q-switched Nd:YAG laser by varying the applied pulse energy on bone samples. The breakdown process was evidenced by plasma luminescence and an audible noise from acoustic wave generation. Temporal behavior of the optical pulse and laser-induced plasma for dry and wet cases are shown in Figure 5.8. It can be seen in both cases that the plasma developed within approximately 4 ns of the incident laser pulse (Figure 5.8(a)). The plasma signal exhibited a profile that initially resembled the envelope of the laser pulse, and it reached peak intensity in ~20 ns regardless of the radiant exposure. Both signals showed the plasma exponential decay after the peak, and later, the plasma luminescence was suddenly quenched, followed by a secondary exponential component (Figure 5.8(b)). It is also noted that after approximately 50 ns, dry and wet cases began to yield different temporal behaviors of plasma evolution. Beyond 50 ns, plasma generated during wet ablation displayed a faster decay time, converging to the reference state more rapidly, compared to that of dry ablation. Various decay constants for both dry and wet cases were estimated by means of exponential decay curve-fitting ($y = y_0 + A \cdot \exp[-(x - x_0)/\tau]$, y_0 : offset, A : amplitude, x_0 : center, τ : decay constant), shown in Figure 5.9(a). In general, the plasma decay time linearly increased with radiant exposure, and the first plasma decay was up to five times faster than the second decay. Compared to the dry case, the plasma intensity dropped more rapidly during the wet ablation. Figure 5.9(b) shows the

comparison of plasma duration between two cases as a function of radiant exposure ($n = 10$). The plasma thresholds were measured from the extrapolated curves, and two conditions yielded a comparable threshold of 3.5 J/mm^2 , which corresponded to the transition in peak acoustic amplitudes (Figure 5.7). Upon plasma formation, the lifetimes for dry and wet ablation increased with the radiant exposure. At a higher radiant exposure, the plasma of the dry case lasted for a few microseconds, up to twice as long as that of the wet (Figure 5.9(b)).

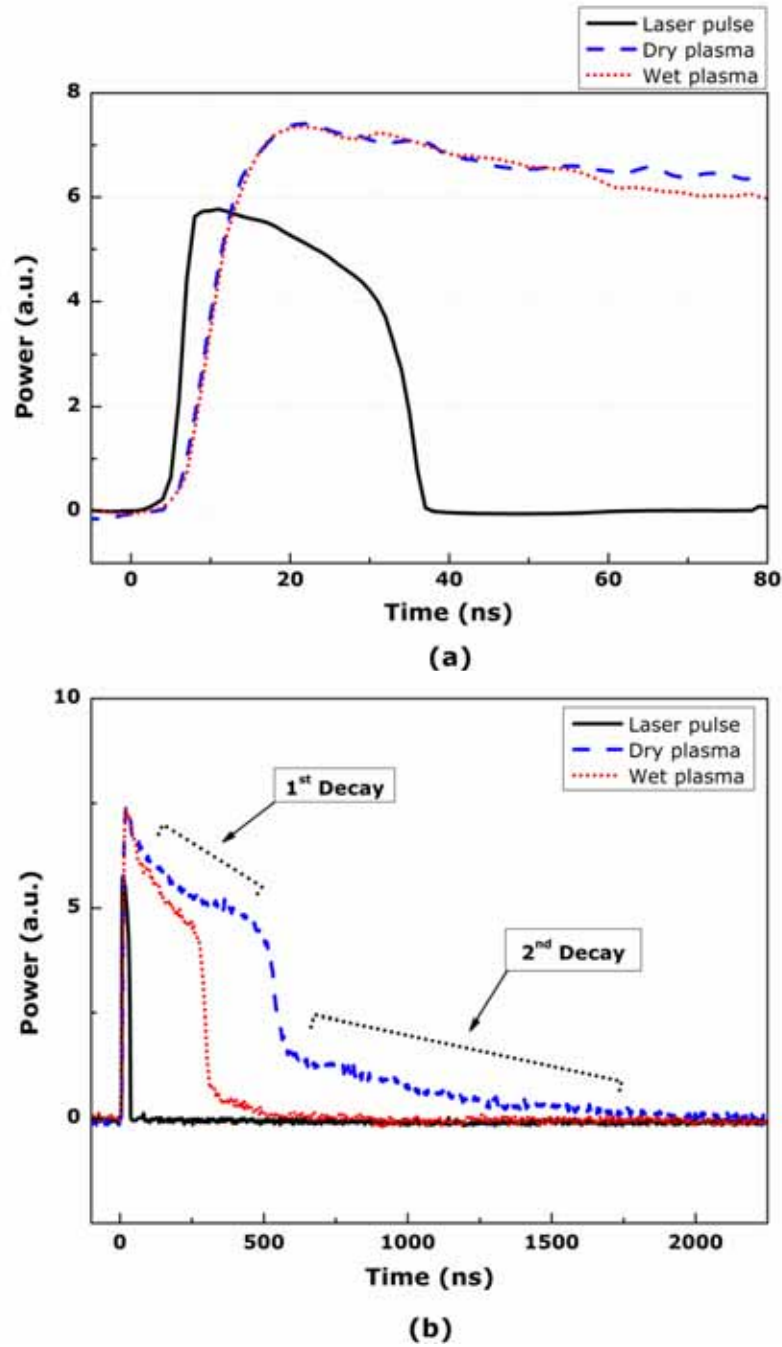


Figure 5.8. Temporal laser pulse and plasma transient detected by a fast photodetector for dry and wet cases at the radiant exposure $H = 17.7 \text{ J/mm}^2$ on the time scale ranging (a) from 0 to 80 ns and (b) from 0 to 2.25 μs (entire signal trace)

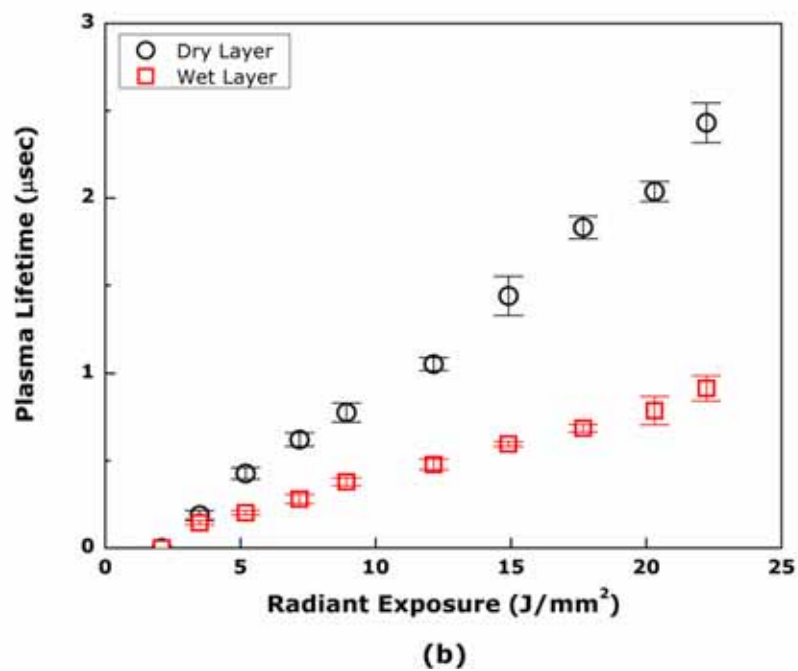
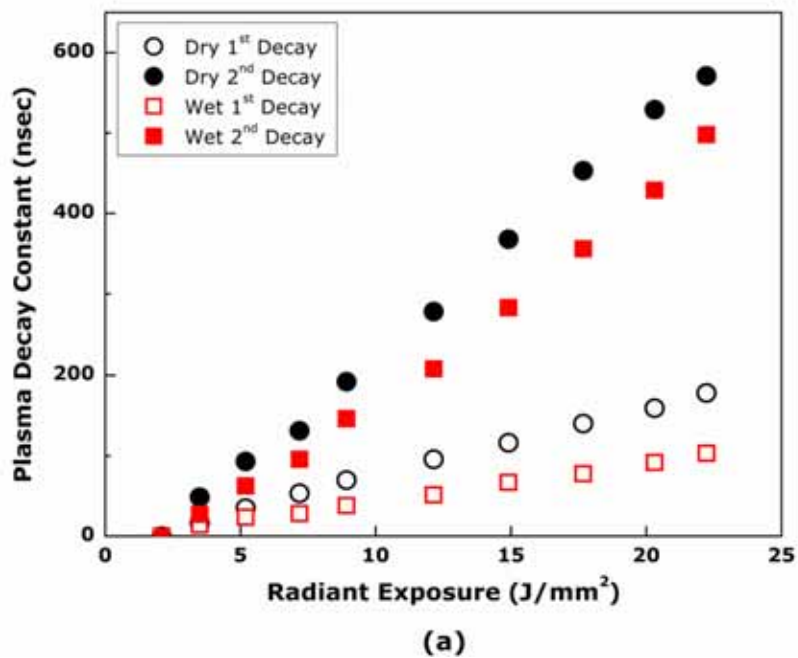


Figure 5.9. Comparison of laser-induced plasma between dry and wet cases. (a) plasma decay constant and (b) plasma lifetime ($n = 10$)

5.5 DISCUSSION

Nanosecond laser-induced ablation efficiency of the dry and wet conditions was compared for bovine bone samples as a function of radiant exposure with one, ten, and twenty pulses. Laser ablation assisted by a transparent liquid layer enhanced ablation efficiency compared to direct irradiation (Figure 5.3). Craters up to three times deeper with volume up to six times greater volume were observed under the wet condition. Asymmetric crater shapes with irregular contours, shown in Figure 5.2, evidenced photomechanical effects during both dry and wet ablation processes. Observation with an optical microscope showed that the single pulse damage thresholds for both dry and wet cases were 3.5 J/mm^2 and 2.1 J/mm^2 respectively. The threshold radiant exposures for measurable acoustic excitation were identical for both cases at 2.1 J/mm^2 . However, upon pressure wave generation, the acoustic excitation of the wet condition was higher than that of the dry case over the entire radiant exposure. The measurable plasma was first detected with a radiant exposure of 3.5 J/mm^2 for both cases. It should be noted that the damage threshold of the wet condition corresponded to that of acoustic excitation whereas the damage threshold of the dry condition was identical with that of plasma initiation.

Laser-induced ablation under the wet condition has been investigated in a few previous studies [12–16], [27–29]. It was reported that wet ablation lowered the damage threshold, defined as the lowest radiant exposure to cause surface

deformation, and promoted ablation performance via explosive liquid vaporization for the radiant exposure near the damage threshold [14]. At a higher radiant exposure regime, the plasma confinement in a water environment significantly enhanced the laser-induced acoustic and shock waves, consequently promoting material removal efficiency [12,13,15,16,27–29].

The lower damage threshold of the wet condition agrees well with previous studies [14,30]. Considering 1) higher acoustic excitation near the damage threshold and 2) a damage threshold lower than that of plasma formation, the reduced damage threshold of wet ablation can be attributed to the explosive vaporization. Prior to the plasma formation, nanosecond laser light absorption by the sample leads to rapid surface heating. Thus, thermal conduction from the sample surface to the liquid layer increases the water temperature possibly beyond its equilibrium saturation temperature causing the liquid water to become superheated. When the superheated liquid becomes unstable, it can approach the spinodal limit, which is a critical temperature of 647 K for water. Near the spinodal limit, the liquid experiences a great density fluctuation, consequently giving rise to homogeneous generation of vapor bubbles as well as validating the expectation of explosive vaporization [14,30]. In the vaporization of the superheated liquid, the pressure inside the bubble P_{ve} should exceed the vapor pressure at equilibrium, which can be estimated to be

$$P_{ve} = P_{sat}(T_l) \cdot \exp \left[\frac{v_l \cdot (P_l - P_{sat}(T_l))}{RT_l} \right] \quad (5.2)$$

where T_l , P_{sat} , P_l , v_l , and R are the temperature of the superheated liquid, the saturation pressure at the liquid temperature, the pressure of the superheated liquid, specific volume, and gas constant respectively [31]. As the temperature approaches $0.83T_c$ (T_c : thermodynamic critical temperature of water), the pressure calculated in equation 2 increases close to the saturation pressure at the liquid temperature with intense density fluctuations [32]. Once a vapor bubble grows to a size greater than a critical radius, it grows spontaneously, accompanying spherical shock wave generation [33]. Therefore, as multiple homo- and/or hetero-geneous micro-bubble nuclei rapidly grow and expand, a strong compressive pressure wave can be emitted, which possibly accounts for a contribution to higher acoustic amplitude at the threshold as well as a lower damage (ablation) threshold for wet ablation prior to plasma formation (Figures 5.4 and 5.7).

The optical breakdown for both dry and wet cases commenced about 4 ns after the laser pulse was applied over the entire radiant exposure, and both plasmas simultaneously reached the peak intensity in ~20 ns (Figure 5.8(a)). Once plasma is initiated due to direct light absorption of a sample, the plasma becomes the main absorber of the remaining pulse energy, resulting in plasma

expansion [10]. Previous studies reported that the plasma luminescence is almost a replica of the input pulse [34,35], so the sudden quenching of both plasma signals can be explained by the reproduction of temporal behavior of the pulse, followed by a secondary exponential decay of the order of up to a microsecond (Figure 5.8(b)). When the plasma was generated, the plasma under wet condition yielded a fast decay after 50 ns in spite of the identical peak time with dry condition. This implies that more energy transfer to the surrounding media was involved in ablation under water compared to the dry case. This dissipation can be attributed to thermal conduction throughout plasma expansion from high temperature plasma to the surrounding media, which might have started about 15 ns after the applied pulse ended. Due to the fact that thermal conductivity of water ($k_w = 0.611 \text{ W/m}\cdot\text{K}$ at 300 K) is higher than that of air ($k_a = 0.0267 \text{ W/m}\cdot\text{K}$ at 300 K), more thermal energy during plasma expansion was possibly transferred to a water layer, reducing plasma life time in association with a fast decay transient (Figure 5.9(b)). Since optical breakdown in water requires an irradiance of more than 10^{11} W/cm^2 and the maximum irradiance tested in the current study was $7.41 \times 10^{10} \text{ W/cm}^2$, we assume that plasma formation occurred at the surface of the bone rather than on the water. In addition to the faster decay of plasma in the presence of a liquid layer, it should be noted that an abrupt increase of acoustic excitation was observed at 3.5 J/mm^2 that corresponded to the plasma threshold radiant exposure. The faster decay of plasma and the abrupt increase of

acoustic excitation under the wet condition can be explained by the plasma confinement in the liquid layer. It was reported that the laser-induced plasma could be confined in the liquid layer presenting on the target surface, consequently inducing higher pressure amplitude and longer shock wave duration than the dry condition in spite of the partial absorption of the incoming laser pulse by plasma screening [12,13,15,16,27,28].

An analytical model was previously developed to predict laser-induced pressures in the confined geometry [27]. A simple one-dimensional model described three different phases of the confined plasma process (laser heating, adiabatic cooling, and plasma expansion) and evaluated the pressure development inside the plasma. The maximum pressure (P_{max}) generated by the laser-induced plasma in water environment was estimated by the following equation,

$$P_{water} \text{ (Pa)} = \sqrt{\frac{2\alpha}{2\alpha + 3}} \cdot \sqrt{E_0} \cdot \sqrt{Z_t} \quad (5.3)$$

where α is a constant fraction of the internal energy representing the thermal energy and E_0 is the incident laser irradiance (W/cm^2). Z_t is the characteristic impedance ($\text{kg}/\text{m}^2\text{s}$) between the bone sample and the water layer, given by

$$\frac{1}{Z_t} = \frac{1}{Z_{bone}} + \frac{1}{Z_{water}} \quad (5.4)$$

where Z_{bone} and Z_{water} are the impedances of the bone sample and the water respectively. By assuming a bone density of 1417 kg/m^3 and a speed of sound of 3000 m/s (based on Table 5.1), $Z_{bone} = 4.251 \times 10^6 \text{ kg/m}^2\text{s}$ and $Z_{water} = 1.48 \times 10^6 \text{ kg/m}^2\text{s}$. For the sake of comparison, the maximum pressure during ablation in air was given by the empirical relation,

$$P_{air} \text{ (Pa)} = b \cdot E_0^{(n+1)} \cdot \lambda^n \cdot \tau_p^{0.5 \cdot n} \quad (5.5)$$

where b and n are material-dependent coefficients, λ laser wavelength (μm), and τ_p pulse duration (ns) [27]. Since material removal was photomechanically induced, fracture toughness can be an important parameter to evaluate the susceptibility of bone to initial failure [36]. Material with higher fracture toughness is less likely to fracture by crack propagation; one can assume that the maximum pressure of dry ablation at the plasma threshold is equivalent to the tensile strength applied to crack growth. If $n = -0.3$ based on previous studies and b is determined by the tensile stress estimated from the fracture toughness of bone in Table 5.1, one can approximately obtain that the ratio P_{water}/P_{air} varies from 1.7 to 1.17 over the irradiance range $11.7 - 74.1 \text{ GW/cm}^2$, shown in Figure 5.10. Thus, the liquid confinement appears to achieve higher compressive pressure during plasma formation/expansion over the entire irradiance, which can partially explain a discrepancy in peak acoustic amplitudes between dry and wet ablation in Figure 5.7.

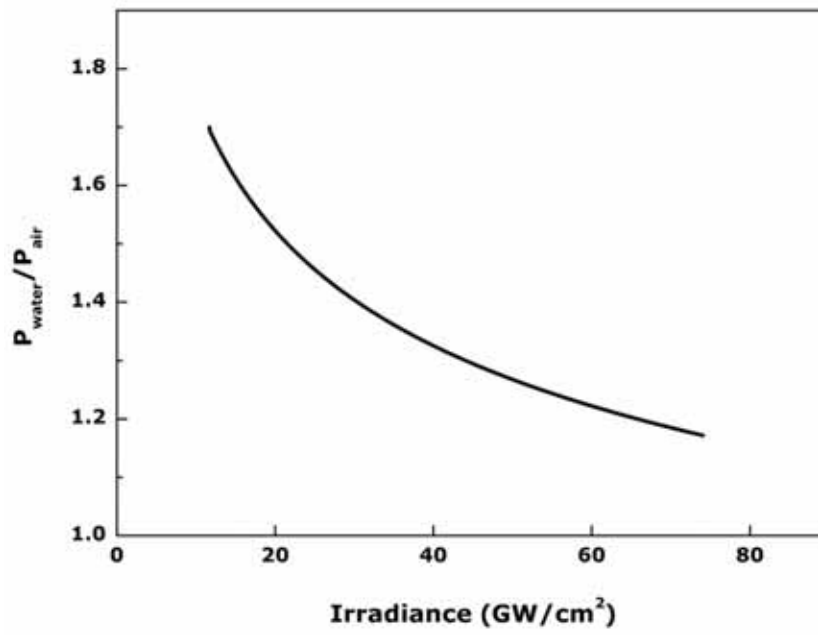


Figure 5.10. Ratio of $P_{\text{water}}/P_{\text{air}}$ based on 1-D analysis of pressure generation induced by plasma process.

Given the fact that the plasma formation for nanosecond pulses is always accompanied with shock wave generation [10], it should be noted that the acoustic impedance of water is $Z_{water} = 1.48 \times 10^6 \text{ kg/m}^2\text{s}$, which is much greater than that of air ($Z_{air} = 410 \text{ kg/m}^2\text{s}$). If the water-sample interface yields a volumetric space during the plasma expansion, the shock wave is assumed to propagate from the space, which is treated as a perfect gas, to the water layer [27]. Therefore, supposing that air is a perfect gas, the pressure reflection coefficient, R for wet ablation is given by

$$R = \frac{Z_{water} - Z_{air}}{Z_{water} + Z_{air}} \quad (5.6)$$

Since R is approximately equal to 1, the induced shock wave propagating out of the sample surface could be mostly reflected at the interface between air and water without phase change (pressure doubling [20]), so more residual compressive waves were possibly applied to the sample surface (Figure 5.6).

Since the plasma formation is associated with a significant temperature increase, up to 15000 K [37], it is expected that micro-bubble generation emits strong pressure via explosive vaporization in a liquid layer causing additional photomechanical impact. Also, once the bubbles are generated and expanded, they can coalesce into macro-size bubbles. While these macro-bubbles collapse in the vicinity of a surface during/after the ablation process, a high-speed, wall-

directed reentrant jet can be initiated in the bubbles, and consequently, the liquid-jet with outward radial flow can interact with the sample as additional shock wave impact [33]. The acoustic augmentation of the jet P_{imp} (Pa) can be estimated using the following equation

$$P_{imp} = \frac{Z_{bone} \cdot Z_{water}}{Z_{bone} + Z_{water}} \cdot V_{jet} \quad (5.7)$$

where Z_{bone} and Z_{water} are the acoustic impedances of water and bone respectively ($Z_{bone} = 4.251 \times 10^6$ kg/m²s and $Z_{water} = 1.48 \times 10^6$ kg/m²s). If the liquid-jet velocity V_{jet} near a boundary is assumed to be 80 m/s based on a previous study [33], the acoustic impact can correspond to a pressure of 90 MPa, which exceeds the fracture toughness of the bone sample. Therefore, the acoustic enhancement by cavitation bubble collapses can also account for the more pronounced amplitude of the acoustic transient over the entire radiant exposure. It was observed that the liquid vapors were explosively ejected at higher radiant exposure. Hence, in the plasma regime, a combination of confined-plasma, impedance difference at the interface, more explosive vaporization, and jet formation can be responsible for the augmentation of compressive pressure along with longer shock wave durations, leading to enhanced photomechanical effects (Figure 5.6). Future measurement of acoustic signals beyond 10 μ s time frame

will clarify how cavitation collapse after plasma expansion contributes to the wet ablation process.

In the case of dry ablation, the acoustic threshold was lower than the damage threshold at 3.5 J/mm^2 . Thus, the initial pressure emission resulted from thermoelastic expansion at a radiant exposure of 2.1 J/mm^2 , which was below sample damage. Upon plasma initiation at 3.5 J/mm^2 (Figure 5.9), the acoustic emission was assumed to be combined with the thermoelastic wave as well as plasma-induced shock wave generation, subsequently leading to photomechanical damage on the sample. In addition, since the sample was kept in a saline solution at room temperature prior to experimentation, a rapid temperature increase by light absorption possibly induced internal explosion of the interstitial water inside the bone as a mechanical impact. Therefore, it is supposed that material removal for the dry case was mainly attributed to plasma formation, and the acoustic transient was associated with a combination of thermoelastic pressure, plasma-induced shock wave, and recoil momentum. In order to confirm the dynamics implied with the acoustic transient and post-ablation process, high-speed imaging of both dry and wet cases will be performed in the future study.

In Figure 5.3, ablation depth and efficiency for both the dry and wet cases started saturating at the radiant exposure of 8.9 J/mm^2 . Saturation was also found in the acoustic amplitude graph in Figure 5.7. One of possible explanations for this phenomenon is plasma shielding [38,39]. Once plasma formation starts at the

laser focus, the plasma absorbs and scatters further incident laser light, expanding toward the laser beam during the pulse. Since the plasma partially or fully screens the incident pulse, less energy is delivered to the sample for ablation. Increased shielding effect during plasma formation at higher irradiance was thereby responsible for the saturation of the pressure and ablation efficiency observed for our experiments. Additionally, previous studies have experimentally and analytically shown that both maximum pressure and transmission of plasma approached saturation at the same irradiance threshold, which validated the hypothesis that the plasma shielding was attributed to the pressure saturation, consequently limiting the ablation efficiency [12,13,27]. In our experiments, although wet ablation obtained up to 6 times higher peak pressure and greater ablation efficiency respectively than the dry case, it should be noted that above an irradiance of $2.97 \times 10^{10} \text{ W/cm}^2$, plasma shielding played a significant role in limiting ablation performance. Therefore, an efficient bone ablation rate with a liquid confinement can be achieved below the irradiance of increased plasma shielding effect.

5.6 CONCLUSION

Biological hard tissue ablation in a liquid confinement has been investigated with a Q-switched Nd:YAG laser. It was found that the application of a water layer increased the ablation efficiency up to six times via explosive

liquid vaporization and plasma confinement. The correlation between acoustic and damage thresholds under the wet condition suggests that the explosive vaporization of the superheated liquid was responsible for the lower damage (ablation) threshold along with the higher acoustic amplitude in the near-threshold regime. In the plasma regime, the reduced lifetime of plasma indicates that the optical breakdown was confined to the liquid layer, consequently intensifying acoustic coupling efficiency at the interface. Two other mechanisms have been proposed for the enhanced photomechanical excitation. The augmented photomechanical effect under the wet condition is considered to be the main cause of the improved ablation performance. Above an irradiance of $2.97 \times 10^{10} \text{ W/cm}^2$, acoustic pressure and ablation efficiency were maintained at the saturation level, which was attributed to increased plasma shielding effects. It can be concluded that the liquid layer on the target surface facilitates the augmentation of bone ablation efficiency although it accompanies a limitation of plasma shielding.

5.7 REFERENCES

1. Moore JH. Laser energy in orthopedic surgery. Amsterdam: Excerpta Medica, 1973.
2. Clayman L, Fuller T, Becnman H. Healing of continuous-wave and rapid superpulsed carbon dioxide laser-induced bone defects. J Oral Maxillofac Surg 1978;36:932-937.
3. Eyrych GKH. Laser-osteotomy induced changes in bone. Med Laser Appl 2005;20:25-36.
4. Peavy GM, Reinisch L, Payne JT, Venugopalan V. Comparison of Cortical Bone Ablations by Using Infrared Laser Wavelengths 2.9 to 9.2

5. Forrer M, Frenz M, Romano V, Altermatt HJ, Weber HP, Silenok A, Istomyn M, Konov VI. Bone-ablation mechanism using CO₂ lasers of different pulse duration and wavelength. *Appl Phys B* 1993;56:104-112.
6. Izatt JA, Sankey ND, Partovi F, Fitzmaurice M, Rava RP, Itzkan I, Feld MS. Ablation of calcified biological tissue using pulsed laser hydrogen fluoride laser radiation. *IEEE J Quantum Electron* 1990;26:2261-2270.
7. Kitai MS, Sobol EN, Sviridov AP, Omel'chenko AI. Manifestations of photochemical reactions in bone tissue on exposure to the ultraviolet radiation of an Eximer laser. *Biophysics* 1996;41:1151-1157.
8. Walsh JT, Flotte TJ, Deutsch TF. Er:YAG laser ablation of tissue: effect of pulse duration and tissue type on thermal damage. *Lasers Surg Med* 1989;9:314-326.
9. Wong B, Sung V, Berns MW, Svaasand LO, Neev J. Holmium-YAG laser ablation characteristics in calvarial lamellar and cortical bone: the role of water and tissue micro-architecture. *Lasers Med Sci* 1995;10:181-188.
10. Niemz MH. *Laser-Tissue Interactions*. Berlin, Germany: Springer-Verlag, 1996.
11. Jacques SL. Role of tissue optics and pulse duration on tissue effects during high-power laser irradiation. *Appl Opt* 1992;32:2447-2454.
12. Berthe L, Fabbro R, Peyre P, Tollier L, Bartnicki E. Shock waves from a water-confined laser-generated plasma. *J Appl Phys* 1997;82:2826-2832.
13. Berthe L, Fabbro R, Peyre P, Bartnicki E. Wavelength dependent of laser shock-wave generation in the water-confinement regime. *J Appl Phys* 1999;85:7552-7555.
14. Kim D, Oh B, Lee H. Effect of liquid film on near-threshold laser ablation of a solid surface. *Appl Surf Sci* 2004;222:138-147.
15. Dupont A, Caminat P, Bournot P. Enhancement of material ablation using 248, 308, 532, 1064 nm laser pulse with a water film on the treated surface. *J Appl Phys* 1995;78:2022-2028.
16. Zhu S, Lu YF, Hong MH, Chen XY. Laser ablation of solid substrates in water and ambient air. *J Appl Phys* 2001;89:2400-2403.
17. Hale GM, Querry MR. Optical constants of water in the 200 nm to 200 μ m wavelength region. *Appl Opt* 1973;12:555-563.
18. Vogel A, Noack J, Nahen K, Theisen D, Busch S, Parlitz U, Hammer DX, Noojin GD, Rockwell BA, Birngruber R. Energy balance of optical breakdown in water at nanosecond to femtosecond time scales. *Appl Phys B* 1999;68:271-280.
19. Duck FA. *Physical properties of tissue: a comprehensive reference book*. London: Academic Press, 1991.
20. Blackstock DT. *Fundamentals of physical acoustics*. New York: John

- Wiley & Son, Inc., 2000.
21. Mills AF. Basic heat and mass transfer. London: Prentice-Hall, Inc., 1999.
 22. Evans JA, Tavakoli MB. Ultrasonic attenuation and velocity in bone. *Phys Med Biol* 1990;35:1387-1396.
 23. Athanasiou KA, Zhu CF, Lanctot DR, Agrawal CM, Wang X. Fundamentals of Biomechanics in Tissue Engineering of Bone. *Tissue Eng* 2000;6:361-381.
 24. Siegman AE, Sasnett MW, Johnston Jr. TF. Choice of Clip Levels for Beam Width Measurements Using Knife-Edge Techniques. *IEEE J Quantum Electron* 1991;27:1098-1104.
 25. Huang D, Swanson EA, Lin CP, Schuman JS, Stinson WG, Chang W, Hee MR, Flotte TJ, Gregory K, Puliafito CA, Fujimoto JG. Optical coherence tomography. *Science* 1991;254:1178-1181.
 26. Izatt JA, Kulkarni MD, Yazdanfar S, Barton JK, Welch AJ. In vivo bidirectional color doppler flow imaging of picoliter blood volumes using optical coherence tomography. *Opt Lett* 1997;22:1439-1441.
 27. Fabbro R, Fournier J, Ballard P, Devaux D, Virmont J. Physical study of laser-produced plasma in confined geometry. *J Appl Phys* 1990;68:775-784.
 28. Devaux D, Fabbro R, Tollier L, Bartnicki E. Generation of shock waves by laser-induced plasma in confined geometry. *J Appl Phys* 1993;74:2268-2273, 1993.
 29. Zhu S, Lu YF, Hong MH. Laser ablation of solid substrates in a water-confined environment. *Appl Phys Lett* 2001;79:1396-1398.
 30. Kim D, Lee H. Enhanced ablation and photoacoustic excitation in near-threshold laser ablation of liquid-coated surfaces. *J Appl Phys* 2001;89:5703-5706.
 31. Carey VP. Liquid-vapor Phase-Change Phenomena. Washington: Hemisphere, 1992.
 32. Kelly R, Miotello A. Comments on explosive mechanisms of laser sputtering. *Appl Surf Sci* 1996;96-98:205-215.
 33. Isselin JC, Alloncle AP, Autric M. On laser induced single bubble near a solid boundary: Contribution to the understanding of erosion phenomena. *J Appl Phys* 1998;84:5766-5771.
 34. Docchio F. Lifetimes of Plasmas Induced in Liquids and Ocular Media by Single Nd:YAG Laser Pulses of Different Duration. *Europhys Lett* 1988;6:407-412.
 35. Docchio F, Regondi P, Capon MRC, Mellerio J. Study of the temporal and spatial dynamics of plasmas induced in liquids by nanosecond Nd:YAG laser pulses. 2: Plasma luminescence and shielding. *Appl Opt* 1988;27:3669-3674.

36. Zhong P, Chuong C, Preminger G. Characterization of fracture toughness of renal calculi using a microindentation technique. *J Mater Sci Lett* 1993;12:1460-1462.
37. Barnes PA, Rieckhoff KE. Laser induced underwater sparks. *Appl Phys Lett* 1968;13:282-284.
38. Docchio F, Regondi P, Capon MRC, Mellerio J. Study of the temporal and spatial dynamics of plasmas induced in liquids by nanosecond Nd:YAG laser pulses. 1: Analysis of the plasma starting times. *Appl Opt* 1988;27:3661-3668.
39. Vogel A, Nahen K, Theisen D, Noack J. Plasma Formation in Water by Picosecond and Nanosecond Nd:YAG Laser Pulses - Part I: Optical Breakdown at Threshold and Superthreshold Irradiance. *IEEE J Sel Top Quantum Electron* 1996;2:847-860.

Chapter 6: Investigations on Laser Hard Tissue Ablation under Various Liquid Environments

6.1 ABSTRACT

The purpose of this study was to investigate the effect of liquid environments upon laser bone ablation. A long-pulsed Er,Cr:YSGG laser was used to ablate bovine bone tibia at various radiant exposures under dry, wet (using water or perfluorocarbon), and spray environmental conditions. Energy loss by application of liquid during laser irradiation was evaluated, and ablation performance for all conditions was quantitatively measured by Optical Coherence Tomography (OCT). Microscope images were also used to estimate thermal side effects in tissue after multiple-pulse ablation. Wet (water) and spray conditions equally attenuated the 2.79 μm wavelength laser beam. Higher transmission efficiency was obtained using a layer of perfluorocarbon. Dry ablation exhibited severe carbonization due to excessive heat accumulation. Wet (water) condition resulted in similar ablation volume to the dry case without carbonization. The perfluorocarbon layer produced the largest ablation volume but some carbonization due to the poor thermal conductivity. Spray induced clean cutting

with slightly reduced efficiency. Liquid-assisted ablation provided significant beneficial effects such as augmented material removal and cooling/cleaning effects during laser osteotomy.

6.2 INTRODUCTION

Infrared laser osteotomy has several potential advantages over mechanical drills and oscillating saws used in orthopedics such as no mechanical vibration, non-contact intervention, intricate cut geometry, and hemostatic and aseptic effects [1,2]. Quantitative studies have been performed to characterize bone ablation with various wavelengths and pulse durations [3-8]. Since the main absorbers of bone are water (12 – 15 % weight) and hydroxyapatite (60 % weight) [8,9], infrared lasers, of which wavelengths correspond to absorption peaks of the bone components, for example, Er:YAG (wavelength $\lambda = 2.94 \mu\text{m}$) and CO₂ ($\lambda = 9.6 \mu\text{m}$), have been used. The proposed mechanism for long-pulsed lasers was thermo-mechanical: light absorption by water and/or mineral bone components could lead to thermal expansion, consequently inducing decomposition of bone structure [8].

In order to prevent dehydration of tissue and thermal damage to the surrounding tissue due to rapid temperature increase, application of a water film or water droplets in laser ablation has been investigated in dentistry [10-18]. Previous studies demonstrated that the addition of water in dental treatment

improves surface morphology and ablation efficiency as well as lowers pulpal temperature. In the case of bone ablation, thermal side effects should be avoided since temperature elevation between 44 and 47 °C may lead to bony tissue necrosis [2]. In addition, material processing studies showed that lower damage threshold and enhanced ablation performance can be achieved with the application of a transparent water layer [19,20]. The augmentation of ablation efficiency is due to the explosive water vaporization in the strongly superheated liquid layer [20].

In this report, we describe the effects of various liquid environments on biological bone tissue ablation, compared to direct ablation (termed the “dry condition”). Two different liquid environments were tested: application of a liquid layer using either water or perfluorocarbon (termed the “wet ablation”) and pressurized water spray (“spray ablation”). Since a perfluorocarbon liquid (PFCL) $[\text{CF}_3(\text{CF}_2)_n\text{CF}_3]$ is biocompatible with high specific gravity and low viscosity, the liquid has been used as oxygen carriers in vitreoretinal applications [21,22]. In contrast to the high water absorption peak in the mid-infrared regime, perfluorocarbon liquid (PFCL) is a relatively transparent liquid (absorption coefficient $\mu_a = 0.05 \text{ mm}^{-1}$ at $\lambda = 2.94 \text{ }\mu\text{m}$ [21]). A conventional Er,Cr:YSGG laser system ($\lambda = 2.79 \text{ }\mu\text{m}$) was employed with various energy settings. Bone samples in air and liquid environments were evaluated to characterize the role of liquid environments and thermal damage during laser osteotomy. Ablation

performance was also compared as function of radiant exposure with multiple pulses.

6.3 MATERIALS AND METHODS

6.3.1 SPECIMEN

Fresh bovine tibia samples were irradiated for *in vitro* laser-tissue ablation experiments. The bone specimens were rinsed in tap water to remove hemocytes after the connective tissue and periosteum were peeled away. In order to obtain a flat surface, the target surface was polished using sandpaper with a grain size of 30 μm . Sanded samples were stored in a saline solution at 4 °C prior to experimentation, possibly minimizing changes in hydration. Four different experimental conditions were evaluated: dry, wet (water or perfluorocarbon), and spray conditions. In case of dry ablation, the samples were desiccated at room temperature for 48 hours and ablated without applying a liquid layer or using water spray. For wet ablation, a plastic (Depron) ring with 1 mm thickness was attached on top of a sample surface to maintain a consistent thickness of liquid layer. Two different liquids were tested to perform liquid-assisted tissue ablation: distilled water and perfluorocarbon (Perfluorodecalin, Oakwood Products, Inc.). The liquids were deposited inside the ring prior to laser-pulse irradiation for each experiment. Lastly, under spray condition, a built-in pressurized water spray irrigation system was utilized. The system produced a flow rate of 8 ml/min

using distilled water, and in order to achieve a stable flow rate, the water spray was initiated and terminated about 3 seconds pre and post laser pulse, respectively. Optical and thermal properties of the target materials are listed in Table 6.1.

Table 6.1. Optical and thermal properties of bone, water, and perfluorocarbon [9,23-25]

Material Property	Bone	Water	Perfluorocarbon
Absorption coefficient (cm^{-1}) at 2.79 μm	2120	5300	< 0.5
Thermal Conductivity ($\text{W/m}\cdot\text{K}$)	0.373 – 0.496	0.611	0.067
Boiling point (K)	N/A	373	415

6.3.2 EXPERIMENTAL SETUP

To ablate bovine bone tissues, a conventional Er,Cr:YSGG laser (Waterlase MD, BioLase Technology, Irvine, CA) was employed. The system emitted laser pulses at 2.79 μm with a pulse duration (τ_p) of up to 150 μsec . The incident pulse energy ranged from 5 mJ to 200 mJ, and a sequence of five pulses at a repetition rate of 10 Hz was applied to the target. A schematic illustration of the experimental setup is shown in Figure 6.1. The laser light was delivered through a fiber optic system to handpiece containing a sapphire tip with a diameter of 600 μm and a divergence of 8°. The handpiece also included a built-in water spray irrigation system, so it was used to produce a flow rate of 8 ml/min in case of spray condition. With an energy meter (EPM 2000, Molelectron, Portland, OR) along with a pyroelectric joulemeter (J50, Molelectron), the output pulse energy was measured before and after every bone ablation test. The fiber tip was replaced if the measured energy was reduced by more than 15 % of the initial output energy to avoid experimental artifacts due to fiber damage. The sample was placed on a three-axis translation stage, and a new irradiation spot was adjusted after irradiation at each energy level. To perform bone ablation, the laser pulse was delivered normal to the sample surface, and the gap between the fiber tip and the tissue was maintained approximately 500 μm for all the experiments, which provided a 500 μm thick liquid layer on top of the sample surface. Osteotomy cuts of bovine bone applying multiple sequences of five laser

pulses at 10 Hz were performed with various conditions. In case of formation of channel in the bone, the sample was moved laterally with a resolution of 200 μm every five pulses.

Attenuation of the laser beam by liquid layers and water spray was determined. A 5 mm thick CaF_2 window was placed 500 μm in front of the fiber to block the water droplets and spray, and a Molectron energy probe was used to measure transmittance of a single laser pulse through the CaF_2 window. In case of wet ablation, a 1 mm thick plastic ring was attached on the window to maintain a consistent liquid layer, and two liquids such as water and perfluorocarbon were tested. Energy measurements with and without the application of liquid layers and water spray as a function of pulse energy were compared to quantify the efficiency of light transmission.

Bone ablation was characterized in terms of ablation performance for dry, wet (water or perfluorocarbon), and spray conditions respectively. Ablation craters were produced with five pulses as a function of radiant exposures. Crater dimensions were measured with an optical coherence tomography (OCT) system ($\lambda_0 = 1290 \text{ nm}$, $\Delta\lambda = 42 \text{ nm}$, and $P = 2.2 \text{ mW}$) with lateral and axial resolutions of $\sim 20 \mu\text{m}$ [26,27]. A series of vertical cross-sectional images parallel to the laser beam axis were scanned and acquired over the entire crater with a step-size between images of 37 μm . Crater volume was quantitatively estimated with

image processing software. Also, the craters were observed with an optical microscope to compare quality of laser ablation and morphological deformation.

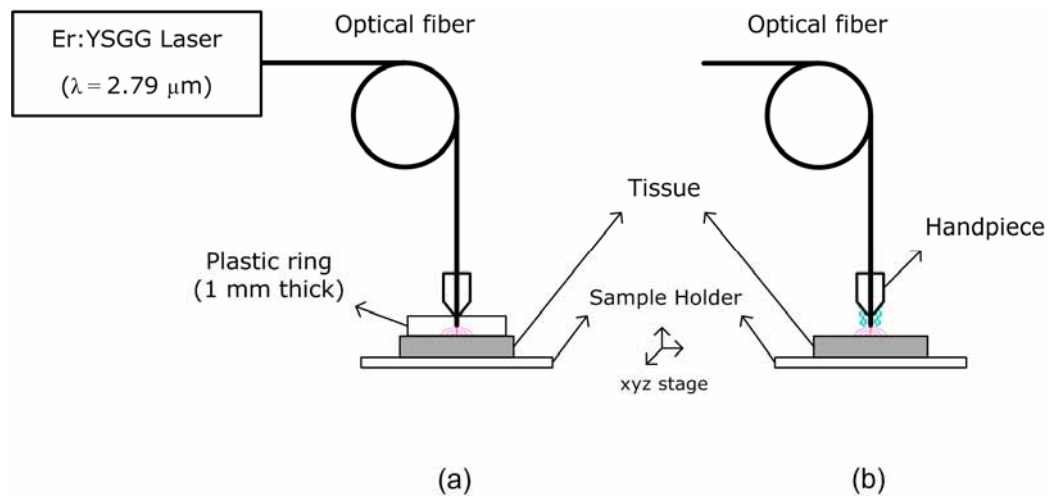


Figure 6.1. Experimental setup for bone ablation study under different environments: (a) wet ablation using water and perfluorocarbon and (b) spray ablation using water. Note the 500 μm distance between fiber tip and the sample surface.

6.4 RESULTS

6.4.1 ENERGY LOSS MEASUREMENT

The transmission of the laser beam through a 1 mm water layer (1 mm perfluorocarbon layer, water spray of 8 ml/min) as a function of incident energy is shown in Figure 6.2. Transmission efficiency through the water layer and spray were almost identical with a linear relationship ($R^2 = 0.99$) between the incident and transmitted energy. The reduction in transmission was a result of light absorption by the water. However, in case of perfluorocarbon layer, the transmission was approximately 20 mJ higher due to lower absorption at the 2.79 μm wavelength (Table 6.1).

6.4.2 ABLATION EFFICIENCY

Ablation performance for various conditions was compared to understand the effects of liquid environments on bone ablation. Dimensions of ablation craters for dry, wet, and spray ablation are compared in Figure 6.3 as a function of radiant exposure. A sequence of five pulses at 10 Hz was applied to the bone samples with radiant exposures per pulse ranging from 8.5 J/cm² to 59 J/cm². Regardless of the experimental condition, ablation volume increased with radiant exposure. Ablation volumes induced by both dry and wet (water) ablation were comparable over all exposures tested; wet ablation with perfluorocarbon produced a 15 % higher ablation volume. Spray ablation was slightly less effective along

with approximately a 17 % reduction in ablation volume, compared to dry and wet (water) conditions.

6.4.3 THERMAL SIDE EFFECTS

Cross-sectional OCT and top-view microscope images of ablation craters and osteotomy cuts of bone samples for four different conditions: dry, wet (water and perfluorocarbon), and spray ablation are shown in Figure 6.4. All the cases were irradiated with five pulses (10 Hz) at various radiant exposures. In the dry condition, OCT images had irregular surface deformation and there was severe charring. Black carbonization surrounded by a white recrystallization rim was observed in the microscope image of the osteotomy cut indicating thermal damage of surrounding tissue. This damage was due to excessive heat accumulation during/after laser irradiation, leading to reduction of ablation efficiency (Figure 6.4(a)). Wet ablation with water produced a rough wall surface with a relatively wider crater compared to the dry condition; we did not see any indication of thermal injury on the peripheral tissue (Figure 6.4(b)). With perfluorocarbon, the wet condition produced the largest ablation crater with a relatively smooth surface; however, some thermal damage was found around the spot and even in the channel (Figure 6.4(c)). Craters produced by spray ablation were particularly clean with no thermal damage; compared to wet (water) ablation, the crater width of the spray case was narrower and deeper with a cone-shape and smoother ablation wall (Figure 6.4(d)).

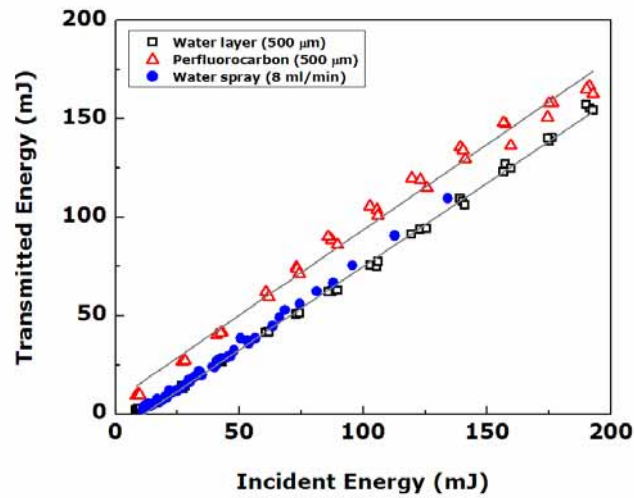


Figure 6.2. Energy transmission as a function of incident pulse energy for three conditions: 500 μm water layer, 500 μm perfluorocarbon layer, and water spray of 8 ml/min

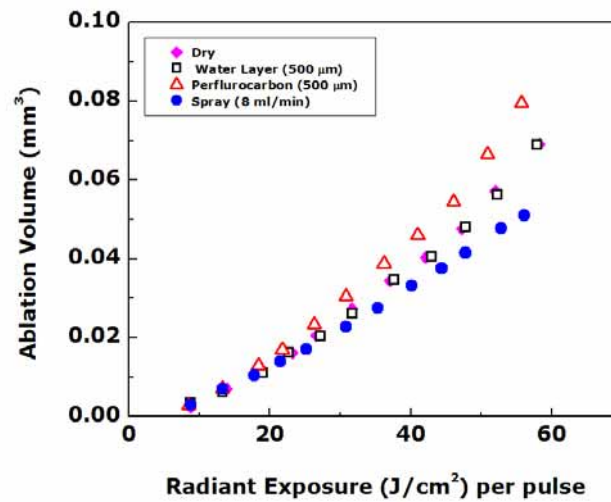


Figure 6.3. Comparison of ablation volume measured with OCT as a function of radiant exposure with five pulses for various experimental conditions: dry, wet (500 μm water and perfluorocarbon layers), and spray (water, flow rate = 8 ml/min) ablation

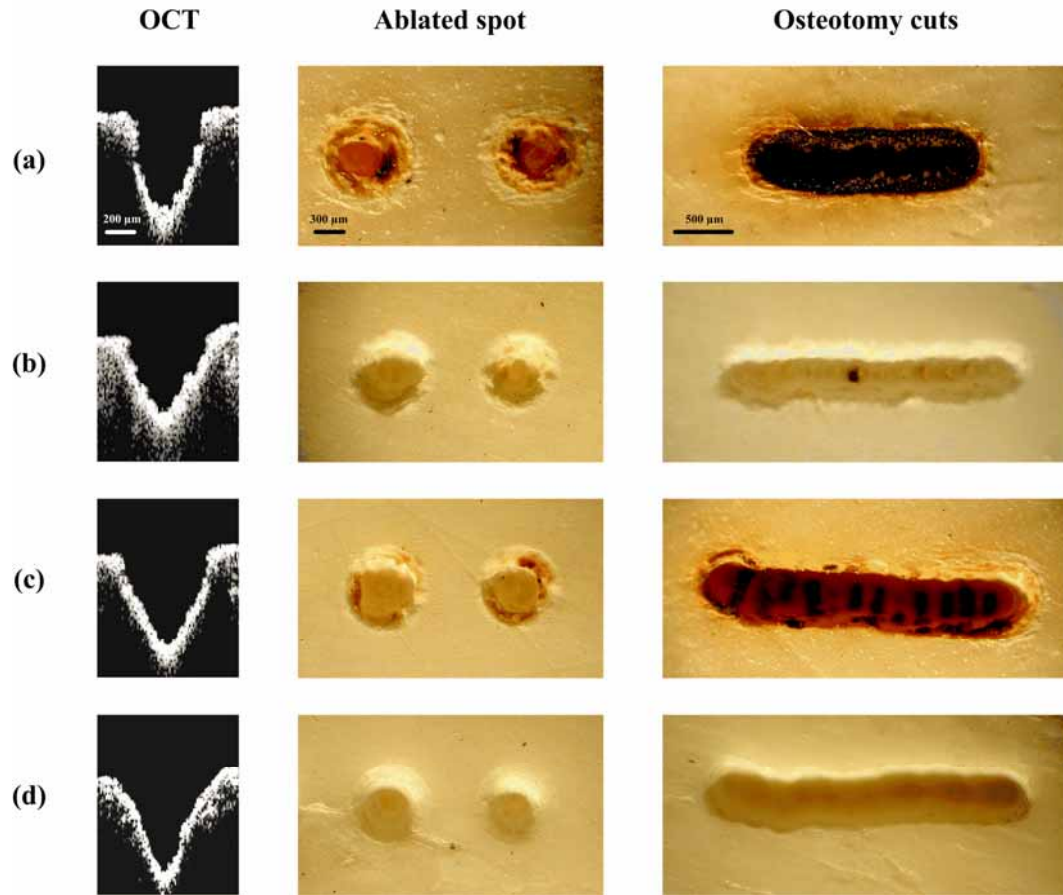


Figure 6.4. Cross-sectional OCT (the leftmost column, $H = 47 \text{ J/cm}^2$) and top view (the middle column, $H = 42 \text{ J/cm}^2$ for the left and $H = 37 \text{ J/cm}^2$ for the right spot) images of bone tissues ablated with a sequence of five pulses. Another top view image (the rightmost column) shows osteotomy cuts with multiple sequences of five pulses at $H = 47 \text{ J/cm}^2$ (lateral resolution = 200 μm every five pulses). Four different conditions were tested: (a) dry, (b) wet (500 μm water layer), (c) wet (500 μm perfluorocarbon layer), and (d) spray ablation (flow rate of 8 ml/min)

6.5 DISCUSSION

Laser ablation of bovine bone tissues with a sequence of five pulses was investigated for various conditions: dry, wet (water and perfluorocarbon), and spray ablation (water with a flow rate of 8 ml/min). The perfluorocarbon with an absorption coefficient less than 0.001 % of water had the highest transmission efficiency (Figure 6.2) and volume of bone removal (Figure 6.3); however, some thermal damage was seen in the ablation crater. Severe thermal damage (carbonization) was associated with dry ablation due to excessive heat accumulation while ablation using either a water layer or spray prevented thermal injury to the peripheral tissue because of the cooling effect of the water. The wet (water) ablation produced rough and irregular surface deformations whereas the spray ablation created rather clean, cone-shaped cutting possibly due to photo-mechanical effects through water vaporization and convective motion.

Since the laser pulse ($\tau_p \sim 150 \mu\text{s}$) was longer than $100 \mu\text{s}$, the ablation process took place concomitantly with irradiation. The thermal diffusion time when optical penetration depth $<$ spot size was given by [28]

$$\tau_p = 1/4\alpha\mu_a^2 \quad (6.1)$$

where α is the thermal diffusivity ($1.5 \times 10^{-7} \text{ m}^2/\text{s}$ for bone [9]) and μ_a is the absorption coefficient (2120 cm^{-1} for bone in Table 6.1). Since the estimated $\tau_p = 40 \mu\text{s}$, thermal energy was conducted from the absorption volume during the laser

pulse. During dry ablation, heat transported to adjacent tissue caused irreversible thermal damage. In addition, carbonization occurred where temperatures exceeded 150 °C [29]. Excessive heat accumulation/diffusion due to long time periods of heating possibly initiated the release of carbon, leading to a blackening in color (Figure 6.4 (a)) and evidencing the thermal injury. Since the bone sample for the dry ablation was desiccated prior to experimentation, the main absorber of the sample was hydroxyapatite, and thus, internal explosion of interstitial water in the bone was not the main ablation mechanism for this case.

Application of a water layer promoted ablation performance through explosive liquid vaporization with a lower damage threshold [19,30]. In the case of wet (water) ablation, the generation of water vapor carried away excess heat, preventing excessive temperature increase of adjacent tissue. No thermal injury (carbonization) was observed with wet (water) ablation. The water layer blocks (absorbs) a portion of the laser pulse, yet the efficiency of both dry and wet (water) ablation was comparable (Figure 6.3) because of water vaporization. At the onset of laser irradiation, high absorption of water (5300 cm^{-1} at $2.79\text{ }\mu\text{m}$) initiated a vaporization process creating a water vapor channel that transmitted the rest of laser pulse to the sample surface (“Moses effect” [31]). Energy absorption increased the temperature of the water inside the tissue and/or in the layer beyond its equilibrium saturation temperature, causing explosive water vaporization with large pressure transients [30]. The irregular surface of the crater wall also

represented additional mechanical effects during the vaporization process. Therefore, strong acoustic transients during rapid water vaporization exerted a significant abrasive force upon the ablated crater surface, promoting ablation performance and compensating for the lower optical energy coupling.

In order to reduce the energy loss by water absorption, a perfluorocarbon layer with low IR absorption was tested. Similar to wet (water) ablation, liquid vaporization enhanced ablation efficiency. During laser irradiation, sufficient heat was transferred to superheat the liquid perfluorocarbon, consequently inducing rapid vaporization concomitant with strong pressure emission. It was also noted that ablation efficiency with a perfluorocarbon layer increased with higher radiant exposure (Figure 6.3). In spite of delivering more energy to the bone compared to water (Figure 6.2), the laser-induced crater using the perfluorocarbon had much less thermal damage than dry ablation (Figure 6.4(c)). Since the liquid perfluorocarbon had a thermal conductivity ($0.067 \text{ W/m}\cdot\text{K}$) and heat of vaporization (78.7 kJ/kg), which were much lower than the properties of water ($0.611 \text{ W/m}\cdot\text{K}$ and 2260 kJ/kg , respectively) [24], less heat was removed during ablation, inducing some thermal damage (Figure 6.4(c)). However, more energy transmission to the sample and liquid vaporization during/after the pulse produced the most efficient ablation performance compared to other experimental conditions (Figure 6.3).

The spray ablation achieved exceedingly clean cuts with smooth crater surface without thermal damage. Similar to wet (water) ablation, water inhibited excessive temperature rise, and rapid vaporization of interstitial water and water spray possibly promoted additional mechanical impact on the crater wall. We believe that the convective motion of water spray pushed the water out the crater wall [32]; the water flow effectively removed debris (cleaning effect) and cooled the sample surface. Reduced ablation efficiency was attributed to lower light transmission as well as light scattering by small water particulates. When a laser beam strikes small water droplets, photons are scattered and/or absorbed. The narrow, sharp-cone shape of the crater suggested that the laser light was preferentially scattered in the forward direction (water particulate larger than the laser wavelength), limiting ablation volume. Therefore, the forward scattering with water spray absorption during spray ablation provided a deeper, shaper cut with less ablation volume.

In terms of ablation volume efficiency, the perfluorocarbon layer provided the most efficient method for laser osteotomy. However, thermal side effects (some carbonization) due to low heat of vaporization do not prevent tissue necrosis. A different type of perfluorocarbon with better thermal properties will be tested as an alternative liquid to improve ablation performance and reduce thermal side effect. In addition, to assess thermal effects during laser ablation with and without liquid application, histological examination of the bone tissues

should be implemented in a future study. Lastly, spray-assisted laser ablation achieves clean and controllable osteotomy cutting with the highest depth per ablation volume efficiency. In order to obtain augmented ablation volume efficiency without thermal damage, a combination of perfluorocarbon and spray system should be investigated. During water-assisted ablation, the liquid provides cooling minimizing thermal damage; in addition, acoustic/mechanical impact enhances ablation performance while cleaning the surface. In case of clinical applications, rapid cutting of bone without thermal damage is highly desirable; therefore, spray ablation can be a feasible means for laser osteotomy since it outperforms the other techniques in terms of deep sharp cuts as shown in our experiments.

6.6 CONCLUSION

Laser osteotomy using a long-pulsed Er,Cr:YSGG laser was investigated with various environmental conditions: dry, wet (water or perfluorocarbon), and spray ablation. The application of a perfluorocarbon layer removed the largest ablation volume relative to the other conditions. However, poor thermal characteristics of perfluorocarbon induced much lower thermal damage than the severe carbonization associated with dry ablation. Wet (water) ablation produced ablation volumes comparable to dry ablation without any indication of carbonization. Additional mechanical effects resulting from waver vaporization

were possibly responsible for compensation of ablation efficiency in spite of water absorption. Lastly, spray combined with the Er,Cr:YSGG laser case induced clean cutting assisted by convective motion of water flow and limited temperature increase in the tissue, producing narrow sharp cuts. Liquid-assisted ablation can provide significant beneficial effects such as augmented material removal, liquid cooling, and abrasive cleaning effects during laser bone treatments.

6.7 REFERENCES

1. Ivanenko MM, Eyrich G, Bruder E, Hering P. In vitro incision of bone tissue with a Q-switch CO₂ laser. Histological examination. *Lasers Life Sci* 2000;9:171-179.
2. Eyrich GKH. Laser-osteotomy induced changes in bone. *Med Laser Appl* 2005;20:25-36.
3. Gonzalez C, Van De Merwe WP, Smith M, Reinisch L. Comparison of the erbium yttrium aluminum garnet and carbon dioxide lasers for in vitro bone and cartilage ablation. *Laryngoscope* 1990;100:13-17.
4. Izatt JA, Sankey ND, Partovi F, Fitzmaurice M, Rava RP, Itzkan I, Feld MS. Ablation of calcified biological tissue using pulsed laser hydrogen fluoride laser radiation. *IEEE J Quantum Electron* 1990;26:2261-2270.
5. Li Z-Z, Reinisch L, Van De Merwe WP. Bone ablation with Er:YAG and CO₂ laser: study of thermal and acoustic effects. *Lasers Surg Med* 1992;12:79-85.
6. Forrer M, Frenz M, Romano V, Altermatt HJ, Weber HP, Silenok A, Istomyn M, Konov VI. Bone-ablation mechanism using CO₂ lasers of different pulse duration and wavelength. *Appl Phys B* 1993;56:104-112.
7. Peavy GM, Reinisch L, Payne JT, Venugopalan V. Comparison of Cortical Bone Ablations by Using Infrared Laser Wavelengths 2.9 to 9.2 μm . *Lasers Surg Med* 1999;26:421-434.
8. Ivanenko MM, Fahimi-Weber S, Mitra T, Wierich W, Hering P. Bone Tissue Ablation with sub- μs Pulses of a Q-switched CO₂ Laser:

- Histological Examination of Thermal Side-Effects. *Lasers Med Sci* 2002;17:258-264.
9. Duck FA. Physical properties of tissue: a comprehensive reference book. London: Academic Press, 1991.
 10. Rizioiu IM, DeShazer L. New laser-matter interaction concept to enhance hard tissue cutting efficiency. *SPIE Proc* 1994;2134A:
 11. Wigdor H, Visuri SR, Walsh JT J. Effect of Water on Dental Material Ablation of the Er:YAG laser. *SPIE Proc* 1994;2128:267-272.
 12. Rizioiu I, Kimmel AI, Eversole LR. The effects of an Er,Cr:YSGG laser on canine oral hard tissues. *SPIE Proc* 1996;2922:74-83.
 13. Visuri SR, Walsh JT J., Wigdor HA. Erbium Laser Ablation of Dental Hard Tissue: Effect of Water Cooling. *Lasers Surg Med* 1996;18:294-300.
 14. Majarson B, Sustercic D, Lukac M. Influence of water spray on Er:YAG ablation of hard dental tissues. *SPIE Proc* 1997;3192:82-87.
 15. Rizioiu I, Kohanghadosh F, Kimmel AI, Eversole LR. Pulpal thermal responses to an erbium, chromium:YSGG pulsed laser hydrokinetic system. *Oral Surg Oral Med Oral Pathol Oral Radiol Endod* 1998;86:220-223.
 16. Fried D, Ashouri N, Breunig T, Shori R. Mechanism of Water Augmentation During IR Laser Ablation of Dental Enamel. *Lasers Surg Med* 2002;31:186-193.
 17. Freiberg RJ, Cozean C. Pulsed erbium laser ablation of hard dental tissue: the effects of atomized water spray vs water surface film. *SPIE Proc* 2002;4610:74-84.
 18. Staninec M, Xie J, Le CQ, Fried D. Influence of an Optically Thick Water Layer on the Bond-Strength of Composite Resin to Dental Enamel After IR Laser Ablation. *Lasers Surg Med* 2003;33:264-269.
 19. Zhu S, Lu YF, Hong MH, Chen XY. Laser ablation of solid substrates in water and ambient air. *J Appl Phys* 2001;89:2400-2403.
 20. Kim D, Oh B, Lee H. Effect of liquid film on near-threshold laser ablation of a solid surface. *Appl Surf Sci* 2004;222:138-147.
 21. Wesendahl T, Janknecht P, Ott B, Frenz M. Erbium:YAG laser ablation of retinal tissue under perfluorodecalin: determination of laser-tissue interaction in pig eye. *Invest Ophthalmol Visual Sci* 2000;41:505-512.
 22. Chang S, Zimmerman N, Iwamoto T. Experimental vitreous surgery. *Am J Ophthalmol* 1987;103:29-37.
 23. Hibst R, Keller U. Er:YAG laser for dentistry: basics, actual questions, and perspectives. *SPIE Proc* 1994;2327:76-86.
 24. Mackanos MA, Jansen ED, Shaw BL, Sanghera JA, Aggarwal I, Katzir A. Delivery of midinfrared (6 to 7- μ m) laser radiation in a liquid environment using infrared-transmitting optical fibers. *J Biomed Opt* 2003;8:583-593.

25. Mills AF. Basic heat and mass transfer. London: Prentice-Hall, Inc., 1999.
26. Huang D, Swanson EA, Lin CP, Schuman JS, Stinson WG, Change W, MR H., Flotte TJ, Gregory K, Puliafito CA, Fujimoto JG. Optical coherence tomography. *Science* 1991;254:1178-1181.
27. Izatt JA, Kulkarni MD, Yazdanfar S, Barton JK, Welch AJ. In vivo bidirectional color doppler flow imaging of picoliter blood volumes using optical coherence tomography. *Opt Lett* 1997;22:1439-1441.
28. Vogel A, Venugopalan V. Mechanisms of Pulsed Laser Ablation of Biological Tissues. *Chem Rev* 2003;103:577-644.
29. Niemz MH. Laser-Tissue Interactions. Berlin, Germany: Springer-Verlag, 1996.
30. Kang HW, Lee H, Chen S, Welch AJ. Enhancement of Bovine Bone Ablation Assisted by a Transparent Liquid Layer on a Target Surface. *IEEE J Quantum Electron* 2006;42:633-642.
31. Chan KF, Vassar GJ, Pfefer TJ, Teichman JMH, Glickman RD, Weintraub ST, Welch AJ. Holmium:YAG Laser Lithotripsy: A Dominant Photothermal Ablative Mechanism With Chemical Decomposition of Urinary Calculi. *Lasers Surg Med* 1999;25:22-37.
32. Frenz M, Romano V, Zweig AD, Weber HP. Instabilities in laser cutting of soft media. *J Appl Phys* 1989;66:4496-4503.

Chapter 7: Effect of Liquid Thickness on Laser Ablation Efficiency (Experimental Study)

7.1 ABSTRACT

The purpose of this study was to investigate the effect of liquid thickness on laser ablation efficiency. Both Q-switched Nd:YAG and free-running Er:YAG lasers were used to ablate PMMA samples in the presence of a water layer. The thickness of the liquid layer varied from 500 μm to 3 mm. Ablation performance as a function of liquid thickness for both lasers was quantitatively measured by Optical Coherence Tomography (OCT). For the Q-switched Nd:YAG laser, wet ablation produced up to three times greater ablation volume than dry ablation, and the ablation efficiency decreased with increase of liquid thickness. On the other hand, for the Er:YAG laser, wet ablation with a 500 μm layer of water produced comparable ablation volume to dry ablation. Ablation performance decreased as the liquid layer thickness increased. Q-switched laser ablation assisted by a thin liquid layer efficiently augmented material removal while ablation efficiency of a long-pulsed Er:YAG laser decreased as water thickness was increased.

7.2 INTRODUCTION

Liquid-assisted laser ablation has been investigated in a number of engineering and clinical applications: laser surface cleaning [1,2], laser shock peening/micromachining [3,4], laser osteotomy [5], and dental tissue ablation [6,7]. In order to appreciate the effect of liquid layer on laser ablation, a variety of laser parameters such as wavelength [8,9], pulse duration [10], and radiant exposure [11] have been examined. Recent studies have demonstrated increased ablation efficiency for material machining in the presence of a liquid layer [10-12]. We have shown in our previous study that the liquid-assisted ablation with short pulse durations ($\tau_p < 1 \mu\text{s}$) had lower thresholds as well as higher volume removal than direct irradiation. The improved ablation performance with a liquid layer was associated with explosive vaporization and confinement of plasma expansion [5]. Even spray-assisted ablation with a $2.79 \mu\text{m}$ long pulse laser increased ablation efficiency up to twice greater than direct ablation. The mechanism was rapid water vaporization and ensuing microexplosion of water droplets imparting ablative momentum to the sample [7].

According to previous studies, a liquid-confined environment for laser ablation was achieved in several ways: ejecting saturated vapor controlled by a heater [13], flowing water film on top of the sample [9], emerging the sample in the water cuvette [11], and depositing a water droplet by using a syringe [6]. Due to various liquid-assisted configurations, different liquid thicknesses were

employed during ablation. In this study, experiments were carried out to understand the effect of liquid layer thickness on enhancement of ablation performance. We quantified ablation volume as water thickness was varied from 500 μm to 3 mm. Both short-pulsed Q-switched Nd:YAG and long-pulsed free-running Er:YAG lasers were used to examine the role of liquid layer during material removal.

7.3 MATERIALS AND METHODS

Experiments were performed with Q-switched Nd:YAG (wavelength $\lambda = 1064$ nm and pulse duration $\tau_p = 30$ ns at FWHM) and free-running Er:YAG lasers ($\lambda = 2.94$ μm and $\tau_p = 275$ μs at FWHM). The applied pulse energy levels were set at 400 mJ for the Q-switched Nd:YAG and 300 mJ for the Er:YAG. A sequence of five pulses at a repetition rate of 1 Hz was applied to the target. The schematic illustration for the ablation experiments presented in Figure 7.1 was used for both laser systems. A beam splitter was placed in the beam path to monitor the pulse energy. The laser pulse was reflected at an angle of 90° using a 1064 nm BK 7 mirror (CVI laser, Albuquerque, NM) for the Q-switched Nd:YAG and a gold mirror for the Er:YAG. A convex CaF_2 lens with a focal length of 100 mm was used to focus the laser beam on the target surface with a spot diameter of 300 μm for both lasers. Energy detectors (PE25BB-DIF, Ophir Optonics Inc.,

Danvers, MA for 1064 nm and J50, Molelectron, Portland, OR for 2.94 μm) were used to monitor the applied pulse energy during the experiment.

The target sample used in our experiments was a 5 mm thick polymethylmethacrylate (PMMA, black, 2.5×2.5 cm). In order to perform liquid-assisted ablation (termed the “wet ablation”), a plastic (Depron) ring was attached on top of a sample surface maintaining a consistent liquid layer thickness. Four different thicknesses of plastic rings were tested: 500 μm , 1 mm, 2 mm, and 3 mm, which provided different thicknesses of the liquid layer. Prior to laser irradiation, distilled water was deposited inside the ring. The absorption coefficients of water at the wavelengths of interest (1064 nm and 2.94 μm) were 0.13 cm^{-1} and 12500 cm^{-1} , respectively [14,15]. In case of PMMA, the absorption coefficients were found to be approximately 0.1 cm^{-1} at 1064 nm and > 11000 cm^{-1} at 2.94 μm [16-18]. No plastic ring was used for direct ablation (termed the “dry ablation”), which presented a control measurement.

Ablation craters were produced with a sequence of five pulses (1 Hz). Five craters were created at each water thickness. Laser-induced craters were examined using an Optical Coherence Tomography (OCT) system ($\lambda_0 = 1290 \text{ nm}$, $\Delta \lambda = 42 \text{ nm}$, and $P = 2.2 \text{ mW}$) with lateral and axial resolutions of $\sim 20 \mu\text{m}$ [19,20]. A series of vertical cross-sectional images parallel to the laser beam axis were scanned and acquired over the entire crater with a step-size between images

of 33 μm . Crater volume was quantitatively estimated with image processing software.

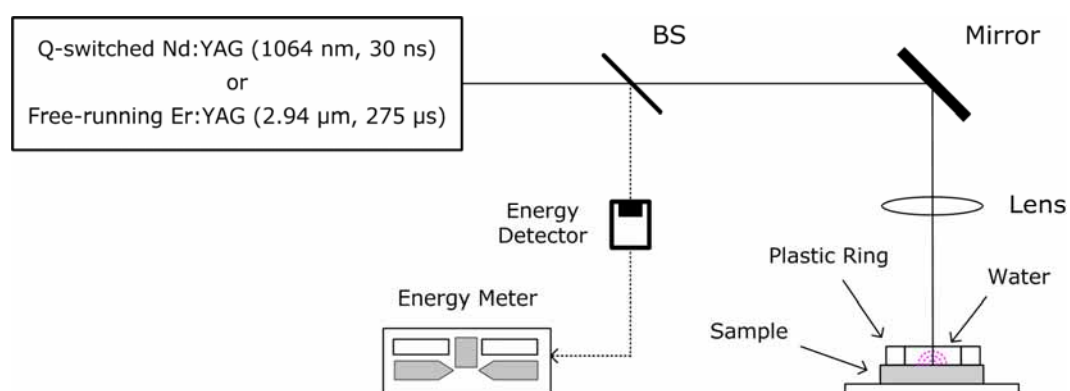


Figure 7.1. Experimental setup for liquid-assisted laser ablation. Four different liquid layer thicknesses were tested (500 μm , 1 mm, 2 mm, and 3 mm).

7.4 RESULTS

The OCT cross-sectional images of irradiated PMMA samples are shown in Figure 7.2. The top row was produced by five Nd:YAG pulses at 5.7 J/mm^2 . The bottom row was produced by five Er:YAG pulses at 4.2 J/mm^2 . Figure 7.2(a) and (b) show the images of direct (dry) ablation and liquid-assisted ablation with a $500 \text{ }\mu\text{m}$ water layer, respectively. The crater induced by wet ablation had a larger crater depth and width than those of dry ablation. Both dry and wet ablation produced relatively rough and irregular contours. In case of the Er:YAG laser, Figure 7.2(c) and (d) present the crater topography of dry and wet (using a 3 mm water layer) ablation. In contrast to the 1064 nm laser results, dry ablation with the $2.94 \text{ }\mu\text{m}$ laser light produced deeper and wider crater shape than wet ablation. A relative clean cut was achieved with dry $2.94 \text{ }\mu\text{m}$ ablation while wet ablation caused extruded ridges around the irradiation spot.

Ablation volume produced with the two laser systems as a function of liquid layer thickness are shown in Figure 7.3. No liquid thickness (0 mm) represents dry ablation. In case of the Q-switched laser, wet ablation with the entire thicknesses tested produced higher ablation volume, compared to dry ablation, and the ablation efficiency with a liquid layer increased up to approximately three times greater than the dry case; application of the water layer played a significant role in augmenting material removal. The best liquid thickness was $500 \text{ }\mu\text{m}$ for nanosecond pulse regime in our experiments, but the

ablation volume gradually decreased as the liquid layer became thicker than 500 μm . For the free-running Er:YAG laser, the ablation volume decreased inversely proportional to increase of liquid thickness. The wet ablation with a 500 μm liquid layer showed comparable ablation volume with the dry case. However, as the liquid thickness increased, the ablation efficiency became lower, decreasing by approximately 50 % with respect to the dry ablation.

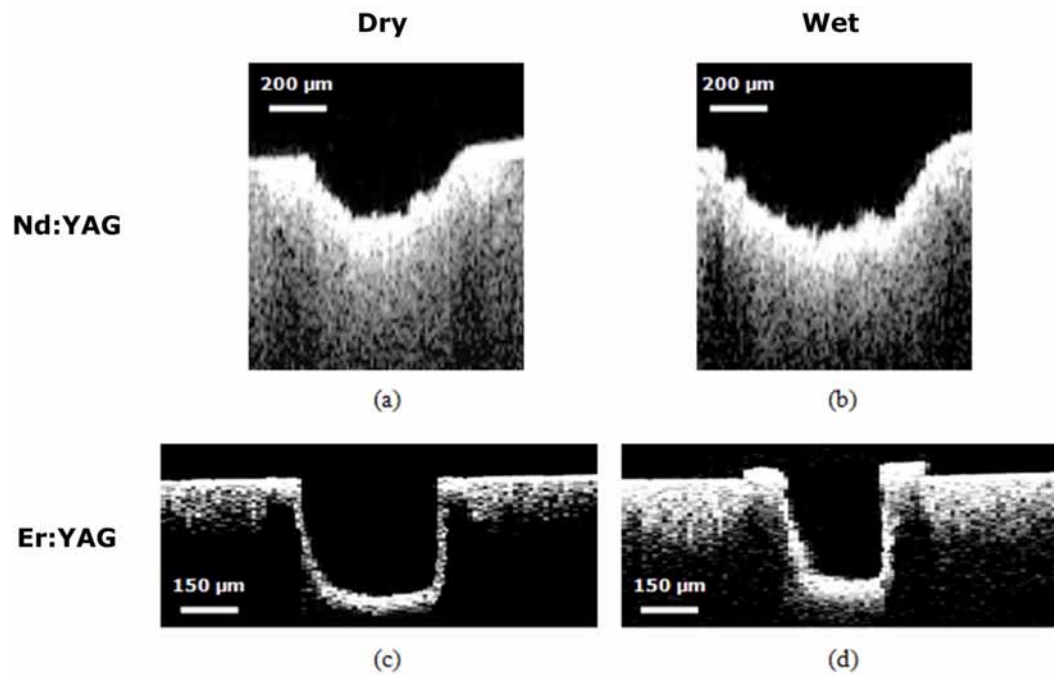
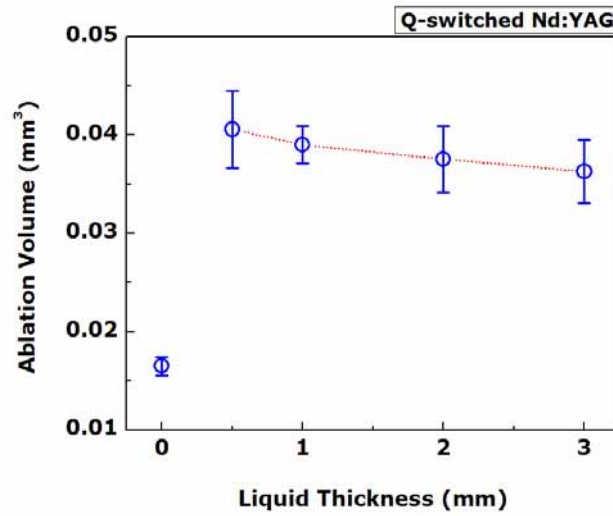
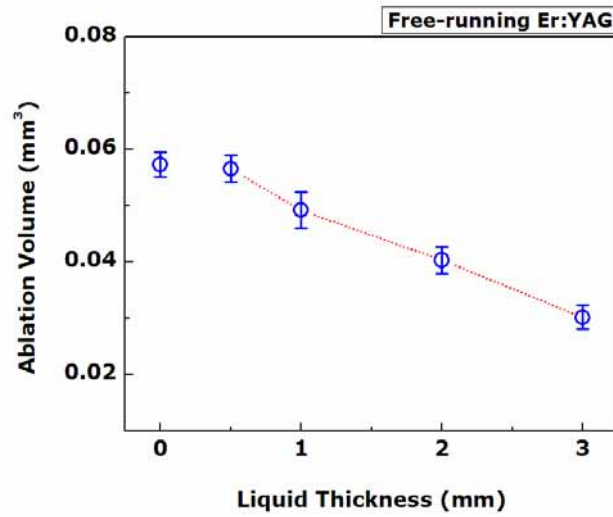


Figure 7.2. OCT cross-sectional images of laser-induced craters using a Q-switched laser at 5.7 J/mm^2 per pulse for a dry case (a) and a wet case with a 500 μm liquid layer (b) and using a free-running Er:YAG laser at 4.2 J/mm^2 per pulse for a dry case (c) and a wet case with a 3 mm liquid layer (d).



(a)



(b)

Figure 7.3. Ablation efficiency as a function of applied liquid thickness using a sequence of five pulses from each of the two laser systems: (a) Q-switched Nd:YAG at 5.7 J/mm^2 per pulse and (b) free-running Er:YAG at 4.2 J/mm^2 per pulse ($n = 5$). Note that 0 mm thickness represents dry ablation.

7.5 DISCUSSION

In the case of a Q-switched Nd:YAG laser, wet ablation promoted ablation efficiency up to three times greater than dry ablation (Figure 7.3(a)). Rough crater shapes with irregular contour evidenced photomechanical effects during both dry and wet ablation processes (Figure 7.2). Due to an irradiance of 19 GW/cm², the optical breakdown with the Q-switched Nd:YAG laser pulses was observed. Plasma luminescence and an audible noise from acoustic wave generation substantiated the breakdown process during laser irradiation. According to previous studies, the augmented ablation performance during wet ablation was explained by additional mechanical effects. Owing to a significant temperature increase (up to 15000 K [21]) during plasma formation, thermal conduction to the liquid layer caused the water to become superheated, inducing homogeneous generation of vapor bubbles. The pressure inside the bubble P_{ve} was estimated using

$$P_{ve} = P_{sat}(T_l) \cdot \exp\left[\frac{v_l \cdot (P_l - P_{sat}(T_l))}{RT_l}\right] \quad (7.1)$$

where T_l , P_{sat} , P_l , v_l , and R are the temperature of the superheated liquid, the saturation pressure at the liquid temperature, the pressure of the superheated liquid, specific volume, and gas constant respectively [5]. As the water temperature approached $0.83T_c$ (T_c : thermodynamic critical temperature of

water), the pressure described above increased close to the saturation pressure at the liquid temperature, initiating bubble formation with spherical shock wave generation. We suggest that this gave rise to additional mechanical impact, enhancing ablation efficiency. In addition, when the plasma is confined in the water layer [11] and since the acoustic impedance of water ($Z_{water} = 1.48 \times 10^6$ kg/m²s) is greater than that of air ($Z_{air} = 410$ kg/m²s) [5], shock waves induced by water vaporization and plasma formation are reflected at the interface between air and water; more compressive waves are applied to the sample, leading to more material removal [5]. Lastly, during both spherical and hemispherical bubble collapses near a rigid boundary, a high-speed, liquid jet impinges on the sample surface [22]; the jet during bubble collapse possibly involves high impulsive pressure as additional mechanical force improving ablation efficiency.

According to Figure 7.3(a), the wet ablation efficiency decreased with the layer thickness. Since water had a relatively high heat of vaporization of 2260 kJ/kg [23], a thicker water layer increased heat loss during/after laser irradiation, which decreased temperature rise, possibly limiting pressure generation during bubble formation/collapse (equation 7.1). This would account for diminished ablation performance with liquid thickness. We conclude that a thinner liquid layer with a short-pulsed laser is desirable to enhance laser ablation efficiency. The thinnest layer we could reliably test in this research was

500 μm . In order to apply a liquid layer thinner than 500 μm , it may be possible to use a thinner plastic ring with water and add a surfactant to the water to reduce surface tension. In addition, a liquid-puffing system ejecting saturated vapor on the sample surface can be used to form a thin liquid film, of which thickness was estimated to be dozens of microns [24].

On the other hand, a free-running Er:YAG laser beam was absorbed within a few microns in the water surface. Since the pulse duration was longer than 100 μs , the underlying mechanism was associated with photothermal processes. According to a previous study, the direct irradiance of the sample in water environment is induced only through a laser-induced vapor channel (the “Moses effect”) [25]. At the onset of laser irradiation, high absorption of water (12500 cm^{-1} at 2.94 μm) initiated a vaporization process producing a water channel and transmitting the rest of the laser pulse; as a thicker water layer was applied, more light energy was required to create a channel. In addition, it was conceivable that up to 500 μm , the explosive liquid vaporization maintained comparable ablation performance with that of dry ablation, but with thicker layers, energy coupling with the target became lower, diminishing the ablation efficiency (Figure 7.3(b)). Our previous study showed that only 30 % of the energy for a 275 μs pulse with a pulse energy of 50 mJ reached the target through a 1 mm water layer [26]. It was confirmed that the target absorbed more light energy at 2.94 μm rather than 1064 nm due to larger ablation volume

produced by the Er:YAG laser (Figure 7.2(a) and (c)). In addition, after the onset of laser irradiation, water cooling during melting state of the sample possibly resulted in formation of extruded rims around the spot (Figure 7.2(d)). Hence, due to energy loss by high water absorption, application of a thin water layer ($\leq 500 \mu\text{m}$) can be required for a long-pulsed Er:YAG laser in order to prevent any reduction in ablation efficiency.

7.6 CONCLUSION

Liquid-assisted ablation efficiency with both Q-switched Nd:YAG and free-running Er:YAG lasers was evaluated as a function of liquid thickness ranging from $500 \mu\text{m}$ to 3 mm . Due to additional mechanical impacts, wet ablation with the Q-switched Nd:YAG laser showed up to three times higher ablation volume than dry ablation. More heat dissipation with a thicker liquid layer reduced ablation efficiency, which was still greater than the dry case; a thinner liquid layer ($\leq 500 \mu\text{m}$) was thought to be advantageous in terms of ablation performance. In case of long-pulsed Er:YAG laser, wet ablation efficiency decreased by up to 50 % of dry case as the liquid layer became thicker. Due to higher absorption coefficient of water at $2.94 \mu\text{m}$, the energy loss during water vaporization limited the amount of the laser energy transmitted to the sample, consequently decreasing ablation efficiency.

7.7 REFERENCES

1. She M, Kim D, Grigoropoulos CP. Liquid-assisted pulsed laser cleaning using near-infrared and ultraviolet radiation. *J Appl Phys* 1999;86:6519-6524.
2. Tam AC, Leung WP, Zapka W, Ziemlich W. Laser-cleaning techniques for removal of surface particulates. *J Appl Phys* 1992;71:3515-3523.
3. Choo KL, Ogawa Y, Kanbargi G, Otra V, Raff LM, Komanduri R. Micromachining of silicon by short-pulse laser ablation in air and under water. *Mater Sci Eng, A* 2004;372:145-162.
4. Zhang W, Yao YL, Noyan IC. Microscale Laser Shock Peening of Thin Films, Part 1: Experiment, Modeling and Simulation. *J Manuf Sci-T ASME* 2004;126:10-17.
5. Kang HW, Lee H, Chen S, Welch AJ. Enhancement of Bovine Bone Ablation Assisted by a Transparent Liquid Layer on a Target Surface. *IEEE J Quantum Electron* 2006;42:633-642.
6. Fried D, Ashouri N, Breunig T, Shori R. Mechanism of Water Augmentation During IR Laser Ablation of Dental Enamel. *Lasers Surg Med* 2002;31:186-193.
7. Kang HW, Rizioiu I, Welch AJ. Mechanism of Spray-assisted Laser Ablation of Dental Hard Tissue. *Biophys J* 2006; submitted
8. Dupont A, Caminat P, Bournot P. Enhancement of material ablation using 248, 308, 532, 1064 nm laser pulse with a water film on the treated surface. *J Appl Phys* 1995;78:2022-2028.
9. Berthe L, Fabbro R, Peyre P, Bartnicki E. Wavelength dependent of laser shock-wave generation in the water-confinement regime. *J Appl Phys* 1999;85:7552-7555.
10. Ren J, Kelly M, Heeselink L. Laser ablation of silicon in water with nanosecond and femtosecond pulses. *Opt Lett* 2005;30:1740-1742.
11. Lu J, Xu RQ, Chen X, Shen ZH, Ni XW, Zhang SY, Gao CM. Mechanisms of laser drilling of metal plates underwater. *J Appl Phys* 2004;95:3890-3894.
12. Zhu S, Lu YF, Hong MH, Chen XY. Laser ablation of solid substrates in water and ambient air. *J Appl Phys* 2001;89:2400-2403.
13. Kim D, Oh B, Lee H. Effect of liquid film on near-threshold laser ablation of a solid surface. *Appl Surf Sci* 2004;222:138-147.
14. Hale GM, Querry MR. Optical constants of water in the 200 nm to 200 μm wavelength region. *Appl Opt* 1973;12:555-563.
15. Hibst R, Keller U. Er:YAG laser for dentistry: basics, actual questions, and perspectives. *SPIE Proc* 1994;2327:76-86.

16. Beyer O, Nee I, Havermeyer F, Buse K. Holographic recording of Bragg gratings for wavelength division multiplexing in doped and partially polymerized poly(methyl methacrylate). *Appl Opt* 2003;42:30-37.
17. Yamamoto K, Ishida H. Optical Theory Applied to Infrared Spectroscopy. *Vibrational Spectrosc* 1994;8:1-36.
18. Barnier F, Dyer PE, Monk P, Snelling HV, Rourke H. Fibre optic jacket removal by pulsed laser ablation. *J Phys D: Appl Phys* 2000;33:757-759.
19. Huang D, Swanson EA, Lin CP, Schuman JS, Stinson WG, Chang W, Hee MR, Flotte TJ, Gregory K, Puliafito CA, Fujimoto JG. Optical coherence tomography. *Science* 1991;254:1178-1181.
20. Izatt JA, Kulkarni MD, Yazdanfar S, Barton JK, Welch AJ. In vivo bidirectional color doppler flow imaging of picoliter blood volumes using optical coherence tomography. *Opt Lett* 1997;22:1439-1441.
21. Barnes PA, Rieckhoff KE. Laser induced underwater sparks. *Appl Phys Lett* 1968;13:282-284.
22. Isselin JC, Alloncle AP, Autric M. On laser induced single bubble near a solid boundary: Contribution to the understanding of erosion phenomena. *J Appl Phys* 1998;84:5766-5771.
23. Mackanos MA, Jansen ED, Shaw BL, Sanghera JA, Aggarwal I, Katzir A. Delivery of midinfrared (6 to 7- μ m) laser radiation in a liquid environment using infrared-transmitting optical fibers. *J Biomed Opt* 2003;8:583-593.
24. Hong MH, Koh ML, Zhu S, Lu YF, Chong TC. Steam-assisted laser ablation and its signal diagnostics. *Appl Surf Sci* 2002;197-198:911-914.
25. Chan KF, Vassar GJ, Pfefer TJ, Teichman JMH, Glickman RD, Weintraub ST, Welch AJ. Holmium:YAG Laser Lithotripsy: A Dominant Photothermal Ablative Mechanism With Chemical Decomposition of Urinary Calculi. *Lasers Surg Med* 1999;25:22-37.
26. Chan KF, Lee H, Teichman JMH, Kameron A, McGuff HS, Vargas G, Welch AJ. Erbium:YAG laser Lithotripsy Mechanism. *J Urol* 2002;168:436-441.

Chapter 8: Mechanisms of Spray-assisted Laser Ablation of Dental Hard Tissue

8.1 ABSTRACT

The objective of this study was to understand the dominant mechanism(s) for dental enamel ablation with the application of water spray. A free-running Er,Cr:YSGG laser was used to ablate human enamel tissue at various radiant exposures. Distilled water was sprayed to the sample surface, and desiccated samples were also tested with direct irradiation for comparison. The optimal flow rate was examined by comparing ablation volumes at various radiant exposures and spray flow rates. The ablation threshold for each condition and the transmission loss by water absorption were quantified as a function of radiant exposure. In order to identify dominant ablation mechanisms, transient acoustic waves and temperature increase were compared, and Schlieren flash photograph also was performed. Ablation efficiency was evaluated with Optical Coherence Tomography (OCT). Ablation efficiency increased slightly as spray flow rate decreased. Single pulse damage threshold for spray condition was 2.1 J/cm^2 , which was 60 % higher than that of dry (1.2 J/cm^2). Due to water absorption, the

application of water spray reduced energy transmission efficiency. Spray ablation increased ablation volume up to twice with approximately six times higher peak acoustic amplitude as compared to the dry condition. The temperature distribution indicated the cooling effect of water spray which helps prevent thermal side effects. Dry ablation showed irregular surface deformation, charring, and peripheral cracks while craters for spray samples were relatively clean without thermal damage. In spite of the higher damage threshold due to water absorption, spray ablation enhanced both the laser-induced acoustic transients and the ablation efficiency over the entire range of radiant exposures, compared to dry ablation. The enhanced pressure and ablation performance of the spray-assisted process was associated with rapid vaporization of water spray, material ejection with recoil stress, interstitial water explosion, and/or liquid-jet formation. With water cooling and abrasive/disruptive mechanical effects, the spray ablation can be a safe and efficient modality for dental treatment.

8.2 INTRODUCTION

Applications of infrared (IR) lasers in dental research has been investigated since 1960s; lasers have included CO₂, Nd:YAG, Ho:YAG, and Er:YAG [1-6]. Dental ablation studies have demonstrated that these lasers can remove caries and hard dental tissues and be used in root canal preparation with more or less thermal effects. Compared to conventional mechanical drills, non-

contact laser surgery eliminates vibrations and permits more precise and comfortable removal of caries. The main IR energy absorbers for enamel are water and hydroxyapatite since enamel comprises of 85 – 95 % carbonated hydroxyapatite, 8 – 12 % water, and 2 – 3 % protein and lipids [7,8]. In case of Er:YAG dental ablation ($\lambda = 2.94 \mu\text{m}$), the primary mechanism reported is the thermo-mechanical interaction due to the high absorption peak of water at $2.94 \mu\text{m}$. Laser irradiation at this wavelength rapidly heats interstitial water, resulting in explosive removal of the outer layers of the enamel [9-13].

When medical lasers are used without water or cooling, physical limitations such as irreversible thermal damage to hard tissue structures may occur due to a combination of long pulse duration and high radiant exposures which results into a high temperature rise and heat conduction. However, no thermal damage has been reported when using the Er:YAG laser because of its high absorption and resulting micron penetration depth. Thermal and/or mechanical damage can be avoided through application of water during laser ablation [14-23]. The water prevents pulpal heating and dehydration of the irradiated tissue which would otherwise result in tissue thermal damage and reduced tissue ablation [17,21]. The use of water improves ablation efficiency and surface morphology [20]. Rapid water vaporization and/or ensuing microexplosions are believed to remove tissue debris and surface asperities in the irradiated tissue [14,20,21,23].

One type of laser considered effective for ablation of hard and soft tissues is the Er,Cr:YSGG ($\lambda = 2.79 \mu\text{m}$). With the assistance of a mixture of air and water droplets, this laser effectively removes hard dental tissues [24,25]. The absorption coefficient of water at $2.79 \mu\text{m}$ is $\mu_a = 5300 \text{ cm}^{-1}$, which is lower by more than two folds than that at $2.94 \mu\text{m}$ ($\mu_a = 12500 \text{ cm}^{-1}$), and the $2.79 \mu\text{m}$ wavelength corresponds to an absorption peak of hydroxyapatite [26,27]. Therefore, the Er,Cr:YSGG using a sapphire fiber tip and water spray is proposed as an alternative laser system for safe and efficient dental ablation.

Understanding the dominant mechanism(s) of water-assisted dental ablation is necessary in order to exploit and control the laser dental treatment in a predictable and efficient manner. In this study, the spray-assisted enamel ablation was characterized by quantifying the ablation threshold and ablation efficiency as a function of the free-running type pulse of the Er,Cr:YSGG used to irradiate tissue at various parameter and spray flow rates. Ablation performance was compared for dry and spray enamel samples as a function of radiant exposure. By measuring acoustic wave generation and dynamic imaging of the ablation process, the role of water spray during material removal was examined.

8.3 MATERIALS AND METHODS

8.3.1 SPECIMEN

Tissue samples were derived from freshly extracted adult human molars. The teeth were cut with a dental diamond band saw to create a flat surface with a thickness of 1 ~ 2 mm. Dehydration was minimized by storing all samples in sterile water at 4 °C for no more than a week. The cross-sectional area of enamel was irradiated, and two different sample conditions were tested: samples were either desiccated at room temperature for 48 hours or stored in sterile water prior to experimentation. The desiccated teeth were ablated without using a water spray system (termed the “dry condition”); on the other hand, hydrated samples were ablated using the water spray during laser ablation (termed the “spray condition”). Distilled water was used in an aerated water spray system. Optical, thermal, and mechanical properties of the target materials are summarized in Table 8.1.

Table 8.1. Optical, thermal, and mechanical properties of water and enamel [26,28-30]

Material Properties	Water	Human Enamel
Optical Absorption Coefficient (cm^{-1}) at 2.79 μm	5300	636
Thermal Conductivity ($\text{W/m}\cdot\text{K}$)	0.611	0.88 – 1.07
Fracture Toughness ($\text{MPa}\cdot\text{m}^{1/2}$)	N/A	0.7 – 1.27

8.3.2 LASER SOURCE AND WATER SPRAY SYSTEM

Enamel samples were ablated with using a clinical Er,Cr:YSGG laser (Waterlase MD, BioLase Technology, Irvine, CA). The laser system was set at 10 Hz, and either a single pulse or a sequence of ten pulses was applied to the target. The pulse duration varied between 100 μ s and 150 μ s as a function of pulse energy from 3 mJ to 200 mJ. The laser energy was delivered through a fiber optic system to a handpiece containing a sapphire tip with a diameter of about 600 μ m and a divergence of 8°. The output pulse energy of the delivery system was measured with an energy meter (EPM 2000, Molectron, Portland, OR) along with a pyroelectric joulemeter (J50, Molectron, Portland, OR) before and after each irradiation of the enamel sample. In order to avoid possible artifacts due to fiber tip damage during tissue ablation, the tip was replaced if the measured energy was reduced by more than 15 % of the initial output energy. In addition, the handpiece included a built-in pressurized water spray irrigation system with adjustable flow rates ranging from 2.8 ml/min to 22.8 ml/min. To achieve a stable flow rate, the water spray was initiated and terminated three seconds pre and post laser pulse, respectively. With and without using the water spray system, enamel ablation was characterized in terms of ablation performance and pressure generation. A schematic illustration of the experimental setup is shown in Figure 8.1. A 1.5 mm thick CaF₂ window (Edmund Optics, Barrington, NJ) was inserted into the laser system to produce a triggering signal. Using a lens

system, the reflected light from the window was focused onto a fast Si photodetector (1 ns rise time, J12-18C-R250U, EG&G, Montgomeryville, PA), which produced a triggering signal for digital oscilloscope (TDS3054, Tektronix, Beaverton, OR) to measure the temporal profile of optical pulses and acoustic transients. The irradiation spot on the target was adjusted with a three-axis translation stage. The gap between the fiber tip and the tissue sample was maintained at approximately 500 μm for all the experiments, which is a clinically accepted working distance.

8.3.3 HIGH-SPEED IMAGING AND ACOUSTIC WAVE MONITORING

In order to observe the dynamics of ablation process, Schlieren flash photography was performed (Figure 8.1). A Xenon flashlamp (5 μs typical exposure time, MVS-2601, EG&G, Salem, MA) was used to illuminate the fiber tip during laser irradiation and to image the ablation process at the instant time $t_0 + \Delta t$ (t_0 : laser onset time and Δt : delay time between laser onset and illumination). A white diffusing screen was placed in front of one flashlamp fiber. By means of using a delay generator (DGD 535, Stanford Research Systems, Sunnyvale, CA), a sequence of delay times (Δt) provided images of the ablation process from the beginning of laser onset. This experiment required repeated irradiations to create a complete sequence of the ablation process, and a new position was ablated at each time. Concurrent images on the dynamics of enamel ablation were captured

at various times by a high-speed camera (FASTCAM Super 3K, Photron, San Diego, CA) operating at 1000 frames per second and transferred to a recorder. Imaging was performed using the transmittance (shadowgraph) and/or reflectance modes.

Laser-induced acoustic waves were monitored using a piezoelectric airborne transducer (132A42, PCB Piezoelectronics, Depew, NY) with a bandwidth of 1 MHz and a sensitivity of 0.308 mV/Pa. The microphone was positioned at a distance of 15 mm from the sample surface under an angle of 30 ° to the beam axis (Figure 8.1). The optical pulse and acoustic signals were simultaneously recorded on a digital oscilloscope for post-experimental processing and FFT analysis.

8.3.4 BEAM PROFILE

Figure 8.2 shows a schematic diagram for measuring the beam profile. The beam profile at the sapphire fiber tip was imaged with a microscope objective (magnification = 30, NA = 0.4) on to a beam profiler (Pyrocam I, Spiricon, Logan, UT) that was placed at the image plane. The beam profiler was triggered by a photodetector, and the acquired images were transferred to a personal computer equipped with a frame grabber. To determine the degree of deviation from the TEM₀₀ mode, a Gaussian fit was performed using software installed in the beam profiler.

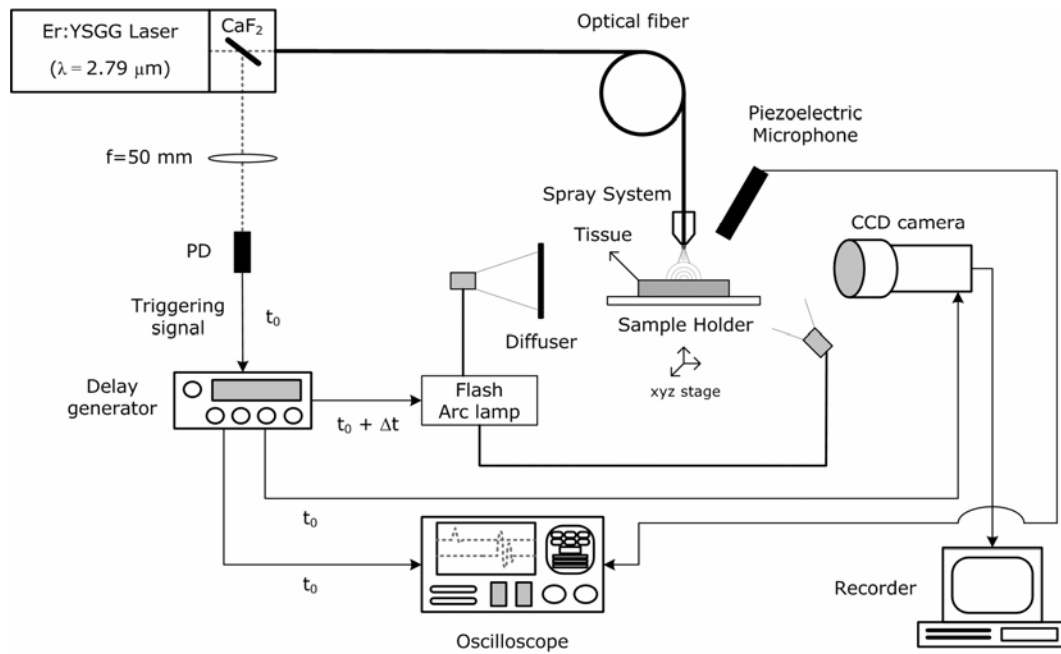


Figure 8.1. Schematic illustration of experimental set-up for laser-induced acoustic measurement and Schlieren flash photography during enamel tissue ablation (PD: photodetector, t_0 : laser onset time, and Δt : delay time)

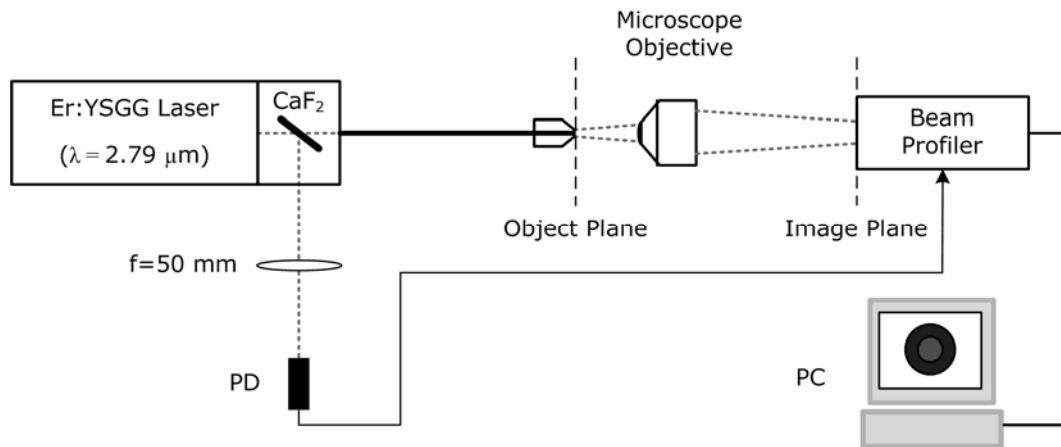
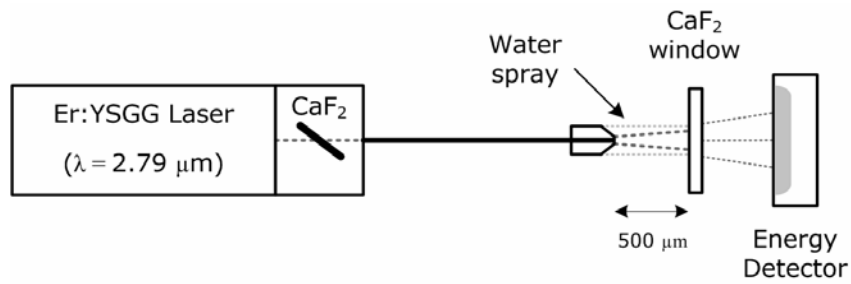


Figure 8.2. Experimental set-up to measure the beam profile at the distal end of the delivery fiber and sapphire tip

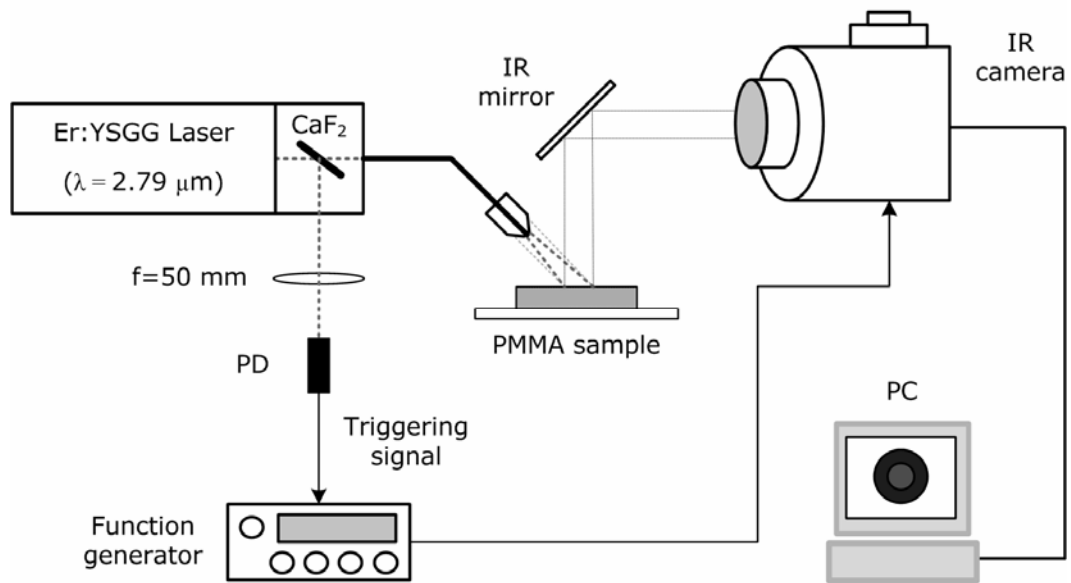
8.3.5 LIGHT TRANSMISSION AND TEMPERATURE MEASUREMENT

Attenuation of the laser beam by the water spray was determined using the experimental setup shown in Figure 8.3(a). A 5 mm thick CaF_2 window was placed 500 μm in front of the fiber tip to block the water spray, and a Molelectron energy probe was used to measure the laser energy transmitted through the CaF_2 window. Energy measurements with and without the application of water spray as a function of radiant exposure were compared to quantify the efficiency of light transmission.

The effect of water spray on the temperature distribution during irradiation of a hard tissue phantom approximately 500 μm in front of the fiber tip at 45° was evaluated with different radiant exposures using the system described in Figure 8.3(b). Polymethyl-methacrylate (PMMA, black, $2.5 \times 2.5 \times 0.5$ cm) was selected as a phantom to obtain a larger flat surface. A temperature response was induced by a single laser pulse in the PMMA; the radiant exposures were chosen higher than the dry damage threshold of the PMMA (approximately 0.91 J/cm^2). Placing an IR mirror at 45° to detect emissivity from the target, an infrared focal plane array (IP-FPA) camera (Phoenix model, Indigo Systems, Santa Barbara, CA) with a 3–5 μm bandwidth provided thermal images (frame rate = 100 Hz) of the irradiated PMMA surface for dry and spray cases. The camera was triggered by a function generator (33120A, Hewlett Packard, Palo Alto, CA), and internal and external filters prevented any of the laser light to reach the camera detectors.



(a)



(b)

Figure 8.3. Experimental arrangements to (a) quantify the efficiency of light transmission and (b) measure temperature distribution during a single laser pulse with and without water spray

8.3.6 ABLATION THRESHOLD AND EFFICIENCY

The threshold for single pulse ablation of enamel was defined as the incident radiant exposure to induce either mass ejection or surface disruption. A single laser pulse was applied and a double blind study was performed to prevent biased decisions. The pulse energy was altered around the anticipated threshold level ($n = 33$). Each pulse was scored as a 1 (mass ejection or surface deformation) or a 0 (no mass ejection or surface deformation). Forward illumination and dark background were employed to visualize plume formation during dry ablation. For spray samples, surface deformation was observed using an optical microscope. Results were post-experimentally analyzed using *Probit* analysis [31]. The ablation threshold was specified as the radiant exposure at which ablation occurred with a 50 % probability. The probabilistic approach considered localized variations in optical, thermal, and mechanical properties of a specimen that could potentially influence the ablation threshold values.

Multiple pulse ablation craters were produced with ten pulses as a function of radiant exposure and spray flow rate at a certain radiant exposure. Ablation efficiency was determined for dry and spray conditions. Crater dimensions were measured with an optical coherence tomography (OCT) system ($\lambda_0 = 1290$ nm, $\Delta\lambda = 42$ nm, and $P = 2.2$ mW) with lateral and axial resolutions of ~ 20 μm [32,33]. A series of vertical cross-sectional images parallel to laser beam axis were scanned and acquired over the entire crater with a step-size between images of 43

μm. Crater volume was quantitatively estimated with image processing software. Also, the craters were observed with an optical microscope to compare quality of laser ablation and morphological deformation.

8.4 RESULTS

8.4.1 BEAM PROFILE

Image of the Er,Cr:YSGG laser beam without spray measured with a pyroelectric solid-state camera is shown in Figure 8.4. With the software using a least square method, the correlation between the measured data and the fitted Gaussian profiles was defined as

$$G_c = 1 - \frac{\sum |I_M - I_C|}{\sum I_M} \quad (8.1)$$

where G_c = Gaussian correlation, I_M = measured intensity, and I_C = fitted Gaussian intensity. The laser produced a multimode beam that deviated from TEM₀₀ mode with a correlation of 0.851. Overall, the Er,Cr:YSGG laser created a cone shape beam with randomly located hotspots around the peak intensity slightly deviated from the beam center line.

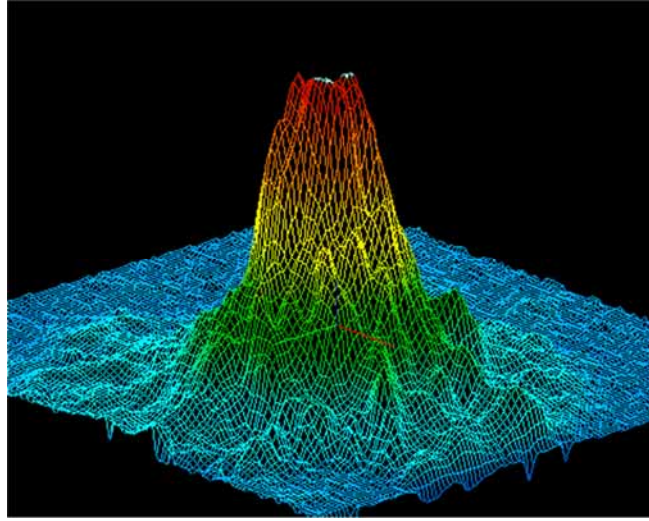


Figure 8.4. Beam profile of the Er,Cr:YSGG laser (pulse energy $Q_0 = 10$ mJ)

8.4.2 EFFECT OF WATER SPRAY FLOW RATE

In order to determine the optimal water spray flow rate, ablation volume was evaluated as a function of flow rate. The laser-induced enamel craters were produced using three different radiant exposures ($H = 13, 28$, and 52 J/cm^2 per pulse) with ten pulses, and five different flow rates were tested: 2.8, 8, 12.5, 16.8, and 22.8 ml/min. Ablation volume at various radiant exposures and flow rates are compared in Figure 5. No water spray was applied at the flow rate of 0 ml/min, which provided a control measurement. It was observed that ablation volume increased with the applied radiant exposure and decreased as the flow rate increased for all the radiant exposures. Application of water spray produced up to approximately three times larger volume than the control ablation. At a flow rate

of 2.8 ml/min, increasing radiant exposure augmented ablation volume (Figure 8.5). As radiant exposure approximately doubled from 13 J/cm² to 28 J/cm², ablation volume increased by a factor of five. Another doubling of radiant exposure to 52 J/cm² caused a factor of ten increased in ablation volume; application of the water spray played a significant role in augmenting enamel ablation. In addition, at the radiant exposure of 52 J/cm², the ablation volume difference between the lowest (2.8 ml/min) and highest (22.8 ml/min) flow rates was approximately 17 %. The flow rate used in current dental treatments is typically set at 8 ml/min, and since both 2.8 ml/min and 8 ml/min produced comparable ablation efficiency, the remaining experiments were performed using flow rate of 8 ml/min.

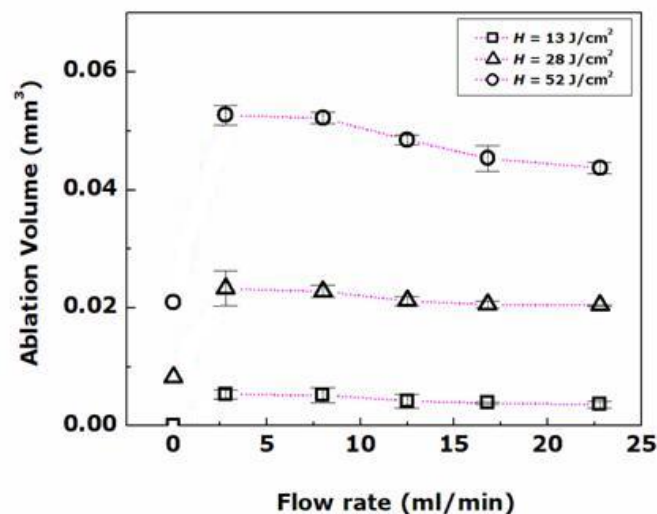


Figure 8.5. Comparison of ablation volume as a function of radiant exposure and water spray flow rate ($n = 3$)

8.4.3 ABLATION THRESHOLD

The threshold radiant exposure was obtained using *Probit* analysis. Ablation thresholds for dry and spray samples are shown in Figure 8.6. The thresholds for dry and spray conditions occurred at 1.2 J/cm^2 and 2.1 J/cm^2 respectively. Since water highly absorbs $2.79 \text{ }\mu\text{m}$ light, the radiant exposure at the sample was less than the ‘no spray’ radiant exposure.

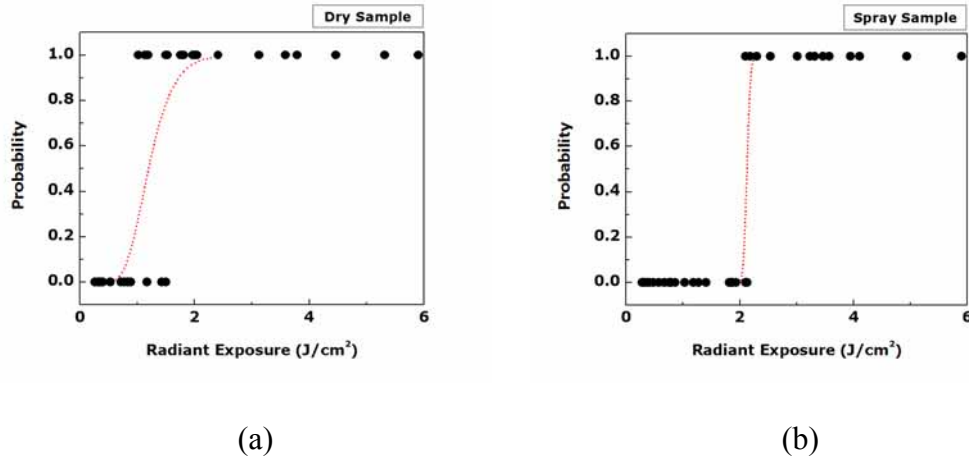


Figure 8.6. *Probit* curves of ablation thresholds for dental enamel under different sample conditions: (a) dry ($H_{th} = 1.2 \text{ J/cm}^2$) and (b) spray ($H_{th} = 2.1 \text{ J/cm}^2$) ($n = 33$ and flow rate = 8 ml/min)

8.4.4 TRANSMISSION MEASUREMENT

Since the spray ablation threshold was approximately 60 % higher than the dry case, energy transmission through the spray was determined. The transmitted radiant exposure was plotted as a function of incident radiant exposure (Figure

8.7). A linear relationship ($R^2 = 0.99$) was observed between the incident and transmitted radiant exposures; however, the onset of energy transmission did not occur until the incident radiant exposure reached at approximately 2 J/cm^2 . Therefore, we believe that 2 J/cm^2 is required to induce a vapor channel in the spray to deliver the remaining laser pulse. Material removal process was initiated beyond this threshold (Figure 8.6).

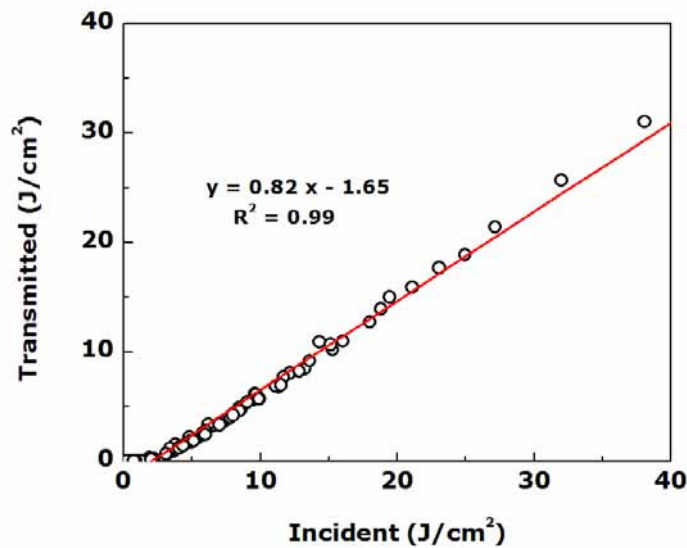


Figure 8.7. Energy transmission as a function of incident radiant exposure (flow rate = 8 ml/min)

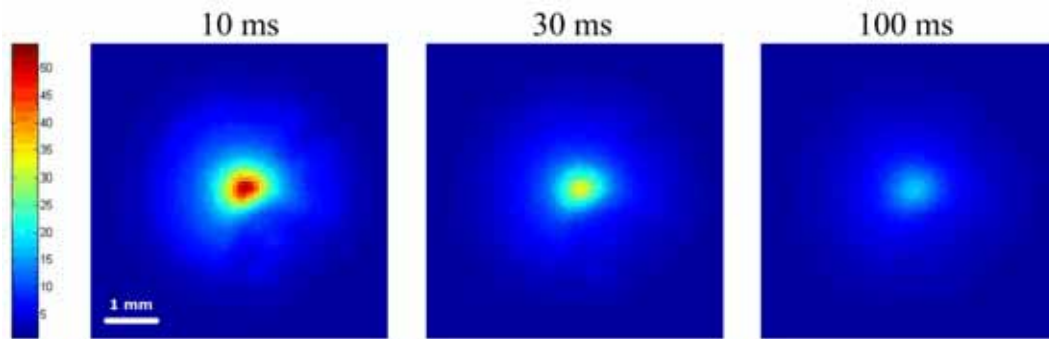
8.4.5 TEMPERATURE MEASUREMENT

To evaluate the effect of water spray on the thermal distribution, the transient 2-dimensional surface temperature induced by a single laser pulse was

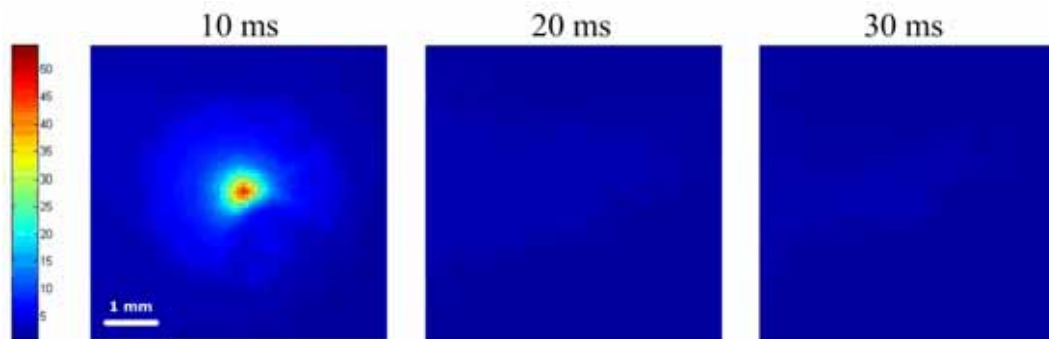
measured for the dry and spray cases. PMMA was chosen instead of dental tissue due to its higher damage threshold to test thermal convective motion of water spray during subablative radiant exposures. Thermal imaging (frame rate = 100 Hz) of both dry and spray cases was employed at 1.3 J/cm^2 and 3.6 J/cm^2 , respectively (Figure 8.8(a) and (b)). The water spray was not synchronized with the laser pulse to ensure the stabilization of spray flow rate (initiated and terminated three seconds pre and post pulse). The laser-induced temperature increase for dry condition was 51°C ; on the other hand, the spray condition temperature increase was only 40°C with higher radiant exposure than dry case. The laser-induced temperature increase of dental tissue would be lower due to the difference in PMMA and enamel optical/thermal properties. In Figure 8.8(a), the fiber tip was positioned in the center of the image, and the heat diffusion at the irradiated spot during dry ablation took longer than 100 ms with the presence of thermal damage on the surface. However, the spray condition initially showed lower temperature, followed by more rapid heat diffusion without any indication of collateral disruption, compared to dry condition (Figure 8.8(b)). As the time elapsed after the laser onset, the heat at the irradiated spot diffused out and at 20 ms, it completely disappeared on the image, which implied that the thermal diffusion caused by water spray cooling and dynamics of water flow possibly reduced heat accumulation time, leading to prevention of thermal damage.

8.4.6 ABLATION EFFICIENCY

In order to understand the role of water spray in enamel ablation, ablation performance for dry and spray cases was compared. Figure 8.9 shows top-view microscope and cross-sectional OCT images for both conditions. Dry and spray cases were irradiated with ten pulses at 38.7 J/cm^2 and 35.8 J/cm^2 per pulse, respectively. The dry sample had irregular surface deformation, charring, and randomly distributed peripheral cracks, which possibly indicated thermal injury due to excessive heat accumulation during/after laser irradiation (Figure 8.9(a)). Craters for spray samples were relatively clean without any indication of thermal damage. The crater width of spray-assisted ablation was wider than that of dry ablation (Figure 8.9). Dimensions of ablation craters for both dry and spray cases are compared in Figure 8.10. Ten pulses with various radiant exposures per pulse ranging from 3.4 to 51 J/cm^2 were applied to the enamel samples. Regardless of sample condition, ablation volume increased with radiant exposure. The volume induced by the spray ablation was up to twice larger than the dry condition. Although ablation threshold (surface disruption) for the dry condition occurred at 1.2 J/cm^2 (Figure 8.6(a)), the mass removal measured with the OCT system required 3.5 J/cm^2 .



(a) Dry



(b) Spray

Figure 8.8. Thermal images of heat diffusion measured by IR thermal camera during (b) dry ($H = 1.3 \text{ J/cm}^2$ and $\Delta T = 51 \text{ }^\circ\text{C}$) and (c) spray process ($H = 3.6 \text{ J/cm}^2$ and $\Delta T = 40 \text{ }^\circ\text{C}$) (Note that the flow rate was 8 ml/min. Temperature increase index is displayed in the far left column, and time elapsed after the onset of the $150 \text{ } \mu\text{s}$ laser pulse is shown above each image)

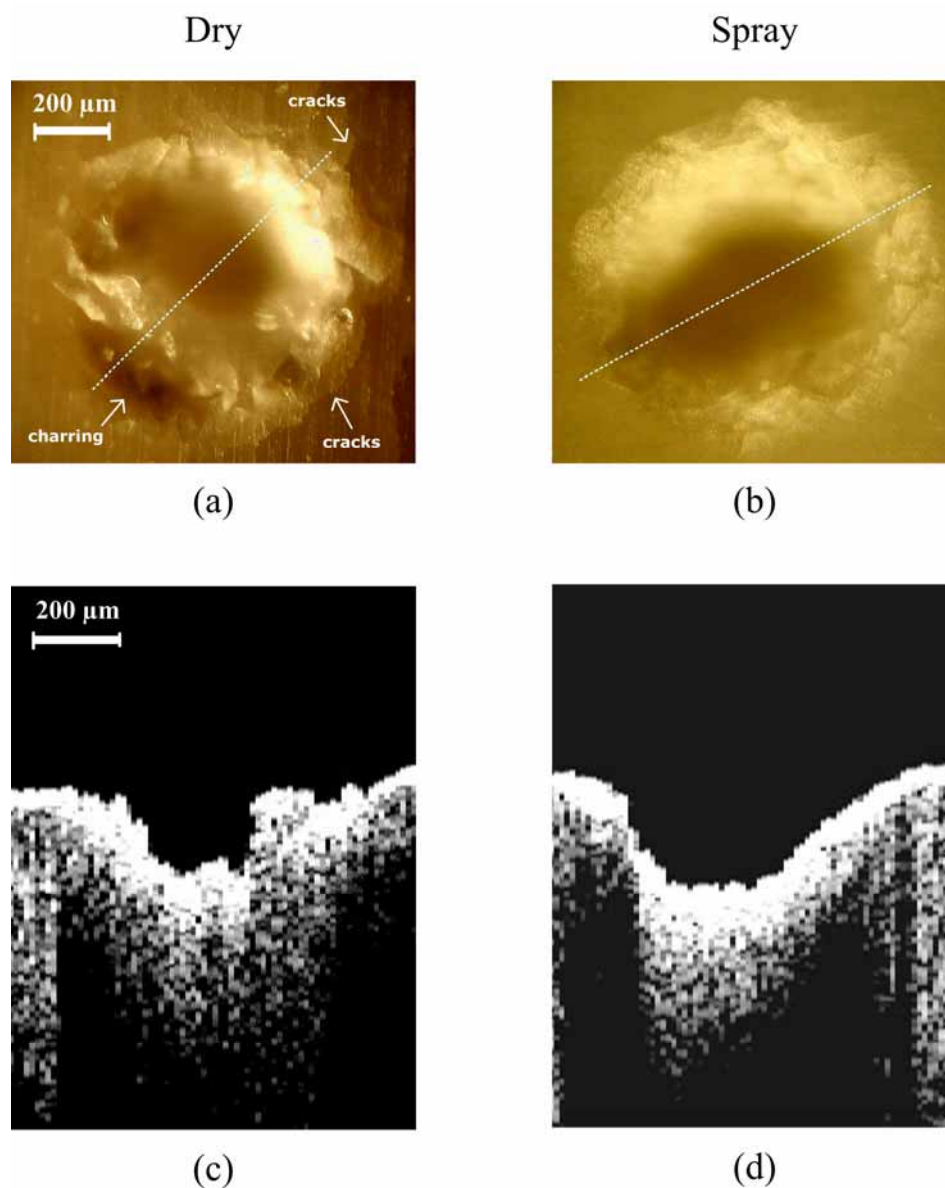


Figure 8.9. Top view ((a) and (b)) and cross-sectional OCT ((c) and (d)) images of enamel tissues ablated with ten pulses for dry ((a) and (c), $H = 38.7 \text{ J/cm}^2$ per pulse) and spray ablation ((b) and (d), $H = 35.8 \text{ J/cm}^2$ per pulse). Note that flow rate = 8 ml/min and each dotted line in (a) and (b) indicates a cross-section of the crater for OCT image.

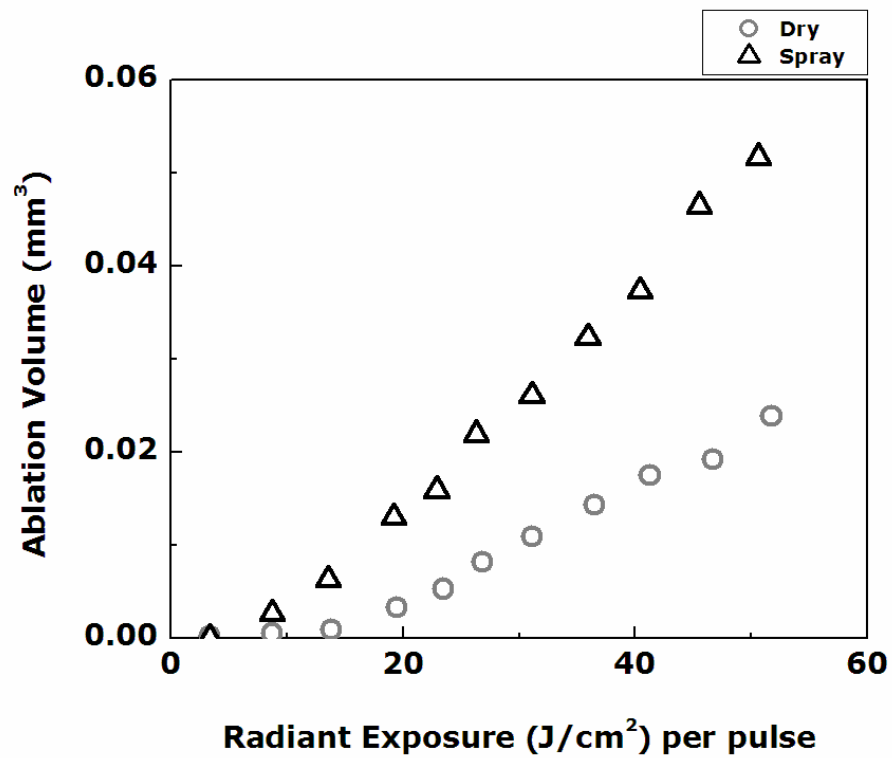


Figure 8.10. Comparison of ablation volume measured with OCT for dry and spray conditions as a function of radiant exposure with ten pulses (flow rate = 8 ml/min)

8.4.7 PRESSURE MEASUREMENTS

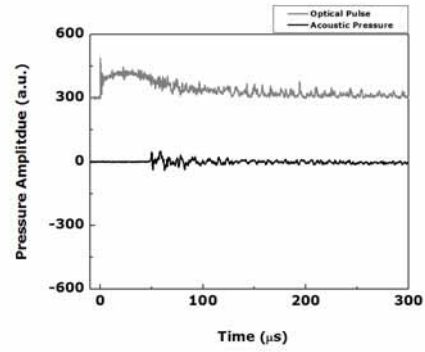
The signatures of acoustic transients during enamel ablation under dry and spray conditions were investigated at various radiant exposures. Typical traces, which were the average of ten signals at $H = 18.1 \text{ J/cm}^2$, of optical pulse and microphone signals for both cases are presented in Figure 8.11(a) and (b). Additionally, for the purpose of comparison, pressure measurements were performed during laser spray irradiation on a CaF_2 window (500 μm distance). This non ablative irradiation produced an acoustic emission induced by water vaporization (Figure 8.11(c)). For all three cases, the acoustic signals were generated approximately 45 μs after the beginning of the laser pulse. Since the speed of sound for air is 343 m/s at 20 °C [34], the propagation time of pressure wave through the distance (15 mm) between the sample surface and the microphone ensured a temporal delay between the onset of the laser pulse and the acoustic wave of 44 μs . The acoustic shapes of spray with and without ablation initially produced a bipolar wave with a peak amplitude higher than that of the dry ablation. In order to compare different acoustic signals, time window FFT analysis was performed on the initial part of the transducer signals (Figure 8.12) since the acoustic waves for the dry ablation were mainly generated during the first 50 μs of the signal. Two frequency spectra for the spray conditions with and without ablation were also compared in Figure 8.12(b). In general, the amplitude of the frequency spectra for the spray ablation was up to twenty times greater than

that for the dry case, possibly showing the enhanced ablation performance assisted by water spray. In addition, although the amplitude generated by the spray with no ablation was about three times greater than that of the spray ablation, the peak in the ablative spray spectrum at 80 kHz was relatively well correlated with the non ablative spray case (Figure 8.12(b)). Peak acoustic amplitudes for dry and spray conditions with a single pulse measured at 15 mm from the sample surface are compared at various radiant exposures in Figure 8.13. Spray ablation produced stronger pressure magnitudes than the dry ablation over the entire radiant exposures. The peak pressure amplitude of the spray case was found be six times greater than the dry condition. In Figure 8.13, the peak compressive stress (P_{peak}) for the dry case was curve-fitted by the following expression:

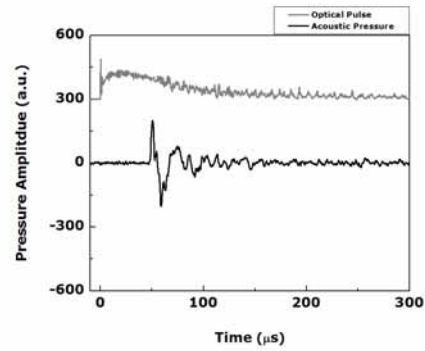
$$P_{peak} (Pa) = \Lambda \cdot (H - H_{th})^{2/3} \quad (8.1)$$

where Λ ($\text{kg}^{1/3} \cdot \text{cm}^{4/3} / \text{s}^{2/3} \cdot \text{m}^{7/3}$) is a arbitrary parameter for best fitting the given data, H (J/cm^2) is the incident radiant exposure (J/cm^2), and H_{th} (J/cm^2) is the dry ablation threshold of $1.2 \text{ J}/\text{cm}^2$. The equation represents a model of steady-state surface vaporization [35], based on the assumption that the pressure generated during plume expansion is proportional to the recoil stress exerted on the tissue. In case of spray ablation, additional pressure induced by rapid water vaporization along with the recoil stress could be coupled together into the target. Hence, the

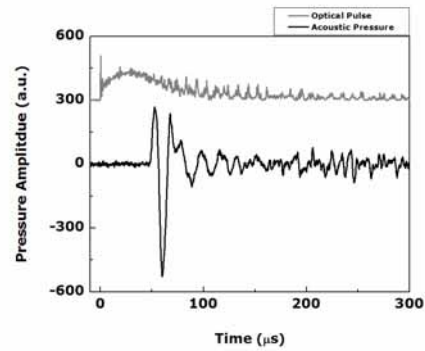
piezoelectric microphone performed a direct measurement of overall acoustic transients in the ablation process. It should also be noted that the actual pressure amplitude at the surface is much greater than the measured pressure due to wave propagation loss.



(a) Dry

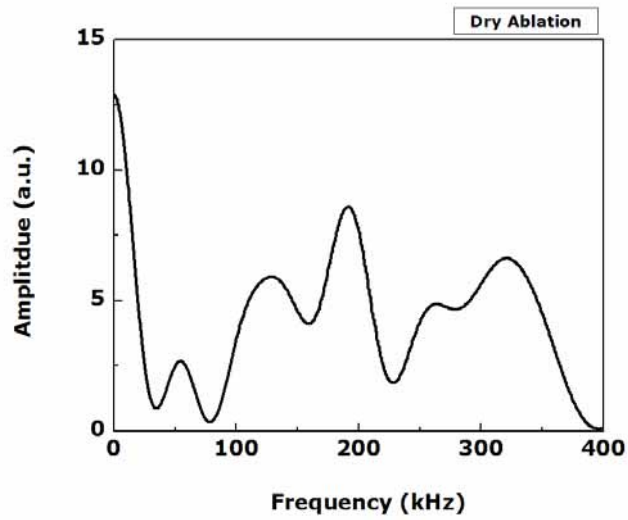


(b) Spray

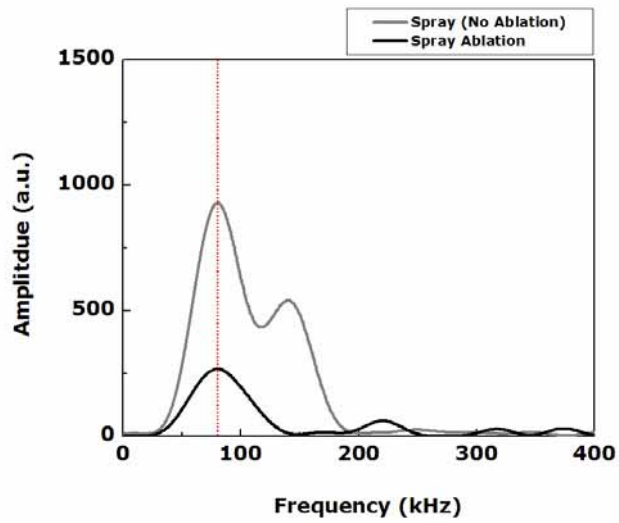


(c) Spray (no ablation)

Figure 8.11. Temporal behaviors of the Er,Cr:YSGG laser pulse (top) and the measured transient pressures (bottom) for (a) dry and (b) spray ablation from the enamel surface and for (c) spray (no ablation) from the glass surface. Note difference in scale. ($H = 18.1 \text{ J/cm}^2$, average of ten signals, and flow rate = 8 ml/min)



(a) Dry



(b) Spray

Figure 8.12. FFT analysis of acoustic signal for (a) dry and (b) spray ablation. In case of spray condition, the acoustic signal induced by the spray on a non ablative material is included for comparison. Note difference in scale. ($H = 18.1 \text{ J/cm}^2$, average of ten signals, and flow rate = 8 ml/min)

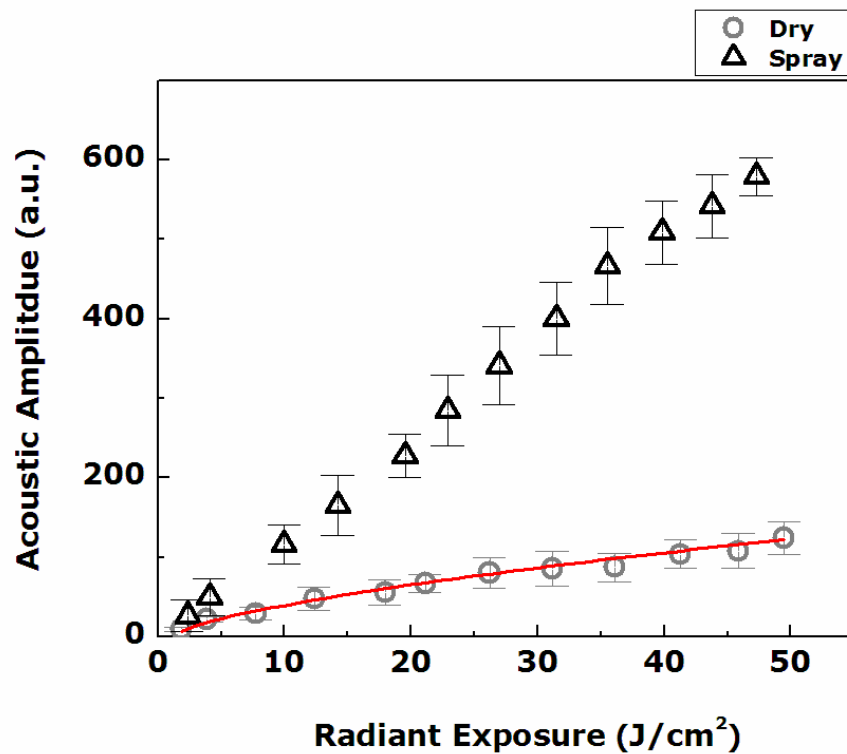
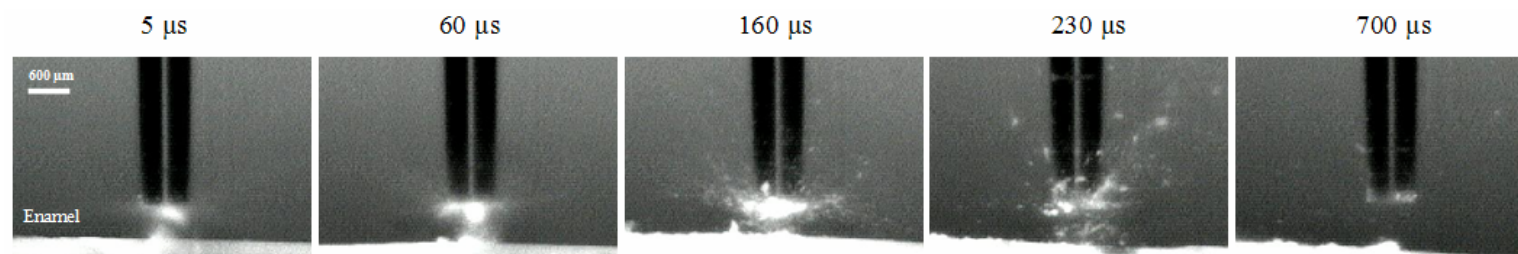


Figure 8.13. Comparison of acoustic amplitudes at 15 mm from the enamel sample surface for dry and spray cases as a function of radiant exposure with a single pulse ($n = 10$, initial radiant exposure = 3.5 J/cm^2 , and flow rate = 8 ml/min). The line through dry ablation was based upon a curve fit using equation 8.2.

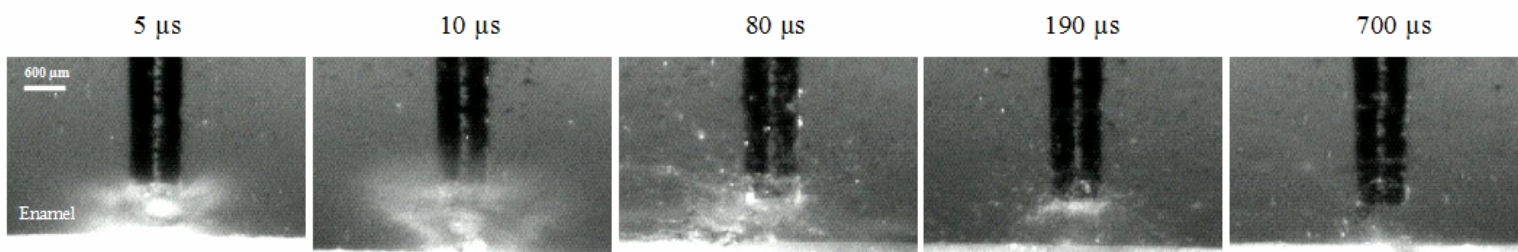
8.4.8 HIGH-SPEED IMAGING

To understand the dynamics of the ablation process for different conditions, fast flash images of enamel ablation were acquired with the Er,Cr:YSGG laser at the radiant exposure of 32.5 J/cm^2 . Figure 8.14 presents a sequence of material removal for the dry and spray conditions. In case of the dry sample, an ablation plume was initially visible $5 \mu\text{s}$ after the onset of the laser pulse. The remainder of the laser pulse passed through the plume. $230 \mu\text{s}$ after the onset of the laser pulse, most of the ejected mass was removed from the beam path between fiber tip and sample, and at $700 \mu\text{s}$, no remaining debris was observed. The dry ablation produced a prolonged ‘flash’ in the beam path, which lasted up to $500 \mu\text{s}$, long after the Er,Cr:YSGG laser pulse ended. This whitish ‘glow’ possibly resulted from strong interaction between the incident laser pulse and debris in air and/or violent chemical decomposition. The chemical decomposition might have released sufficient energy to induce the prolonged glow long after the end of the laser pulse. On the other hand, the spray ablation initially showed violent water explosion with glow formation over the enamel surface $5 \mu\text{s}$ after the laser onset. The rapid expansion of water vaporization proceeded for up to $50 \mu\text{s}$, and the glow lasted for approximately $30 \mu\text{s}$, which was much shorter than that the dry case. Unlike the dry case, any distinctive plume ejection/propagation was hardly observed around fiber tip $150 \mu\text{s}$ after the laser onset although water vapors possibly interrupted clear imaging of dynamics

of the ablation plume. From the time-resolved photographs, it was noted that the spray ablation initiated water vaporization as well as enamel ablation, and compared to the dry condition, water spray flow/water vaporization rapidly washed away ablation plume and reduced the sustaining time of the glow that could be involved in fiber damage and thermal effects to peripheral tissue.



(a) Dry



(b) Spray

Figure 8.14. Compilation of enamel ablation process for (a) dry and (b) spray conditions. Note that the radiant exposure was 32.5 J/cm^2 . Time elapsed after the onset of the $150 \mu\text{s}$ laser pulse is shown above each image.

8.5 DISCUSSION

Laser ablation data as a function of radiant exposure for a single and a sequence of ten pulses were analyzed for dry and spray conditions. Tests using spray indicated maximum material removal for flow rates between 2.8 ml/min and 8 ml/min (Figure 8.5). The volume of enamel removed using water spray with the laser pulses was up to twice greater than dry condition. The fine, dusty, emulsified plume formation depicted in the time-resolved images (Figure 8.14(a)) was supportive of a photothermal process during dry ablation while spray ablation was subject to explosive liquid vaporization with augmented pressure which indicated hydro-photothermal and hydro-mechanical effects (Figures 8.13 and 8.14(b)). Hydro-photothermal effects are produced as a result of rapid vaporization of water spray while the hydro-mechanical effects are the result of a combination of processes such as acoustic emission during explosive liquid vaporization and interstitial water expansion, surface effects of shear stress on the crater wall, and liquid-jet formation during microbubble collapses near a surface. Single pulse ablation thresholds for dry and spray cases were 1.2 J/cm^2 and 2.1 J/cm^2 , respectively. Transmission loss caused by absorption of a portion of the laser energy by the spray increased the ablation threshold of the spray condition (Figure 8.7). Spray-assisted ablation significantly reduced heat diffusion time with less temperature increase, compared to dry ablation (Figure 8.8).

Water film or spray-assisted laser ablation has been investigated previously [14,16,18,20,21,24]. The water spray increased ablation efficiency up to twice greater than dry ablation via rapid water vaporization imparting an ablative momentum to the sample surface (termed the “hydrokinetic effect” [14]). The impact momentum induced substantial mechanical ablation on the target surface, subsequently removing ablation debris and undesirable non-apatite calcium phosphate phases. [20,36]

In this study, it was determined that the minimum radiant exposure necessary to create a vapor channel through water spray was 2 J/cm^2 in our experiments (Figure 8.7). The channel provides an open path for delivery of part of the pulse energy. This minimum delivery dose is undoubtedly influenced by the experimental situation, but it illustrates that the entire laser pulse does not reach the target. A previous study showed that the direct irradiance of the sample in water environment was allowed only through a laser-induced vapor channel (the “Moses effect”) [37]. The absorption coefficient (μ_a) of Er,Cr:YSGG laser wavelength in water is 5300 cm^{-1} (shown in Table 8.1), which corresponds to the $1/e$ light penetration depth ($\delta = 1/\mu_a$) of $2 \text{ }\mu\text{m}$ according to Beer’s Law [38]. Figure 8.15 shows an image of the Er,Cr:YSGG laser-induced vapor channel of maximum depth in water at $90 \text{ }\mu\text{s}$ after the onset of the laser pulse resulting from a radiant exposure of $H = 1.8 \text{ J/cm}^2$. According to partial vaporization theory, the formation of small vapor nucleation bubbles initially occurs at nucleation sites in

front of the fiber tip, and these bubblets coalesce to form a vapor channel through rapid expansion of individual bubblets produced by the remaining portion of the laser pulse [39,40]; according to the image, the cone shaped vapor channel produced with a radiant exposure of 1.8 J/cm^2 is approximately $500 \text{ }\mu\text{m}$ in depth (Figure 8.15). In case of spray ablation, the vapor channel produced at ablation threshold should be at least $500 \text{ }\mu\text{m}$ in depth, which is in accordance to the time-resolved photograph image. Since the density of water was 1602 times greater than that of vapor (at $100 \text{ }^\circ\text{C}$, $\rho_{\text{water}} = 958 \text{ kg/m}^3$ and $\rho_{\text{vapor}} = 0.598 \text{ kg/m}^3$), the absorption coefficient of vapor decreased to approximately 3.3 cm^{-1} [29,37]; consequently, laser energy was transmitted to the exposed enamel surface through the water vapor channel. Furthermore, the initial surface deformation during spray ablation occurred at 2.1 J/cm^2 , which was slightly above the radiant exposure of 2 J/cm^2 required for energy transmission.

Laser-induced ablation with a pulse duration longer than $100 \text{ }\mu\text{s}$ and no water spray produced acoustic pressure through transient heating and ablative recoil during material ejection. A previous study reported that during the material vaporization phase, the expansion of vapor plume generated acoustic waves correlated to the intensity of spikes from the laser pulse [41]. Upon the inception of material ejection, a strong bipolar acoustic transient was produced [42], and later, the ensuing material ejection was responsible for smaller and irregular fluctuations of the acoustic signal amplitude. Several studies used a microphone

to quantitatively measure the acoustic waves [43-45]. Laser-induced stress generated in tissue was correlated to the pressure wave measured with a piezoelectric microphone that was coupled into the surrounding air, showing that the acoustic transients coupled into the air medium were proportional to acoustic waves measured in the tissue. Amplitudes were different due to the acoustic impedance at the air-tissue interface [46].

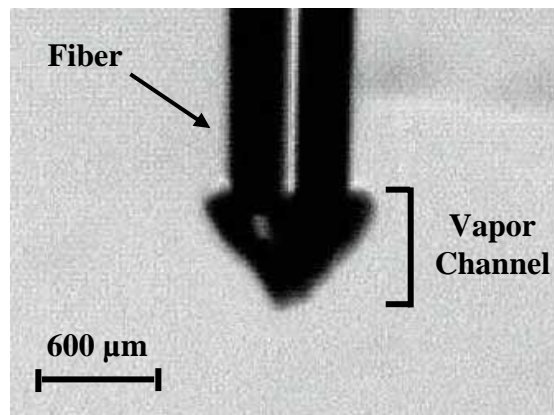


Figure 8.15. A time-resolved photograph of a laser-induced vapor channel in water at 90 μs after the onset of laser pulse ($H = 1.8 \text{ J/cm}^2$)

Dry Ablation

For laser pulses longer than 100 μs , material removal occurred concomitantly with laser irradiation. In the case of dry ablation, the initial part of laser pulse corresponded to the generation of a pressure pulse, indicating the onset of ablation event (Figure 8.11(a)). The thermal diffusion time (τ_{th}) for enamel within the 150 μs laser pulse was calculated, using the following equation:

$$\tau_{th} = \frac{\delta^2}{4\alpha} \approx 155 \mu\text{s} \quad \text{when } \delta \ll \text{spot size} \quad (8.2)$$

where α is the thermal diffusivity ($4 \times 10^{-7} \text{ m}^2/\text{s}$ for enamel [47]). Since the pulse duration ($\tau_p \sim 150 \mu\text{s}$) was slightly shorter than the thermal diffusion time ($\tau_{th} = 155 \mu\text{s}$), Er,Cr:YSGG laser ablation of desiccated enamel tissue was a surface-mediated process [35]. Upon laser irradiation, a layer of high temperature and pressure plume gas began to expand rapidly along with the formation of a shock front emanating from the surface. By applying the laws of conservation of mass, momentum, and energy, the peak pressure (P_{peak}) in the expanding vapor plume was expressed as

$$P_{peak} = \left\{ \left[\frac{\gamma_1(\gamma_1 + 1)P_a}{2} \right]^{1/2} \left[\frac{(\gamma_2 - 1)E_0}{c_1\gamma_2} \right] \right\}^{2/3} \quad (8.3)$$

where P_a is the ambient pressure (Pa), γ_1 and γ_2 are the ratio of specific heats in ambient air and vapor plume respectively, c_1 is the speed of sound in the

surrounding air (m/s), and E_0 is the laser irradiance (W/m^2). Using the differentiation $E_0 = H/\tau_p$ and assuming that the ablation threshold was required to initiate material ejection, which was subtracted from the applied radiant exposure, Equation 8.4 became Equation 8.2 introducing the arbitrary parameter Λ . This parameter represented the fraction of the acoustic energy being coupled into the transducer and had to satisfy the condition [35]:

$$\Lambda \leq \left\{ \left[\frac{\gamma_1(\gamma_1 + 1)P_a}{2} \right]^{1/2} \left[\frac{(\gamma_2 - 1)}{c_1\gamma_2\tau_p} \right] \right\}^{2/3} \quad (8.4)$$

According to Figure 8.13, measured peak pressures for dry ablation followed the curve provided by Equation 8.2 using $H_{th} = 1.2 \text{ J}/\text{cm}^2$. This suggests that dry ablation is a steady-state surface vaporization process. Since the dry sample was desiccated prior to experimentation, we would not expect internal explosion of interstitial water in the enamel to be the dominant ablation mechanism(s). However, heating of the material does produce stress. The acoustic transients during material removal for dry case were mainly attributed to recoil stress induced by plume ejection.

Spray Enhanced Ablation

In contrast to the dry case, the initial pressure signature for spray ablation was a bipolar wave over $20 \mu\text{s}$ (Figure 8.11(b)) with about six times greater peak

pressure amplitudes (Figure 8.13), which increased rather linearly with the radiant exposure over the range of exposures tested. FFT analysis of the data in Figure 8.11(b) and (c) demonstrated a correlation of frequency spectrum at 80 kHz between spray (no ablation) and spray ablation along with higher magnitude than dry ablation (Figure 8.12). In addition, due to overall larger compressive and tensile waves (shown in Figure 8.11(c)), the spray (no ablation) showed about three times greater amplitude of the FFT analysis than the spray ablation (Figure 8.12(b)).

According to the image of water vaporization shown in Figure 8.14, the spray ablation process associated with higher acoustic amplitude can be explained by a phase explosion of water spray [48]. In the absence of stress confinement because of the long laser pulse duration [49], once the temperature reaches the spinodal limit ($T_s = 290\text{ }^{\circ}\text{C}$), a phase change with water expansion through vaporization eventually occurs. Absorption of the laser beam increases the water temperature possibly beyond its equilibrium saturation temperature, causing the liquid water to become superheated. Due to heat diffusion and the deflection of the beam near the critical point, the temperature becomes homogeneously distributed; therefore, a partial vaporization as saturated vapor and liquid separated from metastable liquid can be initiated. The occurrence of rapid water expansion through a rapid vaporization process is accompanied by large pressure transients [50], which can be characterized by a bipolar shape with a leading

positive compression wave and a trailing negative rarefaction wave (Figure 8.11(b)). The Schlieren images in Figure 8.14(b) show the onset of rapid vaporization of water near the target surface and in the beam path occurred at 5 μ s after the onset of the pulse. The rapid water vaporization process produces an N-shape wave with spherical propagation because an acoustic wave caused by the explosion experiences phase inversion due to the mechanics of acoustic source expanding and collapsing [34]. In comparison with nanosecond laser pulses, the type of pulse used in this study is capable of providing thermal confinement but no stress confinement. As a result of the 150 μ s free-running laser pulse, the pressure induced from rapid vaporization with thermal confinement is responsible for the pressure measured in Figure 8.11(b). Therefore, strong acoustic transients during rapid water vaporization exert a significant abrasive force upon the enamel surface, leading to augmented pressure amplitudes and ablation performance.

Since the discrepancy between the spray ablation threshold and the threshold radiant exposure for energy transmission was $H = 0.1 \text{ J/cm}^2$, the temperature increase (ΔT) of water contained in the enamel by this radiant exposure difference was roughly estimated using the following equation [48]:

$$\Delta T = \frac{\mu_a H}{\rho_{water} c_v} \quad (8.5)$$

where μ_a is the absorption coefficient (5300 cm⁻¹ for water at 2.79 μm as shown in Table 8.1), ρ_{water} is the density (996 kg/m³ at 25 °C for water), and c_v is the specific heat capacity at constant volume (4178 J/kg·K at 25 °C for water). The calculated temperature rise was approximately 127 °C, which is higher than water boiling point, so during spray ablation, the internal explosion of interstitial water could be partially responsible for higher pressure amplitude.

Previous studies show that during vapor bubble collapse in the vicinity of a surface in terms of ablation process, a high-speed, wall-directed reentrant jet can be initiated in the bubbles, and the liquid jet formation with outward radial flow can provide additional mechanical impact (termed the “water hammer pressure”) on the sample [51]. The impact pressure of this jet can be given by

$$P_{\text{imp}} = \rho_{\text{water}} c_{\text{water}} v_{\text{jet}} \cdot \frac{\rho_{\text{enamel}} c_{\text{enamel}}}{\rho_{\text{water}} c_{\text{water}} + \rho_{\text{enamel}} c_{\text{enamel}}} \approx \rho_{\text{water}} c_{\text{water}} v_{\text{jet}} \quad (8.6)$$

where ρ_{water} and ρ_{enamel} are density and c_{water} and c_{enamel} are the speed of sound for water and enamel, respectively ($\rho_{\text{water}} = 998 \text{ kg/m}^3$ and $c_{\text{water}} = 1481 \text{ m/s}$ [34]). If the liquid-jet velocity v_{jet} near a rigid boundary is assumed to 80 m/s based on a previous study [52], the computed impact pressure is 120 MPa, which exceeds the fracture toughness of enamel, shown in Table 8.1. With the formation of a water layer during water spray propagation, micro-bubbles can potentially be generated inside the layer during/after laser ablation; consequently, although the impact

pressure is dependent of bubble-size and rate of energy deposition, the collapse of potential micro-bubbles could very much contribute to acoustic enhancement (Figure 8.13). However, in order to initiate bubble formation, the water layer on top of the enamel should be thicker than a critical size required for bubble inception. Hence, further investigations on water film and micro-bubble formation needs to be performed to evaluate the effect of liquid-jet formation on spray enamel ablation with a laser.

Due to the conservation of momentum and energy, the acoustic energy measured by the microphone for the spray condition combines the effects of (1) rapid water vaporization, (2) recoil stress during material ejection, (3) micro-explosion due to the rapid expansion of water inside the tissue, and (4) liquid-jet impact; the total measured pressure could proportionally correspond to an integration of acoustic excitations coupled into the sample during/after spray ablation. The measured pressure amplitudes undoubtedly deviated from real values owing to poor acoustic matching of the air medium and nonlinearity of wave propagation during plume ejection; nevertheless, the acoustic stresses recorded in air should still reveal valuable information about dynamic behavior of enamel ablation in terms of the application of water spray. In Figure 8.12(b), it was observed that the magnitude of the spray (no ablation) in the frequency domain was higher than that of the spray ablation in spite of the comparable acoustic impedances for enamel tissue and window ($Z_{enamel} = 13.3 \times 10^6 \text{ kg/m}^2\text{s}$

and $Z_{window} = 12.9 \times 10^6 \text{ kg/m}^2\text{s}$, respectively [28,34]). During the spray ablation, plume ejection and water vaporization associated with the turbulent flow in the ablated site possibly caused variations in enamel density and, hence, acoustic impedance. Therefore, the change of the acoustic impedance during the spray ablation resulted in less wave reflection at the air-tissue interface along with weaker initial tensile amplitude than the non ablative spray case (Figure 8.11(b) and (c)). However, the comparable dominant frequency (80 kHz) for both spray (no ablation) and spray ablation implied that the laser-induced water vaporization played a significant role in augmenting the acoustic pressure, which possibly contributed to improvement of ablation performance as an additional mechanical impact (Figures 8.10 and 8.11). Therefore, a combination of explosive water vaporization (abrasive effect), material ejection with recoil stress, micro-explosion due to rapid water expansion, and jet formation during spray enamel ablation can be responsible for the augmentation of peak acoustic amplitude with longer pressure durations, resulting in the pronounced ablation efficiency (Figures 8.10 and 8.13).

Ablation Volume

As laser-induced ablation concurrently commences during the 150 μs laser pulse, steady-state models are valid for ablation performance in terms of radiant exposures well above the threshold (H_{th}). Thus, once the threshold is exceeded,

Hibst *et al.* [26] and Vogel *et al.* [48] describe a linear dependence of the ablated crater depth (d) on incident radiant exposure (H) as follows:

$$d = \frac{H - H_{th}}{h_{abl}} \quad (8.7)$$

where h_{abl} is the energy required for ablation per unit volume (J/cm^3). In our experiments, Figure 8.10 shows a linear relationship between ablation volume and the applied radiant exposures above the threshold. In the case of dry ablation, the linear relation appeared at the radiant exposure ($\geq 14 \text{ J}/\text{cm}^2$), and relatively poor ablation efficiency took place because of debris shielding [48]. During the laser pulse, debris in the beam path absorbed and scattered the incident laser light which produced a hot or whitish “glow” (Figure 8.14(a)). Thus, it is expected that the part of the laser pulse reaching the tissue surface decreases with decreasing ablation efficiency, and with multiple pulses, more shielding effects take place in the deeper craters. The amount of debris shielding is determined by the absorption coefficient and plume density. As for the quality of laser ablation, the desiccated sample created irregular and rough crater contours (Figure 8.9(a) and (c)). The spatial beam distribution of the Er,Cr:YSGG (Figure 8.4) is considered to be partially responsible for the crater shape. The randomly located high intensity spots around the peak intensity induce an inhomogeneous temperature

distribution with local centers of vaporization, leading to uneven bulky material removal and irregular crater shape.

Spray ablation demonstrated about twice larger ablation volume at tested radiant exposures with wider truncated-cone shape, and a linear relationship between the applied radiant exposure and volume was shown in Figure 8.10. The V-formed shape of the crater after applying ten successive pulses into the same crater (shown in Figure 8.9(d)) may be a result of spray water flowing into the crater between consecutive laser pulses [53]. With high intensity of the laser pulse during water spray, vaporization of water in the existing crater generates a vapor channel. The laser-induced pressure during water vaporization pushes the water out radially and up along the crater wall [54]; shear stress is exerted on the crater wall, resulting in more material removal. However, the effect of shear stress needs to be theoretically and experimentally evaluated in the future study. The water flow also removes debris (plume cleaning effect) and cools the surface. Therefore, the spray-assisted cutting creates a V-form without any thermal damage of the peripheral tissue and with increasing ablation volume, compared to the dry case. The expansion of water vapor inside the crater during multiple pulses possibly induces an additional mechanical tearing, leading to the enhanced ablation performance. Moreover, the wide and relatively uniform crater shape can be attributed to the theory of light scattering by small water particulates during laser irradiation [21]. When a laser beam strikes, scattering is produced as

a result of the small water droplets (scatterers) causing the photons to be scattered and/or absorbed by the scatterers. The laser light can be scattered preferentially in all directions (water particulate smaller than laser wavelength) or in the forward direction (water particulate larger than the wavelength). Although the diameter of the spray water droplet could not be evaluated in our experiment, the wider crater shape of spray ablation (Figure 8.9(d)) includes the effect of light scattering during laser-water interaction.

Spray Cooling Effect

In Figure 8.8, the spray ablation showed rapid heat diffusion with less temperature variation, indicating effect of water cooling. Since the thermal conductivity of water is approximately 30 times greater than that of air (0.0267 W/m·K), more thermal energy was possibly transferred to the spray, cooling the enamel surface via vaporization and convection processes. Figure 8.14(b) shows that due to the cooling effect of the spray, the glow in the beam path lasted for about 30 μ s, which was much shorter than for the dry condition. According to temperature measurements in Figure 8.8, one can roughly estimate the temperature increase in the water spray to reduce the heat in the PMMA. 10 ms after a single pulse irradiation at $H = 3.6 \text{ J/cm}^2$, the sample weighing 1 mg induced a temperature increase of 40 °C (Figure 8.8(b)). With a specific heat of 1466 J/kg·K [55], the PMMA acquired an energy rate (E) of approximately 6 J/s.

Since the heat flux was from the target to the flowing water (Figure 8.8), the water remained at room temperature. Provided that the calculated energy rate of $E = 6 \text{ J/s}$ was convected by the water from the PMMA, the temperature rise (ΔT) in the water spray can be approximated [17] from

$$E = \rho_{\text{water}} c_v V \Delta T \quad (8.8)$$

where ρ_{water} is the density of water ($= 996 \text{ kg/m}^3$ at $25 \text{ }^\circ\text{C}$) and c_v is the specific heat of water ($\approx 4180 \text{ J/kg}\cdot\text{K}$). For a volume flow rate (V) of 8 ml/min , the temperature increase in the water is calculated about $11 \text{ }^\circ\text{C}$, which could be required for convective cooling of the PMMA sample. These calculations are all based on heat transfer without considering the fact that during the ablation process, the entire volume of tissue above ablation threshold is ejected together with the heat deposited during the process. In this case, the calculations presented that the effect of water as a coolant are not entirely representative of the residual heat transferred to adjacent tissues during ablation. Thus, even if the value is not based on an exact energy balance, it may infer that considerable cooling of the enamel is achieved with relatively small temperature increase in the spray. Although Figure 8.8(b) shows the temperature distribution under spray condition, IR camera imaging depth should be deeper than thickness of the water layer on top of the sample surface to provide information on temperature increase during spray ablation. Hence, additional investigations on thickness of the water layer

during spray application should be performed. In addition, RizoIU *et al.* measured *in vivo* pulpal temperature changes in beagle dog cuspid by using thermocouples [19]. According to their results, the dry case increased the temperature up to 14 °C while the spray case induced a 2–3 °C drop in temperature instead. Since irreversible damage to tooth pulpal tissue is initiated with pulpal temperature in excess of 5.5 °C [17,19], it is correct to consider that the application of water spray is thermally safe for tooth enamel ablation without any adverse temperature effect on the dental pulp (Figure 8.9(b)).

8.6 CONCLUSION

Dental enamel tissue ablation using a free-running Er,Cr:YSGG laser assisted by water spray was the main goal of this study. The application of water spray demonstrated an increase in ablation volume up to twice with about a six times higher peak acoustic amplitude when compared to ablation without the spray. The enhanced ablation efficiency was associated with rapid water vaporization, material ejection with recoil stress, interstitial water explosion, and liquid-jet formation. On the other hand, dry ablation was a surface-mediated ablation process associated with acoustic transients mainly induced by recoil stress during plume ejection. In addition, unlike the dry ablation, a wide and truncated-cone crater shape was produced by spray ablation due to water flow expulsion and light scattering by water particulates. High thermal conductivity of

water and the exothermic nature of the vaporization process were attributed to the low temperature increase and heat accumulation in the tissue. Although under spray ablation conditions, the energy applied was reduced because of the reduction in transmission efficiency and higher ablation threshold occurred due to absorption in the water spray, the spray ablation compensated for the drawbacks by the enhanced mechanical effects along with water cooling, leading to the augmentation of enamel ablation efficiency; therefore, as a safe and efficient modality, the spray-assisted ablation can provide significant beneficial effects for caries removal, cavity preparation, and placement of restorative dental materials in dental treatment.

8.7 REFERENCES

1. Stern RH, Sognnaes RF, Goodman F. Laser effect on in vitro enamel permeability and solubility. *J Am Dent Assoc* 1966;78:838-843.
2. Stern RH, Vahl J, Sognnaes RF. Ultra structural observations of pulsed carbon dioxide laser effects. *J Dent Res* 1972;51:455-460.
3. Quintana E, Marques F, Roca I, Torres V, Salgado J. Some morphologic changes induced by Nd:YAG laser on the noncoated enamel surface: A scanning electron microscopy study. *Lasers Surg Med* 1992;12:131-136.
4. Altschuler G, Belikov A, Erofeev A. Human tooth enamel and dentin damage by holmium laser radiation. *SPIE Proc* 1992;1643:454-463.
5. Burkes EJ, Hoke J, Gomes E, Wolbarsht M. Wet versus dry enamel ablation by Er:YAG laser. *J Prosthet Dent* 1992;67:847-851.
6. Neev J, Pham K, Lee JP, White JM. Dentin ablation with three infrared lasers. *Lasers Surg Med* 1996;18:121-128.
7. Curzon MEJ, Featherstone JDB. *Handbook of Experimental Aspects of Oral Biochemistry*. Boca Raton: CRC Press, 1983.
8. Apel C, Meister J, Ioana RS, R F., P H., N G. The Ablation Threshold of Er:YAG and Er:YSGG Laser Radiation in Dental Enamel. *Lasers Med Sci* 2002;17:246-252.

9. Walsh JT J., Deutsch TF. Er:YAG ablation of tissue: Measurement of ablation rates. *Lasers Surg Med* 1989;9:327-337.
10. Izatt JA, Albagli D, Itzdan I, Feld MS. Pulsed laser ablation of calcified tissue: physical mechanisms and fundamental parameters. *SPIE Proc* 1990;1202:133-140.
11. Li Z, Code J, Van de Merwe. Er:YAG laser ablation rate at various fluences and pulse repetition rates. *Lasers Surg Med* 1992;126:625-630.
12. Hibst R, Keller U. Mechanism of Er:YAG laser induced ablation of dental hard substances. *SPIE Proc* 1993;1880:156-162.
13. Farrar SR, Attril DC, Dickinson MR, King TA, Blinkhorn AS. Etch rate and spectroscopic ablation studies of Er:YAG laser-irradiated dentine. *Appl Opt* 1997;36:5641-5646.
14. Rizioiu IM, DeShazer L. New laser-matter interaction concept to enhance hard tissue cutting efficiency. *SPIE Proc* 1994;2134A:309-317.
15. Wigdor H, Visuri SR, Walsh JT J. Effect of Water on Dental Material Ablation of the Er:YAG laser. *SPIE Proc* 1994;2128:267-272.
16. Rizioiu I, Kimmel AI, Eversole LR. The effects of an Er,Cr:YSGG laser on canine oral hard tissues. *SPIE Proc* 1996;2922:74-83.
17. Visuri SR, Walsh JT J., Wigdor HA. Erbium Laser Ablation of Dental Hard Tissue: Effect of Water Cooling. *Lasers Surg Med* 1996;18:294-300.
18. Majarson B, Sustercic D, Lukač M. Influence of water spray on Er:YAG ablation of hard dental tissues. *SPIE Proc* 1997;3192:82-87.
19. Rizioiu I, Kohanghadosh F, Kimmel AI, Eversole LR. Pulpal thermal responses to an erbium, chromium:YSGG pulsed laser hydrokinetic system. *Oral Surg Oral Med Oral Pathol Oral Radiol Endod* 1998;86:220-223.
20. Fried D, Ashouri N, Breunig T, Shori R. Mechanism of Water Augmentation During IR Laser Ablation of Dental Enamel. *Lasers Surg Med* 2002;31:186-193.
21. Freiberg RJ, Cozean C. Pulsed erbium laser ablation of hard dental tissue: the effects of atomized water spray vs water surface film. *SPIE Proc* 2002;4610:74-84.
22. Staninec M, Xie J, Le CQ, Fried D. Influence of an Optically Thick Water Layer on the Bond-Strength of Composite Resin to Dental Enamel After IR Laser Ablation. *Lasers Surg Med* 2003;33:264-269.
23. Altshuler G, Belicov A. Laser abrasive method of hard tissue removal. *Lasers Surg Med* 1999;11:10-11.
24. Stock K, Hibst R, Keller U. Comparison of Er:YAG and Er:YSGG Laser Ablation of Dental Hard Tissues. *SPIE Proc* 1997;3192:88-95.
25. Hossain M, Nakamura Y, Yamada Y, Kimura Y, Matsumoto N, Matsumoto K. Effects of Er,Cr:YSGG Laser Irradiation in Human Enamel

- and Dentin: Ablation and Morphological Studies. *J Clin Laser Med Sur* 1999;17:155-159.
26. Hibst R, Keller U. Er:YAG laser for dentistry: basics, actual questions, and perspectives. *SPIE Proc* 1994;2327:76-86.
 27. Kuroda S, Fowler BO. Compositional, structural, and phase changes in in vitro laser-irradiated human tooth enamel. *Calcif Tissue Int* 1984;36:361-369.
 28. Duck FA. Physical properties of tissue: a comprehensive reference book. London: Academic Press, 1991.
 29. Mills AF. Basic heat and mass transfer. London: Prentice-Hall, Inc., 1999.
 30. Hassan R, Caputo AA, Bunshah RF. Fracture Toughness of Human Enamel. *J Dent Res* 1981;60:820-827.
 31. CP Cain, GD Noojin, L Manning. A Comparison of various probit methods for analyzing yes/no data on a log scale. USAF Armstrong Lab, Tech Rep AL/OE-TR-1996-0102 1996;
 32. Huang D, Swanson EA, Lin CP, Schuman JS, Stinson WG, Chang W, Hee MR, Flotte TJ, Gregory K, Puliafito CA, Fujimoto JG. Optical coherence tomography. *Science* 1991;254:1178-1181.
 33. Izatt JA, Kulkarni MD, Yazdanfar S, Barton JK, Welch AJ. In vivo bidirectional color doppler flow imaging of picoliter blood volumes using optical coherence tomography. *Opt Lett* 1997;22:1439-1441.
 34. Blackstock DT. Fundamentals of physical acoustics. New York: John Wiley & Son, Inc., 2000.
 35. Venugopalan V, Nishioka NS, Mikic BB. The Thermodynamic Response of Soft Biological Tissues to Pulsed Ultraviolet Laser Irradiation. *Biophys J* 1995;69:1259-1271.
 36. Altschuler GB, Belikov AV, Sinelnik YA. A Laser-Abrasive Method for the Cutting of Enamel and Dentin. *Lasers Surg Med* 2001;28:435-444.
 37. Chan KF, Vassar GJ, Pfefer TJ, Teichman JMH, Glickman RD, Weintraub ST, Welch AJ. Holmium:YAG Laser Lithotripsy: A Dominant Photothermal Ablative Mechanism With Chemical Decomposition of Urinary Calculi. *Lasers Surg Med* 1999;25:22-37.
 38. Welch AJ, van Gemert MJC. Optical-thermal response of laser-irradiated tissue. New York: Plenum Press, 1995.
 39. Frenz M, Könz F, Pratisto H, Weber HP. Starting mechanisms and dynamics of bubble formation induced by a Ho:Yttrium aluminum garnet laser in water. *J Appl Phys* 1998;84:5905-5912.
 40. Jasen ED, van Leeuwen TG, Motamedi M, Borst C, Welch AJ. Partial vaporization model for pulsed mid-infrared laser ablation of water. *J Appl Phys* 1995;78:564-571.

41. Nahen K, Vogel A. Investigations on Acoustic On-line Monitoring of IR Laser Ablation of Burned Skin. *Lasers Surg Med* 1999;25:69-78.
42. Morse PM, Ingard KU. *Theoretical Acoustics*. New York: McGrawHill Book Co., 1968.
43. Grad L, Možina J. Optoacoustic Studies of Er:YAG Laser Ablation in Hard Dental Tissue. *SPIE Proc* 1994;2128:456-465.
44. Lukač M, Grad L, Možina J. Optoacoustic Effects during Er:YAG Laser Ablation in Hard Dental Tissue. *SPIE Proc* 1994;2327:93-100.
45. Uhlhorn SR, Mongin D, Mackanos MA, Jansen ED. Effects of IR wavelength on ablation mechanics: A study of acoustic signals. *SPIE Proc* 2001;4257:178-183.
46. Uhlhorn SR. *Free Electron Laser Ablation of Soft Tissue: The Effects of Chromophore and Pulse Characteristics on Ablation Mechanics* (Doctoral Dissertation). Nashville: Vanderbilt University, 2002.
47. Majaron B, Šušterčič D, Lukač M, Skalerič U, Funduk N. Heat diffusion and debris screening in Er:YAG laser ablation of hard biological tissues. *Appl Phys B* 1998;66:479-487.
48. Vogel A, Venugopalan V. Mechanisms of Pulsed Laser Ablation of Biological Tissues. *Chem Rev* 2003;103:577-644.
49. Frenz M, Pratisto H, Konz F, Jansen ED, Welch AJ, Weber HP. Comparison of the effects of absorption coefficient and pulse duration of 2.12 μm and 2.79 μm radiation on ablation of tissue. *IEEE J Quantum Electron* 1996;32:2025-2036.
50. Kang HW, Lee H, Chen S, Welch AJ. Enhancement of Bovine Bone Ablation Assisted by a Transparent Liquid Layer on a Target Surface. *IEEE J Quantum Electron* 2006;42:633-642.
51. Hammitt G. *Cavitation and Multiphase Flow Phenomena*. New York: McGraw-Hill, 1980.
52. Isselin JC, Alloncle AP, Autric M. On laser induced single bubble near a solid boundary: Contribution to the understanding of erosion phenomena. *J Appl Phys* 1998;84:5766-5771.
53. Ith M, Pratisto H, Altermatt HJ, Frenz M, Weber HP. Dynamics of laser-induced channel formation in water and influence of pulse duration on the ablation of biotissue under water with pulsed erbium-laser radiation. *Appl Phys B* 1994;59:621-629.
54. Frenz M, Romano V, Zweig AD, Weber HP. Instabilities in laser cutting of soft media. *J Appl Phys* 1989;66:4496-4503.
55. Luo C, Liu X, Poddar R, Garra J, Gadre AP, Keuren EV, Schneider T, White R, Currie J, Paranjape M. Thermal ablation of PMMA for water release using a microheater. *J Micromech Microeng* 2006;16:580-588.

Chapter 9: Urinary Calculus Fragmentation During Ho:YAG and Er:YAG Lithotripsy

9.1 ABSTRACT

We tested Ho:YAG and Er:YAG laser ablation of human urinary calculi to determine if Er:YAG is a more efficient lithotripsy device. Ablation efficiency of Ho:YAG and Er:YAG lasers was tested at varying energy settings, ranging from the damage threshold to clinical energy setting associated with Ho:YAG laser. Stones of known composition (calcium oxalate monohydrate (COM), cystine, and uric acid (UA)) were irradiated. Crater width, depth, and ablation volumes were determined using an optical coherence tomography (OCT). For all stones and energy settings, the Er:YAG laser produced deeper craters and larger ablation volumes than the Ho:YAG laser. The Ho:YAG laser created wider craters during the multiple pulse process and the shape of craters was irregular. The Er:YAG laser is more efficient than the Ho:YAG laser for lithotripsy. The deeper craters produced by the Er:YAG laser is attributed to the high absorption of energy at its wavelength.

9.2 INTRODUCTION

Since the initial introduction of the continuous CO₂ laser (wavelength $\lambda = 10.6 \mu\text{m}$) to fragment human calculi [1], several laser lithotriptors, including Ho:YAG ($\lambda = 2.12 \mu\text{m}$, pulse duration $\tau_p \sim 250 \mu\text{s}$), Q-switched Nd:YAG ($\lambda = 1.064 \mu\text{m}$, $\tau_p \sim 8\sim 20 \text{ ns}$) and pulsed dye laser ($\lambda = 504 \text{ nm}$, $\tau_p \sim 1 \mu\text{s}$), have been investigated and used clinically [2,3]. For minimally invasive surgery, pulsed laser light is delivered to the urinary system through an optical fiber in conjunction with an ureteroscope. Among many laser lithotriptors, Ho:YAG laser is considered to be the most efficient and versatile tool since it can fragment all compositions of urinary calculi and causes less retropulsive motion than the short pulsed lasers [4-6]. The fragmentation during Ho:YAG laser lithotripsy is initiated through direct pulse energy absorption in a calculus. The absorbed pulse energy is converted to thermal energy that heats the laser-affected zone, leading to fragmentation [7].

Studies using the Free Electron Laser (FEL) between $2 \mu\text{m}$ and $10 \mu\text{m}$ showed more efficient optical absorption at wavelength corresponding to Er:YAG laser compared to Ho:YAG lasers for most stone compositions [8]. Initial studies comparing *ex vivo* laser lithotripsy of urinary calculi showed more efficient fragmentation from Er:YAG versus Ho:YAG irradiation [9]. However, Er:YAG ablation measurements were limited to near calculi-damage threshold energy

since the delivery fiber (sapphire fiber) for the Er:YAG laser was not able to tolerate the strong laser-calculi interaction at high pulse energy.

Since the ablation can be reduced due to the debris shielding at high pulse energy, a comparison of ablation efficiency at high-energy setting is necessary [10, 11]. Considering the higher absorption of Er:YAG laser, it can be subjected to further reduction compared to Ho:YAG laser. This may lead to comparable ablation efficiency at high pulse energy. In this study, we investigated the calculus fragmentation process with long pulsed Ho: YAG and Er: YAG lasers without using a delivery fiber system. Ablation efficiency of two lasers is measured using various energy settings, ranging from the damage threshold energy of calculus to starting energy setting of the clinical Ho:YAG laser. By comparing laser-induced crater width, depth and ablation volume, the feasibility of Er:YAG laser lithotripsy is examined.

9.3 MATERIALS AND METHODS

Calcium Oxalate Monohydrate (COM, > 95%), Cystine (> 95%), and Uric Acid (UA, > 95%) calculus extracted from patients were cut with a dental diamond band saw to create a flat surface with a thickness of 2~3 mm. A number of ablation craters were created on calculus slices using a scientific Er:YAG laser (Schwartz 1-2-3, Orlando, FL, $\lambda = 2.94 \mu\text{m}$, $\tau_p \sim 275 \mu\text{s}$ at FWHM) and a Ho:YAG laser (Schwartz 1-2-3, Orlando, FL, $\lambda = 2.10 \mu\text{m}$, $\tau_p \sim 275 \mu\text{s}$ at

FWHM). The lasers operated in free running mode with a repetition rate of 2 Hz (Figure 9.1). A mechanical shutter in conjunction with a shutter controller was used to block the initial ten pulses, which were unstable. The laser and shutter controller were synchronized using a pulse generator, and the laser pulse was focused onto the surface of calculus by a CaF_2 lens with a focal length of 10 cm.

The spatial beam profiles on the target were determined using 1) a knife-edge method and 2) pyroelectric solid-state camera. A knife-edge was scanned through the beam with a spatial resolution of 20 μm . The transmitted energy past the knife-edge was measured using an energy meter (EPM 2000, Molelectron Detector Inc., Portland, OR) equipped with a pyroelectric joulemeter (J25, Molelectron Detector Inc., Portland, OR). The transmitted energy past the knife-edge was normalized with total energy. The beam diameters were estimated from the knife-edge measurements; we defined the beam diameter as 10 % and 90 % clip points of transmitted energy through the knife-edge. In order to quantify the divergence of beam, the beam diameters at 3 mm and 5 mm away from the focal points were also measured. Figure 9.2 illustrates the schematic diagram of camera based beam measurement system. The beam profile at the focal plane (on target surface) of the focusing lens (CaF_2 I) was imaged with an imaging lens (CaF_2 II, with a focal length of 5 cm). A beam profiler (Pyrocam I, Spiricon, Logan, UT) was placed at the image plane. The beam profiler was based on a pyroelectric detector array that was triggered by an external InAs photo-diode

(EG&G Judson, PA). The acquired images were transferred to a personal computer equipped with a frame grabber. In order to determine the deviation from the TEM₀₀ mode, a Gaussian fit was performed using the software provided for the beam profiler. The software uses a least square method that minimizes the sum of square of the differences between the data and the fitted profile. The correlation, that represents how well the data matches to the fitted Gaussian profiles, is defined as follows;

$$G_c = 1 - \frac{\sum |Z - S|}{\sum Z} \quad (9.1)$$

where G_c = Gaussian correlation, Z = measured intensity, and S = Fitted Gaussian intensity.

By placing a beam splitter in the beam path, pulse energy was monitored using the energy meter and the pyroelectric joulemeter. A mechanical shutter in conjunction with a shutter controller was used to block the initial ten pulses, which were unstable. In order to ensure constant pulse duration and beam diameter, the pumping voltage for the flash lamp was fixed and attenuation filters were used to modify the pulse energy. Ablation craters were produced with a single pulse and five pulses with various energy settings. Laser-induced craters were examined with an Optical Coherence Tomography (OCT) system ($\lambda_0 = 1290$ nm, $\Delta\lambda = 42$ nm, and $P = 2.2$ mW) with a lateral and axial resolution of ~ 20 μ m

to obtain quantitative ablation crater dimensions [12,13]. A series of vertical cross-sectional images (along the laser axis) were obtained over the entire crater. The step-size between images was 40 μm . Crater width, depth and ablation volume were estimated from the OCT cross sections. Craters were also observed with an optical microscope to compare the quality of laser drilling and morphological change. Crater size measures were compared using unpaired Student's t-test. A p -value < 0.05 was considered statistically significant.

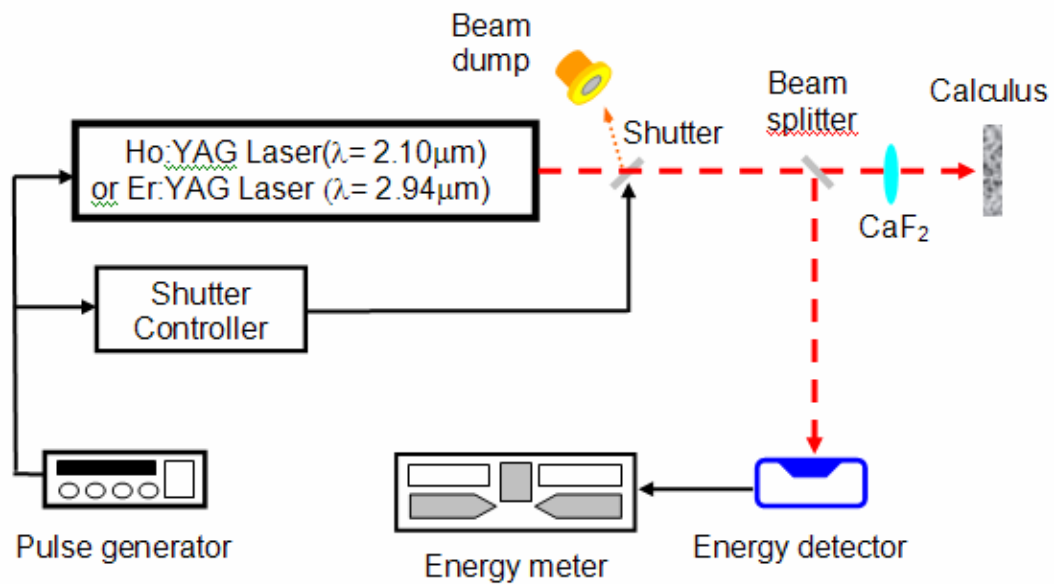


Figure 9.1. Experimental setup for calculus ablation measurement.

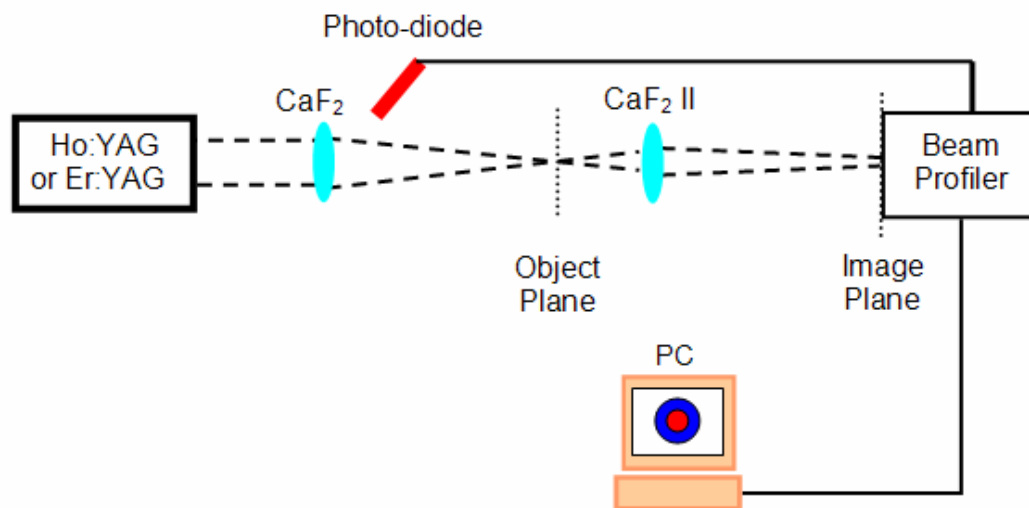


Figure 9.2. Experimental setup used to measure the beam profile at the focal plane (on target surface) during laser lithotripsy.

9.4 RESULTS

9.4.1 BEAM PROFILES

Beam diameters on the target surface were determined using knife-edge scanning through the beam. The transmitted energy past the knife-edge for both laser beams was measured and normalized with total energy (~ 100 mJ). The knife-edge measurements at the focal point (on the target surface) are compared in Figure 9.3. The beam diameter (from 10 % and 90% clip points) of Er:YAG and Ho:YAG measures $276\text{ }\mu\text{m}$ and $292\text{ }\mu\text{m}$, respectively. Since both lasers produced a multimode beam, we defined the beam diameter as the distance between the 10 % and 90 % clip points without multiplying the width adjust factor ($1.104\sqrt{2}$) which is used for the estimation of $1/e^2$ diameter of a Gaussian beam. The increase of beam diameters is displayed as a function of the distance from the focal point (Figure 9.4).

Both lasers produce multimode beams that deviate from TEM_{00} mode (Figure 9.5). Overall, the Er:YAG laser produced a truncated cone shape beam with Gaussian correlation of 0.787. Ho:YAG laser beam has many randomly located hotspots with Gaussian correlation of 0.710.

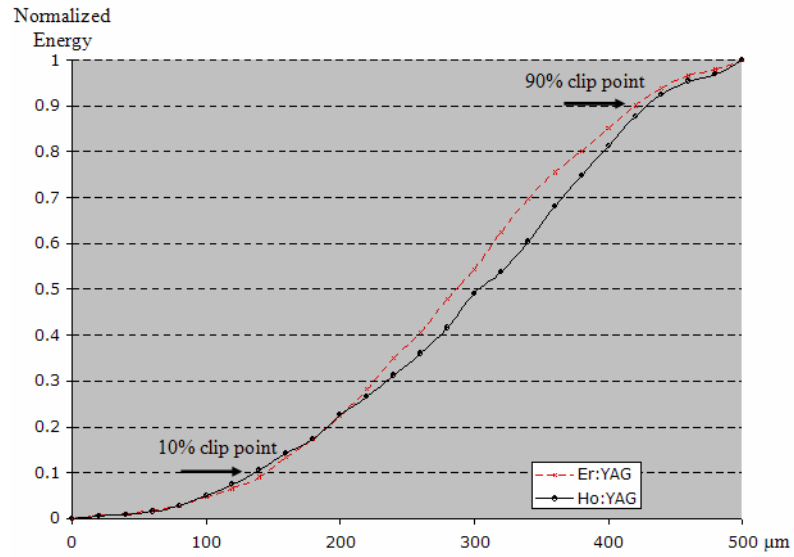


Figure 9.3. Normalized energy transmitted past knife-edge at the focal plane (on target surface). The average of five measurements is presented. Total pulse energy was 100 mJ.

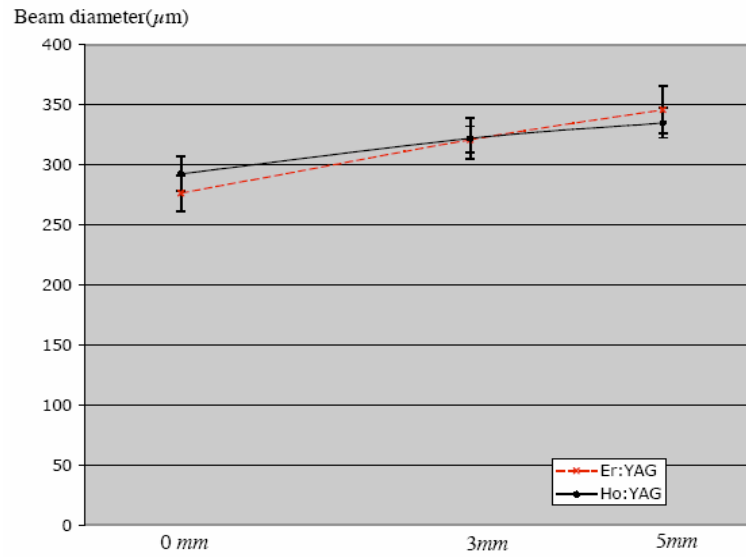
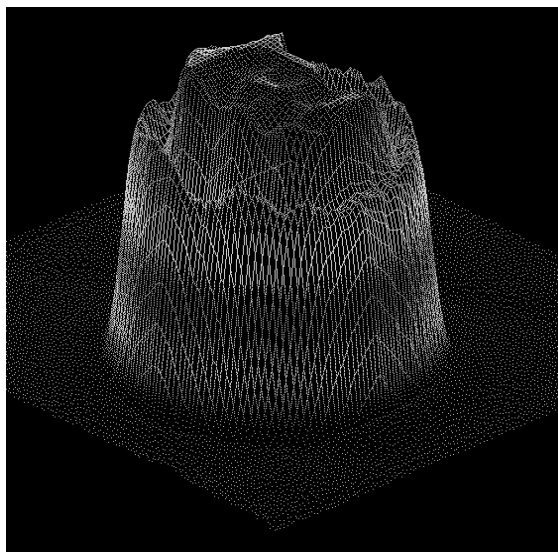
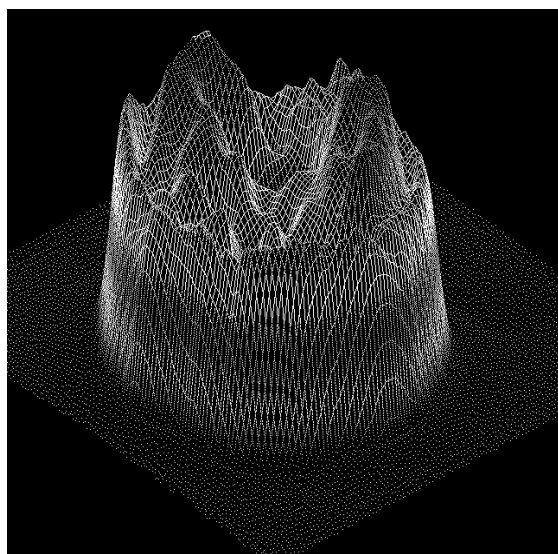


Figure 9.4. Beam diameters as a function of the distance from the focal point. Error bars represent the standard deviation of five measurements. X-axis represents the distance from the focal point while the laser beam diverges.



(a)



(b)

Figure 9.5. Beam profiles measured with a pyroelectric solid-state camera. (a) Er:YAG laser with 20 mJ ($H = 33 \text{ J/cm}^2$) and (b) Ho:YAG laser with 20 mJ ($H = 30 \text{ J/cm}^2$).

9.4.2 CROSS-SECTIONAL PROFILES

After single or five pulse irradiation on calculi, laser-induced craters were scanned using the OCT; typical cross-sectional profiles of COM, Uric Acid, and Cystine calculi are displayed in Figures 9.6-9.8. Regardless of the irradiation wavelength, the depth of craters increased with number of pulses. The widths of Er:YAG-induced craters were comparable, while five-pulses-induced crater of Ho:YAG was wider than the single pulse-induced one. The Er:YAG laser produced deeper craters than the Ho:YAG laser. While Er:YAG yielded smooth crater contours, Ho:YAG made irregular and rough contours.

The observation with an optical microscope revealed significant differences between two wavelengths (Figure 9.9). Er:YAG-induced craters display a fairly rounded crater edge with smooth contours. However, the Ho:YAG produced rough and irregular contours. Crater shape is unpredictable and obviously dependent on the intrinsic morphology of calculus. Ho:YAG laser also produced chippings as well as collateral thermal damage(color change and charring) around the craters.

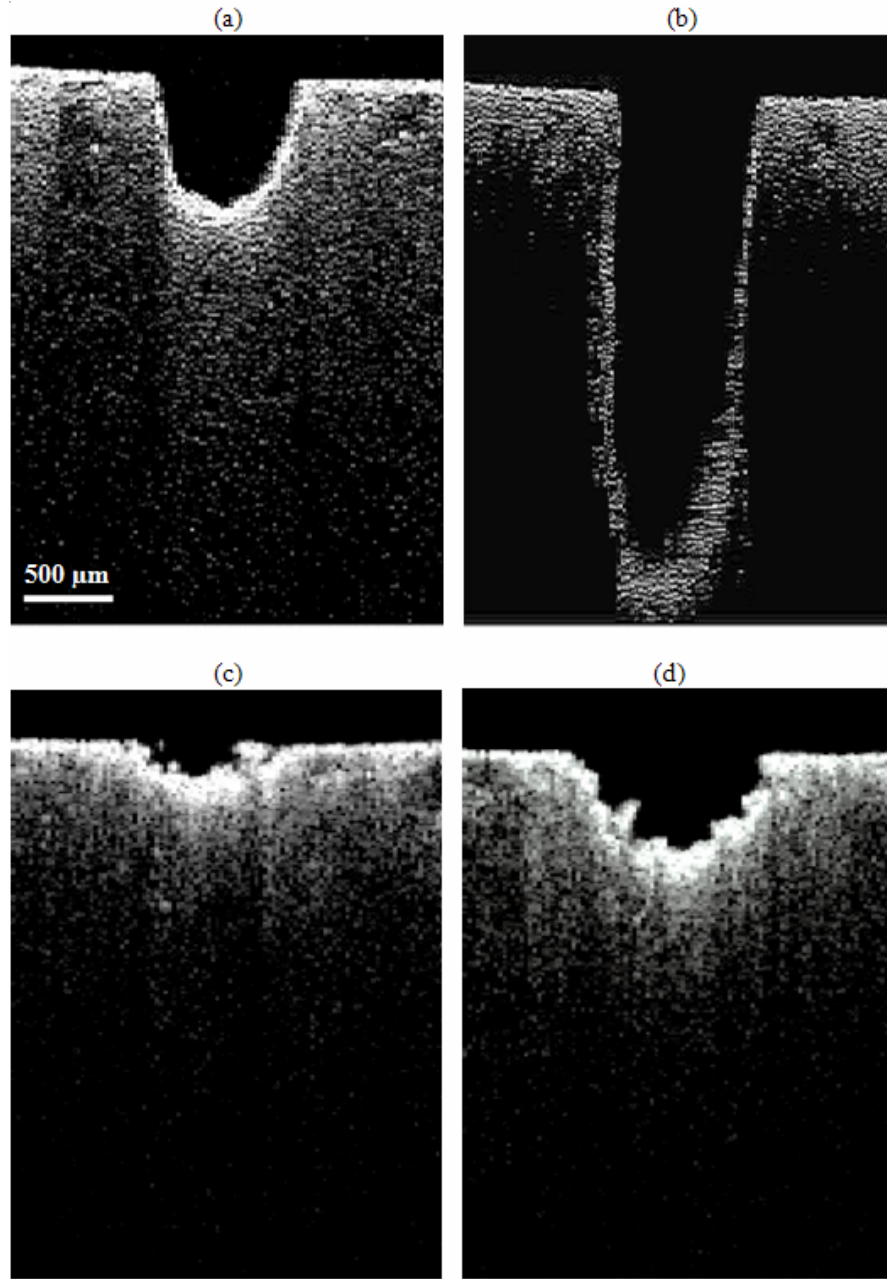


Figure 9.6. Vertical cross-sectional topography of Er:YAG and Ho:YAG laser-induced craters on COM. (a) Er:YAG, Single pulse, $Q_0 = 400$ mJ ($H = 668$ J/cm²), (b) Er:YAG, five pulses, $Q_0 = 400$ mJ ($H = 668$ J/cm²) per pulse, (c) Ho:YAG, Single pulses, $Q_0 = 387$ mJ ($H = 578$ J/cm²), and (d) Ho:YAG, five pulses, $Q_0 = 387$ mJ ($H = 578$ J/cm²) per pulse.

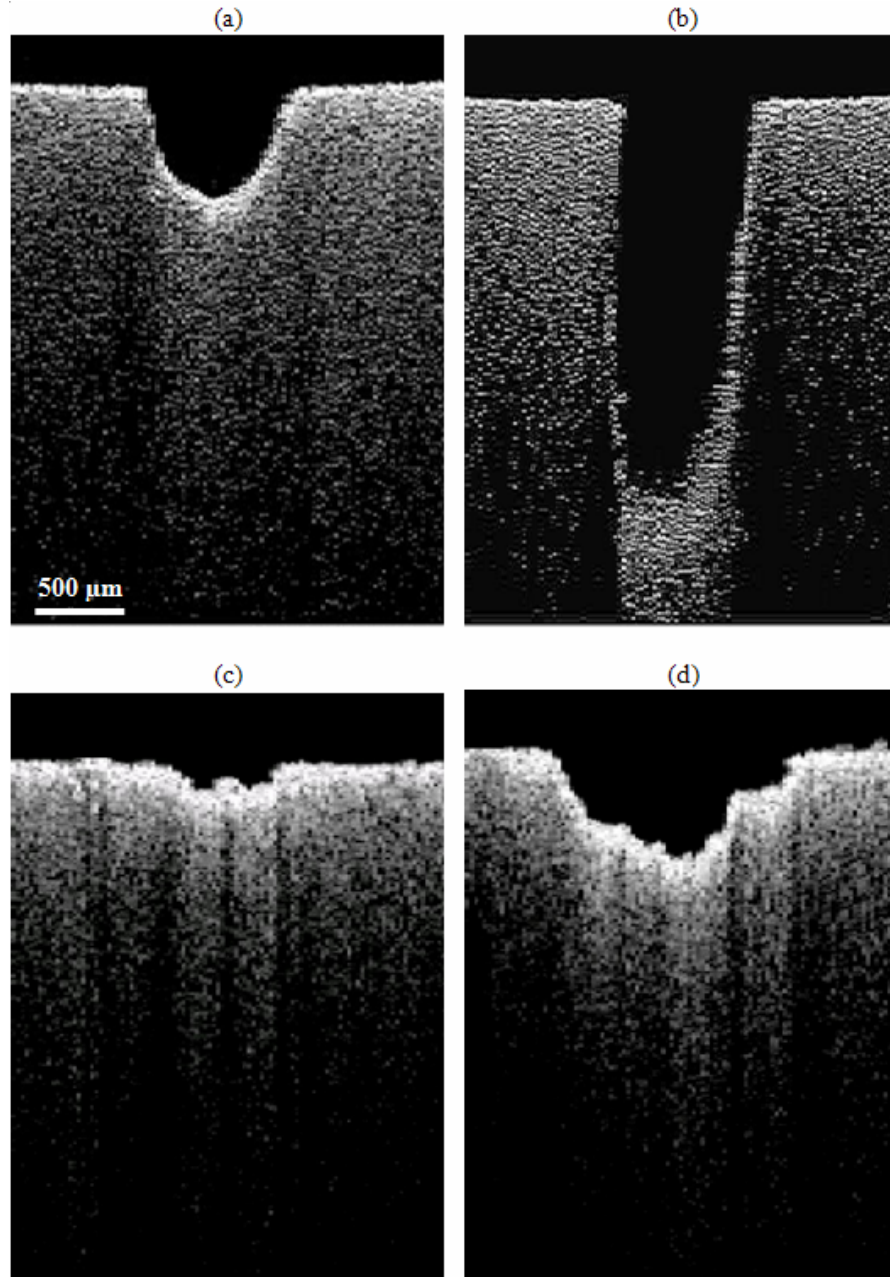


Figure 9.7. Vertical cross-sectional topography of Er:YAG and Ho:YAG laser-induced craters on Uric Acid. (a) Er:YAG, Single pulse, $Q_0 = 479$ mJ ($H = 801$ J/cm²), (b) Er:YAG, five pulses, $Q_0 = 479$ mJ ($H = 801$ J/cm²) per pulse, (c) Ho:YAG, Single pulses, $Q_0 = 439$ mJ ($H = 656$ J/cm²), and (d) Ho:YAG, five pulses, $Q_0 = 439$ mJ ($H = 656$ J/cm²) per pulse.

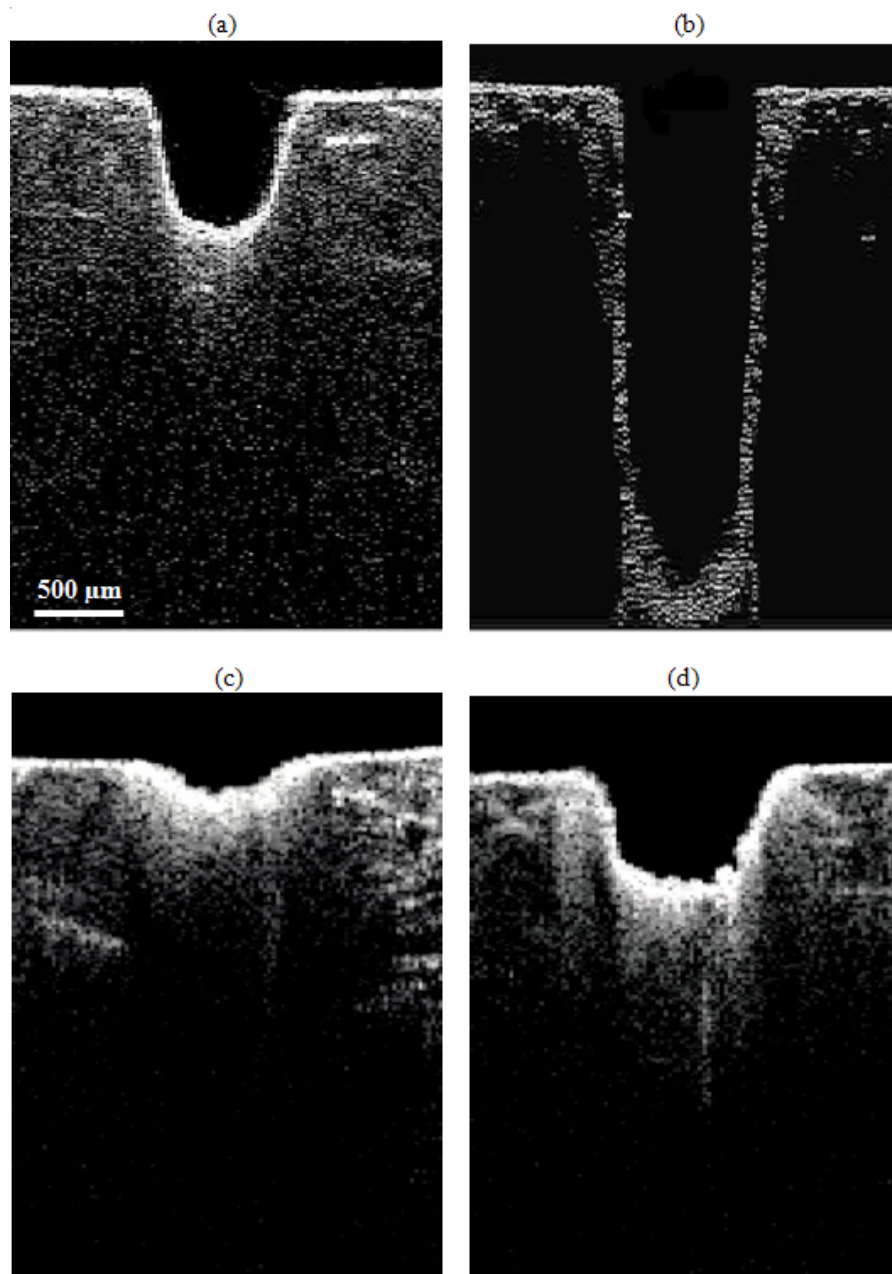


Figure 9.8. Vertical cross-sectional topography of Er:YAG and Ho:YAG laser-induced craters on Cystine. (a) Er:YAG, Single pulse, $Q_0 = 479$ mJ ($H = 801$ J/cm²), (b) Er:YAG, five pulses, $Q_0 = 479$ mJ ($H = 801$ J/cm²) per pulse, (c) Ho:YAG, Single pulses, $Q_0 = 524$ mJ ($H = 782$ J/cm²), and (d) Ho:YAG, five pulses, $Q_0 = 524$ mJ ($H = 782$ J/cm²) per pulse.

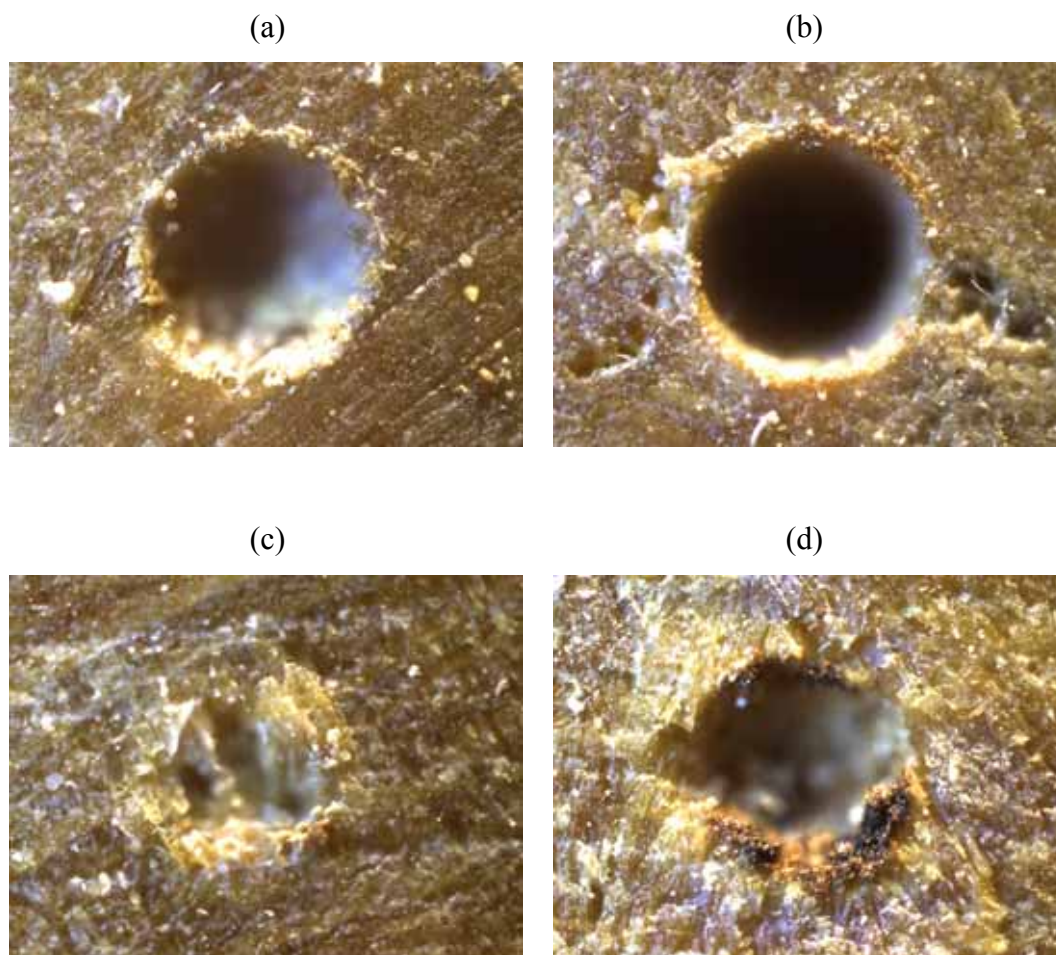


Figure 9.9. Microscopic top views of Er:YAG and Ho:YAG laser-induced craters on Uric Acid. (a) Er:YAG, Single pulse, $Q_0 = 74 \text{ mJ}$ ($H = 124 \text{ J/cm}^2$), (b) Er:YAG, five pulses, $Q_0 = 74 \text{ mJ}$ ($H = 124 \text{ J/cm}^2$) per pulse, (c) Ho:YAG, Single pulses, $Q_0 = 105 \text{ mJ}$ ($H = 157 \text{ J/cm}^2$), and (d) Ho:YAG, five pulses, $Q_0 = 105 \text{ mJ}$ ($H = 157 \text{ J/cm}^2$) per pulse.

9.4.3 CRATER DEPTH AND WIDTH

The crater depth and width of on the calculus are compared quantitatively in Figures 9.10 and 9.11. For all three calculi, the depth increased with radiant exposure and the depth of the Er:YAG laser-induced craters was greater than those using the Ho:YAG (Figure 9.10). Crater depths produced with the Er:YAG laser were up to six times deeper than Ho:YAG induced craters. Higher pulse energy yielded wider craters. The width of five-pulse induced craters of Ho:YAG was larger than single pulse crater ($p < 0.05$), while there was no statistical difference between single and five-pulse craters of Er:YAG ($p > 0.25$).

9.4.4 ABLATION VOLUME

Regardless of stone type and laser wavelength, ablation volume increased with radiant exposure (Figure 9.12). With both single and five-pulse irradiation, Er:YAG yielded higher ablation volume than Ho:YAG over the whole energy level tested. Single Er:YAG pulse produced four to five times larger ablation volume than Ho:YAG for all calculus types. Er:YAG five pulse sequence produced three to four times larger volume than the Ho:YAG sequence. To compare the ablation efficiency of a single pulse and multiple pulses, the ablation volume of five-pulses was normalized with the number of pulses (Figure 9.13). The ablation efficiency of the Ho:YAG does not change with number of pulses,

however the efficiency of multiple Er:YAG pulses decreased about 20~30%, especially for high pulse energies.

Crater depth, width and ablation volume are compared within the same wavelength and number of pulses across compositions. Regardless of laser parameters, the crater sizes of calculi are not significantly different (except two pairs: Er:YAG single pulse, width, cystine vs. uric acid, $p = 0.035$ and Ho:YAG five pulses, width, cystine vs. uric acid, $p = 0.028$).

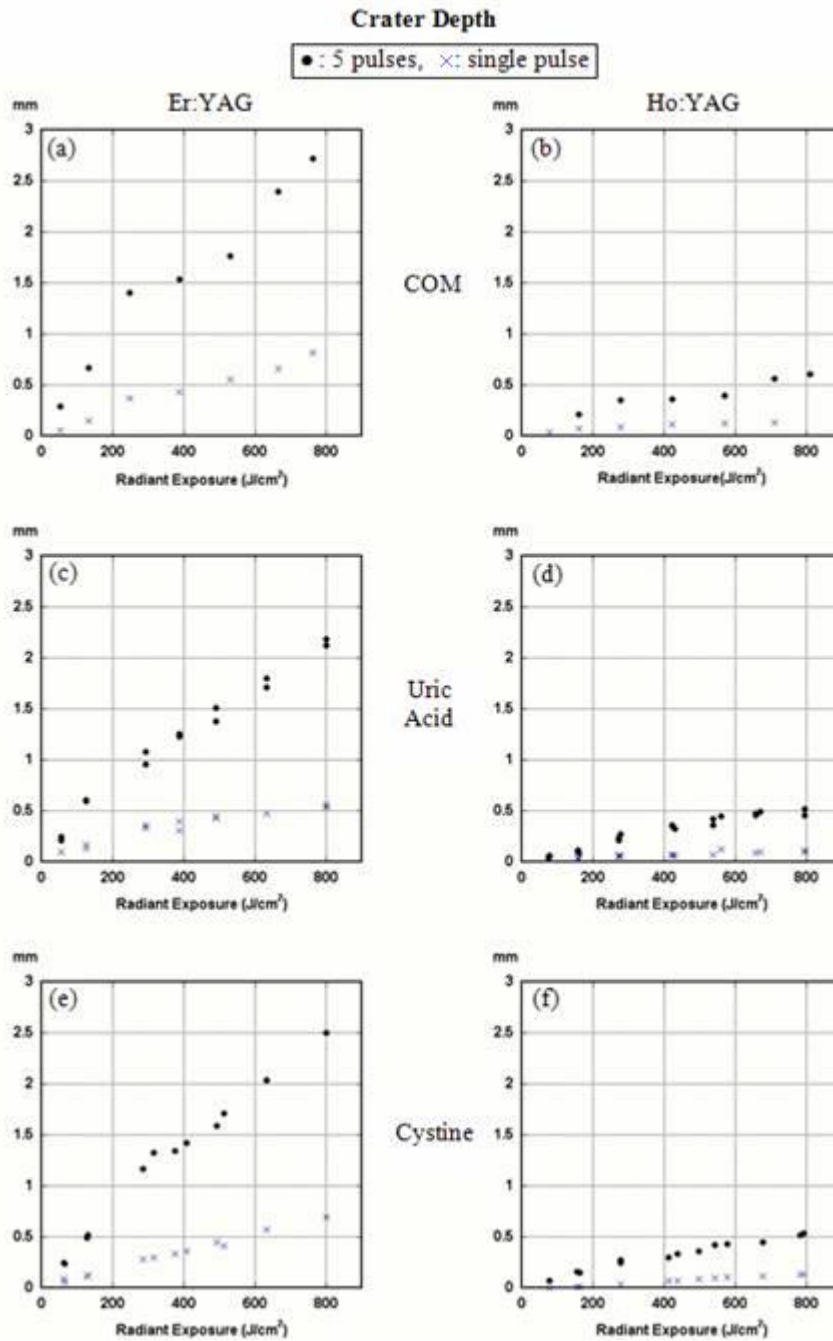


Figure 9.10. Crater depth as a function of radiant exposure per pulse. (a) Er:YAG, COM; (b) Ho:YAG, COM; (c) Er:YAG, Uric Acid; (d) Ho:YAG, Uric Acid; (e) Er:YAG, Cystine; (f) Ho:YAG, Cystine.

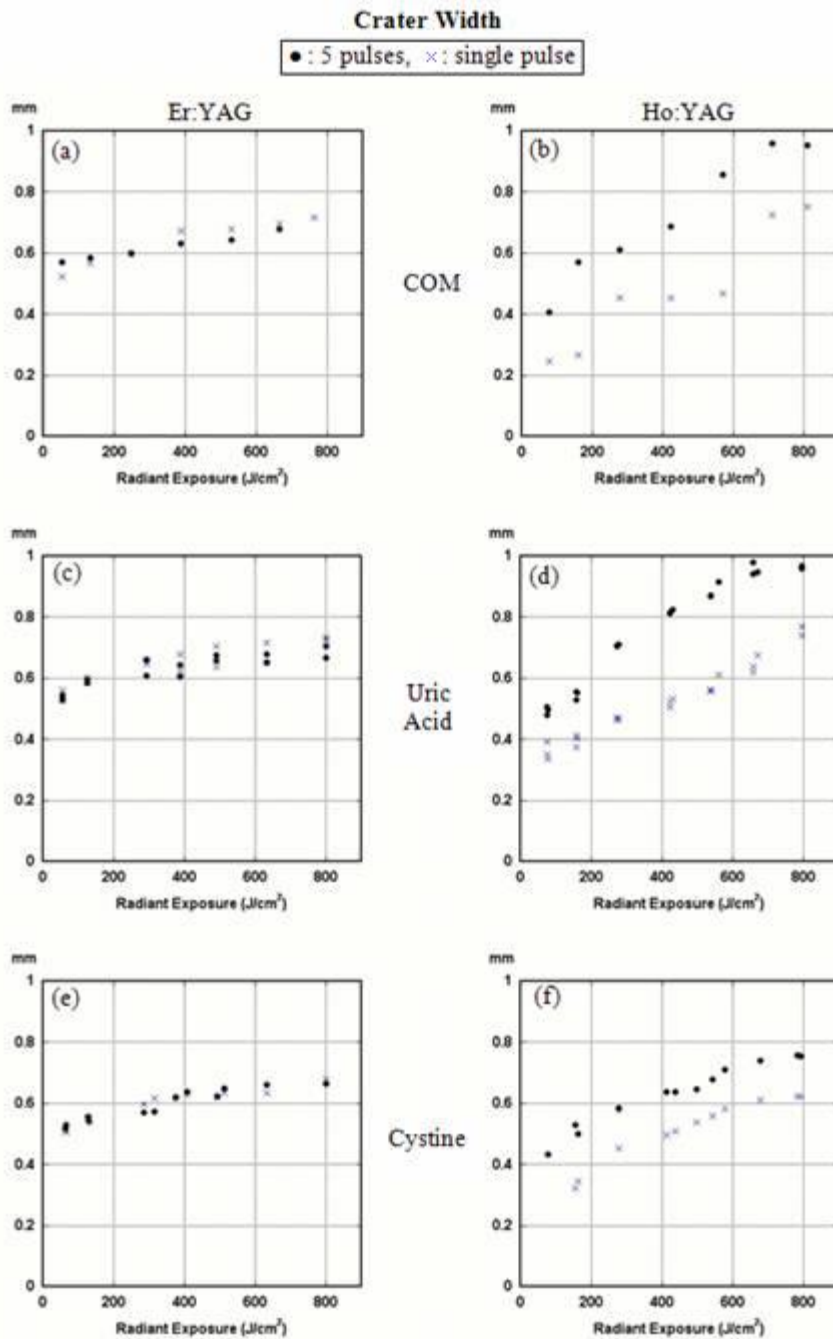


Figure 9.11. Crater width as a function of radiant exposure per pulse. (a) Er:YAG, COM; (b) Ho:YAG, COM; (c) Er:YAG, Uric Acid; (d) Ho:YAG, Uric Acid; (e) Er:YAG, Cystine; (f) Ho:YAG, Cystine.

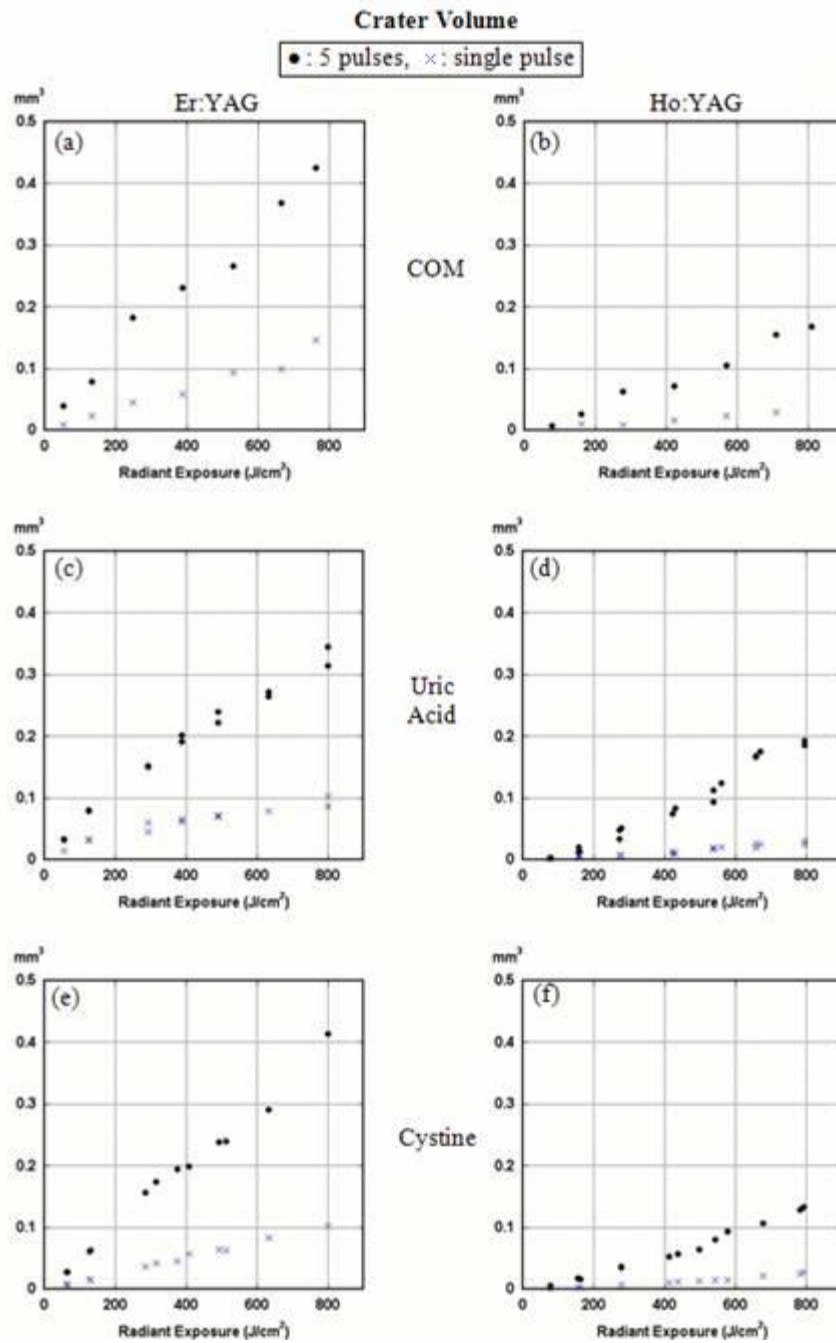


Figure 9.12. Crater volume as a function of radiant exposure per pulse. (a) Er:YAG, COM; (b) Ho:YAG, COM; (c) Er:YAG, Uric Acid; (d) Ho:YAG, Uric Acid; (e) Er:YAG, Cystine; (f) Ho:YAG, Cystine.

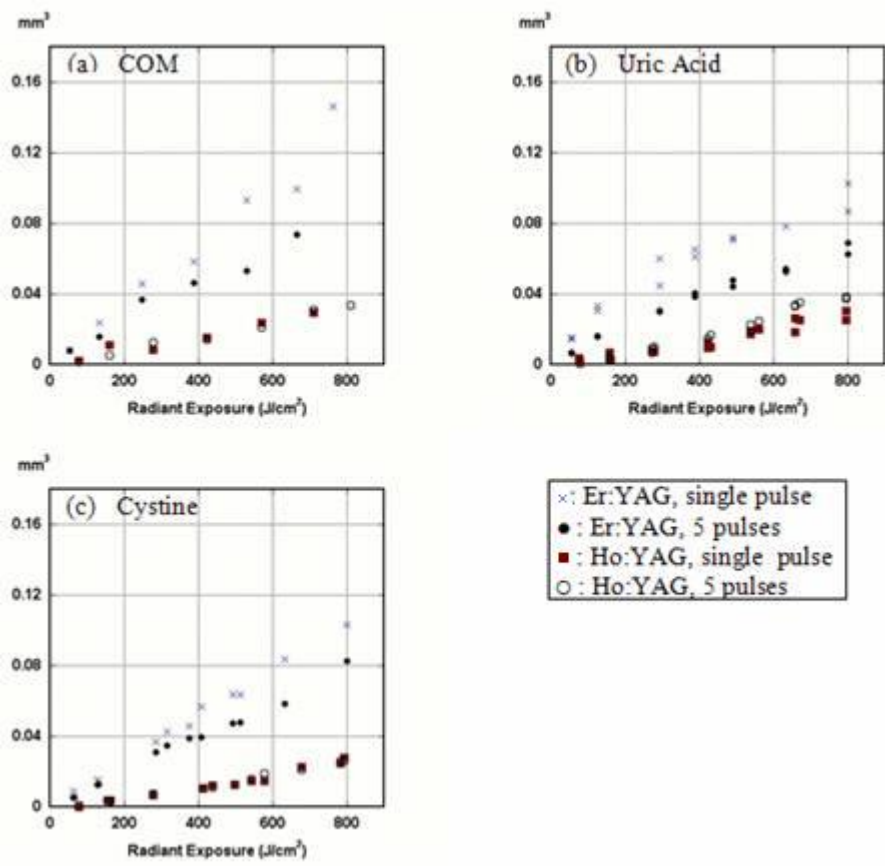


Figure 9.13. Comparison of normalized crater volume of five pulses and the crater volume of single pulse. (a) COM, (b) Uric Acid, and (c) Cystine.

9.5 DISCUSSION

Chan *et al.* and Teichman *et al.* reported that the Er:YAG laser could ablate calculi more efficiently than the Ho:YAG laser, as hypothesized by the higher absorption peak at 2.94 μm which is coincident with the wavelength of the Er:YAG laser [8,9]. However, the pulse energy level for ablation measurements in previous studies was limited to prevent damage to the delivery fiber optics (sapphire fiber) for the 2.94 μm wavelength. Er:YAG pulse energies were no larger than 50 mJ, which was slightly above the threshold for crater production. The optimal energy setting of the Ho:YAG laser in the clinic is from 0.6 to 1 J using a low OH⁻ silica delivery fiber with a diameter of 272~550 μm [14–18]. In this study, we have compared the ablation efficiency of free running Ho:YAG and Er:YAG lasers during the lithotripsy without using a delivery fiber. The fragmentations at super-threshold pulse energy are compared by setting the pulse energies near the clinical energy setting of Ho:YAG laser. Thus, this study provides the first experimental report to compare lithotripsy using both Er:YAG and Ho:YAG lasers at clinically relevant pulse energies.

The cross-sectional topography of ablation craters in Figures 9.6–9.8 provides a visual demonstration of the difference between Er:YAG and Ho:YAG ablation in calculi. Craters produced by the Er:YAG laser are narrower and deeper than craters produced with a Ho:YAG laser at the same pulse energy.

The depth of craters compared quantitatively in Figure 9.10 confirms that Er:YAG laser created deeper craters than Ho:YAG regardless of calculus type and the number of pulses. The superior drilling ability of the free running Er:YAG laser, which did not inflict significant collateral damage, has been demonstrated in numerous studies. Frenz *et al.* reported that the Er:YAG laser is capable of drilling a much deeper hole than the Ho:YAG laser during laser-soft tissue interactions [19,20]. They also compare the shape of bubbles formed during the irradiation of two laser beams into water [21]. The Er:YAG laser generates an elongated cigar-shaped bubble while the Ho:YAG laser makes a pear-shaped bubble. The better drilling capability of the Er:YAG laser is attributed to the high absorption coefficient of tissue, which absorbed Er:YAG light within a shallow penetration depth ($\sim 10\ \mu\text{m}$). Accordingly, sufficient heat for ablation occurs in the laser-affected zone (where photons are directly absorbed) and hot ablated material is ejected before the thermal energy and diffuses to neighboring regions. For this reason, the Er:YAG laser can drill more efficiently than Ho:YAG laser during lithotripsy.

As for the quality of laser drilling, Er:YAG pulses produce craters with fairly nice and smooth contour. In contrast, Ho:YAG pulses create irregular and rough crater contours. Chippings around the craters also suggest a bulky material removal during Ho:YAG process. The discrepancy of spatial beam quality of two lasers is considered to be partially responsible for the difference in crater shapes.

Overall, the Er:YAG beam has a truncated cone shape. This profile could lead to the maximum temperature at the center of the beam, resulting in a Gaussian-like crater. However, randomly located hotspots of Ho:YAG laser beam would induce the inhomogeneous temperature distribution, producing local centers of vaporization. This local vaporization and expansion of vapor will lead to the bulky material removal and the irregular crater shape. The resultant crater will have an irregular and unpredictable shape dependent on the intrinsic mechanical property of calculus.

Er:YAG and Ho:YAG ablation yields differences in crater widths as well (Figure 9.11). The width of five-pulse induced crater of Ho:YAG is larger than that of single pulse crater ($p < 0.05$), while there is no statistical difference between single- and five-pulse craters of Er:YAG. The heat diffusion and the scattering of incident light could determine the lateral extension of ablation (crater width) and overall crater shape. Given the thermal diffusivity (α) of most tissues and dielectric materials is less than $0.5 \text{ mm}^2/\text{s}$ [22] and the pulse duration (τ_p) of free running lasers is about $275 \text{ }\mu\text{s}$, the heat diffusion length ($l_d = \sqrt{\alpha\tau_p}$) during the pulse is at most $12 \text{ }\mu\text{m}$. Since the widening of Ho:YAG crater measures a few hundreds micrometers, the heat conduction minimally contributes to the augmented width of the crater during the pulse (once the laser pulse stops, no more ablation take place during a free running laser lithotripsy [7]). An ablation crater could be wider than the actual laser beam diameter if the scattering of the

incident light causes photons to be distributed beyond the beam diameter. Since the absorption of Ho:YAG light is much smaller than that of Er:YAG laser, the scattering of Ho:YAG beam can be more significant than that of Er:YAG light. Accordingly, the Ho:YAG light can be distributed more laterally in target, resulting in a wider crater than the Er:YAG laser. Future measurement of absolute absorption and scattering coefficients of calculus will clarify how significantly light scattering contributes to the lateral distribution of absorbed photons.

Based on temperature profile, the collateral thermal damage and the vapor expansion, we propose two additional mechanisms that can explain the widening of Ho:YAG laser-induced craters. Figure 9.14 compares the temporal evolution of ablation process and temperature rise along the depth. Because of the high absorption coefficient, the Er:YAG produces a sharper gradient of temperature with depth; thus a smaller fraction of the Er:YAG pulse duration is required to reach the ablation threshold temperature (T_{th}). In the illustration, the surface temperature of the Er:YAG target is assumed to have reached the threshold value at the first time step and the ablation process begins. The ablation front of Er:YAG moves deeper and deeper into the calculus, while the Ho:YAG laser is still depositing energy into the calculus without any material ablation (time steps 2-4). The surface temperature of the Ho:YAG is assumed to approach the threshold value at time step 5, and the profile near the surface (ablation front) is

magnified and shown in Figure 9.14(c). The highlighted zone (ablation zone) indicates the region where temperature is higher than the ablation threshold, and material in this region is about to be ablated. Since the penetration depth of the Er:YAG laser is shallower than Ho:YAG, Er:YAG laser deposits energy into thin superficial layer (superficial energy accumulation). Consequently, material in the ablation zone will be ablated without hindrance of the above material. On the other hand, the Ho:YAG laser penetrates deep, resulting in a gradual and deep temperature profile (volumetric energy accumulation). As a result of that, the ejection of materials deeper in the ablation zone will be interrupted by the material close to the surface and triggering more lateral and axial (downward) expansion of vapor than the Er:YAG laser process. Accordingly, further ablation beyond the beam diameter during Ho:YAG laser process can take place by this lateral expansion of vaporized material. This lateral expansion of vapor can contribute in part to the irregular contour and the bulky material removal of Ho:YAG laser crater. Frenz *et al.* observed that the Ho:YAG pulse ($\tau_p = 400 \mu\text{s}$)-induced craters on human meniscus have much larger width than the beam diameter. They attribute the crater widening to the vapor expansion [19]. Walsh *et al.* also suggested that the expansion of the vapor contributes to the tearing of the soft tissue [23,24]. This thermo-mechanical effect should be distinguished from the shock wave, which is induced by the plasma expansion and cavitation collapse during short-pulsed laser ($\tau_p < 1 \mu\text{s}$) lithotripsy [25–28].

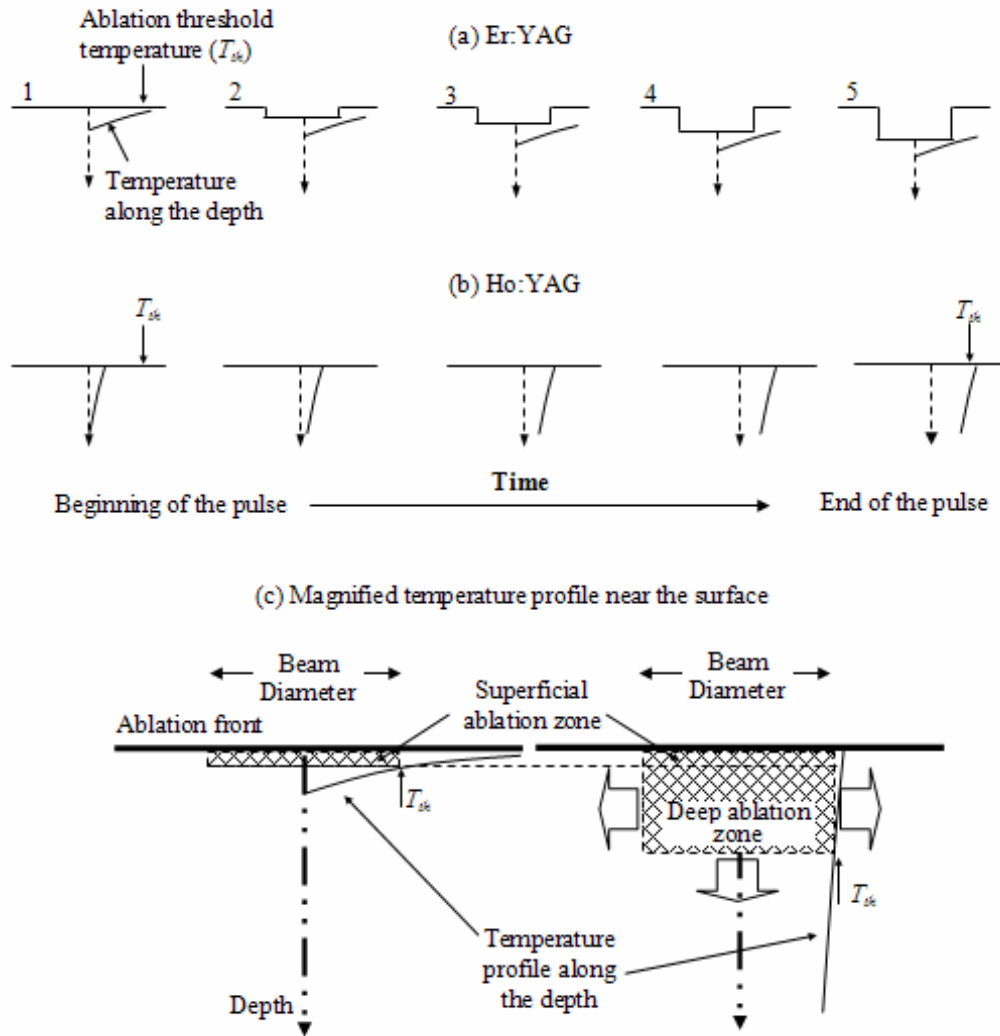


Figure 9.14. Temporal evolution of ablation process and temperature as a function of depth. The scattering of the light has been neglected. Numbers indicate the time sequence. The highlight indicates the ablation zone. Both lasers have a flat top beam with the same diameter. The scattering of the light was neglected. Bold arrows in the Ho:YAG process indicate the lateral and axial expansion of ablated material in deep ablation zone.

Second mechanism takes into account the collateral damage during the Ho:YAG laser lithotripsy. Because of the lower absorption, the first Ho:YAG pulse produces collateral damage zone near the ablation craters that extends beyond the beam diameter (Figure 9.9). The following pulse induces more ablation, and the ablated vapor expands with high thermal and mechanical energy. Since the tissue in the collateral damage region had been weakened by the previous pulse, the lateral expansion of vapor can lead to additional material removal in the collateral damage zone. This process is repeated for the subsequent pulses and the crater width keeps growing. The crater widening can be minimal during the Er:YAG process due to the insignificant collateral thermal damage. In contrast to the soft tissue application of laser, the drilling quality of laser is not a major concern of urologist during the lithotripsy. Since the objective of lithotripsy is rapid fragmentation of calculus to small particles, the ablation volume is the most important criterion in determining which laser is a better lithotripter. Regardless of the number of pulses and wavelength, the Er:YAG laser produces more ablation than the Ho:YAG laser, mainly due to deeper drilling. Comparing the ablation efficiency, Er:YAG was also superior to Ho:YAG for both single- and five-pulses, which suggests the Er:YAG laser is a good candidate for the next generation of laser lithotripter.

The ablation efficiency of Er:YAG decreased with the number of pulses while that of Ho:YAG does not change. We attribute the reduced efficiency of

multiple Er:YAG laser pulse to (1) the reduced radiant exposure on deeper ablation front due to the divergence of beam and (2) debris shielding. As the beam travels beyond the focal plane of the focusing CaF_2 lens, its diameter gets larger due to the divergence of beam. Consequently, the radiant exposure on the ablation front gets reduced as the crater become deeper and deeper. Since the multiple Er:YAG pulse produces deep craters, it is expected that the ablation efficiency drops as a result of decreased radiant exposure. The debris shielding is another phenomenon that can explain the reduced efficiency of Er:YAG laser beam [29–31]. Once the debris is generated during the laser-tissue interaction, the remaining part of the laser pulse will be partially absorbed and scattered by the debris (termed “debris shielding”), reducing the pulse energy that reaches the target and diminishing the ablation efficiency. The amount of debris shielding is determined by the absorption coefficient, density, and extension of debris in the beam path. More debris shielding takes places during the multiple pulse process, as the crater gets deeper and it makes debris stay in the beam path longer [32]. As a result of this, the ablation efficiency of Er:YAG during multiple pulses can be diminished compared to the single-pulse process. Ho:YAG pulse is also subjected to the debris shielding; however, the amount of shielding is smaller than that of Er:YAG pulse. That is because (1) the crater is shallower and wider, (2) less debris in the beam path is produced, and (3) the absorption coefficient of debris is lower. In addition to these, the onset of Ho:YAG pulse ablation is

slower than that of Er:YAG pulse due to the lower absorption. As a result of this, the interaction time between the pulse and debris is shorter for Ho:YAG laser compared to Er:YAG laser for a given pulse duration. Due to the combination of the less reduction of radiant exposure, less shielding, and the widening of the craters, the ablation efficiency of Ho:YAG multiple pulses did not decrease compared to that of single pulse. During laser lithotripsy, the calculus is subjected to random movement due to (1) recoil of the calculus after the pulse and (2) irrigation and body flow [33]. Because of this, the chance of irradiating the same spot on the calculus is fairly low, and the efficiency drop by Er:YAG laser by multiple pulses becomes minimal. The ablation volume data indicate that the Er:YAG laser is a better fragmentation tool than the Ho:YAG laser for a given pulse energy.

The statistical analysis indicates that there is no significant difference in ablation rate among calculus types tested in this research. Since the ablation of free running laser lithotripsy is initiated by the photo-thermal effect [7,34], we can postulate that the absorption coefficient and decomposition temperature are the most important parameters for ablation efficiency. Future measurement of absolute absorption coefficient and decomposition temperature of calculi will clarify the ablation dependence on calculus type.

Despite the inherent superiority of Er:YAG energy to fragment stones compared to Ho:YAG energy, the endoscopic application of Er:YAG laser is still

limited due to the lack of a practical mid-Infrared (IR) delivery system. There are a few of mid-IR transmitting optical fibers, including chalcogenide, germanium oxide, sapphire, zirconium fluoride, and hollow waveguides [35–39]. To be employed as an endoscopic delivery system, the fiber needs to be biocompatible, flexible, and robust to tolerate the strong laser-tissue interaction at the fiber tip. None of above-mentioned fibers can meet all requirements for endoscopic application. Hybrid fibers have been proposed, in order to overcome the limitations associated with bare fibers. Chaney *et al.* employed a hybrid germanium-silica fiber to protect the germanium fiber tip from a damage induced by the strong pulse stone interaction [40,41]. With the hybrid fiber, they were able to deliver one order of magnitude higher pulse energy than the bare germanium oxide fiber. A similar approach is being pursued using a hollow wave guide with a sealing cap [11,42]. The biocompatibility and bending loss issues should be resolved for a clinical use. Although these hybrid techniques still do not deliver the pulse energy high enough for efficient lithotripsy, further improvement is expected from an advanced assembly and protective cap.

9.6 CONCLUSION

Ablation efficiencies in terms of the crater width, depth and ablation volume were compared for Er:YAG and Ho:YAG laser lithotripsy. Pulse energies as high as the clinical setting of Ho:YAG lithotripsy has been used to test

the feasibility of Er:YAG lithotripsy. Three different types of calculus (COM, Uric Acid, and Cystine) were tested in order to determine the variation between target calculi. Regardless of the calculus type, the Er:YAG laser produced deeper craters than Ho:YAG over the whole energy range tested. Due to deeper drilling, Er:YAG pulse produced up to five times more ablation volume than the Ho:YAG pulse. Er:YAG laser yielded nice and regular crater contours, however, Ho:YAG induced irregular and rough craters. The deeper crater of the Er:YAG laser attributes to its superior drilling ability. The hotspots on beam, volumetric energy deposition, and the collateral thermal damage is considered to create the contour irregularities and crater widening of Ho:YAG laser pulse process. Superior drilling makes the Er:YAG laser a better lithotripter, as it fragments the calculus more efficiently than the currently used Ho:YAG. It suggests that advancements in optical fiber delivery systems should make the Er:YAG laser available for clinical urological lithotripsy.

9.7 REFERENCES

1. Mulvaney WP, Beck CW. The laser beam in urology. *J Urol* 1968;99:112–115.
2. Dretler SP. Laser lithotripsy: A review of 20 years of research and clinical applications. *Lasers Surg Med* 1988;8:341–356.
3. Chan KF, Pfefer TJ, Teichman JMH, Welch AJ. A perspective on laser lithotripsy: The fragmentation processes. *J Endourol* 2001;15:257–273.
4. Yiu MK, Liu PL, Yiu TF, Chan AYT. Clinical experience with holmium:YAG laser lithotripsy of ureteral calculi. *Lasers Surg Med* 1996;19:103–106.

5. Adams DH. Holmium:YAG laser and pulsed dye laser: A cost comparison. *Lasers Surg Med* 1997;21:29–31.
6. Grasso M, Chalik Y. Principles and applications of laser lithotripsy: Experience with the holmium laser lithotrite. *J Clin Laser Med Surg* 1998;16:3–7.
7. Chan KF, Vassar GJ, Pfefer TJ, Teichman JMH, Glickman RD, Weintraub ST, Welch AJ. Holmium:YAG laser lithotripsy: A dominant photothermal ablative mechanism with chemical decomposition of urinary calculi. *Lasers Surg Med* 1999;25:22–37.
8. Chan KF, Choi B, Vargas G, Hammer DX, Sorg B, Pfefer TJ, Teichman JMH, Welch AJ, Jansen ED. Free electron laser ablation of urinary calculi: An experimental study. *IEEE J Sel Top Quantum Electron* 2001;7:1022–1033.
9. Teichman JMH, Chan KF, Cecconi PP, Corbin NS, Kamerer AD, Glickman RD, Welch AJ. Erbium:YAG versus holmium: YAG lithotripsy. *J Urol* 2001;165:876–879.
10. Teichman JMH, Vassar GJ, Glickman RD. Holmium:Yttrium-Aluminum-Garnet lithotripsy efficiency varies with stone composition. *Urology* 1998;52:392–397.
11. Iwai K, Shi YW, Matsuura Y, Miyagi M, Saito S, Arai Y. Characteristics of calculus fragmentation with Er:YAG laser light emitted by an infrared hollow optical fiber with various sealing caps. *Appl Opt* 2005;44:3266–3270.
12. Huang D, Swanson EA, Lin CP, Schuman JS, Stinson WG, Chang W, Hee MR, Flotte T, Gregory K, Puliafito CA, Fujimoto JG. Optical coherence tomography. *Science* 1991; 254:1178–1181.
13. Izatt JA, Kulkarni MD, Yazdanfar S, Barton JK, Welch AJ. In vivo bidirectional color Doppler flow imaging of picoliter blood volumes using optical coherence tomography. *Opt Lett* 1997;22:1439–1441.
14. Vassar GJ, Teichman JMH, Glickman RD. Holmium:YAG lithotripsy efficiency varies with energy density. *J Urol* 1998;160:471–476.
15. Spore SS, Teichman JMH, Corbin NS, Champion PC, Williamson EA, Glickman RD. Holmium:YAG lithotripsy:optimal power settings. *J Endourol* 1999; 13; 559–566.
16. Teichman JMH. Holmium:YAG lithotripsy for large renal and bladder calculi: Strategies for efficient lithotripsy. *J Endourol* 1999;13:477–482.
17. Kourambas J, Delvecchio FC, Preminger GM. Low-power holmium laser for the management of urinary tract calculi, strictures, and tumors. *J Endourol* 2001;15:529–532.
18. Knudsen B, Stallman KJ, Glickman RD, Denstedt JD, Teichman JMH. Comparison of seven holmium:YAG laser fibers. *J Endourol* (in press).

19. Frenz M, Pratisto H, Konz F, Jansen ED, Welch AJ, Weber HP. Comparison of the effects of absorption coefficient and pulse duration of 2.12 μm and 2.79 μm radiation on laser ablation of tissue. *IEEE J Quantum Electron* 1996;32:2025–2036.
20. Pratisto H, Frenz M, Ith M, Altermatt HJ, Jansen ED, Weber HP. Combination of fiberguided pulsed erbium and holmium laser radiation for tissue ablation under water. *Appl Opt* 1996;35:3328–3337.
21. Pratisto H, Ith M, Frenz M, Weber HP. Infrared multiwavelength laser system for establishing a surgical delivery path through water. *Appl Phys Lett* 1995;67:1963–1965.
22. Duck FA. *Physical Properties of Tissue: A Comprehensive Reference Book*. San Diego, CA: Academic Press; 1990.
23. Cummings JP, Walsh JT. Tissue tearing caused by pulsed laser-induced ablation pressure. *Appl Opt* 1993;32:494–503.
24. Walsh JT, Flotte TJ, Deutsch TF. Er:YAG laser ablation of tissue: Measurement of ablation rates. *Lasers Surg Med* 1989;9:314–326.
25. Rink K, Delacretaz G, Salathe RP. Fragmentation process induced by nanosecond laser pulses. *Appl Phys Lett* 1992;61:2644–2646.
26. Rink K, Delacretaz G, Salathe RP. Fragmentation process of current laser lithotriptors. *Lasers Surg Med* 1995;16:134–146.
27. Rink K, Delacretaz G, Salathe RP. Fragmentation process induced by microsecond laser pulses during lithotripsy. *Appl Phys Lett* 1992;61:258–260.
28. Bhatta KM. Lasers in urology. *Lasers Surg Med* 1995;16:312–330.
29. Majaron B, Sustercic D, Lukac M, Skaleric U, Funduk N. Heat diffusion and debris screening in Er: YAG laser ablation of hard biological tissues. *Appl Phys B* 1998;66:479–487.
30. Nahen K, Vogel A. Plume dynamics and shielding by the ablation plume during Er: YAG laser ablation. *J Biomed Opt* 2002;7:165–178.
31. Walsh JT, Deutsch TF. Measurement of Er:YAG laser ablation plume dynamics. *Appl Phys B* 1991;5:2217–2224.
32. Nishioka NS, Domankevitz Y. Reflectance during pulsed holmium laser irradiation of tissue. *Lasers Surg Med* 1989;9:375–381.
33. Lee H, Ryan TR, Kim J, Choi B, Arakeri NV, Teichman JMH, Welch AJ. Dependence of calculus retropulsion dynamics on fiber size and laser energy during Ho:YAG lithotripsy. *J Biomech Eng* 2004;126:506–515.
34. Chan KF, Lee H, Teichman JMH, Kameron A, McGuff HS, Vargas G, Welch AJ. Erbium:YAG laser lithotripsy mechanism. *J Urol* 2002;168:436–441.
35. MerbergGN. Current status of infrared fiber optics for medical laser power delivery. *Lasers Surg Med* 1993;13:572–576.

36. Reiss SM. New frontiers emerge in optical fibers. *Biophotonics Int* 2001;8(11):44–51.
37. Harrington JA. *Infrared fibers and their applications*. Bellingham, WA: SPIE Press; 2004.
38. Levin K, Tran D, Tchaponnikov A, Fried NM. Specialty fiber expands infrared laser applications. *Biophotonics Int* 2004;11(4):41–43.
39. Fried NM. Potential applications of the erbium:YAG laser in endourology. *J Endourol* 2001;15(9):889–894.
40. Chaney CA, Yang Y, Fried NM. Hybrid germanium/silica optical fibers for endoscopic delivery of Erbium:YAG laser radiation. *Lasers Surg Med* 2004;34:5–11.
41. Yang Y, Chaney CA, Fried NM. Erbium:YAG laser lithotripsy using hybrid germanium/silica optical fibers. *J Endourol* 2004;18:830–835.
42. Iwai K, Shi YW, Nito K, Matsuura Y, Kasai T, Miyagi M, Saito S, Arai Y, Ioritani N, Okagami Y, Nemec M, Sulc J, Jelinkova H, Zavoral M, Kohler O, Drlik P. Erbium:YAG laser lithotripsy by use of a flexible hollow waveguide with an end-scaling cap. *Appl Opt* 2003;42:2431–2435.

Chapter 10: Dependence of Calculus Retropulsion on Pulse Duration During Ho:YAG Laser Lithotripsy

10.1 ABSTRACT

The purpose of this study was to investigate the effect of optical pulse duration on stone retropulsion during Ho:YAG ($\lambda = 2.12 \mu\text{m}$) laser lithotripsy. A clinical Ho:YAG laser with two selectable pulse durations was employed to fragment calculus phantoms and to evaluate stone phantom retropulsion. At a given pulse energy, optical pulse durations were divided into two discrete conditions: short pulse (τ_p : 120 ~ 190 μsec at FWHM) and long pulse (τ_p : 210 ~ 350 μsec at FWHM). Plaster of Paris calculus phantoms were ablated at different energy levels using optical fibers of varying diameters (273, 365, and 550 μm in core size). The dynamics of the recoil action of a calculus phantom was monitored using a high-speed camera; the laser-induced craters were evaluated with Optical Coherent Tomography (OCT). Bubble formation and collapse were recorded with a fast flash photography setup, and acoustic transients were measured with a hydrophone. Shorter pulse durations produced more stone retropulsion than longer pulses at any given pulse energy. Regardless of pulse

duration, higher pulse energy and larger fibers resulted in larger ablation volume and retropulsion ($p < 0.05$). For shorter pulse durations, more rapid bubble expansion was observed and higher amplitudes of the collapse pressure wave were measured ($p < 0.05$). Less retropulsion and equivalent fragmentation occurred when Ho:YAG pulse duration increased.

10.2 INTRODUCTION

Intracorporeal laser lithotripsy for fragmentation of urinary calculi began in the mid 1980s [1-6]. The clinically available laser lithotrites are the pulsed-dye laser, the frequency-doubled double pulsed Nd:YAG laser (FREDDY), and the Ho:YAG laser [7-9]. The long-pulse Ho:YAG laser is the most efficient and versatile tool for lithotripsy. The Ho:YAG laser fragments all stone compositions and produces less stone migration (retropulsion) during treatment than the short pulsed lasers [10-14]. The dominant mechanism in Ho:YAG laser lithotripsy is photothermal along with minor effects of acoustic emission [15]. Direct light absorption of the urinary calculi increases the temperature of the irradiated volume above the ablation threshold, consequently causing the ejection of fragmented breakdown products. In addition, absorption of laser energy by water between stone and fiber tip induces vapor bubble formation and collapse with shock wave generation. During laser-calculus interaction, the urinary calculus is subject to retropulsion forces induced by the combined effects of ablated particle

ejection, interstitial water vaporization, and bubble expansion/collapse [16-18]. Thus, due to the recoil momentum, the calculus is displaced away from the light delivery fiber. Retropulsive stone movement prolongs operative time owing to the cumbersome process required to reorient the endoscopic fiber toward the new calculus position.

Previous retropulsion studies quantified calculus retropulsion distance by varying optical pulse energy, pulse repetition rate, and fiber diameter [19-21]. Retropulsion increased with applied pulse energy and optical fiber diameter. Further, a recent study reported that a longer pulse width reduced calculus retropulsion distance during a procedure without diminishing ablation efficiency significantly [22]. This study was performed at a single pulse energy setting, and the discrete pulse widths (350 and 700 μsec) described in the study were electrical pulse widths, without characterization of the optical pulse widths.

Since calculus retropulsion can change with optical pulse width and pulse energy, the measurements of optical pulse duration at various energy levels are relevant [21,22]. In this study, we investigate how the optical pulse duration characterizes calculus fragmentation and migration in a water environment with a variable pulse Ho:YAG laser. Stone movements and ablation efficiency are compared with a single pulse as a function of pulse energy and optical fiber diameter. Bubble formation/collapse and accompanying acoustic pressure wave generation are described in terms of stone migration. By measuring retropulsion

distance, ablation volume, and laser-induced pressure, the role of optical pulse duration during Ho:YAG laser lithotripsy was examined.

10.3 MATERIALS AND METHODS

Calculus phantoms were prepared for retropulsion study. The phantoms were made from plaster of Paris (calcium phosphate) with a mass of 150 mg and a volume of 125 mm^3 ($5 \times 5 \times 5 \text{ mm}$). The tensile strength of plaster of Paris (2.0 MPa) approximates that of human calcium and struvite calculi (0.1 to 3.4 MPa) [14]. A transparent rectangular tube ($7 \times 10 \text{ mm}^2$ in size) was utilized as an *in vitro* model of a human ureter, and both ends of the tube were sealed with polymer clay. During retropulsion tests, the calculus phantom was placed in the tube, which was filled with a saline solution prior to laser lithotripsy. In order to minimize the effect of ablation debris on stone movement, the bottom of the tube was cleaned after each test and the saline solution was replaced after every five measurements. Potential experimental error due to friction and drag force was thought to be insignificant since the identical experimental conditions were employed for the two pulse durations.

A variable pulse Ho:YAG laser ($\lambda = 2.12 \text{ }\mu\text{m}$, Odyssey 30, Convergent Laser Technologies, CA) was used. The applied pulse energy ranged from 0.4 to 1.2 J in increments of 0.2 J. The laser system produced two optical pulse conditions due to different electrical pulse durations. Figure 10.1(a) shows the

temporal profiles of two optical pulses measured by a photodetector at the energy of 800 mJ. Pulse duration was dependent on laser pulse energy, and at each energy level, two optical pulses existed, which were designated as short pulse (τ_p : 120 ~ 190 μ sec at FWHM) and long pulse (τ_p : 210 ~ 350 μ sec at FWHM) for the sake of comparison (Figure 10.1(b)).

Stone retropulsion experiments were conducted using a single pulse. Three different diameters of OH⁻ fibers (273, 365, and 550 μ m,) were tested to evaluate the effect of fiber diameter on stone recoil. Each test at every energy level was performed with five measurements. A schematic illustration for this study is presented in Figure 10.2(a). Prior to laser irradiation, an optical fiber was placed in contact with a target sample through the sealing clay, and the irradiation spot was adjusted with a three-axis translation stage to be centered on the sample. The output energy of the fiber was measured with an energy meter (EPM 2000, Molectron, OR) along with a pyroelectric joulemeter (J50, Molectron, OR) after every five measurements. In order to avoid possible artifacts due to fiber tip damage during lithotripsy, the output energy of the fiber was measured after each test. The fiber was repolished if the measured energy was reduced by more than 15 % of the initial output energy.

By means of a delay generator (DGD 535, Stanford Research Systems, CA), a high-speed camera (FASTCAM Super 3K, Photron, CA) was synchronized with the laser system to image the entire retropulsion process and to

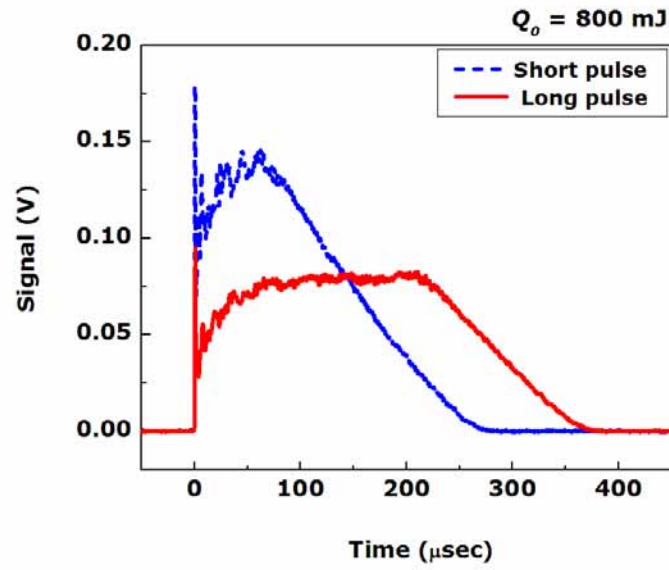
measure the net stone migration distance. In this *in vitro* study, only the axial displacement of the sample was measured since the lateral movement of *in vivo* calculus during laser lithotripsy is significantly restricted by the wall of the ureter in the clinic [21]. The experiment examines the relative retropulsion for two different laser pulse durations. We believe that *in vitro* distances will be representative of stone retropulsion in the softer (more friction) ureter. An illumination light source was applied to the sample in the tube, and the high-speed camera captured the movement of the sample at 1000 frames per second after the onset of laser irradiation. All the acquired images were transferred to the recorder. For the cavitation study, the process of bubble formation/collapse, dependent on optical pulse duration, was monitored using Schlieren flash photography. The Ho:YAG laser was triggered at time t_0 , and a Xenon flashlamp (5 μ s typical exposure time, MVS-2601, EG&G, MA) illuminated the fiber tip in water during laser irradiation to image the cavitation process at the instant time $t_0 + \Delta t$. A sequence of delay times (Δt) controlled by the pulse generator provided images of complete cavitation events. All the images at the various times were captured by a high-speed camera, providing concurrent information on the dynamics of cavitation bubbles. Imaging was performed using the transmittance (shadowgraph) mode. Figure 10.2(b) displays the setup for the fast flash photography experiment.

The laser-induced pressure transients during bubble formation/collapse were measured using a PVDF needle hydrophone (45 ns rise time, HNS hydrophone, Onda Corporation, CA). Pressure measurements were conducted for two different configurations: (1) laser irradiation in clear water and (2) ablation of calculus phantom in contact mode. The hydrophone was placed a few millimeters away from the center of bubble or calculus surface to avoid possible damage due to shock wave generation or ejected fragments (Figure 10.2(b)). Five pressure measurements were performed for each configuration described above.

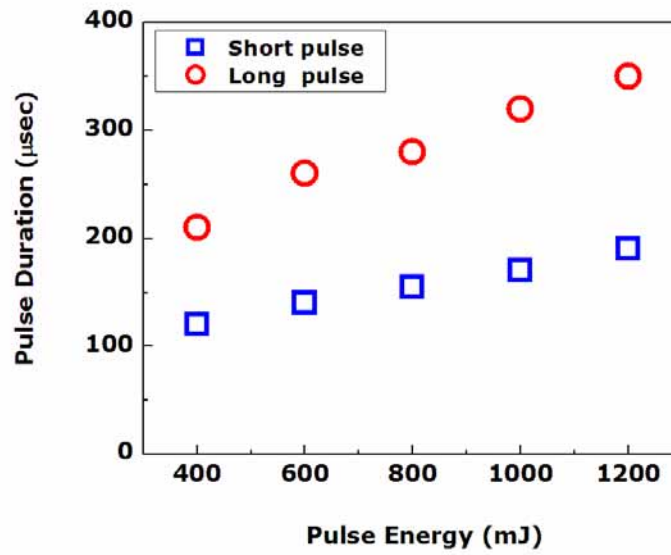
Ablation craters were produced with a single pulse of various settings. Laser-induced craters were examined using an Optical Coherence Tomography (OCT) system ($\lambda_o = 1290$ nm, $\Delta\lambda = 42$ nm, and $P = 2.2$ mW) with lateral and axial resolution of ~ 20 μm to obtain quantitative ablation dimensions [23,24]. A series of vertical cross-sectional images (direction parallel to laser beam propagation) were obtained over the entire crater. The step-size between images was 33 μm . Ablation volume was estimated from the OCT cross sections for each pulse duration regime.

We analyzed ablation crater volumes and retropulsion distances as a function of pulse energy and fiber diameters. Since the clinical objective of laser lithotripsy is to produce maximal fragmentation with minimal retropulsion, we normalized retropulsion for ablation crater volumes. Results were compared

using paired t -tests and one-way analysis of variance (ANOVA). A p -value < 0.05 was considered statistically significant.

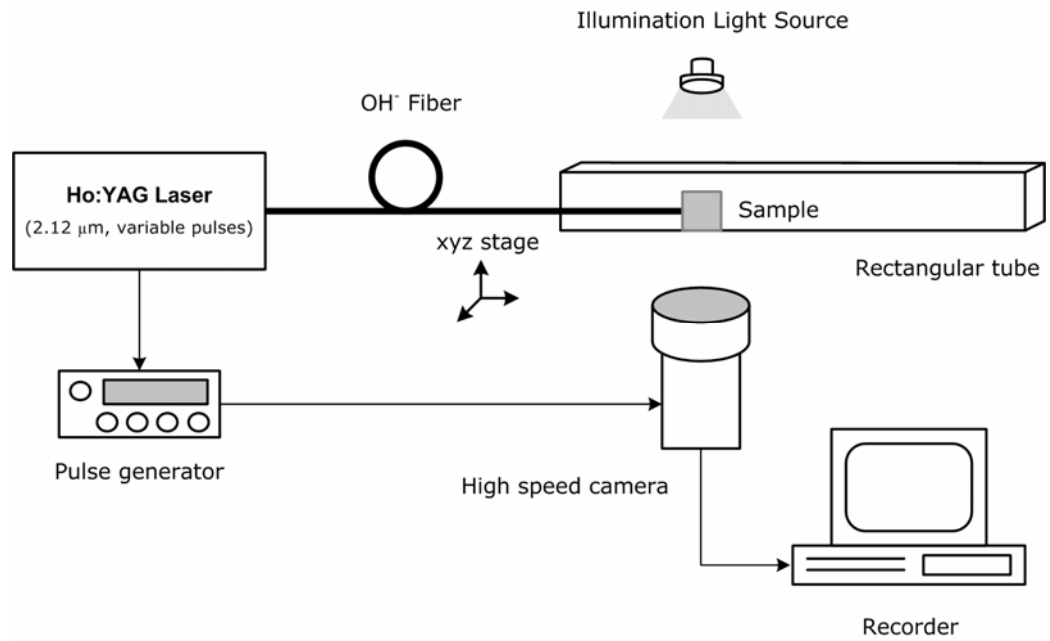


(a)

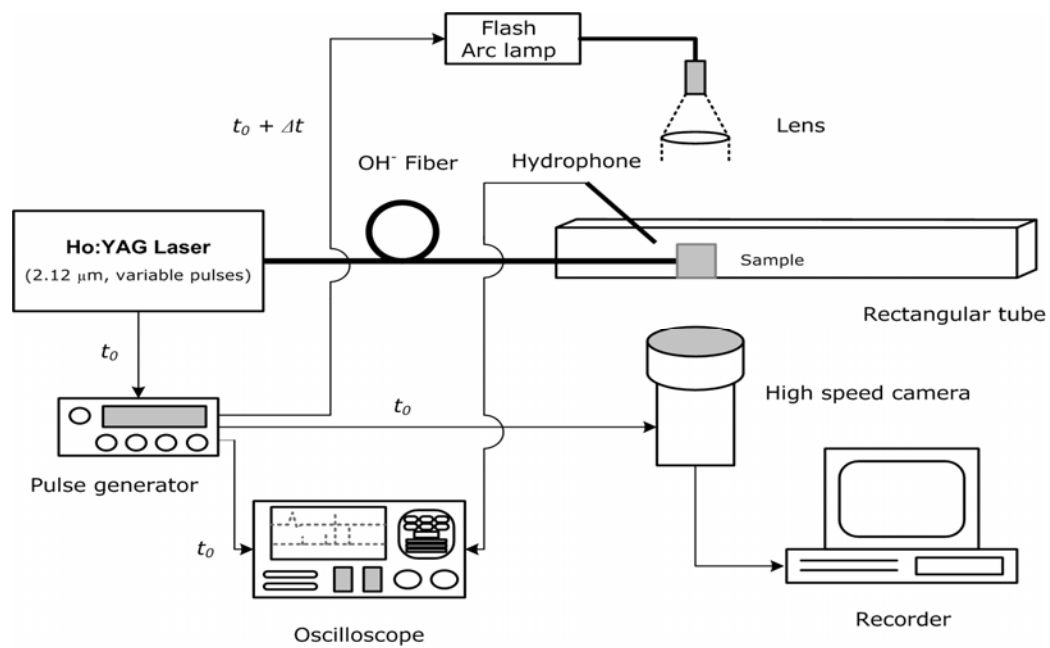


(b)

Figure 10.1. Two different pulse duration regimes of the clinical Ho:YAG laser: (a) optical pulse profiles measured by a photodetector ($Q_0 = 800$ mJ and $n = 32$) and (b) various pulse durations as a function of laser pulse energy.



(a)



(b)

Figure 10.2. Experimental setup for retropulsion study (a) to monitor the stone movement during laser lithotripsy and (b) to image the cavitation process using fast flash photography and to measure the laser-induced acoustic transients.

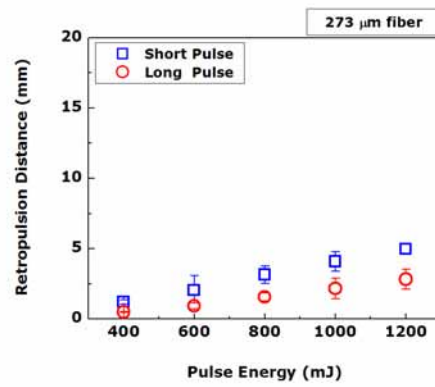
10.4 RESULTS

10.4.1 RETROPULSION DISTANCE MEASUREMENTS

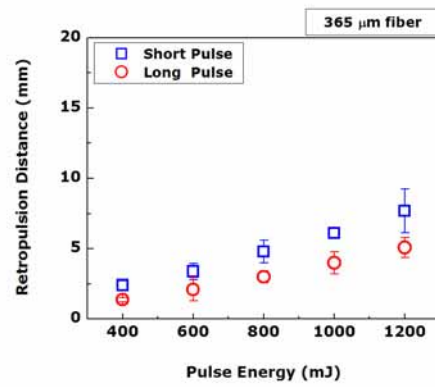
For short and long pulse durations, retropulsion increased as pulse energy and fiber diameter increased (Figure 10.3). Compared to the longer pulse, the shorter pulse durations induced 30 % to 50 % more stone retropulsion movement for a single pulse energy ($p < 0.05$). With a single pulse using a 550 μm fiber, the shorter pulse moved the stone phantom up to 16 mm where as the long pulse induced approximately 12 mm of stone retropulsion.

10.4.2 ABLATION VOLUME MEASUREMENTS

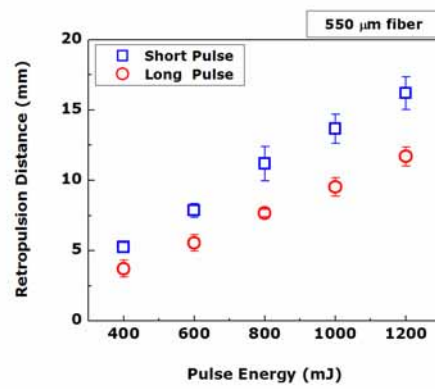
Regardless of pulse duration and fiber diameter, ablation volume increased with pulse energy (Figure 10.4). For the shorter pulse, the measured volumes for all fiber diameters were comparable ($p > 0.05$) at each pulse energy. However, for the longer pulse duration, the differences among ablation volumes of all the fibers were statistically significant ($p < 0.05$); the volumes increased with the diameter of the fiber by up to approximately 15 % at each energy level. Additionally, for any selected pulse energy, the ablation volume produced with the shorter pulse durations was larger than that with the longer pulse.



(a)

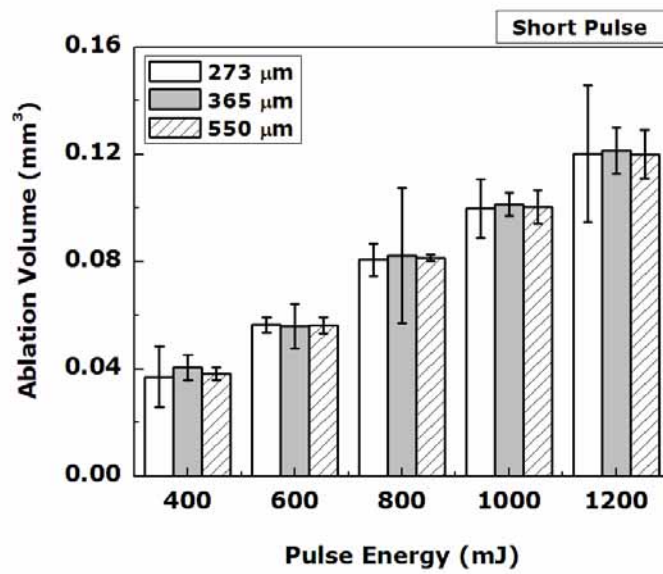


(b)

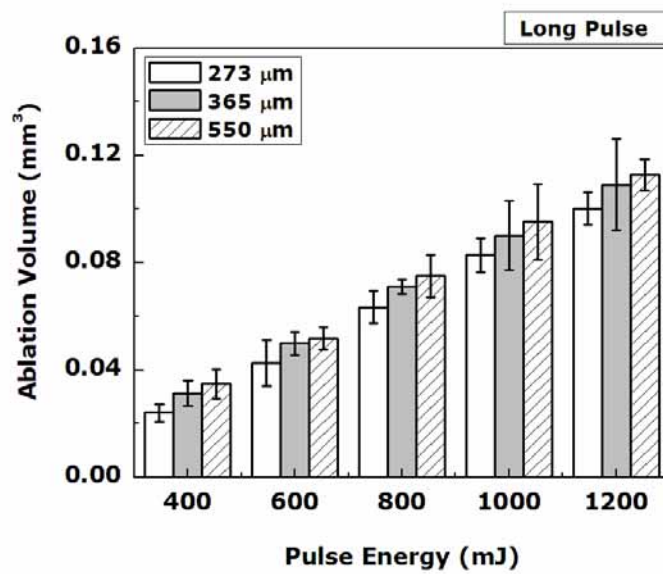


(c)

Figure 10.3. Comparison of stone retropulsion induced with a single Ho:YAG pulse as a function of pulse energy for three different diameters of fibers: (a) 273 μm , (b) 365 μm , and (c) 550 μm ($n = 5$).



(a)



(b)

Figure 10.4. Ablation volume as a function of pulse energy and fiber diameter using (a) short pulse and (b) long pulse durations ($n = 5$)

10.4.3 COMPARISON OF NORMALIZED STONE RETROPULSION

Normalized retropulsion increased with fiber diameter for both pulse durations (Figure 10.5). Retropulsion was comparable at all energy levels regardless of pulse duration and fiber diameter. For all the fibers, the shorter pulse induced approximately 30 % more retropulsion per unit volume than the longer pulse did (Figure 10.5).

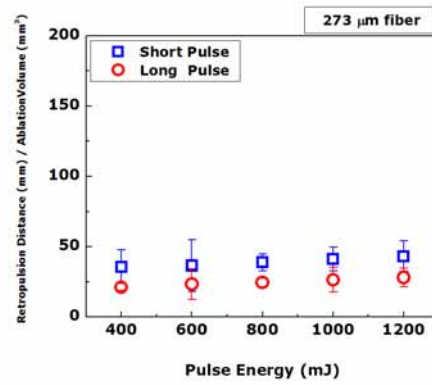
10.4.4 FAST-FLASH PHOTOGRAPHY OF LASER-INDUCED BUBBLE FORMATION

Fast flash images of the dynamics of bubble formation and collapse were acquired with the Ho:YAG laser set at the pulse energy of 800 mJ using a 365 μm fiber. Figure 10.6 presents a compilation of the bubble expansion and collapse sequence in water at room temperature for short ($\tau_p \sim 150 \mu\text{sec}$ at FWHM) and long pulse ($\tau_p \sim 280 \mu\text{sec}$ at FWHM) durations. In general, the shorter pulse-induced bubble was pear-shaped whereas the longer pulse initially produced a pear-shaped bubble, which later appeared as an elongated cylindrical shape due to continuous expansion of parts of the bubble, farther away from the fiber tip. In addition, a real collapse phase and re-expansion of the bubble were observed for the shorter pulse; on the other hand, the longer pulse did not collapse forcefully and re-expansion was not observed. From the time-resolved photographs, it was noted that the shorter pulse durations induced more rapid bubble expansion, which was initiated at the time of 30 μsec after the onset of laser pulse. A faster

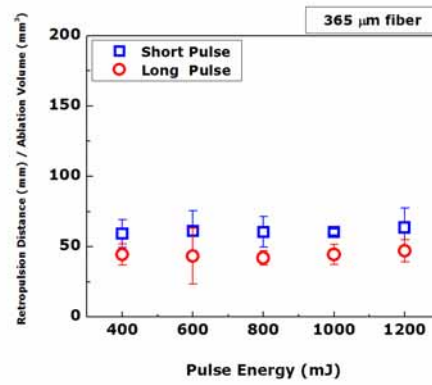
bubble collapse was also observed for the shorter pulse. However, the longer pulse initiated the bubble formation at 80 μsec and showed slower bubble collapse.

10.4.5 ACOUSTIC TRANSIENTS: ABLATION IN WATER

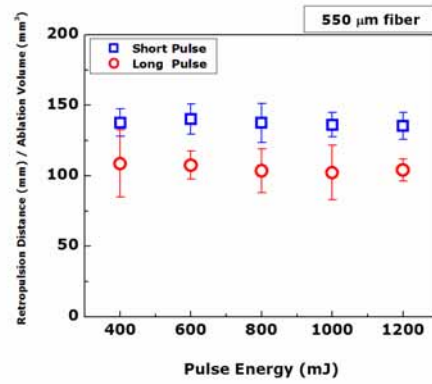
Figure 10.7 shows a temporal profile of the Ho:YAG laser pulses (short pulse of $\sim 150 \mu\text{sec}$ and long pulse of $\sim 280 \mu\text{sec}$ at FWHM) at 800 mJ using a 365 μm fiber and the corresponding pressure transients during bubble expansion and collapse. The pressure transients were measured by a hydrophone in water and corrected to 2 mm away from the center of the bubble. Multiple collapse waves were observed for both pulse durations; a pressure bump with insignificant pressure amplitude was detected after the laser onset as well. However, the shorter pulse caused faster bubble collapse, which was initiated at 450 μsec , compared to the longer pulse. In addition, the amplitude of the first collapse pressure wave of the short pulse was approximately 63 bars, which was about two times greater than that of the long pulse, compared to the collapse pressure of about 33 bars ($p < 0.05$).



(a)

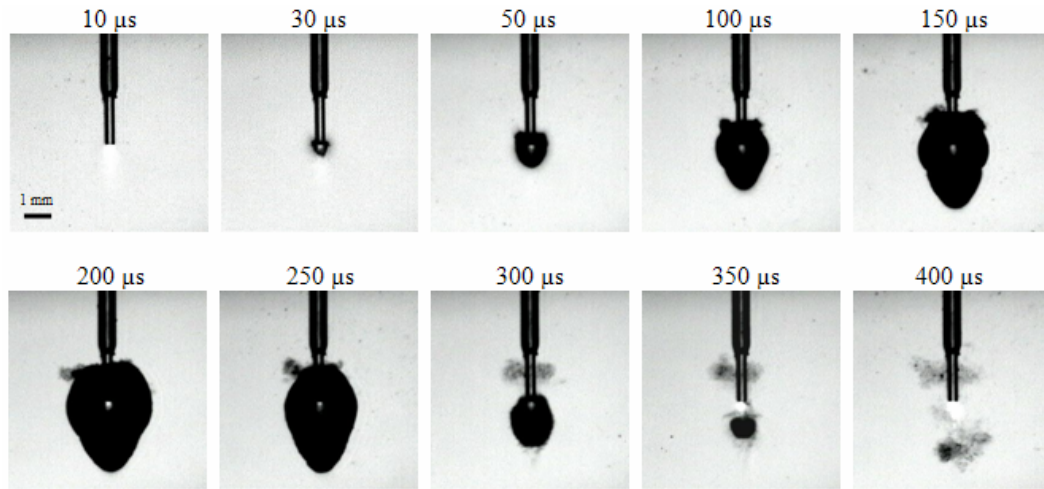


(b)

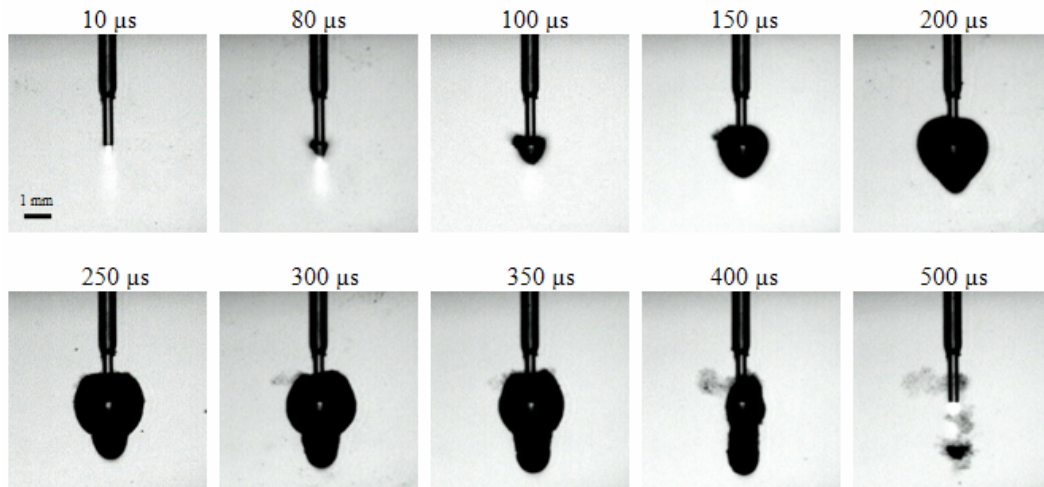


(c)

Figure 10.5. Retropulsion distance normalized with ablation volume as a function of pulse energy for various fibers with a diameter of (a) 273 μm , (b) 365 μm , and (c) 550 μm ($n = 5$).

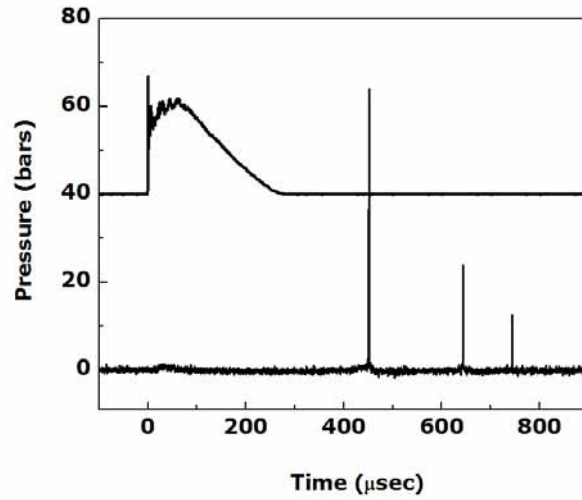


(a)

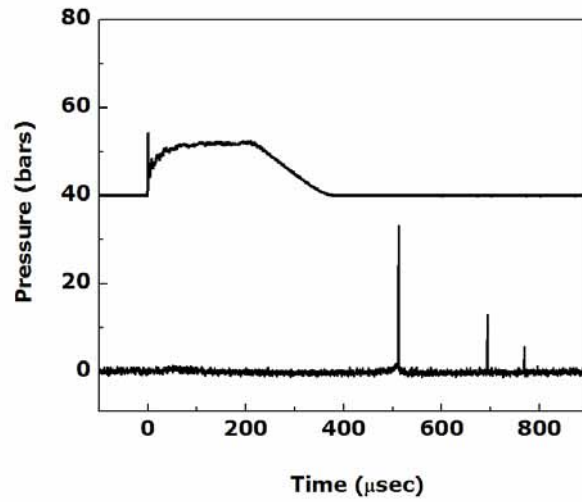


(b)

Figure 10.6. Compilation of bubble expansion and collapse in water at room temperature for two laser pulse durations: (a) short pulse ($\tau_p \sim 150 \mu\text{sec}$ at FWHM) and (b) long pulse ($\tau_p \sim 280 \mu\text{sec}$ at FWHM). Note that the fiber diameter was $365 \mu\text{m}$ and the pulse energy was 800 mJ . Time elapsed after the onset of the laser pulse is shown above each image.



(a)



(b)

Figure 10.7. Temporal profile of the Ho:YAG laser pulses (top) and the measured pressure for each figure: (a) short pulse ($\tau_p \sim 150 \mu\text{sec}$ at FWHM) and (b) long pulse ($\tau_p \sim 280 \mu\text{sec}$ at FWHM). Note that the fiber diameter was $365 \mu\text{m}$ and the pulse energy was 800 mJ. A small pressure bump characteristic of both pulses was detected after laser onset. Bubble collapse occurred at 450 μsec and 510 μsec respectively producing a pressure peak > 20 bars. Rebound and recollapse were also detected approximately 100 μs after the first bubble collapse.

10.4.6 COMPARISON OF BUBBLE COLLAPSE

Since the peak amplitudes of the pressure waves were generated only during bubble collapse, the effect of cavitation collapse on stone retropulsion was investigated. In this experiment, the delivery fiber was suspended in water, and the calculus phantom was located at a distance of ~ 3.5 mm away from the fiber tip. A vapor bubble was produced that did not reach the calculus during the period of either pulse duration. No calculus fragmentation was observed at any time. Figure 10.8 shows the images of stone migration induced by bubble collapse, which were captured by a high-speed camera. The pulse energy was set at 800 mJ with a single pulse. The images showed that after laser irradiation, the bubble collapse induced by the short pulse caused the calculus phantom to move approximately 1.5 mm away from the original location whereas no calculus movement was observed in case of the long pulse even with the presence of bubble formation.

10.4.7 ACOUSTIC TRANSIENTS: ABLATION IN CONTACT MODE

The amplitudes of the bubble collapse pressures for short and long pulse durations were compared during laser lithotripsy (Figure 10.9). The delivery fiber was placed in contact with a calculus sample, and calculus fragmentation was produced with a single pulse at the energy of 800 mJ. A hydrophone was placed 1 mm away from the calculus surface to measure acoustic transients during

cavitation collapse. According to Figure 10.9, the short pulse yielded approximately three times greater amplitude of collapse pressure than the long pulse ($p < 0.05$). The amplitudes of collapse pressure for both pulse durations were correlated with retropulsion movement shown in Figure 10.8; the shorter pulse with higher collapse pressure caused more stone displacement.

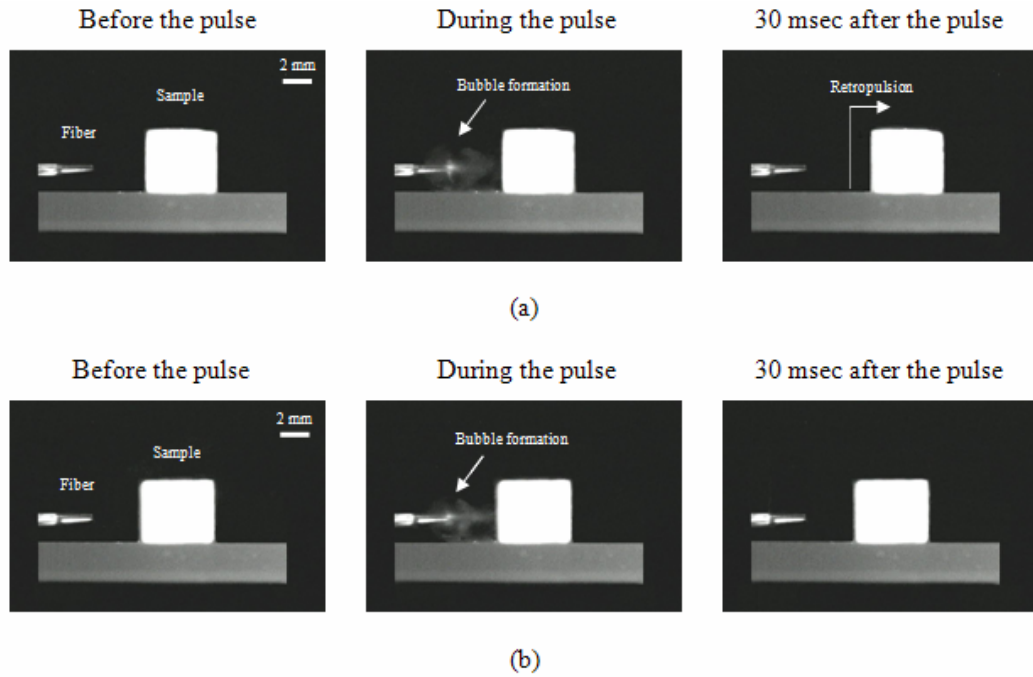


Figure 10.8. Images of calculus retropulsion with noncontact laser lithotripsy at 800 mJ with a single pulse using different pulses: (a) short pulse ($\tau_p \sim 150 \mu\text{sec}$ at FWHM) and (b) long pulse ($\tau_p \sim 280 \mu\text{sec}$ at FWHM). The fiber diameter was $365 \mu\text{m}$. Stone movement of approximately 1.5 mm was observed in case of the short pulse while no movement was seen for the long pulse.

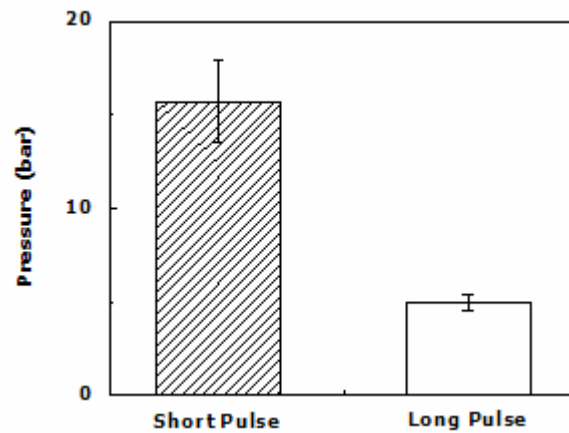


Figure 10.9. Comparison of the amplitudes of collapse pressure produced during lithotripsy with two different pulse durations: short pulse ($\tau_p \sim 150 \mu\text{sec}$ at FWHM) and (b) long pulse ($\tau_p \sim 280 \mu\text{sec}$ at FWHM) ($n = 5$).

10.5 DISCUSSION

A variable long-pulse Ho:YAG laser was used to evaluate the effects of optical pulse duration on calculus fragmentation and retropulsion as a function of pulse energy and fiber diameter with a single pulse. Shorter pulse durations yielded stone displacement up to 1.5 times further and ablation volumes about 1.2 times larger, compared to longer pulses (Figures 10.3 and 10.4). Regardless of pulse duration, an increase in fragmentation and retropulsion was observed with higher pulse energy and larger fiber diameter. When calculus retropulsion was normalized by ablation volume, shown in Figure 10.5, the shorter pulse caused about 30 % more migration than the longer pulse. The shorter pulse produced relatively rapid bubble formation with higher collapse pressure (Figures 10.6 and 10.7) than the longer pulse at the same pulse energy. In addition, based on images captured by a high-speed camera and on pressure measurements, it was observed that bubble collapse was associated with calculus retropulsion; the shorter pulse yielded higher collapse pressure, which was attributed to greater stone migration than the longer pulse (Figures 10.8 and 10.9).

Ho:YAG laser lithotripsy is dominated by thermal breakdown of calculus composition along with direct light absorption and minimal pressure waves [15]. Laser lithotripsy starts when the laser light is transmitted to the calculus through the channel of a vapor bubble, a phenomenon called the “Moses effect” [25,26]. A layer of water 400 μm in depth [27] was rapidly evaporated upon absorption of

the Ho:YAG laser beam, creating a vapor bubble with negligible pressure generation. Photothermal mechanisms of the long-pulsed Ho:YAG have significant clinical implications. The photothermal mechanism implies little risk of collateral damage in an aqueous environment, ejection fragments are small enough to pass painlessly in the urinary tract, all compositions are effectively fragmented, and less retropulsion is produced compared to other lithotripsy modalities [6,15,19-21,27,28].

During laser lithotripsy, human calculus is subject to retropulsion, which necessitates repositioning the fiber tip, prolonging the operation time. Retropulsion is caused by ablation plume ejection due to conservation of momentum [16-19]. Several parameters such as radiant exposure, fiber diameters, direction of plume propagation, and ablation volume determine the recoil momentum of the calculus. Calculus retropulsion increases with pulse energy and fiber diameter and the shape of the crater contributes to augmentation of recoil momentum [20,21]. Reduction in calculus retropulsion was observed for the longer pulse duration while minimally compromising ablation efficiency [22]. Another mechanism associated with bubble dynamics is a high-speed liquid jet induced by asymmetric bubble collapse described as a Kelvin impulse [29]. This is accompanied with a pressure-impulse propagating to the sample boundary, eventually causing the rebound or even rocking motion of the calculus as a part of momentum transfer [21,30]. Analytical models have been developed to interpret

the recoil momentum induced by laser ablation [31]. The “steady-state vaporization” model, appropriate for a long-pulse laser, describes a continuous ablation process by means of the moving ablation front. Estimated recoil stress is based on gas-dynamic equations, for instance, the continuity equation, the Navier-Stokes equation, and the conservation of energy [32].

Pulse Duration

Our reduced calculus migration for the longer pulse durations confirms the results in a previous study showing a reduction in calculus retropulsion for the longer pulse durations while minimally compromising ablation efficiency [22] . Considering the difference in pulse durations at the same pulse energy, less stone movement for longer pulses can be attributed to the occurrence of recoil pressure due to momentum conservation during ablated plume ejection. The absorption of the incident light energy generates heat in the target. Accordingly, the temperature rise at the surface leads to the phase change of the target, resulting in material removal through melting, vaporization, and/or chemical decomposition. Once the ablation process is initiated, the ablated plume is generated as a result of expansion of vapor at the superficial layer. The vapor plume is associated with a strong forward propagation due to the strong temperature and pressure gradients in the axial direction. The species leaving the surface during expansion of gas produces a recoil pressure onto the target [33]. Based on conservation of

momentum, the recoil pressure initially induced by evaporation of the plume from the surface is

$$p_{rec} = 1.79 \rho v \sqrt{\frac{k_B \cdot T_s}{m}} \propto 10^{-5} \cdot P \quad (10.1)$$

where p_{rec} is the recoil pressure (bar), ρ is the density (kg/m³), v is the velocity of ablation front (m/s), k_B is the Boltzmann constant ($= 1.381 \times 10^{-23}$ Ws/K), T_s is the surface temperature (K), m is the mass of plume (kg), and P is the radiant power (actual energy per pulse duration, W). Since the recoil pressure is proportional to the radiant power, the shorter pulse durations with higher power induce larger recoil pressures, which contribute to more calculus fragmentation and migration (Figures 10.3 and 10.4).

Assuming that an equivalent amount of material is removed for short and long pulse durations at the same energy level, the material ejection process with the shorter pulse should be faster, compared to the longer pulse. According to previous studies, the total recoil pressure (p_{tot}) can be expressed as the summation of the pressure of expanding vapor (p_{rec}) and momentum rate induced by plume flow per unit as follows [21,32]:

$$p_{total} = p_{rec} + \frac{m \cdot \Delta v}{A \cdot \Delta t} \quad (10.2)$$

where A is the ablation area (m^2) and t is the time (sec). Given the condition that both pulse durations yield a comparable amount of ablated mass with the equivalent vapor pressure, area and time, the shorter pulse must remove material at a faster rate. The process requires a faster velocity of the ablation front associated with higher recoil pressure and momentum, compared to the case of the longer pulse. Accordingly, the rapid fragmentation caused by the shorter pulse duration may be partially responsible for more calculus retropulsion per unit volume, as shown in Figure 10.5.

Fiber Diameter

Figure 10.3 shows that the calculus migration increased with the fiber diameter: a 550 μm fiber produced the maximum displacement regardless of pulse duration. Crater geometry is hypothesized to be a major contributing factor to increased recoil momentum when using larger fibers [21]. Figure 10.10 shows the cross-sectional OCT images of laser-induced craters produced with different fiber diameters for two pulse durations at 400 mJ. Both short and long pulses demonstrate a similar dependence of crater shape on fiber diameter. At a given pulse energy, laser irradiation with a larger fiber (550 μm) produces wider and shallower craters whereas a smaller fiber (273 μm) yields relatively narrower and deeper craters in agreement with the previous study [21]. Since the ablation plume experiences a strong forward propagation perpendicular to the target

surface [33], the augmented retropulsion associated with the larger fiber is explained by plume particle directions in relation to crater geometry. For the sake of simplicity, propagation velocity and the mass of all particles are assumed to be the same for two different crater shapes as mentioned above. The symmetrical geometry of both craters is also assumed for comparison. During material ejection, the retropulsive force generated by each particle will be normal to the calculus/crater surface and can be resolved into two vector components: one is parallel and the other is perpendicular to recoil direction. Since the perpendicular component (perpendicular with respect to the recoil direction) can be canceled out due to the opposite sign in a symmetrical geometry, the parallel component (parallel with respect to the recoil direction) should correspond to the recoil momentum. Based on a summation of the parallel force vectors and momentum conservation, the larger fiber yields a higher recoil momentum associated with larger parallel components due to wide and shallow geometry of laser-induced craters. Therefore, the shape of the ablated crater can account for the effect of fiber diameter on calculus retropulsion. A detailed description of the retropulsion mechanism dependent on crater geometry can be found in [20,21].

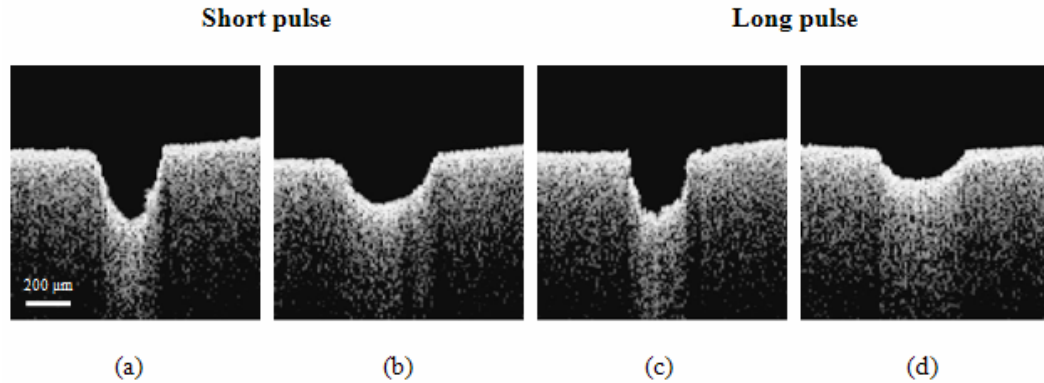


Figure 10.10. Cross-sectional topography of laser-induced craters produced with short pulse ($\tau_p \sim 120 \mu\text{sec}$ at FWHM) using (a) $273 \mu\text{m}$ and (b) $550 \mu\text{m}$ fibers and long pulse ($\tau_p \sim 210 \mu\text{sec}$ at FWHM) using (c) $273 \mu\text{m}$ and (d) $550 \mu\text{m}$ fibers. Note that the applied pulse energy was 400 mJ.

Bubble Dynamics

In Figure 10.6, the short pulse duration produces relatively rapid bubble formation and collapse in water, compared to the long pulse. Multiple pressure peaks with higher collapse pressures occur for the shorter pulse duration in a water environment (Figure 10.7). For a pulse duration of longer than 100 μsec , bubble onset time increases with pulse duration due to the smaller rate of energy deposition in water; the bubble shape also becomes elongated (Figure 10.6) as the pulse duration increases [34]. The amplitude of the bubble collapse pressure wave is strongly dependent on the pulse duration [34]. During Ho:YAG laser lithotripsy, water absorption leads to bubble formation/expansion. Accordingly, since the shorter pulse duration generates a faster rate of bubble growth associated with higher collapse pressure (Figures 10.6 and 10.7), more calculus retropulsion

with the shorter pulse in a water environment can be explained by the pulse-duration dependent dynamics of bubble collapse. Previous studies have demonstrated that a high-speed liquid jet formation takes place when a bubble exists near a solid boundary [33,35]. Due to retarded flow near the boundary, asymmetrical bubble collapse is induced, followed by jet formation directed toward the solid the boundary with a pressure impulse on the target. The generated impulse changes the momentum of the target and even leads to physical damage on the target surface [30,36]. In our experiments, the shorter pulse induces a phantom movement of about 1.5 mm without fragmentation whereas the longer pulse shows no stone migration (Figure 10.8). The shorter pulse yields a higher amplitude of the collapse pressure, compared to the longer pulse (Figure 10.9). Consequently, in addition to higher radiant power and faster plume ejection mentioned previously, the bubble-driven jet formation associated with high collapse pressure accounts for more rebound of calculus during the shorter pulse duration.

Implications

A shorter pulse duration yields more calculus retropulsion owing to higher radiant power, faster plume ejection, and stronger bubble collapse pressure. The effect of shorter pulse duration is responsible for approximately 30 % more stone retropulsion per unit volume (Figure 10.5). Therefore, at a given fiber diameter,

Ho:YAG laser lithotripsy with longer pulse durations will reduce the problem of stone migration during treatment.

Regardless of pulse duration, larger fiber diameters induce more calculus movement because of the larger force vectors parallel to the recoil direction due to crater geometry. As seen in Figure 10.5(a) and (c), doubling the fiber diameter causes three times more retropulsion per volume for both pulse durations. Compared to pulse duration, a reduction in fiber diameter decreases calculus retropulsion more significantly. Hence, as long as the fiber characteristics (diameter, bending curvature, and damage threshold) and ablation efficiency are clinically acceptable, the application of a smaller fiber should be the first choice to minimize stone migration during lithotripsy. By increasing the pulse duration associated with slow plume ejection and weak bubble collapse, the calculus retropulsion and operation time can be further reduced.

The exact role of bubble dynamics and a liquid jet has not been determined. Undoubtedly the separation distance between the delivery fiber tip and calculus is important. In order to clarify how cavitation collapse contributes to the stone migration, high-speed imaging for both short and long pulse durations will be performed in a future study.

10.6 CONCLUSION

The effect of Ho:YAG pulse duration on calculus fragmentation and retropulsion was investigated as a function of pulse energy and fiber diameter. Retropulsion displacement normalized by ablation volume showed that shorter pulse durations yielded more calculus retropulsion possibly due to higher recoil pressure along with faster plume ejection. We believe that larger fibers caused more stone migration regardless of pulse duration because of crater geometry. Our study of bubble dynamics demonstrated that the shorter pulse duration was associated with faster bubble expansion and collapse, and a higher collapse pressure was measured during the shorter pulse duration. The bubble-driven jet formation due to bubble collapse was postulated as one of feasible explanations for augmented calculus movement. It is concluded that the combination of longer laser pulse duration and smaller diameter delivery fibers will minimize calculus retropulsion during Ho:YAG laser lithotripsy.

10.7 REFERENCES

1. Hofstetter A. Lasers in urology. *Lasers Surg Med* 1986;6:412-414.
2. Dretler SP. Laser lithotripsy: a review of 20 years of research and clinical applications. *Lasers Surg Med* 1988;8:341-356.
3. Bhatta KM. Lasers in urology. *Lasers Surg Med* 1995;16:312-330.
4. Vogel A. Nonlinear absorption: intraocular microsurgery and laser lithotripsy. *Phys Med Bio* 1997;42:895-912.
5. Wollin TA, Denstedt JD. The holmium laser in urology. *J Clin Lasers Med & Surg* 1998;16:13-20.

6. Chan KF, Pfefer TJ, Teichman JMH, Welch AJ. A perspective on laser lithotripsy: the fragmentation processes. *J Endourol* 2001;15:257-273.
7. Watson G, Smith N. A comparison of the pulsed dye and holmium lasers for stone fragmentation: *in vitro* studies and clinical experience. *Proc SPIE* 1993;1879:139-142.
8. Tischer C, Koort HJ, Bazo A, Rasch R, Thiede C, World of Medicine Inc., Dept. of Medical Lasers, Orlando and Berlin *et al.* Clinical experiences with a new Frequency-doubled Double-pulse Nd:YAG Laser (FREDDY) for the treatment of urolithiasis. *Proc SPIE* 2002;4609:128-135.
9. Sayer J, Johnson DE, Price RE, Cromeens DM. Endoscopic laser fragmentation of ureteral calculi using the Holmium:YAG. *Proc SPIE* 1993;1879:143-148.
10. Yiu MK, Liu PL, Yiu TF, Chan AYT. Clinical experience with holmium:YAG laser lithotripsy of ureteral calculi. *Lasers Surg Med* 1996;19:103-106.
11. Spindel ML, Moslem A, Bhatia KS, Jassemnejad B, Bartels KE, Powell RC, O'Hare CM, Tytle T. Comparison of holmium and flashlamp pumped dye lasers for use in lithotripsy of biliary calculi. *Lasers Surg Med* 1992;12:482-489.
12. Adams DH. Holmium:YAG laser and pulsed dye laser: A cost comparison. *Lasers Surg Med* 1997;21:29-31.
13. Grasso M, Chalik Y. Principles and Applications of Laser Lithotripsy: Experience with the Holmium Laser Lithotrite. *J Clin Lasers Med & Surg* 1998;1998:3-7.
14. Marguet CG, Sung JC, Springhart WP, L'esperance JO, Zhou S, Zhong P, Albala DM, Preminger GM. In vitro comparison of stone retropulsion and fragmentation of the frequency doubled, double pulse Nd:YAG laser and the holmium:YAG laser. *J Urol* 2005;173:1797-1800.
15. Chan KF, Vassar GJ, Pfefer TJ, Teichman JMH, Glickman RD, Weintraub ST, Welch AJ. Holmium:YAG Laser Lithotripsy: A Dominant Photothermal Ablative Mechanism With Chemical Decomposition of Urinary Calculi. *Lasers Surg Med* 1999;25:22-37.
16. Frenz M, Zweig AD, Romano V, Weber HP. Dynamics in laser cutting of soft media. *Proc SPIE* 1990;1202:22-33.
17. Kuznetsov LI. Recoil momentum at a solid surface during developed laser ablation. *Quantum Electron* 1993;23:1035-1038.
18. Foth HJ, Meyer D, Stockel T. Side effects of laser tissue interaction studied by laser Doppler vibrometry. *Proc SPIE* 2000;4072:392-400.
19. White MD, Moran ME, Calvano CJ, A B.-m., Mehlhaff BA. Evaluation of Retropulsion Caused by Holmium:YAG Laser with Various Power Settings and Fibers. *J Endourol* 1998;12:183-186.

20. Lee H, Ryan T, Teichman JMH, Kim JH, Choi B, Arakeri NV, Welch AJ. Stone retropulsion during holmium:YAG lithotripsy. *J Urol* 2003;169:881-885.
21. Lee H, Ryan RT, Kim JH, Choi B, Arakeri NV, Teichman JMH, Welch AJ. Dependence of Calculus Retropulsion Dynamics on Fiber Size and Radiant Exposure During Ho:YAG Lithotripsy. *J Biomech Eng* 2004;126:507-515.
22. Finley DS, Petersen J, Abdelshehid C, Ahlering M, Chou D, Borin J, Eichel L, McDougall E, Clayman RV. Effect of Holmium:YAG Laser Pulse Width on Lithotripsy Retropulsion *in Vitro*. *J Endourol* 2005;19:1041-1044.
23. Huang D, Swanson EA, Lin CP, Schuman JS, Stinson WG, Chang W, Hee MR, Flotte TJ, Gregory K, Puliafito CA, Fujimoto JG. Optical coherence tomography. *Science* 1991;254:1178-1181.
24. Izatt JA, Kulkarni MD, Yazdanfar S, Barton JK, Welch AJ. In vivo bidirectional color doppler flow imaging of picoliter blood volumes using optical coherence tomography. *Opt Lett* 1997;22:1439-1441.
25. Van Leeuwen TG, van der Veen MJ, Verdaasdonk RM, Borst C. Non-contact tissue ablation by holmium:YSGG laser pulses in blood. *Lasers Surg Med* 1991;11:26-34.
26. Jacques SL. Laser-tissue interactions: photochemical, photothermal, and photomechanical. *Surg Clin N Am* 1992;72:531-558.
27. Jansen ED, van Leeuwen TG, Motamedi M, Borst C, Welch AJ. Temperature dependency of the absorption coefficient of water for mid-infrared laser radiation. *Lasers Surg Med* 1994;14:258-264.
28. Teichman JMH, Vassar GJ, Bishoff JT, Bellman GC. Holmium:YAG lithotripsy yields smaller fragments than lithoclast, pulsed dye laser or electrohydraulic lithotripsy. *J Urol* 1998;159:17-23.
29. Blake JR, Taib BB, Doherty G. Transient cavities near boundaries. part 1: rigid boundary. *J Fluid Mech* 1986;170:479-497.
30. Shangguan H, Casperson LW, Prahl SA. Pressure impulses during microsecond laser ablation. *Appl Opt* 1997;36:9034-9041.
31. Vogel A, Venugopalan V. Mechanisms of pulse laser ablation of biological tissues. *Chem Rev* 2003;103:577-644.
32. Cummings JP, Walsh Jr JT. Tissue tearing caused by pulsed laser-induced ablation pressure. *Appl Opt* 1993;32:494-502.
33. Bäuerle D. *Laser Processing and Chemistry*. Berlin: Springer-Verlag, 2000.
34. Jansen ED, Asshauer T, Frenz M, Motamedi M, Delacretaz G, Welch AJ. Effect of Pulse Duration on Bubble Formation and Laser-induced Pressure

- Waves During Holmium Laser Ablation. *Lasers Surg Med* 1996;18:278-293.
35. Niemz MH. *Laser-Tissue Interactions*. Berlin, Germany: Springer-Verlag, 1996.
 36. CE Brennen. *Cavitation and Bubble Dynamics*. New York: Oxford University Press, 1995.

Chapter 11: Conclusions and Future Studies

11.1 OBJECTIVES

The main purpose of this research was to understand dominant mechanisms involved in IR pulsed laser ablation of biological hard tissue and to achieve efficient material removal with application of a liquid environment. To enhance tissue ablation efficiency as well as to minimize collateral tissue damage, optimal laser parameters (wavelength and pulse duration) with various liquid confinements (liquid layer and water spray) were determined for particular tissue (for example, bone, enamel, and human calculus) properties and clinical situations such as laser osteotomy and laser lithotripsy.

11.2 EFFECT OF LIQUID CONFINEMENT ON ABLATION EFFICIENCY

Enhancement of laser ablation performance assisted by a water layer or water spray was investigated on metals (in Chapters 3 and 4) and biological hard tissues (in Chapters 5-8). As the experimental study in Chapters 3 and 4 indicated, ablation efficiency increased with aid of liquid confinement. It was concluded

that the application of a liquid layer improves optical and acoustical coupling at the surface, resulting in stronger pressure emission via rapid water vaporization and liquid-jet formation. In addition, material properties such as melting point and hardness were significant factors in the degree of material removal during liquid-assisted laser ablation. This finding allows further application of high performance cutting in laser micromachining. However, the physical origin and role of plasma formation during wet metal ablation remains unclear.

As illustrated in Chapters 5, 6, and 7, the study of liquid-assisted laser tissue ablation demonstrated a clinical feasibility in laser osteotomy. It was experimentally shown that explosive vaporization and/or plasma confinement during tissue ablation are responsible for augmented acoustic transients and improved ablation performance. Until this dissertation research, the influence of liquid layer thickness on ablation efficiency was not known. However, by evaluating not only different liquid thicknesses but also various pulse durations, a thinner liquid layer enhances ablation efficiency for both short and long pulse durations. Due to physical limitation of liquid deposition on tissue surface such as surface tension, the application of a thinner layer less than 500 μm remains for future investigations.

One clinical application of liquid was evaluated during laser dental ablation (Chapter 8). It was proposed that diverse mechanisms, for example, rapid vaporization, interstitial water explosion, liquid expulsion with shear stress,

and possibly liquid-jet formation, contribute to improvement of dental ablation when a liquid spray is used in conjunction with the laser pulse. Through this research, spray application during laser dental ablation showed clinical benefits such as additional abrasive effect and water cooling. However, since the cutting efficiency of spray-assisted laser was as much as 50 % lower than a conventional mechanical drill, the optimization of laser and spray parameters still needs more investigations.

11.3 CLINICAL IMPLICATIONS OF LASER LITHOTRIPSY

In order to improve clinical efficiency of pulsed laser lithotripsy, the influence of wavelength and pulse duration on calculus fragmentation was investigated in Chapters 9 and 10, respectively. This dissertation research concluded that the Er:YAG laser ($\lambda = 2.94 \mu\text{m}$) lithotripsy can provide higher efficiency for various types of calculus (COM, Cystine, MAPH, and UA) with less thermal damage, compared to Ho:YAG laser ($\lambda = 2.12 \mu\text{m}$) that is a conventional lithotrite (Chapter 9). However, a major concern is still the lack of a practical infrared fiber to deliver Er:YAG laser endoscopically.

Another experimental study (Chapter 10) demonstrated a feasible means to reduce the operative time and cumbersome process by retropulsive kidney stone movement during clinical Ho:YAG laser lithotripsy: a smaller fiber diameter with a longer pulse duration is highly desirable due to reduction in stone

migration during treatment. Further investigations on the effect of the separation distance between the delivery fiber and calculus are necessary for more efficient laser lithotripsy.

11.4 FUTURE DIRECTIONS

11.4.1 ROLE OF INDIVIDUAL PULSE IN MACROPULSE ABLATION

As one of future studies, the role of each micropulse in macropulse tissue ablation can be investigated. A macropulse consists of a train of micropulses with 1 ps pulse duration. The OPA ps pulse system at the Stanford FEL Center provides a unique system to evaluate the importance of pulse separation and superposition during the macropulse ablation process. Varying the optical path length, the time delay between consecutive micropulses can be used to examine the effect of individual pulse. The dynamics of macropulse ablation will be determined in terms of ablation threshold, number of pulse, and radiant exposure.

11.4.2 MID-INFRARED PULSED LASER ABLATION

Due to the wide differences in the absorption modes of biological tissues, it may not be optimal to ablate tissue using wavelengths associated with water absorption bands. Of particular interests are the Amide I and Amide II vibrational modes at 6.1 μm and 6.45 μm [1]. In addition, pulsed laser interaction with a liquid-layer deposited on the surface has been of interest due to improvement of

ablation efficiency with decreased ablation threshold. Using an IR transparent liquid layer such as perfluorocarbon to lower the macropulse energy for ablation will extend medical application of FEL systems without the expense associated with increasing macropulse energy. Mid-infrared laser ablation will be characterized by means of various wavelengths as well as application of an IR transparent liquid layer.

11.4.3 EVALUATION OF HOLLOW WAVEGUIDE FOR ER:YAG LASER LITHOTRIPSY

Due to several advantages such as low insertion and transmission loss and high flexibility, a hollow waveguide has been proposed as an alternative infrared light delivery system for Er:YAG laser [2,3]. The major drawback is water intrusion into the hollow waveguide during endoscopic applications. Meanwhile, several studies have shown the feasibility of *in vitro* Er:YAG laser lithotripsy with an end-sealed hollow waveguide for calculus fragmentation [4-7]; however, the deterioration of the sealing caps is still problematic. Further investigations on endoscopic applications of the hollow waveguide are still required to achieve efficient delivery of Er:YAG laser light for clinical treatments.

11.5 REFERENCES

1. Harris DC, Bertolucci MD. Symmetry and Spectroscopy: An Introduction to Vibrational and Electronic Spectroscopy. New York: Dover Publications, 1990.
2. Harrington JA, Matsuura Y. Review of hollow waveguide technology. Proc SPIE 1995;2396:4-14.
3. Matsuura Y, Abel T, Harrington JA. Optical properties of small-bore hollow glass waveguides. Appl Opt 1995;34:6842-6847.
4. Kozodoy RL, Pagkalinawan AT, Harrington JA. Small-bore hollow waveguides for delivery of 3- μ m laser radiation. Appl Opt 1996;35:1077-1082.
5. Wang Y, Matsuura Y, Miyagi M. Robust hollow devices and waveguides for Er:YAG laser radiation. Opt Laser Tech 1997;29:449-453.
6. Mohri S, Kasai T, Abe Y, Shi Y, Matsuura Y, Miyagi M. Optical properties of end-sealed hollow fibers. Appl Opt 2002;41:1251-1255.
7. Iwai K, Shi Y, Nito K, Matsuura Y, Kasai T, Miyagi M, Saito S, Arai Y, Ioritani N, Okagami Y, Nemec M, Sulc J, Jelinkova H, Zavoral M, Kohler O, P D. Erbium:YAG laser lithotripsy by use of a flexible hollow waveguide with an end-scaling cap. Appl Opt 2003;42:2431-2435.

APPENDIX A: Calculus Fragmentation in Laser Lithotripsy

A.1 ABSTRACT

The intracorporeal treatment of urinary calculi with lasers is presented, which describes laser-calculus interactions associated with lithotripsy. Reliable fragmentation of calculi with diverse compositions and minimal collateral tissue damage are primarily contingent upon laser parameters (wavelength, pulse duration, and pulse energy) and physical properties of calculi (optical, mechanical, and chemical). The pulse duration governs the dominant mechanism in calculi fragmentation, which is either photothermal or photoacoustical/photomechanical. Lasers with long pulse durations (i.e. $>$ tens of microseconds) induce a temperature rise in the laser-affected zone with minimal acoustic waves; material is removed by means of vaporization, melting, mechanical stress, and/or chemical decomposition. Short-pulsed laser ablation (i.e. $< 10 \mu\text{s}$), on the other hand, produces shock waves, and the resultant mechanical energy fragments calculi. Work continues throughout the world to evaluate the feasibility of advanced

lasers in lithotripsy and to optimize laser parameters and light delivery systems pertinent to efficient fragmentation of calculi.

A.2 INTRODUCTION

Laser lithotripsy for fragmentation of urinary and biliary calculi began in the mid 1980s [1-6]. The first successful clinical application was achieved with a flashlamp pumped pulsed-dye laser beam delivered through an optical quartz fiber [7-20]. The 1 μ s pulsed-dye laser with a wavelength of 504 nm initiated a plasma expansion between the tip of the fiber and the calculus which generated a cavitation bubble. The collapse of the bubble created shock waves [21-24], which were the principal mechanism of fragmentation. The process is called laser-induced shockwave lithotripsy (LISL) [25].

In contrast to LISL, a new treatment modality for lithotripsy was introduced in the mid 1990s with the long-pulsed Ho:YAG laser ($\lambda = 2.12 \mu\text{m}$, $\tau_p = 250 \mu\text{s}$) [26,27]. The fragmentation mechanism of urinary calculi was dominated by a photothermal process with concomitant mechanical stress and chemical decomposition of the irradiated calculus components [28,29]. Fragmentation with the holmium laser irradiation was accompanied with minimal photoacoustical effects [30,31].

Multiple clinical papers demonstrate that the long-pulsed Ho:YAG laser is the current laser of choice for endoscopic lithotripsy of ureteral calculi and of

many renal calculi [32-34]. The principal advantages of the Ho:YAG laser over all other currently available devices for stone fragmentation are that the laser energy can be delivered through small (200 μm diameter) flexible optical fibers permitting use of the laser with a small caliber (7 Fr) flexible ureteroscopes, the ability to fragment all stone compositions, and the ability to break stones into tiny fragments that are easily passed with little risk of ureteral obstruction [35,36].

This paper describes how laser light interacts with water and calculi to explain the underlying mechanism(s) of laser lithotripsy. Lasers and fiber delivery systems are compared and we try to provide some insight into future systems.

A.3 LASER-INDUCED ABLATION (FRAGMENTATION)

The goal of laser-induced ablation is the efficient removal of calculus with minimum damage to surrounding tissue. Response of calculi to intense laser irradiation is a function of laser parameters and material properties of calculus and water. Laser parameters include wavelength, pulse duration, pulse energy, and fiber diameters (spot size) whereas material properties are associated with optical, thermal, mechanical, and chemical properties of calculi [37-45]. The nomenclature of laser parameters and material properties used in this paper is summarized in Table A.1.

Regardless of fragmentation mechanisms, absorption of laser energy (photons) in the calculus or the surrounding water initiates calculus fragmentation. The absorption of laser energy by a calculus or water is characterized by the absorption coefficient, μ_a [cm^{-1}] of the target. The higher the absorption coefficient, the more absorbed laser energy is concentrated at the surface of the target. The fluence, $F(z)$ [J/cm^2] of a laser beam inside a target, which represents the energy distribution as a function of depth, z [cm], is determined by both the incident laser radiant exposure at the surface, H_o [J/cm^2] and the absorption coefficient (μ_a), assuming light scattering is no larger than absorption [37,46]. According to Beer's law, the fluence, $F(z)$ [J/cm^2] exponentially decreases with the depth, z [cm]

$$F(z) = H_o \cdot \exp(-\mu_a \cdot z) \quad (\text{A.1})$$

The optical penetration depth, δ [cm] is the depth at which the energy of the collimated laser is reduced by 37 % (a factor of $1/e$) of the incident energy. This depth is defined as the reciprocal of the wavelength dependent absorption coefficient, $\mu_a(\lambda)$

$$\delta(\lambda) = \frac{1}{\mu_a(\lambda)} \quad (\text{A.2})$$

Table A.1. Nomenclature of laser parameters and tissue properties [37].

Type	Symbol	Description	Definition	Units
Laser Parameters	λ	Laser wavelength		nm or μm
	τ_p	Laser pulse duration	Time extent of a pulse	nsec or μsec
	Q_o	Laser pulse energy	Optical energy delivered per pulse	mJ or J
	F	Fluence	Optical energy per unit area	J/cm^2
	H_o	Radiant exposure	Optical energy delivered per pulse per unit area	J/cm^2
Tissue Properties	μ_a	Absorption coefficient		1/cm
	δ	Optical penetration depth	$\delta = 1/\mu_a$ – mean free path for attenuation event	cm
	α	Thermal diffusivity	Measure of heat flow	mm^2/s
	σ	Speed of sound	Speed of sound in tissue or water	$\text{mm}/\mu\text{s}$
	τ_{th}	Thermal diffusion time	Degree of heat diffusion within optical penetration depth	μsec or msec
	τ_a	Acoustic diffusion time	Degree of acoustic wave diffusion within optical penetration depth	μsec or msec
Other parameters	z	Depth	Depth in tissue	cm
	r_o	Laser spot size	Radius of laser spot on the tissue surface	mm
	P	Pressure	Magnitude of stress wave or shock wave	bar or kbar
	T	Temperature rise	Temperature increase induced by stress wave or shock wave	$^{\circ}\text{C}$

Typically, laser induced tissue ablation is the outcome of combination of two or more mechanisms. Nevertheless, in pursuit of simplicity, we categorize the laser ablation into two groups: photothermal and photoacoustical/photomechanical. Different fragmentation processes contingent upon the pulse duration are delineated in Figure A.1.

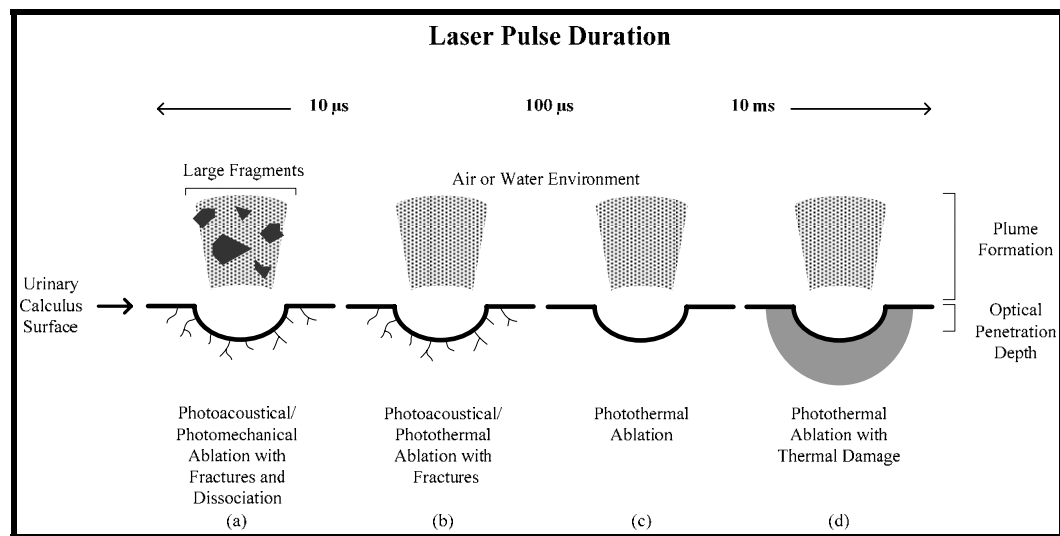


Figure A.1. The primary mechanism for photofragmentation is contingent on pulse duration. (a) Pure photoacoustical/photomechanical ablation is associated with internal fractures and large calculus dissociation. (b) Photothermal ablation with internal fractures involves minor photoacoustical/photomechanical effects. (c) Localized photothermal ablation without collateral damage to adjacent tissue is the most desirable phenomenon for laser lithotripsy. (d) Photothermal ablation with thermal damage to surrounding tissue (carbonization).

A.3.1 PHOTOTHERMAL ABLATION

The temperature rise in calculi induced by laser pulses over 100 μ s the laser-affected zone (where photons are directly absorbed) is the most common feature of the interaction of laser light with matter. The photon energy of the incident laser is absorbed in the target by means of the excitation of electrons and molecules to higher energy levels. Excited particles transfer their energy to neighboring particles through a collision process, resulting in the increase of microscopic kinetic energy. Macroscopically, the increase of kinetic energy is interpreted as the temperature rise that may lead to the phase transfer of the target material. The resultant removal of the melted, vaporized and chemically decomposed material is called *photothermally induced laser ablation (fragmentation)*.

The most challenging issue involving thermally induced ablation is the minimization of collateral damage [47-51]. The thermal energy in the laser-affected zone dissipates into surrounding regions through the process of heat diffusion, generating undesirable collateral damage. Damage to adjacent tissue can be minimized or eliminated by the selection of wavelengths and pulse durations to reduce the degree of thermal diffusion. The time which is required for the initial deposited laser energy to move beyond the laser-affected zone is called thermal diffusion time, τ_{th} [sec] and is

$$\tau_{th} = \frac{\delta^2}{4\alpha} \quad \text{when } r_0 \geq \delta \quad (\text{A.3})$$

$$\tau_{th} = \frac{r_o^2}{4\alpha} \quad \text{when } r_0 < \delta \quad (\text{A.4})$$

where α is the thermal diffusivity [mm^2/s] and r_o is the laser spot radius [mm]. In practice, the penetration depth of laser light in calculi is smaller than the typical spot size. When the laser pulse duration, τ_p [sec] is much shorter than the thermal diffusion time, τ_{th} (i.e. $\tau_p \ll \tau_{th}$), the absorbed energy accumulates within the region of absorbed photons which is characterized by the laser spot diameter and penetration depth of the laser beam. There is little heat diffusion from this region during the laser pulse. This condition is referred to as *thermal confinement* [45]. The localization of deposited energy leads to efficient material removal, i.e. most of the pulse energy is consumed by the “pure” ablation process without significant diffusion of thermal energy to adjacent regions. For example, long-pulsed Ho:YAG and Nd:YAG lasers ($\tau_p = 200\sim 500 \mu\text{s}$) operate in the thermal confinement region. Images of Ho:YAG laser-induced craters of a struvite calculus are shown in Figure A.2. For pulse duration longer than the thermal relaxation time (i.e. $\tau_p > \tau_{th}$), it is difficult to confine the absorbed energy to the ablation process, and thermal damage occurs in the form of coagulation and carbonization of tissue. Optical energy absorbed from CW and millisecond-pulsed lasers is not thermally confined due to the long pulse durations (Figure A.3) [52-53].

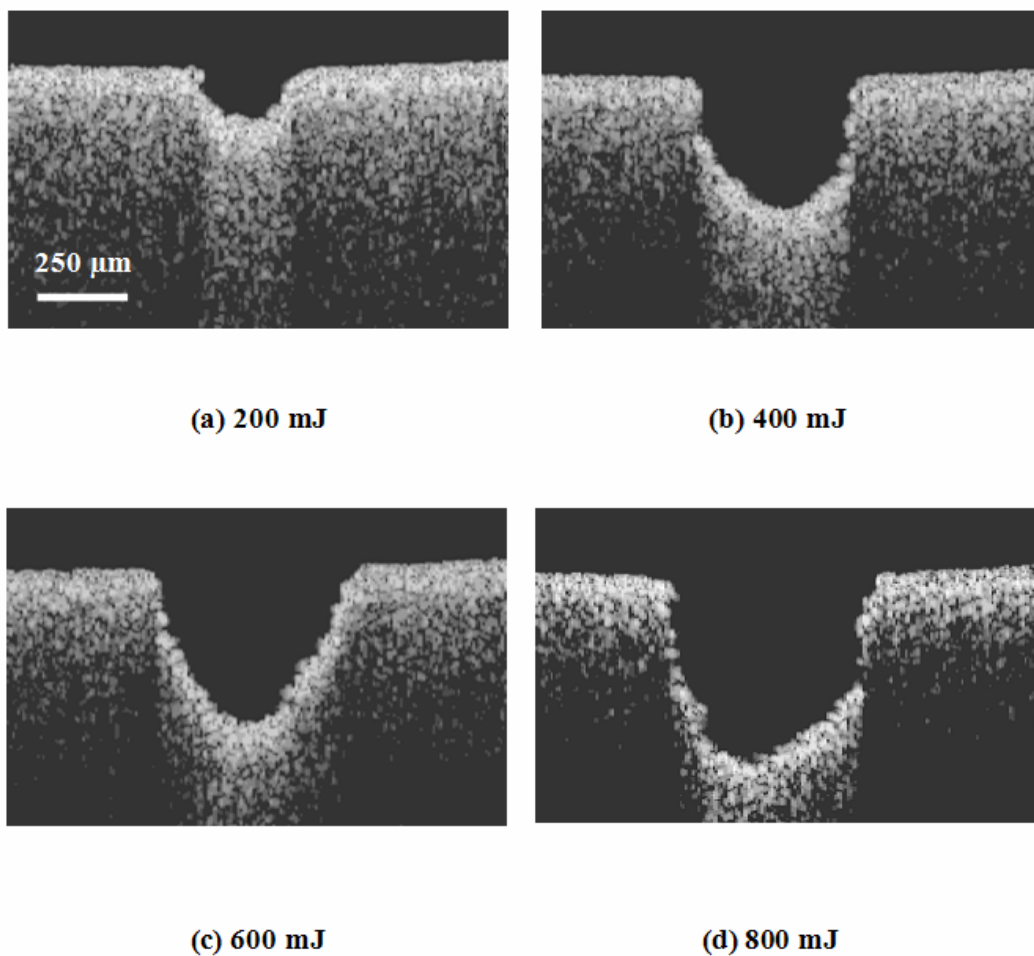


Figure A.2. Cross-sectional topography of laser-induced craters was acquired with optical coherence tomography (OCT). Single pulse of Ho:YAG laser at different levels of laser energy was applied to struvite calculus through 273 μm optical fiber. Localized photothermal ablation created the hemisphere shape crater in the calculus.

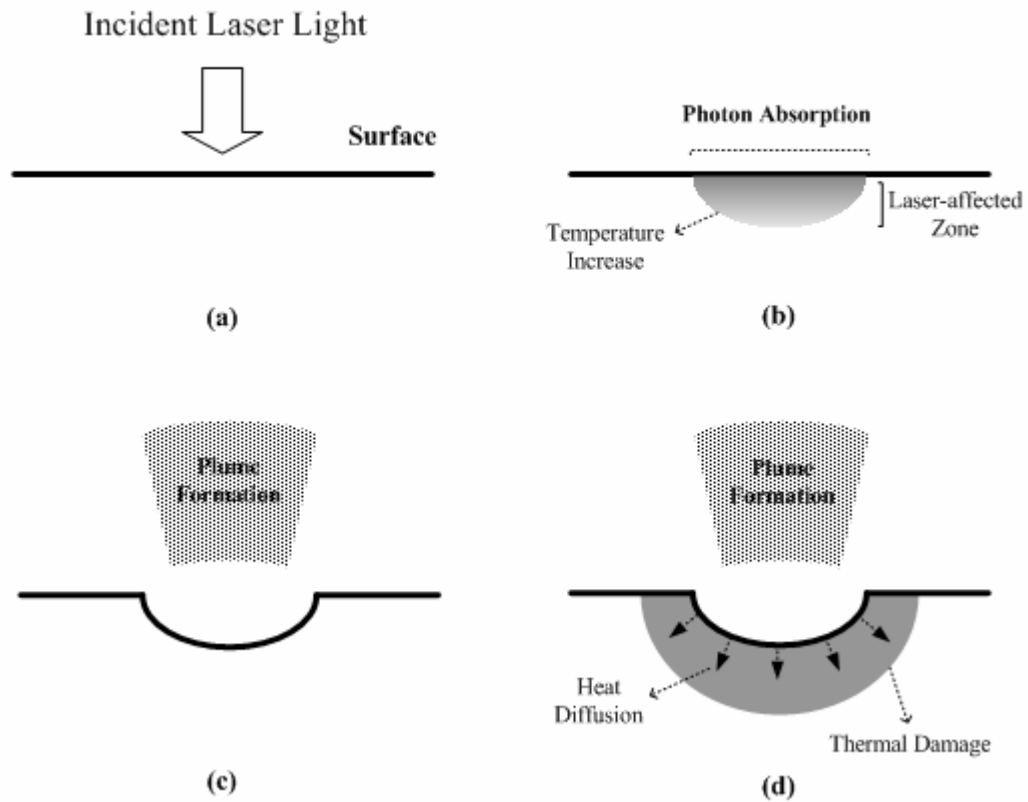


Figure A.3. Schematic illustration of photothermal interaction. (a) Incidence of laser light on the target surface. (b) Optical energy absorption in the laser-affected zone and subsequent temperature rise. (c) Photothermal ablation with plume formation and phase transfer with little heat diffusion for shorter pulse durations (i.e. $\tau_p \ll \tau_{th}$). (d) Laser-induced ablation accompanied with collateral tissue damage (e.g. carbonization or coagulation) due to longer pulse duration (i.e. $\tau_p > \tau_{th}$).

A.3.2 PHOTOACOUSTICAL/PHOTOMECHANICAL ABLATION

The response of materials to sub microsecond laser pulses can be violent and explosive. As a result of the rapid temperature rise, the target experiences an impulsive mechanical excitation that creates stress waves (acoustic and shock waves) [45,54,55]. Bulk material removal induced by the mechanical energy is called *photoacoustically/photomechanically induced ablation (fragmentation)*. In order to excite a stress wave that is strong enough to cause physical damage, the laser pulse duration (τ_p) should be shorter than the acoustic diffusion time, τ_a [sec] which is the time required for the stress wave to propagate out of the zone of absorbed photons. Since the stress wave travels through a medium at the speed of sound, σ [mm/ μ sec], the acoustic diffusion time is defined as

$$\tau_a = \frac{\delta}{\sigma} \quad (\text{A.5})$$

A laser pulse whose duration is shorter than τ_a builds up mechanical energy within the optically affected zone in the form of acoustic waves. This condition is called the *stress confinement condition* [45] and is determined by the following criterion

$$\tau_p < \tau_a \quad (\text{A.6})$$

Photoacoustical/photomechanical effects are characterized by thermoelastic expansion, microexplosion, and shock wave generation.

Thermoelastic Expansion

At a relatively low energy setting, thermoelastic expansion is induced under the stress confinement condition illustrated in Figure A.4. The fluence (F) still follows the Beer's law (Equation A.1). As mentioned in the previous section, the laser energy absorption induces a rapid heating that causes the target medium to undergo an instantaneous mechanical expansion and a compressive pressure (stress wave) is generated in the irradiated volume. The amplitude (P) of the stress wave and the temperature rise (T) is proportional to the product of the laser fluence (F) and the calculus absorption coefficient (μ_a). Both P and T have the form

$$\mu_a \cdot H_o \cdot \exp(-\mu_a \cdot z) \quad (\text{A.7})$$

Once the stress wave is generated, it propagates in two directions: into the target (downward) and out of the target (upward) with half amplitude of the initial value in each direction. While the downward wave propagates deeper without interruption, the upward wave is reflected at the interface between the target and surrounding medium due to the acoustic impedance mismatch. If the impedance of the medium is much smaller than that of the target, this condition called *pressure release surface condition*, the reflected wave changes its sign (phase) and become a negative wave (tensile wave). This rarefactive wave trails the positive wave forming a bipolar wave. If the tensile strength at a certain point in

the target is weaker the strength of the rarefactive wave, the target starts to tear apart, resulting in a bulk material removal. This photomechanical ablation process is called *spallation* (Figure A.4) [56].

Microexplosion

Laser-induced microexplosions can be observed when lasers interact with tissue that contains water. Most soft tissues contain 70-85 % water. For hard tissues, such as bone, teeth, and calculus, the pores between the calcified materials are filled with about 10 % water. When calculi are irradiated with an IR laser whose wavelength is close to the absorption peak of water, vaporization of water takes place. Subsequently, pressure inside the gaps and pores quickly builds, leading to rupturing. This process is called *microexplosion* (Figure A.5) [57,58].

Shock Wave Induced Ablation

The primary ablation process for sub-microsecond laser pulses is associated with shock waves that travel at supersonic speed with strong mechanical energy. Once created, the shock wave induces ablation and fractures inside the calculus. Shock waves are produced during plasma expansion and/or bubble collapse. Sudden thermoelastic expansion generates a stress wave as well.

If the laser light is absorbed by water, a bubble is created and accumulated stress during the pulse duration yields an intense pressure gradient during the expansion of bubble. This shock wave is followed by a second shock wave owing to the collapse of the bubble. Both shock waves are associated with calculus

fragmentation [24,59-61]. As a shock wave propagates throughout the urinary calculus, it may fracture the inside the crystalline structure.

When the calculus is exposed to extremely high irradiance of more than 10^{10} W/cm² and pulse durations less than 1 μ s, a phenomenon called *optical breakdown* occurs [39,40,62-67]. The laser creates numerous ionized molecules and free electrons. These ionized molecules and electrons are ejected from the surface and form a localized cloud called *plasma*. If the plasma is generated before the end of a laser pulse, the remaining pulse energy is absorbed by the plasma. As a result of this, the plasma expands rapidly and eventually collapses [68,69]. As mentioned in the previous section, the rapid expansion of plasma can induce shock waves that produce photomechanical fragmentation (Figure A.6).

For example, the Q-switched Nd:YAG laser ($\tau_p = 8\text{-}20$ ns) and the pulsed dye laser operate in stress-confined region due to short pulse duration and generate a shock wave (i.e. typically pressure $P > 100$ bars) by means of plasma expansion and/or cavitation collapse. The resulting fragmentation is typically called *laser-induced shock wave lithotripsy* (LISL). Craters of cystine induced by the Q-switched Nd:YAG laser are presented in Figure A.7. On the other hand, for pulse durations longer than the acoustic diffusion time (i.e. $\tau_p > \tau_a$), stress relaxation occurs as the acoustic wave escapes the zone of photon absorption. Consequently, the resultant pressure wave induced by long pulse durations is not

strong enough (i.e. typically $P < 20$ bars) to be responsible for initiation of fragmentation.

Laser-induced fragmentation is often the influence of combined mechanisms. For instance, the ejection of melted and vaporized material (photothermally-induced products) is driven by a high pressure field (photomechanically-induced product) which is built in the crater. Due to its high energy, laser-induced plasma always causes additional thermal and mechanical effects in the vicinity of a crater. In addition, most photoacoustical/photomechanical mechanisms begin with the heating of the target, which is a photothermal effect.

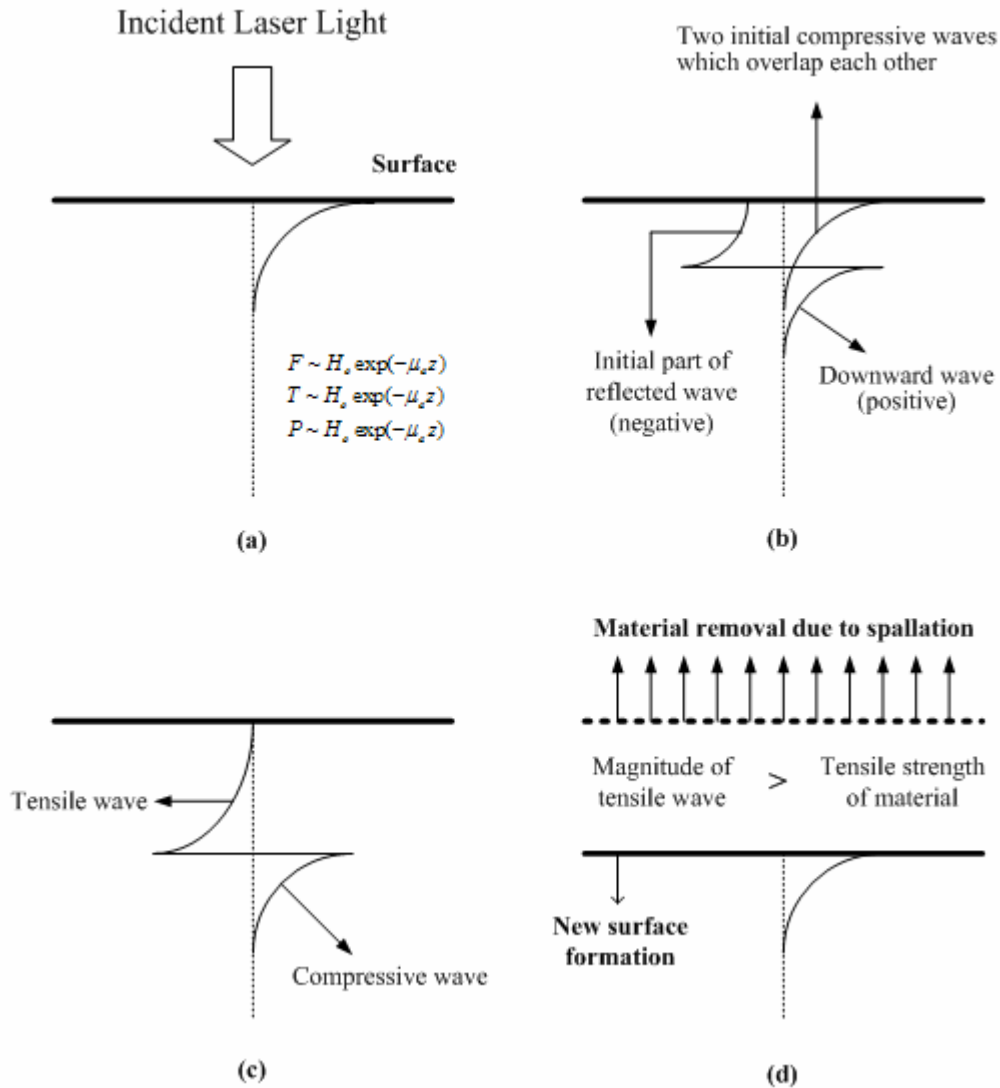


Figure A.4. The illustration describes the spallation process. (a) The incident light produces a temperature and pressure profile that follows the fluence distribution along the laser beam axis. (b) Laser-induced stress waves (initially compressive waves) travel in two directions (upward and downward). The upward wave becomes a tensile wave upon the reflection at the target surface. (c) The wave with two poles keeps propagating into the target. (d) If the material tensile strength at a certain location is weaker than the strength of the tensile wave, spallation (photoacoustical/photomechanical ablation) takes place.

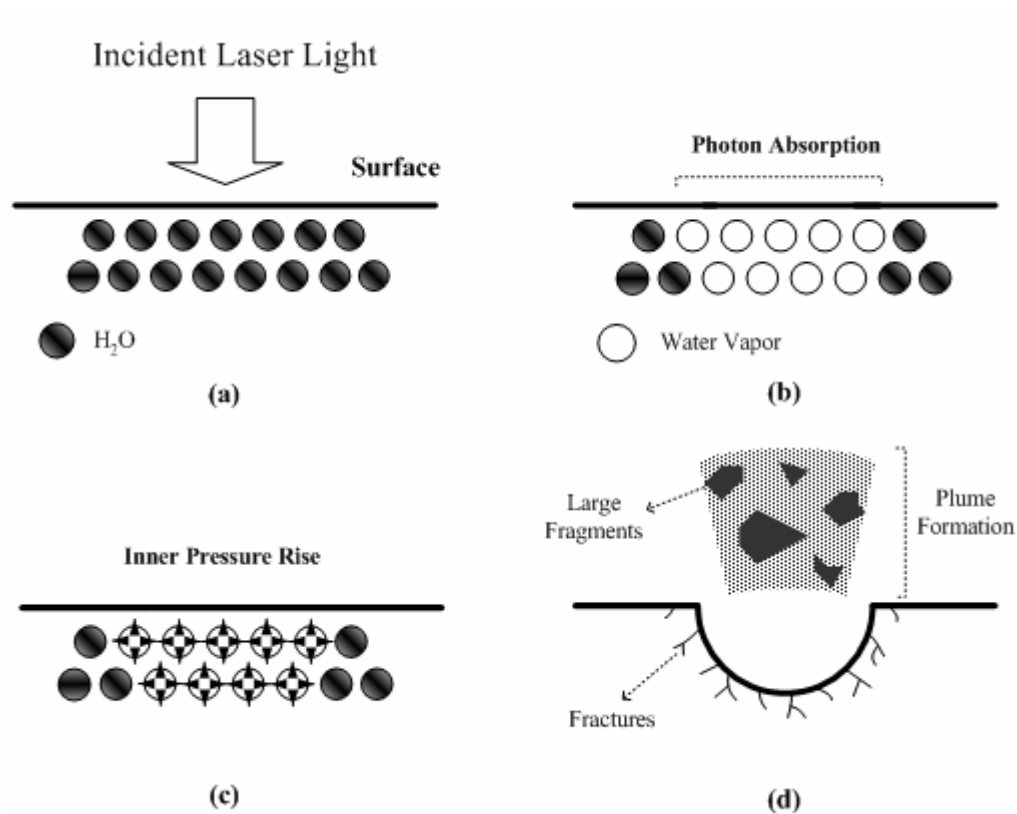


Figure A.5. Laser-induced microexplosion. (a) Incidence of laser light on the tissue containing water. (b) Vaporization of water in the tissue due to optical energy absorption. (c) Pressure increase in water following water vaporization. (d) Photomechanical ablation after rupturing the tissue, associated with large fragments, plume, and internal fractures.

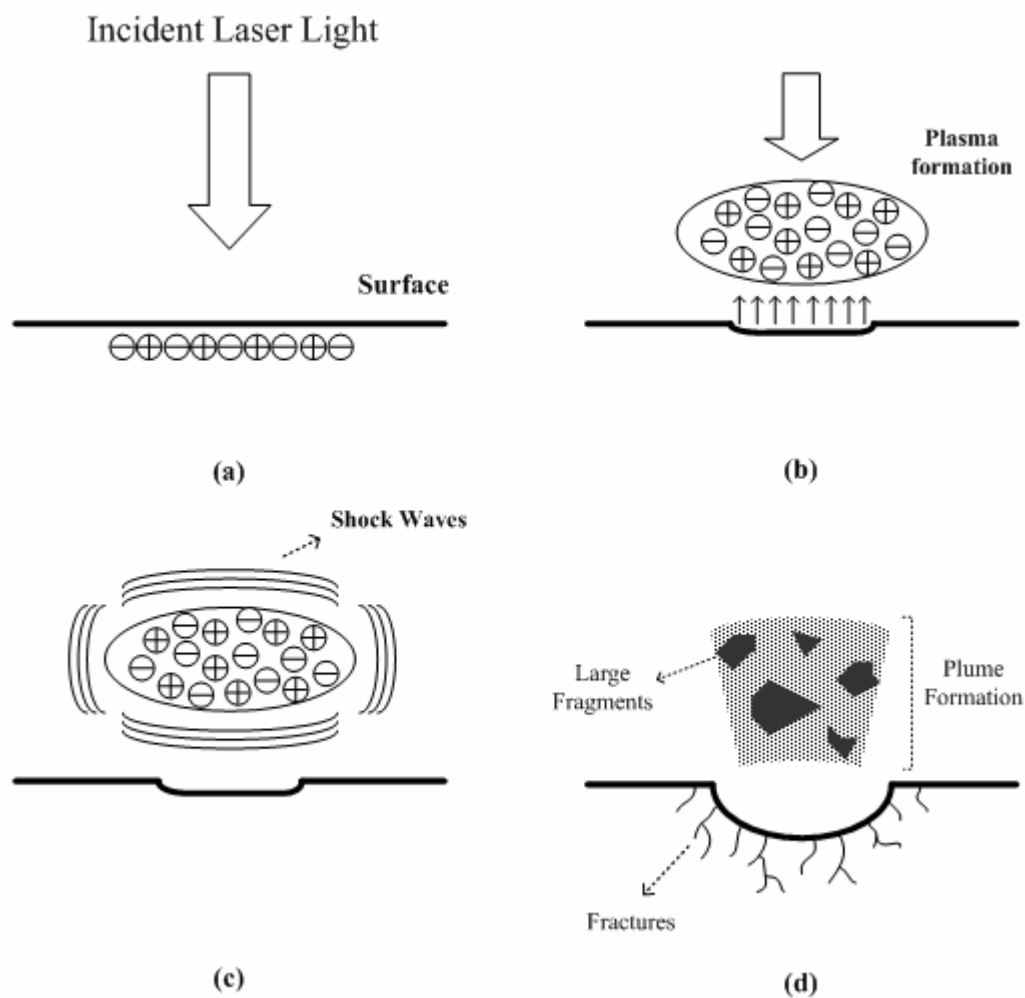


Figure A.6. Schematic illustrations of shock wave induced ablation. (a) The initiation of optical breakdown (ionization process). (b) Plasma formation and its shielding of the incident light in an early stage. (c) Plasma expansion accompanied with generation of shock waves. (d) Photoacoustical ablation with mechanical fractures inside the crater.

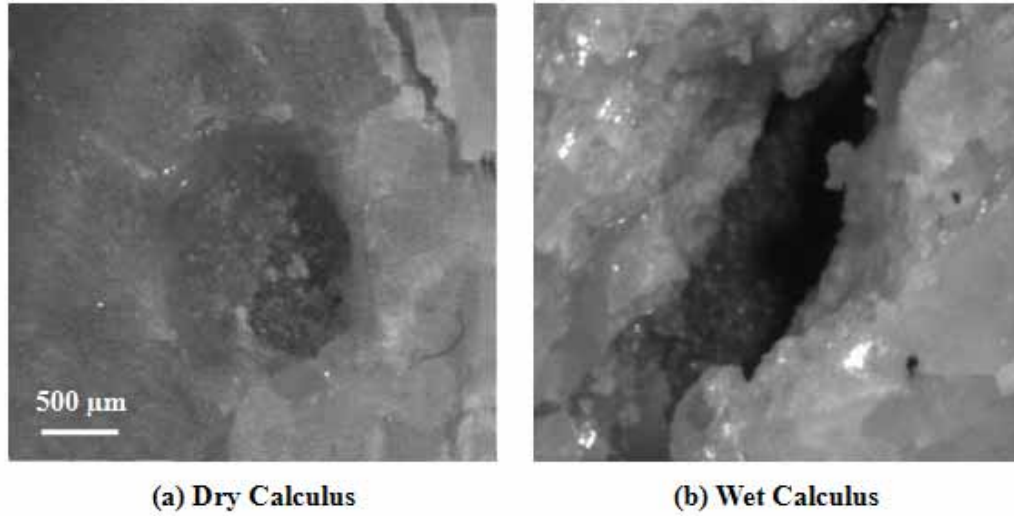


Figure A.7. Top view of laser-induced craters is shown. A Q-switched Nd:YAG laser ($\tau_p = 20$ ns, $r_o = 0.75$ mm, $F = 14$ J/cm²) was irradiated on cystine. Photoacoustical/photomechanical effects caused calculus fragmentation with fracture and large calculus dissociation. (a) 50 pulses of laser light were irradiated on dry calculus. (b) 30 pulses were applied to wet calculus, which was immersed in deionized water for a minimum of 24 hours prior to ablation experiment.

A.4 REVIEW OF LASER LITHOTRIPSY

Four major lithotripsy modalities were employed clinically by the early 1990s: electrohydraulic lithotripsy (EHL), ultrasonic lithotripsy, extracorporeal shockwave lithotripsy (ESWL) and laser lithotripsy [2]. EHL systems created a shock wave by an electrical discharge. However, only fragile calculi could be fragmented and the procedure was performed with a chance of a perforation of the ureter along with deleterious effects on endothelium. Ultrasonic lithotripsy was available for both renal and ureteral calculi, but the requirement for a large caliber and high rigidity ultrasonic probe was impractical for both small caliber ureteroscopes and flexible ureteroscopes commonly used in current clinical practice. ESWL was a minimally noninvasive procedure that generates shock waves outside the body that are focused the kidney or ureteral stone. The convergence of shock waves to this focus effectively fragmented renal calculi. However, ESWL was effective for only some stone compositions and stone-free rates were generally no better than 70 % after treatment. In contrast, laser lithotripsy enabled fragmentation of both ureteral and renal calculi via ultrasmall fibers with minimal tissue damage.

Among many commercially available lasers, the widely accepted devices for lithotripsy are the pulsed-dye laser, the Ho:YAG laser, and the frequency-doubled double-pulse Nd:YAG laser (FREDDY). In this section, the commercially available laser lithotrites are reviewed and their preliminary

ablation mechanism(s) (i.e. photothermal and photoacoustical/photomechanical) is discussed.

Flashlamp-pumped Pulsed-dye Lasers (FPDL)

The flashlamp-pumped pulsed-dye laser ($\lambda = 504$ nm, $\tau_p = 1$ μ s, pulse repetition rate = 5 Hz, $Q_o < 140$ mJ [11,18,20]) is one of clinically available lasers for lithotripsy [1-6]. The laser uses a coumarin green dye to achieve a wavelength of 504 nm, which matches the wavelength for high absorption in calculus while minimizing absorption in adjacent tissue. The ablation threshold is low for the 1 μ s pulse duration, and there is minimal damage to surrounding tissue. The relatively slow 5-Hz repetition rate reduces the effect of residual heat of the previous pulses.

A photoacoustical mechanism is responsible for calculus fragmentation. Localized energy absorption of the laser beam by the calculus initiates the generation and subsequent expansion of plasma, which is confined to surrounding water. Stress confinement during plasma expansion produces a cavitation bubble which collapses after several hundreds of microseconds [70]. It is the shock waves originated from plasma expansion and cavitation bubble collapse that create the photomechanical effects on the calculus.

In an early study, Teng *et al.* [12,70,71] observed a higher ablation efficiency when a calculus was immersed in liquid than when it was suspended in air because of the confined plasma in water. They concluded that the plasma-

mediated shock wave was responsible for calculus fragmentation. Rink *et al.* [23,24] found that the strongest acoustic pressure occurred upon bubble collapse. Their experiments exhibited acoustic transients induced at plasma expansion and subsequent events of cavitation bubble collapses. The pressure amplitude at the first bubble collapse after the pulse was up to five times higher than the pressure wave generated by plasma expansion. They concluded that pulsed-dye laser lithotripsy was governed primarily by cavitation dynamics.

The main drawback of the pulsed-dye laser, however, is the necessity for periodic change of dye in the laser and costly maintenance. Another limitation of the pulsed-dye lasers is the inability to fragment calculus of hard components, for example, cystine and calcium oxalate monohydrate (COM) [15,16]. Moreover, because the pulsed dye laser operates at a wavelength in the middle of the visual spectrum, laser eyewear protection blocks wavelengths close to peak retinal sensitivities, inducing color perception distortions among surgeons while wearing the laser eyewear protection [72].

Ho:YAG Laser

The long-pulsed Ho:YAG laser ($\lambda = 2.12 \mu\text{m}$, $\tau_p = 250 \mu\text{s}$, pulse repetition rate = 5~20 Hz, $Q_o = 200 \text{ mJ} \sim 2 \text{ J}$) has been utilized extensively in lithotripsy since 1995 as a widely accepted clinical laser. The first *in vitro* studies of the free-running Ho:YAG laser lithotripsy ($\lambda = 2.12 \mu\text{m}$, $\tau_p = 250 \mu\text{s}$, $Q_o < 1.5 \text{ J}$) were reported by Jiang *et al.* [73] and Sayer *et al.* [74] In spite of the ability to

fragment all urinary and biliary calculi, including cystine and calcium oxalate monohydrate, initially the underlying mechanism was not identified. Some proposed processes were shock wave effects similar to LISL [75-77] and jet formation due to bubble collapse near the calculus surface [77,78]. Recent studies reported that the ablation mechanism was different from LISL [35,79]. Dushinski and Lingeman [79] confirmed that there was no correlation between mass loss and bubble size. Acoustic effects upon bubble collapse did not influence fragmentation. Inconsequential effects of bubble formation were substantiated by Schmidlin *et al.* [31].

The primary mechanism in Ho:YAG laser lithotripsy is photothermal with minimal acoustic emission due to the long pulse duration of the Ho:YAG laser [28,29]. After laser irradiation, rapid evaporation of water occurs at the gap between the calculus surface and the delivery fiber tip in a liquid environment, inducing an expanding vapor bubble. Chan *et al.* [29] noted that negligible or no pressure transients ($P < 2$ bars) were measured upon cavitation bubble collapse. Although small, there are some minor effects of photoacoustical/photomechanical mechanism on initiation of calculus fragmentation that may assist the resultant ablation process. The first tens of microseconds of the Ho:YAG laser pulse produces a bubble between the calculus and the fiber tip. The bubble forms a channel for the remaining laser pulse that is directly delivered to the calculus (i.e. Moses Effect [80]). The temperature rise

due to calculus absorption contributes to chemical breakdown which weakens the mechanical strength of the irradiated volume, resulting in calculus decomposition and fragmentation in smaller size than LISL [35]. In addition, heating interstitial water within the calculus causes explosive vaporization, which promotes the ejection of calculus fragments from the original calculus. The procedure is associated with minimal collateral thermal damage to surrounding tissue.

Although there is less mechanical force applied to the stone using the Ho:YAG laser versus LISL, there may still be retropulsion due to Newtonian forces as a result of fragment ejection from the stone surface [81]. Technically, Ho:YAG laser lithotripsy is relatively simple to perform. The absence of significant acoustic waves, lack of collateral damage, and tiny stone fragments created imply that the urologist can maintain the optical fiber on the stone surface, discharge the laser directly on the stone, and achieve successful stone fragmentation with little risk of bleeding or tissue injury. It is imperative that the optical fiber tip be visualized throughout the procedure and confirmed to be in contact with the stone surface and not in contact with tissue mucosa or in the ureterscope. Also, as Ho:YAG laser lithotripsy produces tiny fragments, it is slower than other lithotripsy modalities to fragment an entire stone, producing potentially longer surgical times [82].

Frequency-doubled Double-pulse Nd:YAG (FREDDY)

The frequency-doubled double-pulse Nd:YAG (FREDDY) laser ($\lambda_1 = 532$ nm, $\lambda_2 = 1064$ nm, $\tau_p = 1.2$ μ s at 1064 nm, $Q_o = 120$ mJ) is the most recently developed laser for lithotripsy [83]. The use of a KTP crystal in a short pulse Nd:YAG laser converts a portion of the 1064 nm wavelength of the Nd:YAG laser to 532 nm. The FREDDY laser generates a synchronized “double-pulse” of 532 nm and 1064 nm light. During the pulse duration, about 20 % of the output beam is at 532 nm and remainder at 1064 nm [84].

The fragmentation process in FREDDY laser lithotripsy is primarily due to photoacoustical mechanisms without adverse thermal effects. The calculus surface absorbs the green light ($\lambda_1 = 532$ nm) and a low density plasma is generated over the surface. This plasma absorbs the remaining laser light ($\lambda_2 = 1064$ nm). The greatly reinforced plasma expands and generates a cavitation bubble. Subsequently, both plasma onset and cavitation collapse induce a shock wave strong enough to fragment the calculus, which is similar to the FPD [84]. Clinical trials have shown that FREDDY fragments calculi with minimal damage to adjacent tissue [85]. Compared to the pulsed-dye laser and the Ho:YAG laser, FREDDY showed relatively minimal tissue perforation. However, its principal limitation to date has been the high failure rate for fragmentation of cystine and calcium oxalate monohydrate stones, similar to previous experience with the

pulsed dye lasers. Further clinical studies are required to investigate fragmentation time for different calculus compositions.

A.5 FUTURE DEVICES

Research continues to achieve high ablation efficiency, reduced treatment time, and minimal collateral damage. One of the promising lasers for lithotripsy is the Er:YAG laser with a wavelength of 2.94 μm , which is highly absorbed in water. For endoscopic applications, the delivery of the Er:YAG beam will require an efficient IR fiber or waveguide delivery system.

Er:YAG Laser

The Er:YAG laser has been widely employed in dentistry, orthopedics, stapedotomy, burn surgery, and ophthalmology [86-90]. Since Daidoh *et al.* [91] proposed optimal wavelengths of 3 μm and 6 μm for efficient fragmentation of COM and uric acid calculi, the feasibility of Er:YAG laser ($\lambda = 2.94 \mu\text{m}$, $\tau_p = 250\sim 500 \mu\text{s}$) in lithotripsy became of interest, following the studies with a Er:Cr:YAGG laser [92,93]. It was reported that compared to the Ho:YAG laser ($\lambda = 2.12 \mu\text{m}$), the Er:YAG system had lower ablation thresholds and higher ablation efficiencies for a variety of calculi, which suggest that the Er:YAG may be a more efficient lithotrite [88,94-96]. Due to the coincidence of the wavelength ($\lambda = 2.94 \mu\text{m}$) with the water absorption peak in the infrared spectrum,

the Er:YAG laser produces more precise ablation and less thermal damage than the Ho:YAG [89,90].

It is assumed that the Er:YAG laser lithotripsy initially fragments calculi through a photothermal mechanism [97]. Laser energy is delivered to a calculus through a vapor channel that is formed between the fiber tip and the calculus in the first few microseconds of the Er:YAG pulse. The remainder of the pulse is absorbed by the calculus inducing fragmentation, including recrystallization and plume formation. During ablation, insufficient or no shock waves have been measured [97]. Nevertheless, even minor photoacoustical effect may partially aid the resultant fragmentation process. Heat diffusion beyond the optical penetration depth minimizes collateral tissue damage. Investigations on the feasibility of the Er:YAG laser in lithotripsy are in progress. However, a major concern is the availability of fibers to deliver the Er:YAG laser light endoscopically.

Infrared Optical Fibers

Following the progress and medical applications of infrared (IR) lasers, the improvements in light delivery system has focused on efficient and reliable IR fibers to transmit laser light ($\lambda \geq 2 \mu\text{m}$) [98-100]. Conventional IR fibers include zirconium fluoride, germanium oxide, sapphire, and hollow waveguides. The features of each fiber are summarized in Table II. Biomedical applications [101] of the zirconium fluoride (ZrF_4) fiber are limited by its relatively low melting

point and hygroscopic and non-biocompatible properties, which are inappropriate for laser lithotripsy [99,102]. The advantages of the germanium oxide (GeO_2) fiber include high flexibility and low transmission loss, but thermal damage due to the low melting temperature (i.e. low damage threshold) induces a rapid deterioration at the fiber tip during calculi ablation [98,103,104]. The biocompatible sapphire fiber is a leading candidate for use in IR laser applications, transmitting from visible wavelengths to approximately 3.5 μm . This fiber has a high melting point of 2040 °C and low transmission loss of less than 2 dB/m [104-106]. Nevertheless, limited flexibility and high absorption loss at 2.94 μm encumber its applications for endoscopic lithotripsy. In contrast to solid-core fibers mentioned previously, the hollow waveguide consists of air-filled core to deliver optical light, which results in low insertion loss and no end reflection. Besides, high flexibility and low transmission loss of this fiber is a promising candidate for laser light delivery [107-111]. The major drawback, however, is water intrusion into the hollow waveguide. Mohri *et al.* protected the distal end of the fiber with a film of polymer or an quartz sealing cap [112]. *In vitro* studies of Er:YAG laser lithotripsy with an end-sealed hollow waveguide demonstrate the applicability of this method for calculus fragmentation; however, the sealing cap deteriorates during ablation [113]. Further investigations on endoscopic application of the hollow waveguide are still required to achieve efficient light

delivery. Taking advantage of high flexibility and high damage threshold, the germanium oxide (GeO_2) fiber with a sealing cap is a promising delivery system.

Table A.2. Characteristics of infrared optical fibers to deliver Er:YAG laser ($\lambda = 2.94 \mu\text{m}$) light [98-111].

Core Material		Fibers	Advantage	Disadvantage
Solid Core	Glass	Zirconium Fluoride (ZrF ₄)	- Low attenuation loss	- Low glass transition temperature (fragility) - Low melting temperature (low damage threshold) - Non-biocompatible and hygroscopic properties
		Germanium Oxide (GeO ₂)	- High flexibility - Low transmission loss	- Low melting temperature (low damage threshold) - Rapid deterioration at the fiber tip
	Crystal	Sapphire	- High melting temperature of 2040 °C (high damage threshold) - Low transmission loss - Biocompatibility	- Limited flexibility - High absorption loss at 2.94 μm
Hollow Core (air-filled core)		Hollow waveguide	- High power threshold - Low insertion loss - No end reflection	- Limited flexibility - Loss inversely proportional to bending radius and cubic bore diameter - Water or fragments intrusion into the waveguide

A.6 CONCLUSION

This paper has reviewed the photofragmentation process associated with clinical laser lithotripsy. The laser pulse duration determines the primary mechanism(s) in calculus fragmentation, and water/calculus properties dependent on the laser wavelength influence the efficacy of the light-tissue interactions. Long-pulsed lasers ($\tau_p \geq 100 \mu\text{s}$) induce photothermal effects leading to calculus fragmentation while short-pulsed or nanosecond lasers ($\tau_p \leq 10 \mu\text{s}$) contribute to shock wave induced ablation by means of photoacoustical/photomechanical mechanism.

The purpose of ideal laser lithotripsy is to remove urinary and biliary calculi in a minimally invasive or noninvasive manner without tissue damage. Although the pulsed-dye laser and the Ho:YAG laser are used extensively in clinical lithotripsy, exhaustive investigations are still required to establish efficient and reliable treatment of urinary calculi. Furthermore, advanced laser lithotripsy will require new developments in both clinical laser systems and infrared light delivery systems, accompanied with further investigations on the physical properties of a variety of calculi.

A.7 REFERENCES

1. Hofstetter A. Lasers in urology. *Lasers Surg Med* 1986;6:412-4.
2. Dretler SP. Laser lithotripsy: a review of 20 years of research and clinical applications. *Lasers Surg Med* 1988;8:341-56.
3. Bhatta KM. Lasers in urology. *Lasers Surg Med* 1995;16:312-30.
4. Vogel A. Nonlinear absorption: intraocular microsurgery and laser lithotripsy. *Phys Med Bio* 1997;42:895-912.
5. Wollin TA, Denstedt JD. The holmium laser in urology. *J Clin Lasers Med & Surg* 1998;16:13-20.
6. Chan KF, Pfefer TJ, Teichman JMH, Welch AJ. A perspective on laser lithotripsy: the fragmentation processes. *J Endourol* 2001;15:257-73.
7. Watson GM, Jacques SL, Dretler SP, Parrish JA. Tunable pulsed dye laser for fragmentation of urinary calculi. *Lasers Surg Med* 1985;5:160.
8. Watson GM, Murray S, Dretler SP, Parrish JA. The pulsed dye laser for fragmenting urinary calculi. *J Urol* 1987;138:195-8.
9. Dretler S, Watson G, Murray S, Parrish JA. Laser fragmentation of ureteral calculi: clinical experience. *Lasers Surg and Med* 1986;6:191.
10. Nishioka NS, Levins PC, Murray SC, Parrish JA, Anderson RR. Fragmentation of biliary calculi with tunable dye lasers. *Gastroenterology* 1987;93:250-5.
11. Dretler SP, Watson G, Parrish JA, Murray S. Pulsed dye laser fragmentation of ureteral calculi: initial clinical experience. *J Urol* 1987;137:386-9.
12. Teng P, Nishioka NS, Farinelli WA, Anderson RR, Deutsch TF. Microsecond-long flash photography of laser-induced ablation of biliary and urinary calculi. *Lasers Surg Med* 1987;7:394-7.
13. Nishioka NS, Kelsey PB, Kibbi A, Delmonico F, Parrish JA, Anderson RR. Laser lithotripsy: animal studies of safety and efficacy. *Lasers Surg Med* 1988;8:357-62.
14. Bhatta KM, Nishioka NS. Effect of pulse duration on microsecond-domain laser lithotripsy. *Lasers Surg Med* 1989; 9:454-7.
15. Watson G. The pulsed dye laser for urinary calculi in 600 patients. *Proc SPIE* 1990;1200:66.
16. Dretler SP. An evaluation of ureteral laser lithotripsy: 225 consecutive patients. *J Urol* 1990;143:267-72.
17. Vandeursen H, Pittomvils G, Boving R, Baert L. High energy pulsed dye laser lithotripsy: management of ureteral calcium oxalate monohydrate calculi. *J Urol* 1991;145:1146-50.

18. Dretler SP, Bhatta KM. Clinical experience with high power (140mJ), large fiber (320 micron) pulsed dye laser lithotripsy. *J Urol* 1991;146:1228-31.
19. Birkett DH, Lamont JS, O'Keane JC, Babayan RK. Comparison of a pulsed dye laser and electrohydraulic lithotripsy on porcine gallbladder and common bile duct in vitro. *Lasers Surg Med* 1992;12:210-4.
20. Watson G, Smith N. A comparison of the pulsed dye and holmium lasers for stone fragmentation: in vitro studies and clinical experience. *Proc SPIE* 1993;1879:139-42.
21. Teng P, Nishioka NS, Anderson RR, Deutsch TF. Optical studies of pulsed-laser fragmentation of biliary calculi. *Appl Phys B* 1987;42:73-8.
22. Lo EY, Petschek H, Rosen DI. A hydrodynamic model for the laser-induced fragmentation of calculi. *Lasers Life Sci* 1990;3:233-44.
23. Rink K, Delacretaz G, Salathe RP. Influence of the pulse duration on laser-induced mechanical effects. *Proc SPIE* 1994;2077:181-94.
24. Rink K, Delacretaz G, Salathe RP. Fragmentation process of current laser lithotriptors. *Lasers Surg Med* 1995;16:134-46.
25. Schmidt-Kloiber H, Reichel E, Schoffmann H. Laser-induced Shock-Wave Lithotripsy (LISL). *Biomedizinische Technik* 1985;30:173-81.
26. Schafer SA, Durville FM, Jassemejad B, Bartels KE, Powell RC. Mechanisms of biliary stone fragmentation using the Ho:YAG laser. *IEEE Trans Biomed Eng* 1994;41:276-83.
27. Vassar GJ, Teichman JM, Glickman RD. Holmium:YAG lithotripsy efficiency varies with energy density. *J Urol* 1998;160:471-6.
28. Vassar GJ, Teichman JMH, Glickman RD, Weintraub SE, Chan KF, Pfefer TJ, Welch AJ. Holmium:YAG lithotripsy: photothermal mechanism. *J Endourol* 1999;13:181-9.
29. Chan KF, Vassar GJ, Pfefer TJ, Teichman JMH, Glickman RD, Weintraub ST, Welch AJ. Holmium:YAG laser lithotripsy: a dominant photothermal ablative mechanism with chemical decomposition of urinary calculi. *Lasers Surg Med* 1999;25:22-37.
30. Beghuin D, Delacretaz GP, Schmidlin FR, Rink K. Fragmentation process during Ho:YAG laser lithotripsy revealed by time-resolved imaging. *Proc SPIE* 1997;3195:220-4.
31. Schmidlin FR, Beghuin D, Delacretaz GP, Venzi G, Jichlinski P, Rink K, Leisinger HJ, Graber P. Laser lithotripsy with the Ho:YAG laser: fragmentation process revealed by time-resolved imaging. *Proc SPIE* 1998;3245:123-6.
32. Grasso M, Conlin M, Bagley D. Retrograde ureteropyeloscopic treatment of 2 cm or greater upper urinary tract and minor staghorn calculi. *J Urol* 1998;160:346-51.

33. Sofer M, Watterson JD, Wollin TA, Nott L, Razvi H, Denstedt JD. Holmium:YAG laser lithotripsy for upper urinary tract calculi in 598 patients. *J Urol* 2002;167:31-4.
34. Teichman JMH. Acute colic from ureteral calculus. *N Engl J Med* 2004; 350: 684-93.
35. Teichman JMH, Vassar GJ, Bishoff JT, Bellman GC. Holmium:YAG lithotripsy yields smaller fragments than lithoclast, pulsed dye laser or electrohydraulic lithotripsy. *J Urol* 1998;159:17-23.
36. Teichman JMH, Vassar GJ, Glickman RD. Holmium:yttrium-aluminum-garnet lithotripsy efficiency varies with stone composition. *Urology* 1998;52:392-7.
37. Welch AJ, van Gemert MJC. Optical-thermal response of laser-irradiated tissue. New York: Plenum Press; 1995.
38. Niemz MH. Laser-tissue interactions. Berlin: Springer-Verlag; 1996.
39. Baurele D. Laser processing and chemistry. Berlin: Springer; 2000.
40. Miller JC. Laser ablation: principles and applications. Berlin: Springer-Verlag; 1994.
41. Rastegar D. Laser ablation of biological tissue (Doctoral dissertation). Austin: The University of Texas at Austin; 1987.
42. Jansen ED. Pulsed laser ablation of biological tissue: influence of laser parameters and tissue properties on thermal and mechanical damage (Doctoral dissertation). Austin: The University of Texas at Austin; 1994.
43. Chan KF. Pulsed infrared laser ablation and clinical applications (Doctoral dissertation). Austin: The University of Texas at Austin; 2000.
44. Boulnois J. Photophysical processes in recent medical laser development: a review. *Lasers Med Sci* 1986;1:47-66.
45. Jacques SL. Laser-tissue interactions: photochemical, photothermal, and photomechanical. *Lasers Gen Surg* 1992;72:531-58.
46. Jacques SL. Role of tissue optics and pulse duration on tissue effects during high-power laser irradiation. *Appl Opt* 1993;32:2447-54.
47. Ross EV, Domankevitz Y, Skrobal M, Anderson RR. Effects of CO₂ laser pulse duration in ablation and residual thermal damage: Implications for skin resurfacing. *Lasers Surg Med* 1996;19:123-9.
48. Peavy GM, Reinisch L, Payne JT, Venugopalan V. Comparison of cortical bone ablations by using infrared laser wavelengths 2.9 to 9.2 μ m. *Lasers Surg Med* 1999;25:421-34.
49. Gong H, Li C, Li Z. CW-laser-induced thermal and mechanical damage in optical materials. *Proc SPIE* 1998;3578:576-83.
50. Pfefer TJ, Choi B, Vargas G, McNally KM, Welch AJ. Pulsed laser-induced thermal damage in whole blood. *ASME J Biomech Eng* 2000;122:196-202.

51. Jansen ED, Tuong LE, Welch AJ. Excimer, Ho:YAG, and Q-switched Ho:YAG ablation of aorta: a comparison of temperatures and tissue damage in vitro. *Appl Opt* 1993;32:526-34.
52. Watson G, Wickham JEA, Mills TN, Bown SG, Swain P, Salmon PR. Laser fragmentation of renal calculi. *Br J Urol* 1983;55:613-6.
53. Mulvaney WP, Beck CW. The laser beam in urology. *J Urol* 1968;99:112-5.
54. Vogel A, Schweiger P, Frieser A, Asiyo MN, R B. Intraocular Nd:YAG laser surgery: light-tissue interaction, damage range, and reduction of collateral effects. *IEEE J Quantum Electron* 1990;26:2240-60.
55. Esnaliev RO, Oraevsky AA, Letokhov VS, Karabutov AA, Malinsky TV. Studies of acoustical and shock waves in the pulsed laser ablation of biotissue. *Lasers Surg Med* 1993;13:470-84.
56. Paltauf G, Schmidt-Kloiber H. Model study to investigate the contribution of spallation to pulsed laser ablation of tissue. *Laser Surg Med* 1995;16:277-87.
57. Cummings JP, Walsh JT Jr. Tissue tearing caused by pulsed laser-induced ablation pressure. *Appl Opt* 1993;32:494-503.
58. Majaron B, Plestenjak P, Lukac M. Thermo-mechanical laser ablation of soft biological tissue: modeling the micro-explosions. *Appl Phys B* 1999;69:71-80.
59. Jansen ED, Asshauer T, Frenz M, Motamedi M, Delacretaz G, Welch AJ. Effect of pulse duration on bubble formation and laser-induced pressure waves during holmium laser ablation. *Lasers Surg Med* 1996;18:278-93.
60. Rink K, Delacretaz G, Salathe RP. Fragmentation process induced by microsecond laser pulses during lithotripsy. *Appl Phys Lett* 1992;61:258-60.
61. Rink K, Delacretaz G, Salathe RP. Fragmentation process induced by nanosecond laser pulses. *Appl Phys Lett* 1992;61:2644-6.
62. Fradin DW, Bloembergen N, Letellier JP. Dependence of laser-induced breakdown field strength on pulse duration. *Appl Phys Lett* 1973;22:635-7.
63. Puliafito C, Steinert R. Short-pulsed Nd:YAG laser microsurgery of the eye: Biophysical considerations. *IEEE J Quantum Electron* 1984;QE20:1442-8.
64. Dunina TA, Egerev SV, Lyamshev LM, Naugol'nykh KA, Pashin AE. Hydrodynamic effects in the optical breakdown of a liquid. *Sov Phys Acoust* 1982;28:116-21.
65. Griffin RD, Justus BL, Campillo AJ, Goldberg LS. Interferometric studies of the pressure of a confined laser-heated plasma. *J Appl Phys* 1986;59:1968-71.

66. Doukas AG, Zweig AD, Frisoli JK, Birngruber R, Deutsch TF. Noninvasive determination of shock wave pressure generated by optical breakdown. *Appl Phys B* 1991;53:237-45.
67. Itzkan I, Albagli D, Dark ML, Perelman LT, von Rosenberg C, Feld MS. The thermoelastic basis of short pulsed laser ablation of biological tissue. *Proc Natl Acad Sci USA* 1995;92:1960-4.
68. Frenz M. IR-lasers in medicine - basics and applications (Habilitationsschrift). Bern: Universitat Bern; 1998.
69. Vogel A, Hentschel W, Holzfuss J, Lauterborn W. Cavitation bubble dynamics and acoustic transient generation in ocular surgery with pulsed neodymium:YAG lasers. *Ophthalmology* 1986;93:1259-69.
70. Teng P, Nishioka NS, Anderson RR, Deutsch TF. Acoustic studies of the role of immersion in plasma-mediated laser ablation. *IEEE J Quantum Electron* 1987;23:1845-52.
71. Teng P, Nishioka SS, Anderson RR, Deutsch TF. Optical studies of pulsed-laser fragmentation of biliary calculi. *Appl Phys B* 1987;42:73-8.
72. Teichman JMH, Johnson AJ, Yates JT, Angle BN, Dirks MS, Muirhead JT, Thompson IM, Pearle MS. Color vision deficits during laser lithotripsy using safety goggles for coumarin green or alexandrite but not with holmium:YAG laser safety goggles. *J Urol* 1998;159:683-9.
73. Jiang ZX, Whitehurst C, King TA. Fragmentation methods in laser lithotripsy. *Proc SPIE* 1991;1421:88-99.
74. Sayer J, Johnson DE, Price RE, Cromeens DM. Endoscopic laser fragmentation of ureteral calculi using the Holmium:YAG. *Proc SPIE* 1993;1879:143-8.
75. Dushinski JW, Lingeman JE. Urologic applications of the holmium laser. *Tech Urol* 1997;3:60-4.
76. White MD, Moran ME, Calvano CJ, Borhan-Manesh A, Mehlhaff BA. Evaluation of retropulsion caused by holmium:YAG laser with various power setting and fibers. *J Endourol* 1998;12:183-6.
77. van Swol CFP, Verdaasdonk RM, Zeijlemaker BYW, Grimbergen MCM, Boon TA. Optimization of the dosimetry and safety using the Holmium laser for urology. *Proc SPIE* 1998;3245:110-6.
78. Zhong P, Tong HL, Cocks FH, Pearle MS, Preminger GM. Transient cavitation and acoustic emission produced by different laser lithotripters. *J Endourol* 1998;12:371-8.
79. Dushinski JW, Lingeman JE. High-speed photographic evaluation of Holmium laser. *J Endourol* 1998;12:177-81.
80. Isner JM. "Blood," in Cardiovascular laser therapy. Isner JM and Clarke R, eds. New York: Raven Press; 1989.

81. Lee H, Ryan RT, Teichman JMH, Kim J, Choi B, Arakeri NV, Welcg AJ. Stone retropulsion during holmium:YAG lithotripsy. *J Urol* 2003;169:881-5.
82. Teichman JMH, Rao RD, Rogenes VJ, Harris JM. Ureteroscopic management of ureteral calculi: electrohydraulic versus holmium:YAG lithotripsy. *J Urol* 1997;158:1357-61.
83. Koort HJ, Tischer C, Rasch R, Thiede C, WOM World Of Medicine AG Berlin/Germany. Laser induced shockwave generation for use in lithotripsy. *Proc SPIE* 2002;4609:137-40.
84. Zorcher T, Hochberger J, Schrott K, Kuhn R, Schafhauser W. In vitro study concerning the efficiency of the frequency-doubled double-pulse Neodymium:YAG laser (FREDDY) for lithotripsy of calculi in the urinary tract. *Lasers Surg Med* 1999;25:38-42.
85. Tischer C, Koort HJ, Bazo A, Rasch R, Thiede C, World of Medicine Inc., Dept. of Medical Lasers, Orlando and Berlin, North Manchester General Hospital, UK. Clinical experiences with a new Frequency-doubled Double-pulse Nd:YAG Laser (FREDDY) for the treatment of urolithiasis. *Proc SPIE* 2002;4609:128-35.
86. Ertl T, Benthin H, Muller G. Thermal and acoustic problems on root canal treatment with different lasers. *Proc SPIE* 1994;2327:114-24.
87. Li Z, Reinisch L, Van de Merwe WP. Bone ablation with Er:YAG and CO₂ laser: study of thermal and acoustic effects. *Lasers Surg Med* 1992;12:79-85.
88. Pratisto H, Frenz M, Ith M, Romano V, Felix D, Grossenbacher R, Altermitt HJ, Weber HP. Temperature and pressure effects during erbium stapdotomy. *Lasers Surg Med* 1996;18:100-8.
89. Hohenleutner U, Hohenleutner S, Baumler W, Landthaler M. Fast and effective skin ablation with an Er:YAG laser: determination of ablation rates and thermal damage zones. *Lasers Surg Med* 1997;20:242-7.
90. Dietlein TS, Jacobi PC, Kriegelstein GK. Erbium:YAG laser trabecular ablation (LTA) in the surgical treatment of glaucoma. *Lasers Surg Med* 1998;23:104-10.
91. Daidoh Y, Arai T, Komine Y, Nagakura K, Ieda K, Murai M, Nakamura H, Nakagawa M, Kikuchi M, Uchibori M, Inzaki S, Wakaki M. Determination of optimum wavelength for laser photofragmentation of urinary stones. *J Endourol* 1991;5:245-9.
92. D'yakonov GI, Konov VI, Mikhailov VA, Nikolaev DA. Comparative performance of infrared solid-state lasers in laser lithotripsy. *Proc SPIE* 1991;1421:156-62.

93. Bloch MA, Fedorovskii SL, Suslov AM, Mikhailov BA, Pak SK, Shcherbakov IA. In-vitro lithotripsy with Er:Cr:YSGG lasers through fiber. *Proc SPIE* 1993;1879:182-5.
94. Chan KF, Hammer DX, Choi B, Welch AJ, Teichman JMH, McGuff HS, Pratisto H, Jansen ED. Free electron laser lithotripsy threshold radiant exposures. *J Endourol* 1999;14:161-7.
95. Chan KF, Hammer DX, Vargas G, Sorg B, Pfefer TJ, Pratisto H, Jansen ED, Teichman JMH, Welch AJ. Free electron laser ablation of urinary calculi: a preliminary study. *J Urol* 1999;161(supp):369(abstract#1430).
96. Teichman JMH, Chan KF, Cecconi PP, Corbin NS, Kamerer AD, Glickman RD, Welch AJ. Erbium:YAG versus Holmium:YAG lithotripsy. *J Urol* 2001;165:876-9.
97. Chan KF, Lee H, Teichman JMH, Kamerer A, McGuff HS, Vargas G, Welch AJ. Erbium:YAG laser lithotripsy mechanism. *J Urol* 2002;168:436-41.
98. Miyashita T, Manabe T. Infrared optical fibers. *IEEE J Quantum Electron* 1982;18:1432-50.
99. Merberg GN. Current status of infrared fiber optics for medical laser power delivery. *Lasers Surg Med* 1993;13:572-6.
100. Verdaasdonk RM, van Swol CF. Laser light delivery systems for medical applications. *Phys Med Bio* 1997;42:869-94.
101. Frenz M, Pratisto H, Ith M, Konz F, Weber HP. Effects of simultaneously fiber transmitted erbium and holmium radiation on the interaction with highly absorbing media. *Proc SPIE* 1995;2391:517-24.
102. Pryshlak AP, Dugan JR, Fitzgibbon JJ, Saphikon Inc. Advancements in sapphire optical fibers for the delivery of Erbium laser energy and IR sensor applications. *Proc SPIE* 1996;2677:35-42.
103. Olshansky R, Scherer GW. High GeO₂ optical waveguide. *Tech Dig 5th European Conference on Optical Communications (The Netherland)* 1979;12:5-1.
104. Lee H. Pulsed-laser induced material and its clinical applications (Doctoral dissertation). Austin: The University of Texas at Austin; 2003.
105. Nubling RK, Harrington JA. Optical properties of single-crystal sapphire fibers. *Appl Opt* 1997;36:5934-40.
106. Merberg GN, Harrington JA. Optical and mechanical properties of single-crystal sapphire optical fibers. *Appl Opt* 1993;32:3201-9.
107. Harrington JA, Matsuura Y. Review of hollow waveguide technology. *Proc SPIE* 1995;2396:4-14.
108. Matsuura Y, Abel T, Harrington JA. Optical properties of small-bore hollow glass waveguides. *Appl Opt* 1995;34:6842-7.

- 109. Abel T, Hirsch J, Harrington JA. Hollow glass waveguides for broadband infrared transmission. *Opt Lett* 1994;19:1034-6.
- 110. Kozodoy RL, Pagkalinawan AT, Harrington JA. Small-bore hollow waveguides for delivery of 3- μ m laser radiation. *Appl Opt* 1996;35:1077-82.
- 111. Wang Y, Matsuura Y, Miyagi M. Robust hollow devices and waveguides for Er:YAG laser radiation. *Opt Laser Tech* 1997;29:449-53.
- 112. Mohri S, Kasai T, Abe Y, Shi Y, Matsuura Y, Miyagi M. Optical properties of end-sealed hollow fibers. *Appl Opt* 2002;41:1251-5.
- 113. Iwai K, Shi Y, Nito K, Matsuura Y, Kasai T, Miyagi M, Saito S, Arai Y, Ioritani N, Okagami Y, Nemec M, Sulc J, Jelinkova H, Zavoral M, Kohler O, Drlik P. Erbium:YAG laser lithotripsy by use of a flexible hollow waveguide with an end-scaling cap. *Appl Opt* 2003;42:2431-5.

Bibliography

Abel T, Hirsch J, Harrington JA. Hollow glass waveguides for broadband infrared transmission. *Opt Lett* 1994;19:1034-1036.

Adams DH. Holmium:YAG laser and pulsed dye laser: A cost comparison. *Lasers Surg Med* 1997;21:29-31.

Altschuler G, Belicov A. Laser abrasive method of hard tissue removal. *Lasers Surg Med* 1999;11:10-11.

Altschuler G, Belikov A, Erofeev A. Human tooth enamel and dentin damage by holmium laser radiation. *SPIE Proc* 1992;1643:454-463.

Altschuler GB, Belikov AV, Sinelnik YA. A Laser-Abrasive Method for the Cutting of Enamel and Dentin. *Lasers Surg Med* 2001;28:435-444.

Andrew JE, Dyer PE, PH K. Direct etching of polymeric materials using a XeCl laser. *Appl Phys Lett* 1983;43:717-719.

Apel C, Meister J, Ioana RS, R F., P H., N G. The Ablation Threshold of Er:YAG and Er:YSGG Laser Radiation in Dental Enamel. *Lasers Med Sci* 2002;17:246-252.

Arrastia AM. Thermal effects of CO₂ laser on the pulpal chamber and enamel of human primary teeth: An in vitro investigation. *Lasers Surg Med* 1995;16:343-350.

Athanasίου KA, Zhu CF, Lancot DR, Agrawal CM, Wang X. Fundamentals of Biomechanics in Tissue Engineering of Bone. *Tissue Eng* 2000;6:361-381.

Barnes PA, Rieckhoff KE. Laser induced underwater sparks. *Appl Phys Lett* 1968;13:282-284.

Barnier F, Dyer PE, Monk P, Snelling HV, Rourke H. Fibre optic jacket removal by pulsed laser ablation. *J Phys D: Appl Phys* 2000;33:757-759.

Bäuerle D. *Laser Processing and Chemistry*. Berlin: Springer-Verlag, 2000.

Beghuin D, Delacretaz GP, Schmidlin FR, Rink K. Fragmentation process during Ho:YAG laser lithotripsy revealed by time-resolved imaging. *Proc SPIE* 1997;3195:220-224.

Berthe L, Fabbro R, Peyre P, Bartnicki E. Wavelength dependent of laser shock-wave generation in the water-confinement regime. *J Appl Phys* 1999;85:7552-7555.

Berthe L, Fabbro R, Peyre P, Toller L, Bartnicki E. Shock waves from a water-confined laser-generated plasma. *J Appl Phys* 1997;82:2826-2832.

Beyer O, Nee I, Havermeyer F, Buse K. Holographic recording of Bragg gratings for wavelength division multiplexing in doped and partially polymerized poly(methyl methacrylate). *Appl Opt* 2003;42:30-37.

Bhatta KM. Lasers in urology. *Lasers Surg Med* 1995;16:312-330.

Bhatta KM, Nishioka NS. Effect of pulse duration on microsecond-domain laser lithotripsy. *Lasers Surg Med* 1989; 9:454-457.

Birkett DH, Lamont JS, O'Keane JC, Babayan RK. Comparison of a pulsed dye laser and electrohydraulic lithotripsy on porcine gallbladder and common bile duct in vitro. *Lasers Surg Med* 1992;12:210-214.

Blackstock DT. *Fundamentals of physical acoustics*. New York: John Wiley & Son, Inc., 2000.

Blake JR, Taib BB, Doherty G. Transient cavities near boundaries. part 1: rigid boundary. *J Fluid Mech* 1986;170:479-497.

Bloch MA, Fedorovskii SL, Suslov AM, Mikhailov BA, Pak SK, Shcherbakov IA. In-vitro lithotripsy with Er:Cr:YSGG lasers through fiber. *Proc SPIE* 1993;1879:182-185.

Bloembergen N. Laser-induced Electric Breakdown in Solids. *IEEE J Quantum Electron* 1974;10:375-386.

Boulnois J. Photophysical processes in recent medical laser development: a review. *Lasers Med Sci* 1986;1:47-66.

Brennen CE. *Cavitation and Bubble Dynamics*. New York: Oxford University Press, 1995.

Burkes EJ, Hoke J, Gomes E, Wolbarsht M. Wet versus dry enamel ablation by Er:YAG laser. *J Prosthet Dent* 1992;67:847-851.

Cain CP, Noojin GD, Manning L. A Comparison of various probit methods for analyzing yes/no data on a log scale. USAF Armstrong Lab, Tech Rep AL/OE-TR-1996-0102 1996;

Carey VP. *Liquid-vapor Phase-Change Phenomena*. Washington: Hemisphere, 1992.

Çengel YA, Boles MA. *Thermodynamics: an engineering approach*. New York: McGraw-Hill, 1998.

Chan KF. *Pulsed infrared laser ablation and clinical applications (Doctoral Dissertation)*. Austin: The University of Texas at Austin, 2000.

Chan KF, Choi B, Vargas G, Hammer DX, Sorg B, Pfefer TJ, Teichman JMH, Welch AJ. Free electron laser ablation of urinary calculi: an experimental study. *IEEE J Sel Top Quantum Electron* 2001;7:1022-1033.

Chan KF, Choi B, Vargas G, Hammer DX, Sorg B, Pfefer TJ, Teichman JMH, Welch AJ, Jansen ED. Free Electron Laser Ablation of Urinary Calculi: An Experimental Study. *IEEE J Sel Top Quantum Electron* 2001;7:1022-1033.

Chan KF, Hammer DX, Choi B, Welch AJ, Teichman JMH, McGuff HS, Pratisto H, Jansen ED. Free electron laser lithotripsy threshold radiant exposures. *J Endourol* 1999;14:161-167.

Chan KF, Hammer DX, Vargas G, Sorg B, Pfefer TJ, Pratisto H, Jansen ED, Teichman JMH, Welch AJ. Free electron laser ablation of urinary calculi: a preliminary study. *J Urol* 1999;161(supp):369(abstract#1430).

Chan KF, Lee H, Teichman JMH, Kameron A, McGuff HS, Vargas G, Welch AJ. Erbium:YAG laser Lithotripsy Mechanism. *J Urol* 2002;168:436-441.

Chan KF, Pfefer TJ, Teichman JMH, Welch AJ. A perspective on laser lithotripsy: the fragmentation processes. *J Endourol* 2001;15:257-273.

Chan KF, Vassar GJ, Pfefer TJ, Teichman JMH, Glickman RD, Weintraub ST, Welch AJ. Holmium:YAG Laser Lithotripsy: A Dominant Photothermal Ablative Mechanism With Chemical Decomposition of Urinary Calculi. *Lasers Surg Med* 1999;25:22-37.

Chaney CA, Yang Y, Fried NM. Hybrid germanium/silica optical fibers for endoscopic delivery of Erbium:YAG laser radiation. *Lasers Surg Med* 2004;34:5-11.

Chang S, Zimmerman N, Iwamoto T. Experimental vitreous surgery. *Am J Ophthalmol* 1987;103:29-37.

Choo KL, Ogawa Y, Kanbargi G, Otrá V, Raff LM, Komanduri R. Micromachining of silicon by short-pulse laser ablation in air and under water. *Mater Sci Eng, A* 2004;372:145-162.

Clayman L, Fuller T, Becnman H. Healing of continuous-wave and rapid superpulsed carbon dioxide laser-induced bone defects. *J Oral Maxillofac Surg* 1978;36:932-937.

Cummings JP, Walsh Jr JT. Tissue tearing caused by pulsed laser-induced ablation pressure. *Appl Opt* 1993;32:494-502.

Curzon MEJ, Featherstone JDB. *Handbook of Experimental Aspects of Oral Biochemistry*. Boca Raton: CRC Press, 1983.

Daidoh Y, Arai T, Komine Y, Nagakura K, Ieda K, Murai M, Nakamura H, Nakagawa M, Kikuchi M, Uchibori M, Inzaki S, Wakaki M. Determination of optimum wavelength for laser photofragmentation of urinary stones. *J Endourol* 1991;5:245-249.

Daminelli G, Krüger J, Kautek W. Femtosecond laser interaction with silicon under water confinement. *Thin Solid Films* 2004;467:334-341.

Devaux D, Fabbro R, Tollier L, Bartnicki E. Generation of shock waves by laser-induced plasma in confined geometry. *J Appl Phys* 1993;74:2268-2273.

Dietlein TS, Jacobi PC, Krieglstein GK. Erbium:YAG laser trabecular ablation (LTA) in the surgical treatment of glaucoma. *Lasers Surg Med* 1998;23:104-110.

Docchio F. Lifetimes of Plasmas Induced in Liquids and Ocular Media by Single Nd:YAG Laser Pulses of Different Duration. *Europhys Lett* 1988;6:407-412.

Docchio F, Regondi P, Capon MRC, Mellerio J. Study of the temporal and spatial dynamics of plasmas induced in liquids by nanosecond Nd:YAG laser pulses. 1: Analysis of the plasma starting times. *Appl Opt* 1988;27:3661-3668.

Docchio F, Regondi P, Capon MRC, Mellerio J. Study of the temporal and spatial dynamics of plasmas induced in liquids by nanosecond Nd:YAG laser pulses. 2: Plasma luminescence and shielding. *Appl Opt* 1988;27:3669-3674.

Doukas AG, Zweig AD, Frisoli JK, Birngruber R, Deutsch TF. Noninvasive determination of shock wave pressure generated by optical breakdown. *Appl Phys B* 1991;53:237-245.

Downing HD, Williams D. Optical constants of water in the infrared. *J Geophys Res* 1975;80:1656-1661.

Dretler S, Watson G, Murray S, Parish J. Laser fragmentation of ureteral calculi: clinical experience. *Lasers Surg and Med* 1986;6:191.

Dretler SP. Laser Lithotripsy: A review of 20 years of research and clinical applications. *Lasers Surg Med* 1988;8:341-356.

Dretler SP. An evaluation of ureteral laser lithotripsy: 225 consecutive patients. *J Urol* 1990;143:267-272.

Dretler SP, Bhatta KM. Clinical experience with high power (140mJ), large fiber (320 micron) pulsed dye laser lithotripsy. *J Urol* 1991;146:1228-1231.

Dretler SP, Watson G, Parrish JA, Murray S. Pulsed dye laser fragmentation of ureteral calculi: initial clinical experience. *J Urol* 1987;137:386-389.

Duck FA. Physical properties of tissue: a comprehensive reference book. London: Academic Press, 1991.

Dunina TA, Egerev SV, Lyamshev LM, Naugol'nykh KA , Pashin AE. Hydrodynamic effects in the optical breakdown of a liquid. Sov Phys Acoust 1982;28:116-121.

Dupont A, Caminat P, Bournot P. Enhancement of material ablation using 248, 308, 532, 1064 nm laser pulse with a water film on the treated surface. J Appl Phys 1995;78:2022-2028.

Dushinski JW, Lingeman JE. Urologic applications of the holmium laser. Tech Urol 1997;3:60-64.

Dushinski JW, Lingeman JE. High-speed photographic evaluation of Holmium laser. J Endourol 1998;12:177-181.

D'yakonov GI, Konov VI, Mikhailov VA, Nikolaev DA. Comparative performance of infrared solid-state lasers in laser lithotripsy. Proc SPIE 1991;1421:156-162.

Ertl T, Benthin H, Muller G. Thermal and acoustic problems on root canal treatment with different lasers. Proc SPIE 1994;2327:114-124.

Esnaiev RO, Oraevsky AA, Letokhov VS, Karabutov AA, Malinsky TV. Studies of acoustical and shock waves in the pulsed laser ablation of biotissue. Lasers Surg Med 1993;13:470-484.

Evans JA, Tavakoli MB. Ultrasonic attenuation and velocity in bone. Phys Med Biol 1990;35:1387-1396.

Eyrich GKH. Laser-osteotomy induced changes in bone. Med Laser Appl 2005;20:25-36.

Fabbro R, Fournier J, Ballard P, Devaux D, Virmont J. Physical study of laser-produced plasma in confined geometry. J Appl Phys 1990;68:775-784.

Farrar SR, Attil DC, Dickinson MR, King TA, Blinkhorn AS. Etch rate and spectroscopic ablation studies of Er:YAG laser-irradiated dentine. Appl Opt 1997;36:5641-5646.

Felix MP, Ellis AT. Laser-Induced Liquid Breakdown - A Step-By-Step Account. Appl Phys Lett 1971;19:484-486.

Finley DS, Petersen J, Abdelshehid C, Ahlering M, Chou D, Borin J, Eichel L, McDougall E, Clayman RV. Effect of Holmium:YAG Laser Pulse Width on Lithotripsy Retropulsion in Vitro. J Endourol 2005;19:1041-1044.

Forrer M, Frenz M, Romano V, Altermatt HJ, Weber HP, Silenok A, Istomyn M, Konov VI. Bone-ablation mechanism using CO₂ lasers of different pulse duration and wavelength. Appl Phys B 1993;56:104-112.

Foth HJ, Meyer D, Stockel T. Side effects of laser tissue interaction studied by laser Doppler vibrometry. Proc SPIE 2000;4072:392-400.

Fradin DW, Bloembergen N, Letellier JP. Dependence of laser-induced breakdown field strength on pulse duration. Appl Phys Lett 1973;22:635-637.

Freiberg RJ, Cozean C. Pulsed erbium laser ablation of hard dental tissue: the effects of atomized water spray vs water surface film. SPIE Proc 2002;4610:74-84.

Frenz M. IR-lasers in medicine - basics and applications (Habilitationsschrift). Bern: Universitat Bern, 1998.

Frenz M, Könz F, Pratisto H, Weber HP. Starting mechanisms and dynamics of bubble formation induced by a Ho:Yttrium aluminum garnet laser in water. J Appl Phys 1998;84:5905-5912.

Frenz M, Pratisto H, Ith M, Konz F, Weber HP. Effects of simultaneously fiber transmitted erbium and holmium radiation on the interaction with highly absorbing media. Proc SPIE 1995;2391:517-524.

Frenz M, Pratisto H, Konz F, Jansen ED, Welch AJ. Comparison of the effects of absorption coefficient and pulse duration of 2.12 μ m and 2.79 μ m radiation on laser ablation of tissue. IEEE J Quantum Electron 1996;32:2025-2036.

Frenz M, Romano V, Zweig AD, Weber HP. Instabilities in laser cutting of soft media. J Appl Phys 1989;66:4496-4503.

Frenz M, Zweig AD, Romano V, Weber HP. Dynamics in laser cutting of soft media. Proc SPIE 1990;1202:22-33.

Fried D, Ashouri N, Breunig T, Shori R. Mechanism of Water Augmentation During IR Laser Ablation of Dental Enamel. Lasers Surg Med 2002;31:186-193.

Fried NM. Potential applications of the erbium:YAG laser in endourology. *J Endourol* 15;15:889-894.

Gagliano FP, Paek UC. Observation of laser-induced explosion of solid materials and correlation with theory *Appl Opt* 1974;13:274-279.

Garry R, Shelley-Jones D, Mooney P, Phillips G. Six hundred endometrial laser ablations. *Obstetrics & Gynecology* 1995;85:24-29.

Gong H, Li C, Li Z. CW-laser-induced thermal and mechanical damage in optical materials. *Proc SPIE* 1998;3578:576-583.

Gonzalez C, Van De Merwe WP, Smith M, Reinisch L. Comparison of the erbium yttrium aluminum garnet and carbon dioxide lasers for in vitro bone and cartilage ablation. *Laryngoscope* 1990;100:13-17.

Grad L, Možina J. Optoacoustic Studies of Er:YAG Laser Ablation in Hard Dental Tissue. *SPIE Proc* 1994;2128:456-465.

Grasso M, Chalik Y. Principles and Applications of Laser Lithotripsy: Experience with the Holmium Laser Lithotrite. *J Clin Lasers Med & Surg* 1998;1998:3-7.

Grasso M, Conlin M, Bagley D. Retrograde ureteropyeloscopic treatment of 2 cm or greater upper urinary tract and minor staghorn calculi. *J Urol* 1998;160:346-351.

Griffin RD, Justus BL, Campillo AJ, Goldberg LS. Interferometric studies of the pressure of a confined laser-heated plasma. *J Appl Phys* 1986;59:1968-1971.

Hale GM, Querry MR. Optical constants of water in the 200 nm to 200 mm wavelength region. *Appl Opt* 1973;12:555-563.

Hammitt G. Cavitation and Multiphase Flow Phenomena. New York: McGraw-Hill, 1980.

Harrington JA. Infrared fibers and their applications. Bellingham: SPIE Press, 2004.

Harrington JA, Matsuura Y. Review of hollow waveguide technology. *Proc SPIE* 1995;2396:4-14.

Harris DC, Bertolucci MD. Symmetry and Spectroscopy: An Introduction to Vibrational and Electronic Spectroscopy. New York: Dover Publications, 1990.

Hassan R, Caputo AA, Bunshah RF. Fracture Toughness of Human Enamel. *J Dent Res* 1981;60:820-827.

Hibst R, Keller U. Mechanism of Er:YAG laser induced ablation of dental hard substances. *SPIE Proc* 1993;1880:156-162.

Hibst R, Keller U. Er:YAG laser for dentistry: basics, actual questions, and perspectives. *SPIE Proc* 1994;2327:76-86.

Hofstetter A. Lasers in urology. *Lasers Surg Med* 1986;6:412-414.

Hohenleutner U, Hohenleutner S, Baumler W, Landthaler M. Fast and effective skin ablation with an Er:YAG laser: determination of ablation rates and thermal damage zones. *Lasers Surg Med* 1997;20:242-247.

Hong MH, Koh ML, Zhu S, Lu YF, Chong TC. Steam-assisted laser ablation and its signal diagnostics. *Appl Surf Sci* 2002;197-198:911-914.

Hossain M, Nakamura Y, Yamada Y, Kimura Y, Matsumoto N, Matsumoto K. Effects of Er,Cr:YSGG Laser Irradiation in Human Enamel and Dentin: Ablation and Morphological Studies. *J Clin Laser Med Sur* 1999;17:155-159.

Huang D, Swanson EA, Lin CP, Schuman JS, Stinson WG, Chang W, Hee MR, Flotte TJ, Gregory K, Puliafito CA, Fujimoto JG. Optical coherence tomography. *Science* 1991;254:1178-1181.

Imen K, Lee SJ, Allen SD. Laser-assisted micron scale particle removal. *Appl Phys Lett* 1991;58:203-205.

Isner JM. "Blood," in Cardiovascular laser therapy. Isner J., Clarke R., eds., editors. New York: Raven Press, 1989.

Isselin JC, Alloncle AP, Autric M. On laser induced single bubble near a solid boundary: Contribution to the understanding of erosion phenomena. *J Appl Phys* 1998;84:5766-5771.

Ith M, Pratisto H, Altermatt HJ, Frenz M, Weber HP. Dynamics of laser-induced channel formation in water and influence of pulse duration on the ablation of

biotissue under water with pulsed erbium-laser radiation. Appl Phys B 1994;59:621-629.

Itzkan I, Albagli D, Dark ML, Perelman LT, von Rosenberg C, Feld MS. The thermoelastic basis of short pulsed laser ablation of biological tissue. Proc Natl Acad Sci USA 1995;92:1960-1964.

Ivanenko MM, Eyrich G, Bruder E, Hering P. In vitro incision of bone tissue with a Q-switch CO₂ laser. Histological examination. Lasers Life Sci 2000;9:171-179.

Ivanenko MM, Fahimi-Weber S, Mitra T, Wierich W, Hering P. Bone Tissue Ablation with sub- μ s Pulses of a Q-switched CO₂ Laser: Histological Examination of Thermal Side-Effects. Lasers Med Sci 2002;17:258-264.

Ivanenko MM, Hering P. Wet bone ablation with mechanically Q-switched high-repetition-rate CO₂ laser. Appl Phys B 1998;67:395-397.

Iwai K, Shi Y, Nito K, Matsuura Y, Kasai T, Miyagi M, Saito S, Arai Y, Ioritani N, Okagami Y, Nemec M, Sulc J, Jelinkova H, Zavoral M, Kohler O, Drlik P. Erbium:YAG laser lithotripsy by use of a flexible hollow waveguide with an end-scaling cap. Appl Opt 2003;42:2431-2435.

Iwai K, Shi YW, Matsuura Y, Miyagi M, Saito S, Arai Y. Characteristics of calculus fragmentation with Er:YAG laser light emitted by an infrared hollow optical fiber with various sealing caps. Appl Opt 2005;44:3266-3270.

Izatt JA, Albagli D, Itzkan I, Feld MS. Pulsed laser ablation of calcified tissue: physical mechanisms and fundamental parameters. SPIE Proc 1990;1202:133-140.

Izatt JA, Kulkarni MD, Yazdanfar S, Barton JK, Welch AJ. In vivo bidirectional color doppler flow imaging of picoliter blood volumes using optical coherence tomography. Opt Lett 1997;22:1439-1441.

Izatt JA, Sankey ND, Partovi F, Fitzmaurice M, Rava RP, Itzkan I, Feld MS. Ablation of calcified biological tissue using pulsed laser hydrogen fluoride laser radiation. IEEE J Quantum Electron 1990;26:2261-2270.

Jacques SL. Laser-tissue interactions: photochemical, photothermal, and photomechanical. Surg Clin N Am 1992;72:531-558.

Jacques SL. Role of tissue optics and pulse duration on tissue effects during high-power laser irradiation. *Appl Opt* 1993;32:2447-2454.

Jansen ED. Pulsed laser ablation of biological tissue: influence of laser parameters and tissue properties on thermal and mechanical damage (Doctoral Dissertation). Austin: The University of Texas at Austin, 1994.

Jasen ED, van Leeuwen TG, Motamedi M, Borst C, Welch AJ. Partial vaporization model for pulsed mid-infrared laser ablation of water. *J Appl Phys* 1995;78:564-571.

Jansen ED, Asshauer T, Frenz M, Motamedi M, Delacretaz G, Welch AJ. Effect of Pulse Duration on Bubble Formation and Laser-induced Pressure Waves During Holmium Laser Ablation. *Lasers Surg Med* 1996;18:278-293.

Jansen ED, van Leeuwen TG, Motamedi M, Borst C, Welch AJ. Temperature dependency of the absorption coefficient of water for mid-infrared laser radiation. *Lasers Surg Med* 1994;14:258-264.

Jansen ED, Tuong LE, Welch AJ. Excimer, Ho:YAG, and Q-switched Ho:YAG ablation of aorta: a comparison of temperatures and tissue damage in vitro. *Appl Opt* 1993;32:526-534.

Jiang ZX, Whitehurst C, King TA. Fragmentation methods in laser lithotripsy. *Proc SPIE* 1991;1421:88-99.

Kang HW, Lee H, Chen S, Welch AJ. Enhancement of Bovine Bone Ablation Assisted by a Transparent Liquid Layer on a Target Surface. *IEEE J Quantum Electron* 2006;42:633-642.

Kang HW, Lee H, Teichman JMH, Oh J, Kim J, Welch AJ. Dependence of Calculus Retropulsion on Pulse Duration During Ho:YAG Laser Lithotripsy. *Lasers Surg Med* 2006;38:762-772.

Kang HW, Rizioiu I, Welch AJ. Mechanism of Spray-assisted Laser Ablation of Dental Hard Tissue. *Biophys J* 2006; to be submitted

Kang HW, Welch AJ, Simanovskii D, Schwettman AH, Lee H. Laser ablation in a liquid-confined environment using a nanosecond laser pulse. *Opt Express* 2006; to be submitted

Kazakevich PV, Voronov VV, Simakin AV, Shafeev GA. Production of copper and brass nanoparticles upon laser ablation in liquids. *Quantum Electron* 2004;34:951-956.

Kelly R, Miotello A. Comments on explosive mechanisms of laser sputtering. *Appl Surf Sci* 1996;96-98:205-215.

Kim D, Lee H. Enhanced ablation and photoacoustic excitation in near-threshold laser ablation of liquid-coated surfaces. *J Appl Phys* 2001;89:5703-5706.

Kim D, Oh B, Lee H. Effect of liquid film on near-threshold laser ablation of a solid surface. *Appl Surf Sci* 2004;222:138-147.

Kitai MS, Sobol EN, Sviridov AP, Omel'chenko AI. Manifestations of photochemical reactions in bone tissue on exposure to the ultraviolet radiation of an Eximer laser. *Biophysics* 1996;41:1151-1157.

Knudsen B, Stallman KJ, Glickman RD, Denstedt JD, Teichman JMH. Comparison of seven holmium:YAG laser fibers. *J Endourol* (in press)

Koort HJ, Tischer C, Rasch R, Thiede C, WOM World Of Medicine AG B.G. Laser induced shockwave generation for use in lithotripsy. *Proc SPIE* 2002;4609:137-140.

Kourambas J, Delvecchio FC, Preminger GM. Low-power holmium laser for the management of urinary tract calculi, strictures, and tumors. *J Endourol* 2001;15:529-532.

Kozodoy RL, Pagkalinawan AT, Harrington JA. Small-bore hollow waveguides for delivery of 3-mm laser radiation. *Appl Opt* 1996;35:1077-1082.

Kruusing A. Underwater and water-assisted laser processing: Part I - general features, steam cleaning and shock processing. *Opt Laser Eng* 2004;41:307-327.

Kuroda S, Fowler BO. Compositional, structural, and phase changes in in vitro laser-irradiated human tooth enamel. *Calcif Tissue Int* 1984;36:361-369.

Kuznetsov LI. Recoil momentum at a solid surface during developed laser ablation. *Quantum Electron* 1993;23:1035-1038.

Lee H. Pulsed-laser induced material and its clinical applications (Doctoral dissertation). Austin: The University of Texas at Austin, 2003.

Lee H, Kang HW, Teichman JMH, Oh J, Welch AJ. Urinary Calculus Fragmentation During Ho:YAG and Er:YAG Lithotripsy. *Lasers Surg Med* 2006;38:39-51.

Lee H, Ryan RT, Kim JH, Choi B, Arakeri NV, Teichman JMH, Welch AJ. Dependence of Calculus Retropulsion Dynamics on Fiber Size and Radiant Exposure During Ho:YAG Lithotripsy. *J Biomech Eng* 2004;126:507-515.

Lee H, Ryan RT, Teichman JMH, Kim J, Choi B, Arakeri NV, Welch AJ. Stone retropulsion during holmium:YAG lithotripsy. *J Urol* 2003;169:881-885.

Levin K, Tran D, Tchapanjiov A, Fried NM. Specialty fiber expands infrared laser applications. *Biophotonics Int* 2004;11:41-43.

Li Z, Code J, Van de Merwe. Er:YAG laser ablation rate at various fluences and pulse repetition rates. *Lasers Surg Med* 1992;126:625-630.

Li Z, Reinisch L, Van de Merwe WP. Bone ablation with Er:YAG and CO₂ laser: study of thermal and acoustic effects. *Lasers Surg Med* 1992;12:79-85.

Lide DR. *CRC Handbook of Chemistry and Physics*. Boca Raton: Taylor and Francis, 2006.

Lo EY, Petschek H, Rosen DI. A hydrodynamic model for the laser-induced fragmentation of calculi. *Lasers Life Sci* 1990;3:233-244.

Loesel FH, Fischer JP, Götz MH, Horvath C, Juhasz T, Noack F, Suhm N, Bille JF. Non-thermal ablation of neural tissue with femtosecond laser pulses. *Appl Phys B* 1998;66:121-128.

Lu J, Xu RQ, Chen X, Shen ZH, Ni XW, Zhang SY, Gao CM. Mechanisms of laser drilling of metal plates underwater. *J Appl Phys* 2004;95:3890-3894.

Lukač M, Grad L, Možina J. Optoacoustic Effects during Er:YAG Laser Ablation in Hard Dental Tissue. *SPIE Proc* 1994;2327:93-100.

Luo C, Liu X, Poddar R, Garra J, Gadre AP, Keuren EV, Schneider T, White R, Currie J, Paranjape M. Thermal ablation of PMMA for water release using a microheater. *J Micromech Microeng* 2006;16:580-588.

Mackanos MA, Jansen ED, Shaw BL, Sanghera JA, Aggarwal I, Katzir A. Delivery of midinfrared (6 to 7-mm) laser radiation in a liquid environment using infrared-transmitting optical fibers. *J Biomed Opt* 2003;8:583-593.

Majaron B, Plestenjak P, Lukac M. Thermo-mechanical laser ablation of soft biological tissue: modeling the micro-explosions. *Appl Phys B* 1999;69:71-80.

Majaron B, Šušterčič D, Lukač M. Influence of water spray on Er:YAG ablation of hard dental tissues. *SPIE Proc* 1997;3192:82-87.

Majaron B, Šušterčič D, Lukač M, Skalerič U, Funduk N. Heat diffusion and debris screening in Er:YAG laser ablation of hard biological tissues. *Appl Phys B* 1998;66:479-487.

Majaron B, Sustercic D, Lukac M. Influence of water spray on Er:YAG ablation of hard dental tissues. *SPIE Proc* 1997;3192:82-87.

Marguet CG, Sung JC, Springhart WP, L'esperance JO, Zhou S, Zhong P, Albala DM, Preminger GM. In vitro comparison of stone retropulsion and fragmentation of the frequency doubled, double pulse Nd:YAG laser and the holmium:YAG laser. *J Urol* 2005;173:1797-1800.

Matsuura Y, Abel T, Harrington JA. Optical properties of small-bore hollow glass waveguides. *Appl Opt* 1995;34:6842-6847.

Merberg GN. Current status of infrared fiber optics for medical laser power delivery. *Lasers Surg Med* 1993;13:572-576.

Merberg GN, Harrington JA. Optical and mechanical properties of single-crystal sapphire optical fibers. *Appl Opt* 1993;32:3201-3209.

Miller JC. Laser ablation: principles and applications. Berlin: Springer-Verlag, 1994.

Mills AF. Basic heat and mass transfer. Saddle River: Prentice-Hall, Inc., 1999.

Miyashita T, Manabe T. Infrared optical fibers. IEEE J Quantum Electron 1982;18:1432-1450.

Mohri S, Kasai T, Abe Y, Shi Y, Matsuura Y, Miyagi M. Optical properties of end-sealed hollow fibers. Appl Opt 2002;41:1251-1255.

Moore JH. Laser energy in orthopedic surgery. Amsterdam: Excerpta Medica, 1973.

Morse PM, Ingard KU. Theoretical Acoustics. New York: McGrawHill Book Co., 1968.

Motamedi M, Rastegar S, Anvari B. Thermal stress distribution in laser irradiated dental tissue, implications for dental applications. SPIE Proc 1992;1646:315-321.

Mulvaney WP, Beck CW. The laser beam in urology. J Urol 1968;99:112-115.

Nahen K, Vogel A. Investigations on Acoustic On-line Monitoring of IR Laser Ablation of Burned Skin. Lasers Surg Med 1999;25:69-78.

Nahen K, Vogel A. Plume dynamics and shielding by the ablation plume during Er:YAG laser ablation. J Biomed Opt 2002;7:165-178.

Neev J, Pham K, Lee JP, White JM. Dentin ablation with three infrared lasers. Lasers Surg Med 1996;18:121-128.

Nelson JS, Orenstein A, Liaw LL, Berns MW. Mid-infrared Erbium:YAG laser ablation of bone: the effect of laser osteotomy on bone healing. Lasers Surg Med 1989;9:363-374.

Niemz MH. Laser-tissue interactions. Berlin: Springer-Verlag, 1996.

Nishioka NS, Domankevitz Y. Reflectance during pulsed holmium laser irradiation of tissue. Lasers Surg Med 1989;9:375-381.

Nishioka NS, Kelsey PB, Kibbi A, Delmonico F, Parrish JA, Anderson RR. Laser lithotripsy: animal studies of safety and efficacy. Lasers Surg Med 1988;8:357-362.

Nishioka NS, Levins PC, Murray SC, Parrish JA, Anderson RR. Fragmentation of biliary calculi with tunable dye lasers. Gastroenterology 1987;93:250-255.

Nubling RK, Harrington JA. Optical properties of single-crystal sapphire fibers. *Appl Opt* 1997;36:5934-5940.

Olshansky R, Scherer GW. High GeO₂ optical waveguide. *Tech Dig 5th European Conference on Optical Communications (The Netherland)* 1979;12:5-1.

Palik ED. *Handbook of optical constants of solids* New York: Academic Press, Inc., 1985.

Palik ED. *Handbook of optical constants of solids III*. San Diego: Academic Press, Inc., 1988.

Paltauf G, Schmidt-Kloiber H. Model study to investigate the contribution of spallation to pulsed laser ablation of tissue. *Laser Surg Med* 1995;16:277-287.

Peavy GM, Reinisch L, Payne JT, Venugopalan V. Comparison of Cortical Bone Ablations by Using Infrared Laser Wavelengths 2.9 to 9.2 μm . *Lasers Surg Med* 1999;26:421-434.

Pfefer TJ, Choi B, Vargas G, McNally KM, Welch AJ. Pulsed laser-induced thermal damage in whole blood. *ASME J Biomech Eng* 2000;122:196-202.

Pratisto H, Frenz M, Ith M, Altermitt HJ, Jansen ED, Weber HP. Combination of fiberguided pulsed erbium and holmium laser radiation for tissue ablation under water. *Appl Opt* 1996;35:3328-3337.

Pratisto H, Frenz M, Ith M, Romano V, Felix D, Grossenbacher R, Altermitt HJ, Weber HP. Temperature and pressure effects during erbium stapedotomy. *Lasers Surg Med* 1996;18:100-108.

Pratisto H, Ith M, Frenz M, Weber HP. Infrared multi-wavelength laser system for establishing a surgical delivery path through water. *Appl Phys Lett* 1995;67:1963-1965.

Pryshlak AP, Dugan JR, Fitzgibbon JJ, Saphikon Inc. Advancements in sapphire optical fibers for the delivery of Erbium laser energy and IR sensor applications. *Proc SPIE* 1996;2677:35-42.

Puliafito C, Steinert R. Short-pulsed Nd:YAG laser microsurgery of the eye: Biophysical considerations. *IEEE J Quantum Electron* 1984;QE20:1442-1448.

Quintana E, Marques F, Roca I, Torres V, Salgado J. Some morphologic changes induced by Nd:YAG laser on the noncoated enamel surface: A scanning electron microscopy study. *Lasers Surg Med* 1992;12:131-136.

Rastegar D. Laser ablation of biological tissue (Doctoral Dissertation). Austin: The University of Texas at Austin, 1987.

Reiss SM. New frontiers emerge in optical fibers. *Biophotonics Int* 2001;8:44-51.

Ren J, Kelly M, Heeselink L. Laser ablation of silicon in water with nanosecond and femtosecond pulses. *Opt Lett* 2005;30:1740-1742.

Rink K, Delacretaz G, Salathe RP. Fragmentation process induced by microsecond laser pulses during lithotripsy. *Appl Phys Lett* 1992;61:258-260.

Rink K, Delacretaz G, Salathe RP. Fragmentation process induced by nanosecond laser pulses. *Appl Phys Lett* 1992;61:2644-2646.

Rink K, Delacretaz G, Salathe RP. Influence of the pulse duration on laser-induced mechanical effects. *Proc SPIE* 1994;2077:181-194.

Rink K, Delacretaz G, Salathe RP. Fragmentation process of current laser lithotriptors. *Lasers Surg Med* 1995;16:134-146.

Rizioiu I, Kimmel AI, Eversole LR. The effects of an Er,Cr:YSGG laser on canine oral hard tissues. *SPIE Proc* 1996;2922:74-83.

Rizioiu I, Kohanghadosh F, Kimmel AI, Eversole LR. Pulpal thermal responses to an erbium, chromium:YSGG pulsed laser hydrokinetic system. *Oral Surg Oral Med Oral Pathol Oral Radiol Endod* 1998;86:220-223.

Rizioiu IM, DeShazer L. New laser-matter interaction concept to enhance hard tissue cutting efficiency. *SPIE Proc* 1994;2134A:

Ross EV, Domankevitz Y, Skrobal M, Anderson RR. Effects of CO₂ laser pulse duration in ablation and residual thermal damage: Implications for skin resurfacing. *Lasers Surg Med* 1996;19:123-129.

Samsonov GV. Handbook of the physicochemical properties of the elements. New York: IFI-Plenum, 1968.

Sayer J, Johnson DE, Price RE, Cromeens DM. Endoscopic laser fragmentation of ureteral calculi using the Holmium:YAG. Proc SPIE 1993;1879:143-148.

Schafer SA, Durville FM, Jassemnejad B, Bartels KE, Powell RC. Mechanisms of biliary stone fragmentation using the Ho:YAG laser. IEEE Trans Biomed Eng 1994;41:276-283.

Schmidlin FR, Beghuin D, Delacretaz GP, Venzi G, Jichlinski P, Rink K, Leisinger HJ, Graber P. Laser lithotripsy with the Ho:YAG laser: fragmentation process revealed by time-resolved imaging. Proc SPIE 1998;3245:123-126.

Schmidt-Kloiber H, Reichel E, Schoffmann H. Laser-induced Shock-Wave Lithotripsy (LISL). Biomedizinische Technik 1985;30:173-181.

Shangguan H, Casperson LW, Prahl SA. Pressure impulses during microsecond laser ablation. Appl Opt 1997;36:9034-9041.

She M, Kim D, Grigoropoulos CP. Liquid-assisted pulsed laser cleaning using near-infrared and ultraviolet radiation. J Appl Phys 1999;86:6519-6524.

Siegman AE, Sasnett MW, Johnston Jr TF. Choice of clip levels for beam width measurements using knife-edge techniques. IEEE J Quantum Electron 1991;27:1098-1104.

Sofer M, Watterson JD, Wollin TA, Nott L, Razvi H, Denstedt JD. Holmium:YAG laser lithotripsy for upper urinary tract calculi in 598 patients. J Urol 2002;167:31-34.

Spindel ML, Moslem A, Bhatia KS, Jassemnejad B, Bartels KE, Powell RC, O'Hare CM, Tytle T. Comparison of holmium and flashlamp pumped dye lasers for use in lithotripsy of biliary calculi. Lasers Surg Med 1992;12:482-489.

Spore SS, Teichman JMH, Corbin NS, Champion PC, Williamson EA, Glickman RD. Holmium:YAG lithotripsy: optimal power settings. J Endourol 1999;13:559-566.

Staninec M, Xie J, Le CQ, Fried D. Influence of an Optically Thick Water Layer on the Bond-Strength of Composite Resin to Dental Enamel After IR Laser Ablation. Lasers Surg Med 2003;33:264-269.

Stern RH, Sognnaes RF, Goodman F. Laser effect on in vitro enamel permeability and solubility. J Am Dent Assoc 1966;78:838-843.

Stern RH, Vahl J, Sognnaes RF. Ultra structural observations of pulsed carbon dioxide laser effects. J Dent Res 1972;51:455-460.

Stock K, Hibst R, Keller U. Comparison of Er:YAG and Er:YSGG Laser Ablation of Dental Hard Tissues. SPIE Proc 1997;3192:88-95.

Tam AC, Leung WP, Zapka W, Ziemlich W. Laser-cleaning techniques for removal of surface particulates. J Appl Phys 1992;71:3515-3523.

Teichman JMH. Holmium:YAG lithotripsy for large renal and bladder calculi: Strategies for efficient lithotripsy. J Endourol 1999;13:477-482.

Teichman JMH. Acute colic from ureteral calculus. N Engl J Med 2004 (in progress);

Teichman JMH, Chan KF, Cecconi PP, Corbin NS, Kamerer AD, Glickman RD, Welch AJ. Erbium:YAG versus Holmium:YAG lithotripsy. J Urol 2001;165:876-879.

Teichman JMH, Johnson AJ, Yates JT, Angle BN, Dirks MS, Muirhead JT, Thompson IM, Pearle MS. Color vision deficits during laser lithotripsy using safety goggles for coumarin green or alexandrite but not with holmium:YAG laser safety goggles. J Urol 1998;159:683-689.

Teichman JMH, Rao RD, Rogenes VJ, Harris JM. Ureteroscopic management of ureteral calculi: electrohydraulic versus holmium:YAG lithotripsy. J Urol 1997;158:1357-1361.

Teichman JMH, Vassar GJ, Bishoff JT, Bellman GC. Holmium:YAG lithotripsy yields smaller fragments than lithoclast, pulsed dye laser or electrohydraulic lithotripsy. J Urol 1998;159:17-23.

Teichman JMH, Vassar GJ, Glickman RD. Holmium:yttrium-aluminum-garnet lithotripsy efficiency varies with stone composition. Urology 1998;52:392-397.

Teng P, Nishioka NS, Anderson RR, Deutsch TF. Acoustic studies of the role of immersion in plasma-mediated laser ablation. IEEE J Quantum Electron 1987;23:1845-1852.

Teng P, Nishioka NS, Anderson RR, Deutsch TF. Optical studies of pulsed-laser fragmentation of biliary calculi. *Appl Phys B* 1987;42:73-78.

Teng P, Nishioka NS, Farinelli WA, Anderson RR, Deutsch TF. Microsecond-long flash photography of laser-induced ablation of biliary and urinary calculi. *Lasers Surg Med* 1987;7:394-397.

Teng P, Nishioka SS, Anderson RR, Deutsch TF. Optical studies of pulsed-laser fragmentation of biliary calculi. *Appl Phys B* 1987;42:73-78.

Tischer C, Koort HJ, Bazo A, Rasch R, Thiede C, World of Medicine Inc., Dept. of Medical Lasers, Orlando and Berlin *et al.* Clinical experiences with a new Frequency-doubled Double-pulse Nd:YAG Laser (FREDDY) for the treatment of urolithiasis. *Proc SPIE* 2002;4609:128-135.

Uhlhorn SR. Free Electron Laser Ablation of Soft Tissue: The Effects of Chromophore and Pulse Characteristics on Ablation Mechanics (Doctoral Dissertation). Nashville: Vanderbilt University, 2002.

Uhlhorn SR, Mongin D, Mackanos MA, Jansen ED. Effects of IR wavelength on ablation mechanics: A study of acoustic signals. *SPIE Proc* 2001;4257:178-183.

Van Leeuwen TG, van der Veen MJ, Verdaasdonk RM, Borst C. Non-contact tissue ablation by holmium:YSGG laser pulses in blood. *Lasers Surg Med* 1991;11:26-34.

van Swol CFP, Verdaasdonk RM, Zeijlemaker BYW, Grimbergen MCM, Boon TA. Optimization of the dosimetry and safety using the Holmium laser for urology. *Proc SPIE* 1998;3245:110-116.

Vandeursen H, Pittomvils G, Boving R, Baert L. High energy pulsed dye laser lithotripsy: management of ureteral calcium oxalate monohydrate calculi. *J Urol* 1991;145:1146-1150.

Vassar GJ, Teichman JM, Glickman RD. Holmium:YAG lithotripsy efficiency varies with energy density. *J Urol* 1998;160:471-476.

Vassar GJ, Teichman JMH, Glickman RD, Weintraub SE, Chan KF, Pfefer TJ, Welch AJ. Holmium:YAG lithotripsy: photothermal mechanism. *J Endourol* 1999;13:181-189.

Venugopalan V, Nishioka NS, Mikic BB. The Thermodynamic Response of Soft Biological Tissues to Pulsed Ultraviolet Laser Irradiation. *Biophys J* 1995;69:1259-1271.

Verdaasdonk RM, van Swol CF. Laser light delivery systems for medical applications. *Phys Med Bio* 1997;42:869-894.

Visuri SR, Walsh JT J., Wigdor HA. Erbium Laser Ablation of Dental Hard Tissue: Effect of Water Cooling. *Lasers Surg Med* 1996;18:294-300.

Vogel A. Nonlinear absorption: intraocular microsurgery and laser lithotripsy. *Phys Med Bio* 1997;42:895-912.

Vogel A, Busch S, Parlitz U. Shockwave emission and cavitation bubble generation by picosecond and nanosecond optical breakdown in water. *J Acoust Soc Am* 1996;100:148-165.

Vogel A, Hentschel W, Holzfuss J, Lauterborn W. Cavitation bubble dynamics and acoustic transient generation in ocular surgery with pulsed neodymium:YAG lasers. *Ophthalmology* 1986;93:1259-1269.

Vogel A, Nahen K, Theisen D, Noack J. Plasma Formation in Water by Picosecond and Nanosecond Nd:YAG Laser Pulses - Part I: Optical Breakdown at Threshold and Superthreshold Irradiance. *IEEE J Sel Top Quantum Electron* 1996;2:847-860.

Vogel A, Noack J, Nahen K, Theisen D, Busch S, Parlitz U, Hammer DX, Noojin GD, Rockwell BA, Birngruber R. Energy balance of optical breakdown in water at nanosecond to femtosecond time scales. *Appl Phys B* 1999;68:271-280.

Vogel A, Schweiger P, Frieser A, Asiy MN, R B. Intraocular Nd:YAG laser surgery: light-tissue interaction, damage range, and reduction of collateral effects. *IEEE J Quantum Electron* 1990;26:2240-2260.

Vogel A, Venugopalan V. Mechanisms of Pulsed Laser Ablation of Biological Tissues. *Chem Rev* 2003;103:577-644.

Walsh JT, Deutsch TF. Er:YAG laser ablation of tissue: measurement of ablation rates. *Lasers Surg Med* 1989;9:327-337.

Walsh JT, Deutsch TF. Measurement of Er:YAG laser ablation plume dynamics. *Appl Phys B* 1991;52:217-224.

Wang Y, Matsuura Y, Miyagi M. Robust hollow devices and waveguides for Er:YAG laser radiation. *Opt Laser Tech* 1997;29:449-453.

Watson G. The pulsed dye laser for urinary calculi in 600 patients. *Proc SPIE* 1990;1200:66.

Watson G, Smith N. A comparison of the pulsed dye and holmium lasers for stone fragmentation: in vitro studies and clinical experience. *Proc SPIE* 1993;1879:139-142.

Watson G, Wickham JEA, Mills TN, Bown SG, Swain P, Salmon PR. Laser fragmentation of renal calculi. *Br J Urol* 1983;55:613-616.

Watson GM, Jacques SL, Dretler SP, Parrish JA. Tunable pulsed dye laser for fragmentation of urinary calculi. *Lasers Surg Med* 1985;5:160.

Watson GM, Murray S, Dretler SP, Parrish JA. The pulsed dye laser for fragmenting urinary calculi. *J Urol* 1987;138:195-198.

Welch AJ, Kang HW, Lee H, Teichman JMH. Calculus fragmentation in laser lithotripsy. *Minerva Urol Nefrol* 2004;56:49-63.

Welch AJ, van Gemert MJC. Optical-thermal response of laser-irradiated tissue. New York: Plenum Press, 1995.

Wesendahl T, Janknecht P, Ott B, Frenz M. Erbium:YAG laser ablation of retinal tissue under perfluorodecalin: determination of laser-tissue interaction in pig eye. *Invest Ophthalmol Visual Sci* 2000;41:505-512.

White MD, Moran ME, Calvano CJ, A B.-m., Mehlhaff BA. Evaluation of Retropulsion Caused by Holmium:YAG Laser with Various Power Settings and Fibers. *J Endourol* 1998;12:183-186.

Wigdor H, Visuri SR, Walsh JT J. Effect of Water on Dental Material Ablation of the Er:YAG laser. *SPIE Proc* 1994;2128:267-272.

Wollin TA, Denstedt JD. The holmium laser in urology. *J Clin Lasers Med & Surg* 1998;16:13-20.

- Wong B, Sung V, Berns MW, Svaasand LO, Neev J. Holmium-YAG laser ablation characteristics in calvarial lamellar and cortical bone: the role of water and tissue micro-architecture. *Lasers Med Sci* 1995;10:181-188.
- Yamamoto K, Ishida H. Optical Theory Applied to Infrared Spectroscopy. *Vibrational Spectrosc* 1994;8:1-36.
- Yang Y, Chaney CA, Fried NM. Erbium:YAG laser lithotripsy using hybrid germanium/silica optical fibers. *J Endourol* 2004;18:830-835.
- Yavas O, Leiderer P, Park HK, Grigoropoulos CP, Poon CC, Leung WP, Do N, Tam AC. Optical Reflectance and Scattering Studies of Nucleation and Growth of Bubbles at a Liquid-Solid Interface Induced by Pulsed Laser Heating. *Phys Rev Lett* 1993;70:1830-1833.
- Yiu MK, Liu PL, Yiu TF, Chan AYT. Clinical experience with holmium:YAG laser lithotripsy of ureteral calculi. *Lasers Surg Med* 1996;19:103-106.
- Yoo JH, Jeong SH, Mao XL, Greif R, Russo RE. Evidence for phase-explosion and generation of large particles during high power nanosecond laser ablation of silicon. *Appl Phys Lett* 2000;76:783-785.
- Young FR. Cavitation. London: McGraw-Hill, 1989.
- Zapka W, Ziemlich W. Efficient pulsed laser removal of 0.2 mm sized particles from a solid surface. *Appl Phys Lett* 1991;58:2217-2219.
- Zenzie HH, Altshuler GB, Smirnov MZ, Anderson RR. Evaluation of cooling methods for laser dermatology. *Lasers Surg Med* 2000;26:130-144.
- Zhang W, Yao YL, Noyan IC. Microscale Laser Shock Peening of Thin Films, Part 1: Experiment, Modeling and Simulation. *J Manuf Scie-T ASME* 2004;126:10-17.
- Zhigilei LV, Garrison BJ. Microscopic mechanisms of laser ablation of organic solids in the thermal and stress confinement irradiation regimes. *J Appl Phys* 2000;88:1281-1298.

Zhong P, Chuong CJ, Preminger GM. Characterization of fracture toughness of renal calculi using a microindentation technique. *J Mater Sci Lett* 1993;12:1460-1462.

Zhong P, Tong HL, Cocks FH, Pearle MS, Preminger GM. Transient cavitation and acoustic emission produced by different laser lithotripters. *J Endourol* 1998;12:371-378.

Zhu S, Lu YF, Hong MH. Laser ablation of solid substrates in a water-confined environment. *Appl Phys Lett* 2001;79:1396-1398.

Zorcher T, Hochberger J, Schrott K, Kuhn R, Schafhauser W. In vitro study concerning the efficiency of the frequency-doubled double-pulse Neodymium:YAG laser (FREDDY) for lithotripsy of calculi in the urinary tract. *Lasers Surg Med* 1999;25:38-42.

Zweig AD, Weber HP. Mechanical and thermal parameters in pulsed laser cutting of tissue. *IEEE J Quantum Electron* 1987;23:1787-1793.

VITA

Hyun Wook Kang was born in Busan, Korea on January 11, 1976, the son of Myung Ae Kim and Dae Sung Kang. He entered Yonsei University in Seoul, Korea in March, 1994 and received the degree of Bachelor of Engineering in Mechanical Engineering in February 2002. Beginning the Fall of 2002, he entered the Graduate School of University of Texas at Austin, earning the degree of Master of Engineering in Mechanical Engineering in December, 2004. He expects to complete his Doctor of Philosophy in Biomedical Engineering in December, 2006. His research interests include clinical and industrial applications of lasers and optics.

Permanent Address: 63-183 8/5, Dongdaesin 3 dong Seo-gu
Busan, Republic of Korea, 602-103

This dissertation was typed by the author.